# Biophysical Modelling of Antimicrobial Peptide's Interactions with Phospholipid and Lipopolysaccharide Membranes

by

Shokoofeh Nourbakhsh

A thesis
presented to the University of Waterloo
in fulfillment of the
thesis requirement for the degree of
Doctor of Philosophy
in
Physics

Waterloo, Ontario, Canada, 2019

**Examining Committee Membership**

The following served on the Examining Committee for this thesis. The decision of the Examining Committee is by majority vote.

| | |
|---|---|
| External Examiner: | Maikel Rheinstadter<br>Professor, Dept. of Physics and Astronomy, McMaster University |
| Supervisor: | Bae-Yeun Ha<br>Professor, Dept. of Physics and Astronomy, University of Waterloo |
| Internal Member: | Zoya Leonenko<br>Professor, Dept. of Physics and Astronomy, University of Waterloo |
| Internal Member: | Jeff Chen<br>Professor, Dept. of Physics and Astronomy, University of Waterloo |
| External Member: | Mohammad Kohandel<br>Professor, Dept. of Applied Mathematics, University of Waterloo |

## Author's Declaration

I hereby declare that I am the sole author of this thesis. This is a true copy of the thesis, including any required final revisions, as accepted by my examiners.

I understand that my thesis may be made electronically available to the public.

**Abstract**

Antimicrobial peptides (AMPs) are naturally-occurring peptide antibiotics. The way they work has inspired a vigorous search for optimized peptide antibiotics for fighting resistant bacteria. Cationic AMPs cleverly utilize their electrostatic interactions with the bacterial membrane to selectively attack bacteria.

Here, we first present a physical model of membrane selectivity of these peptides. For this, we use model membranes: phospholipid bilayers, possibly carrying a certain fraction of anionic lipids. The simultaneous presence of several competing effects (e.g., lipid demixing and peptide-peptide interactions), however, poses a serious challenge to theoretical analysis. We first examine critically various models of peptide-membrane interactions and map out one, which incorporates adequately these competing effects as well as the geometry of various regions in membranes, occupied by bound peptides, anionic lipids within the interaction range of each peptide, and those outside this range. This leads to a systematically-improved model for peptide selectivity. Using the model, we relate the peptide's intrinsic ($C_{\rm cell}$-independent) selectivity to an apparent, $C_{\rm cell}$-dependent one, and clarify the relative roles of peptide parameters and cell densities in determining their selectivity. A natural consequence of this relationship is that the selectivity is more sensitive to peptide parameters at low cell densities; as a result, the optimal peptide charge, at which the selectivity is maximized, increases with the cell density such that this notion becomes less meaningful at high cell densities. It also enables us to map out intrinsic selectivity from apparent ($C_{\rm cell}$-dependent) one or biologically-relevant one from "conveniently-measured" selectivity. This effort will benefit our endeavour in optimizing the peptide parameters for their enhanced selectivity in a physiological environment.

We extend our effort to examine peptide adsorption on the outer membrane (OM) of Gram-negative bacteria (e.g., *Escherichia coli*). In particular, we focus our effort on developing a model for the interaction between AMPs and the wild-type lipopolysaccharide (LPS) layer in a biologically relevant medium, containing monovalent and divalent salt ions like $Mg^{2+}$. This requires a non-trivial generalization of an earlier coarse-grained model, in which the effects of oligosaccharide and O-antigen chains are ignored. In our model, these effects are captured by modelling the LPS layer as forming a polymer brush on top of its anionic phosphate groups. Using this model, we examine how the presence of oligosaccharide and O-antigen chains modifies the binding of antimicrobials to the LPS layer. Our results demonstrate that the presence of the saccharide brush reduces the number of hydrophobically-bound peptides to the polymer-grafted interface of LPS, compared to the deep-rough LPS layer that lacks the polymer brush. Our LPS brush model predicts $\sim 30\%$ reduction of peptide adsorption, which is consistent with recent experimental measure-

ments. This can be attributed to the steric hindrance of the brush or the excluded-volume interaction of the saccharide chains with peptides. At a low cell density limit, we also note that the total number of peptides trapped within the brush is very small, compared to the number of bound peptides on the LPS interface. This implies that the hydrophobic binding of peptides is insensitive to brush lengths. This, however, does not exclude the possibility of kinetic slowing-down of the binding.

**Acknowledgements**

I would like to thank my supervisor Dr. Bae-Yeun Ha for his support and guidance, throughout my Ph.D. years. He patiently helped me to think like a scientist and provided me constant advice by hourlong conversations and responding to my questions and queries so promptly. No doubt, his care and passion for this research project inspired me to work harder every day, and climb my way up to the defence date. I would also like to thank all the members of my advisory committee, Dr. Zoya Leonenko, Dr. Mohammad Kohandel and Dr. Jeff Chen. Their constructive suggestions and comments improved my work during these years. Furthermore, I am grateful to Prof. Maikel Rheinstadter, who kindly accepted to be the external examiner of my thesis. I also acknowledge helpful discussions with Prof. H. Huang for better insight of antimicrobial peptides' cell selectivity. Moreover, my great respect and appreciation go to Dr. Kamran Kaveh for his support during the early years of my doctoral studies. He was a perfect combination of friend, family and physics mentor.

I must express my gratitude to Siavash, my husband, for his continued support and encouragement. His love and confidence in me promoted so much happiness and joy at many stages of the tough road to my Ph.D. I was also blessed with the love and wisdom of my aunt, Forough, who was always there for me at the time of hardships. She taught me to be a strong, independent, and confident woman. There is a special corner in my heart, which will always hold gratitude for my younger sister, Niloufar; who was always looking out for me. Moreover, I should thank my wonderful friends, Zahra, Nastaran, Jairan, Mahsa, Farshad, and Golsa; they surrounded me all these years by the kindness and caring.

In the end, I would like to thank the Natural Sciences and Engineering Research Council (NSERC) of Canada and the Ontario Ministry of Education for their financial assistance.

*Dedication*

*This Ph.D. thesis is dedicated to my beloved family, Siavash, Ladan, Safa, Forough, Ali, Ebrahim and Niloufar, who were my inspiration for science and never stopped their support and love for me.*

# Table of Contents

# List of Figures

# Chapter 1

# Introduction

## 1.1 Motivation and Goals

The excessive use of conventional antibiotics has raised a serious problem known as antibiotic resistance of bacteria. This has inspired extensive research to design and develop new therapeutic compounds as alternatives for conventional antibiotics. During the last couple of decades, naturally-occurring antibiotics, i.e., antimicrobial peptides (AMPs) have been used as templates for developing new therapeutic agents [15, 16, 17, 18].

AMPs or host defence peptides are part of innate immune system of multicellular organism. Their biostructural features have allowed them to kill a wide range of pathogenic microbes, over billions of years. Nevertheless, they have not induced bacterial resistance easily [19, 20, 21]. During the 1980s, pioneering scientists discovered that these simple amphipathic peptides could rapidly kill almost every species of bacteria [22, 23, 24], many species of fungi [25, 26], and even tumour cells [27, 28], while inactivating viruses [29, 30]. Nevertheless, their design principles are relatively simple. Indeed, much effort has led to the discovery of a tremendous range of different naturally occurring antimicrobial peptides in plants and mammals, such as plant thionins [31], amphibian magainins [32] from skin of the frog, insect cecropins [33] and protegrins [34] from mammalian leukocytes.

The important feature of a "good" AMP as an anti-infective agent is to discriminate between host and pathogen cells. This "quality" of AMPs is often measured by their cell selectivity [35]. It is believed that AMPs exhibit cell selectivity, since they are non-hemolytic at densities well above their required minimum concentration for inhibitory activity against bacteria [36, 35, 37]. In earlier studies [38, 16], this was mainly attributed

to the electrostatic attraction among mainly cationic AMPs and negatively-charged bacterial cells. For some reasons, the peptide-synthesis strategies in developing re-engineered peptides for pharmacological purposes, based on our knowledge of host defence biological AMPs, have not been not successful to date. For instance, in-vitro experiments do not replicate the complex in-vivo environment [39, 2]. Most of the antimicrobial peptides discovered in nature (i.e. like magainin) demonstrate high cell selectivity in vitro assays, yet, they exhibit poor therapeutic index when evaluated in the setting of an infected mammal [2]. As a result, a small number of peptides have been evaluated to date for clinical potential, compared to antibiotic development programs [40], and even many of them with very promising future, such as antimicrobial peptide pexiganan (i.e. a 22-amino-acid membrane disruptor analog of the Xenopus peptide magainin) received disapproval from U.S. Food and Drug Administration (FDA) [41].

In search for a comprehensive picture of AMP's cell selectivity and its complex physiological factors, during the last decades, much effort has been devoted to the biophysical analysis and quantitative assessments of peptide-membrane binding procedures [5, 42, 43, 44, 45, 46], in addition to the biochemical structure and identifications [47, 48]. Despite the diversity of AMPs, experiments by X-ray diffraction, Nuclear Magnetic Resonance (NMR) and circular dichroism (CD) spectroscopies revealed the mutual molecular basis for the cell selectivity; including electrostatic net charge, hydrophobicity per residue, helicity, characteristics of the bilayer membrane and etc. ( [38] and references therein). Along this line, systematic thermodynamic examinations on peptide interaction with membrane-mimetic models (i.e. bilayer vesicles) by Seelig and his research group [43, 45, 49, 50, 51], provided a quantitive foundation for binding energy and the individual steps involved in peptide-membrane binding process. Moreover, Hoawng and colleagues explored many-body effects of the membrane-associated peptides (i.e. non-electrostatic peptide-peptide interaction on the membrane) and developed detailed insights into the peptide-induced elastic deformation of the membrane for a diverse range of lipid composition [42, 44, 52, 53, 54, 55]. In fact, this non-electrostatic cooperative activity of peptides on the membrane is concentration dependant. As a result of this, AMPs rupture target membranes in an "all-or-none" [56] manner [5, 55, 57]. In general, the molar ratio of adsorbed peptides to lipids needs to reach a certain value, known as the threshold concentration ($P/L^*$), in order for AMPs to start their disruptive activities.

Despite the aforementioned achievements in understanding AMP's cell selectivity and in identifying its controlling parameters, the implication of cell-density in the selectivity is not well understood. As pointed out by Matsuzaki [35], there is a long-standing confusion in cell selectivity measurements; since it was often measured with different values of host and bacterial cell densities, i.e. (6 to 10)$\times 10^8$ cells/mL and (1 to 6)$\times 10^5$ colony-forming

units/mL, respectively, which leads to overestimation of the selectivity index, as correctly referred to as an "experimental illusion" [35]. As a result, we need guiding principles to discriminate between intrinsic peptide properties and the external factors such as cell concentration and environmental influences (i.e., noncompetitive or competitive condition). Recent theoretical and experimental studies [6, 4] show a monotonic correlation between selectivity and cell density with a plateau region for relatively small cell densities, commonly referred to as a low-cell-density (or single-cell density) limit. This monotonic relationship could be explained by mapping it onto the well-known binding isotherm of Langmuir model (i.e.see supplementary information of [6]) and reducing the complex sets of involved physiochemical parameters into two general quantities: an effective binding energy per peptide ($w^*$) and the threshold concentration ($P/L^*$). In principle, This relation will give us a quantitative sense of the low cell-density limit, in which peptide selectivity is sensitive to the intrinsic properties of peptides (i.e. through the quantity $w^*$), as well as the role of cell density in determining the selectivity through the threshold bound-peptide-to-lipid ratio $P/L^*$.

My thesis work is devoted to examining to what extent the selectivity is cell-density dependent. To this end, we present a coarse-grained model of cationic AMP cell selectivity, especially one that shows how cell densities ($C_{\text{cell}}$) and microscopic peptide-lipid parameters are intertwined in the selectivity. The simultaneous presence of several competing effects (e.g., lipid demixing and peptide-peptide interactions), however, poses a serious challenge to theoretical analysis. In an effort to map out an accurate model of cell selectivity, we compare various models. Our first coarse-grained model is improved upon the selectivity model of [6], especially by calculating electrostatic interactions more accurately and incorporating the geometry of different regions that are engaged in the interaction range of each peptide, and those outside this range. We further examine the physical origin of the non-monotonic behaviour of the cell selectivity by peptide net charge $Q$, and its relation to the target cell density. Overall, the general picture drawn from this effort is that peptide cell selectivity remains sensitive to peptide parameters (e.g., charge and hydrophobicity) at the low-cell density limit but becomes insensitive beyond this limit. This means that the coarse-grained model enables us to map out intrinsic selectivity from apparent ($C_{\text{cell}}$-dependent) one or biologically-relevant one from "conveniently-measured" selectivity. This effort will benefit our endeavour in optimizing the peptide parameters for their enhanced selectivity in a physiological environment.

We extend our effort to examine peptide adsorption onto the outer membrane (OM) of Gram-negative bacteria, focusing on the interaction between AMPs and the wild-type lipopolysaccharide (LPS) layer in a biologically relevant medium (i.e. containing monovalent and divalent salt ions like $Mg^{2+}$). The physical coarse-grained models of peptide-

ions-LPS were introduced recently [13, 58, 59], but they did not capture the effect of oligosaccharide and O-antigen chains of the wild-type LPS molecules. Here, we present a coarse-grained model for AMPs binding onto the LPS layer, in which oligosaccharide and O-antigen chains are viewed as forming a polymer brush. This brush is the first permeability barrier AMPs should go though [60, 61, 62]. Our model quantitatively explains the protective role of the LPS brush and demonstrates how the core oligosaccharide and O-antigen part of wild-type LPS reduces the number of adsorbed membrane-lytic peptides in physical terms.

## 1.2 Biological Cell Membrane

The biological cell is the fundamental unit of all living organisms [63] and its first appearance on Earth dated back at least 3.5 billion years ago [64]. It consists of diverse macromolecules such as proteins and nucleic acids that is enclosed within a membrane; these molecules are responsible for complex biological tasks inside the cell's dynamic environment [63]. Advanced cells (i.e. those of multicellular, such as plants and animals) come with different size and shape, depending on their functionality; for instance, nerve cells are elongated rods with many branched structures at each end, whereas the mammalian red blood cells adopt a flexible biconcave shape. Most cells are visible under the microscope and have a length scale between 1 and 100 micrometers [1, 63]. Depending on the existence of a membrane-bound nucleus inside a cell, they are categorized into two main groups, called eukaryotic and prokaryotic cells [1, 63]. Prokaryotes include bacteria and archaea and are characterized by the lack of a nucleus to encapsulate their DNA. They are simpler and smaller than eukaryotic cells (i.e. cells in plants, animals, and fungi), and emerged as the first form of life on the Earth [1].

In spite of the immense variety of shapes, sizes and their complex functions, cells exhibit very common constructional substructure, such as membranes. The biomembrane separates all aqueous environments of different composition from each other and selectively controls the passage of molecules and ions inward and outward the cell [65]. In part, it consists of lipid molecules, assembled into a two-dimensional fluid layer (i.e. they can not resist a shear stress in a microscopic view) with thickness 4-5 nm [1]. There are isolated integral proteins embedded inside the phospholipid layer and are used for communication and transportation of the chemical compounds.

The plasma membranes, owing to their constitutional lipids, are sensitive to temperature, stress, and chemical potential; they are considered as thermodynamic systems. For

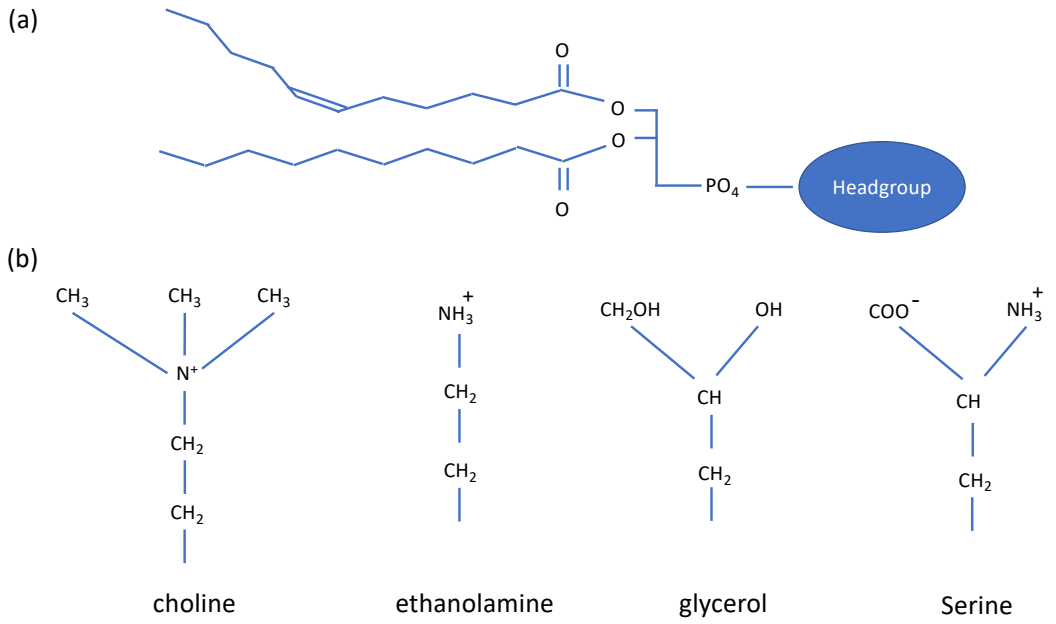


Figure 1.1: Phospholipid molecule structure. (A) shows a phospholipid molecule, consisting of nonpolar double hydrocarbon chains and polar headgroup. (B) commonly found headgroups of phospholipid molecules in cell membranes (this is redraw from Ref. [1] by permission of Cambridge University Press).

instance, the fluidity of the plasma membrane depends on its composition and temperature; at freezing point, the lipid layer undergoes a phase transition and transforms into a rigid structure, known as a gel [65], and the presence of 40% cholesterol molecules in the membrane's composition would increase the stiffness of the lipid layer by approximately two times [1, 65]. It is worth noting that position of the lipid molecules is not fixed and they diffuse horizontally along the surface of the membrane, and also vertically between inner and outer leaflets of the lipid bilayer [1, 65].

### 1.2.1 Lipid bilayer

Lipids are amphipathic molecules. They consists of a hydrophilic headgroup and hydrophobic chain region. Phospholipids are the typical lipids found in the plasma membranes. Their nonpolar chains consist of two fatty acids linked to a glycerol, which is connected to the polar headgroup via a phosphate $PO_4$. Biomembrane phospholipids possess a range of

hydrocarbon chain lengths (i.e. 15-18 carbon atoms and $\approx$ 0.1nm per $CH_4$ group on the chain) and different headgroup compositions [1]. Lipid headgroups are different in their net charge, size, and polarity. Some of the commonly found lipid headgroups in cellular membranes are choline, ethanolamine, glycerol and serine.

In aqueous solutions, lipids self-assembled into closed-shielding structures, depending on their concentration. Amphiphilic lipids aggregates into bilayers, micelles and inverted micelles in the aqueous environments and shield their hydrocarbon region from the solution to reduce the unfavourable contact energy [1, 65]. However, the formation of the lipid cluster lowers their freedom in a system, and hence decreases the overall entropy. Thus, there is a competition between energy, which favours the aggregation, and entropy that favours the distribution of lipids throughout the solution. This leads to a threshold concentration value, called the critical micelle concentration (CMC) [1]. In fact, whether the energy or entropy of the amphipathic dominates the free energy depends to the lipid density. At low lipid densities, the entropy per particle dominates and the solution (monomeric) phase is favoured, while at high density, self-assembling energy favours the condensed phase [1, 66].

The lipid chemical nature and its molecular geometry determine the aggregated structure in aqueous solutions. Depending on the ratio of headgroup size to chain cross section area, the spatial region occupied by a lipid in a spherical or cylindrical micelle could be imagined to look like an ice-cream cone or a wedge-shaped slice of pizza [1, 66]. While, single-chain hydrocarbon chains tend to form micelles, dual-chain phospholipids with moderate headgroup size prefer bilayers; lipids with small headgroup would form inverted micelles.

Earlier experimental investigations of the cell membranes revealed their lipid-bilayer structure. Gorter and Grendel [67] in 1925 extracted lipids from red blood cells of different sources such as man, dog, exc., and used Langmuir film balance to measure surface area. They found that surface area of the lipids' monofilms was within error exactly two times of the surface area of their source cells, measured by microscopic images, which led them to proposed the lipid double-layer construction with headgroups outwards. This experiment and later structure observations by Danielli and Davson [68] (1935) provided the first evidences of lipid-bilayer composition in the cell membranes.

### 1.2.2 Red Blood Cell Membrane

The plasma membrane of red blood cells (RBCs) is more chemically heterogeneous than a pure phospholipid bilayer, and in addition to membrane-embedded proteins, they contains

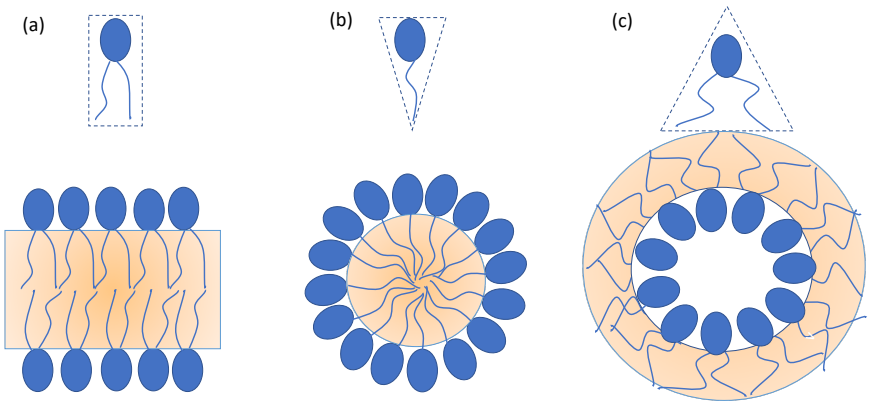


Figure 1.2: Geometry of phospholipid molecules. Lipid self-assembled structure in aqueous solution depends on its molecular shape. (a) Cylindrical lipids form bilayer, (b) single fatty acids look like cone and aggregate into micelles, and (c) small headgroup-to-chain area tends to build inverted micelles. Orange shade regions indicate hydrophobic regions.

∼40 mol% cholesterol, which adds stiffness and higher compressibility to the cell membrane [1, 65]. Cholesterols belong to the one of major eukaryotic lipid molecules, sterols (prokaryotes have essentially none), and their pure concentrations do not form lipid bilayers. X-ray diffraction experiments show the 50% to 60% maximum solubility of sterols in phospholipids [69].It is evident that the presence of cholesterol in the plasma membranes increases their resistance both to compression and to bending [70] via condensing acyl chain packing. However, the change in compression modulus ($K_{\mathrm{A}}$) as a function of the cholesterol fraction is not at all linear [71]. The compression modulus, $K_{\mathrm{A}}$, of RBC membranes are about two times larger than pure phospholipid bilayers [1, 71, 70].

In contrast to the evenly distributed cholesterols within the two leaflets of the same RBC membrane, phospholipid composition is different across the bilayer and leads to a small surface electrostatic potential (∼0.8 mv) [1]. This voltage difference is reflected in the distribution of the charged lipids in the inner and outer layer of the membrane. While the outer monolayer mostly is composed of zwitterionic phosphatidylcholine (PC) and sphingomyelin, phosphatidylethanolamine (PE) and negatively-charged phosphatidylserine (PS) form the inner layer. This membrane asymmetry is critical for the cell integrity and its transportation function [1, 65].

In the laboratory, studies of mechanically-simple cells like RBCs and bacterial cells are often carried out with model membranes such as liposomes or artificial vesicles, which

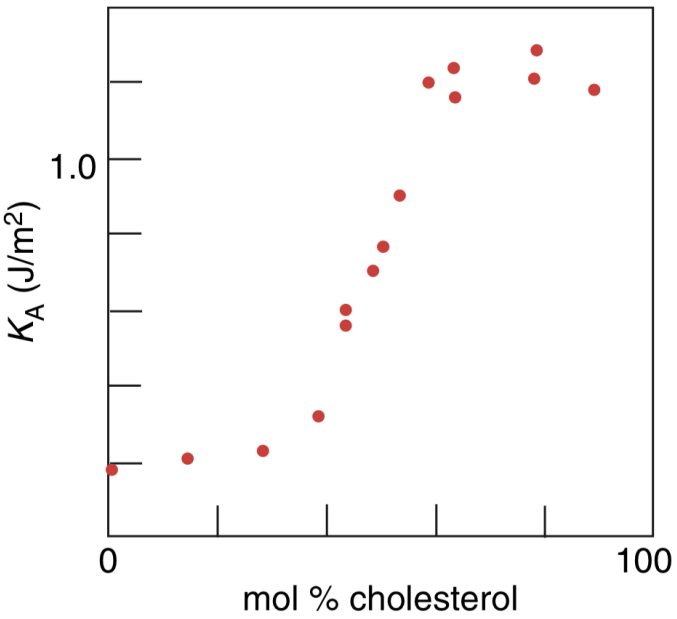


Figure 1.3: The area compression modulus, $K_A$, of SOPPC bilayers as a function of cholesterol composition. This plot of results is reused from Ref. [1] by permission of Cambridge University Press.

are structurally similar to the biological counterpart. The micron-meter model vesicles are manufactured from lipids and other molecules, allowing their shape to be determined systematically as a function of size and composition. For instance, small unilamellar liposome vesicle (SUV, with one lipid bilayer) and the large unilamellar vesicle (LUV) help one understand many physical aspects of the biological membrane, itself, such as compression, binding adsorption, cell membrane lysis, etc. [1, 65].

### 1.2.3 Bacterial Cell Membrane

In spite of the simplicity of the bacterial cells, they are well-developed species, carrying distinctive biological mechanisms and cellular structures. These micrometer-long organisms belong to the simplest and smallest form of life, prokaryotes, and discern themselves from eukaryotes by lacking a nucleus inside their cell [1]. Despite the absence of a nucleus in bacterial cells, their complex structure of the cell envelope distinguishes them from the eukaryotes. The majority of eukaryotic cells such as animal cells (i.e. algae and plants

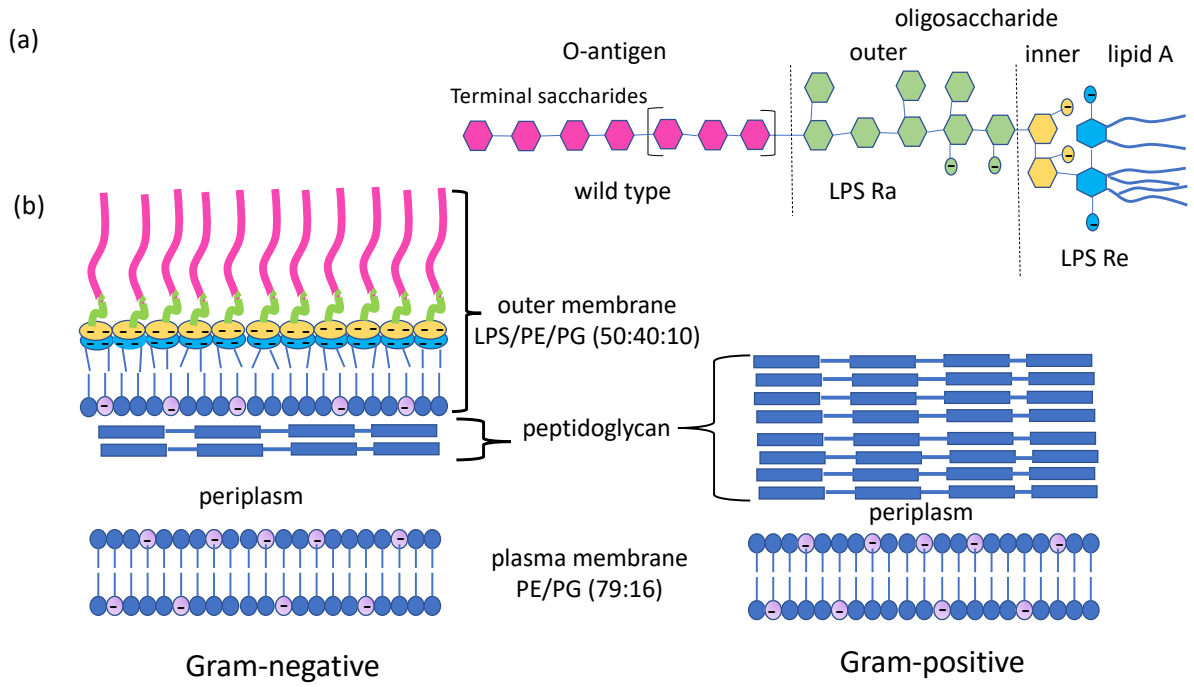


Figure 1.4: schematic view of bacterial cell membranes. (a) illustrates the molecular structure of a LPS molecule, consisting of several parts, called Lipid A (blue), inner (yellow) and outer (green) oligosaccharide and O-antigen (dark pink). Wild-type LPS includes the whole molecular parts, although mutant LPS Ra and Re lack O-antigen and outer oligosaccharide, receptively. (b). demonstrates the cell envelope structure in Gram-negative and Gram-positive bacterial cells. Outer membrane in the Gram-negative bacterial cell consists of an asymmetric bilayer of LPS layer in outer leaflet and phospholipids in inner leaflet.

share most of the characteristics of the bacterial cell envelope) contain only a phospholipid membrane to shield their interior cell from the outside, while bacterial cell envelope is a multilayered protection structure and plays a crucial role in the cell survival. The envelope is composed of four major parts; outer membrane (depending on bacterial type, this part might be missing from the envelope cell), the cell wall, the periplasm space and the cytoplasmic membrane [1, 63].

Depending on the bacterial type, i.e., Gram-negative or Gram-positive, the cell envelope possesses different structure and properties [1, 63]. Employing the long-standing Gram-stain methodology, bacterial cells exhibit different responses to certain dyes, as a result of their different exterior cell envelope. While Gram-positive's envelope includes a thick

and mechanically strong peptidoglycan cell wall, Gram-negative's cell wall is thin and is sandwiched between the outer membrane (OM) and the inner cytoplasmic membrane. However, the cell wall of the both bacterial types has the same responsibility and provides unity and solidarity to the cell. In addition to acting as a filtering mechanism, the main function of the cell wall is to control the internal pressure with respect to the outside environment of the cell by preventing over-expansion when water and other substances enter the cell [1, 63].

The OM of Gram-negative bacteria is a highly asymmetric bilayer membrane and serves as a transition barrier to prevent entry of noxious compounds and at the same time allow influx of the nutrient molecules [72]. The outer leaflet of the OM is mainly composed of lipopolysaccharide (LPS), but the inner layer includes mostly phospholipids such as phosphoethanolamine (PE) and phosphatidylglycerol (PG). The LPS layer is a good barrier to harmful foreign molecules such as antibiotics and lysozyme and contains a negative surface charge on the cell membrane to stabilize the overall membrane structure. It acts as an endotoxin [73]. Recent works showed that LPS is secreted by bacterial outer membranes as part of their normal physiological activities and their presence inside the animal's blood evokes strong immune responses [74].

## 1.3 Antimicrobial Peptides

The immune system of all living organisms, from humans to plants to insects replies on small ($<$ 10 kDa) host-defence molecules, called antimicrobial peptides (AMPs). These antimicrobial agents are naturally occurring antibiotics and hold a great promise in the development of new antimicrobial treatments for two specific reasons; first, they able to kill a diverse range of pathogenic threats such as Gram-negative and Gram-positive bacteria [22, 23, 24], enveloped viruses [29, 30], fungi [25, 26]; even a few peptides have also been found to be cytotoxic to tumour cells [27, 28]. Second, their anciently-selected antimicrobial mechanism would not easily induce resistance. In fact, the conventional antibiotic drugs kill pathogenic bacteria mainly by causing enzymatic or genetic interferences to the pathogens. A a result of their prolonged exposure, these microorganisms can evolve to resist the antimicrobial attack via structural evolution [75]. However, AMPs' mechanism of action is very different and mainly involves membrane disruption. It is evolutionally harder to undertake membrane repairing within the action periods of minutes [75].

AMPs have a similar structure to proteins, but they are shorter in size or contain less amino acid sequences (between 15 to 50 amino acids) [2, 16]. These peptides often carry two or more positively charged amino acids like arginine, lysine and histidine (later is charged in

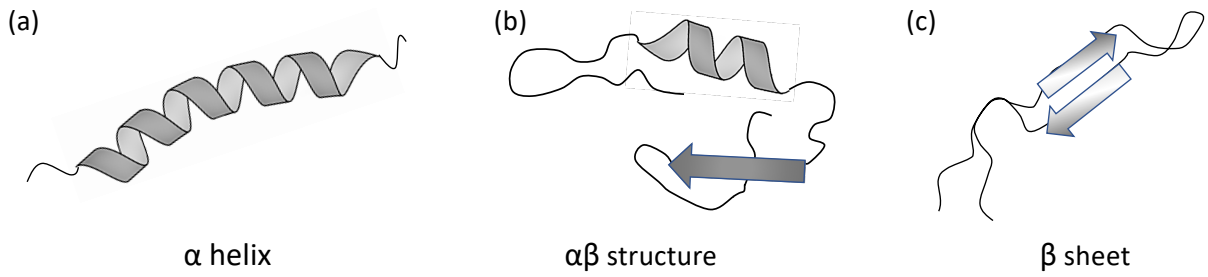


Figure 1.5: Representation of the secondary structures of antimicrobial peptides, induced by hydrophobic interface of the bilayer lipid. It includes (a) $\alpha$-helix, (b) $\beta$-sheet, and (c) $\alpha\beta$ structure with both $\alpha$-helices and $\beta$-sheet.

acidic environments, only) and include a large number of hydrophobic residuals (generally $> 50\%$). Many of these peptides are unstructured (random coil) in solution, while folding up into their secondary structure ($\alpha$-helix, $\beta$-strand or $\alpha\beta$-structure) upon partitioning onto the biological membranes [2, 16]. Fig. 1.5 shows different secondary structures of AMPs upon binding onto the membrane. These secondary structures are amphipathic arrangements, stabilized by hydrogen bonding, where the hydrophilic residues are aligned along one side and the hydrophobic residues are aligned along the opposite side. In fact, the membrane lipid bilayer induces the secondary structures and divides the peptide into two sides of hydrophobic and hydrophilic parts. These amphiphilic structures and their ability to associate with membranes is the most important and common characteristic of most AMPs [16]. Their membrane permeabilization is not the sole mechanism. Many of AMPs do not permeabilize membranes; they pass though the plasma membrane, bind to the intracellular targets inside the cell and interfere with the cell function or its survival [2, 16].

It is believed that AMPs selectively target the pathogens and discriminate between the host and invaded microbial cell [35, 36, 37]. One of the most important features of AMPs is their ability to recognize the target cell in the crowd of host cells via the existing difference in lipid compositions of the host and target cells. While primary investigations of the cell selectivity [16, 38] suggested electrostatic interactions play the prominent role in attraction between mainly cationic AMPs and negatively-charged bacterial membranes, the recent biophysical studies [55, 57] have changed this simple view and described a multifactorial complex system that a combination of several different effects in the peptide-membrane system determines the cell selectivity and the killing process, simultaneously. In section 1.4, we explore a comprehensive review on this matter.

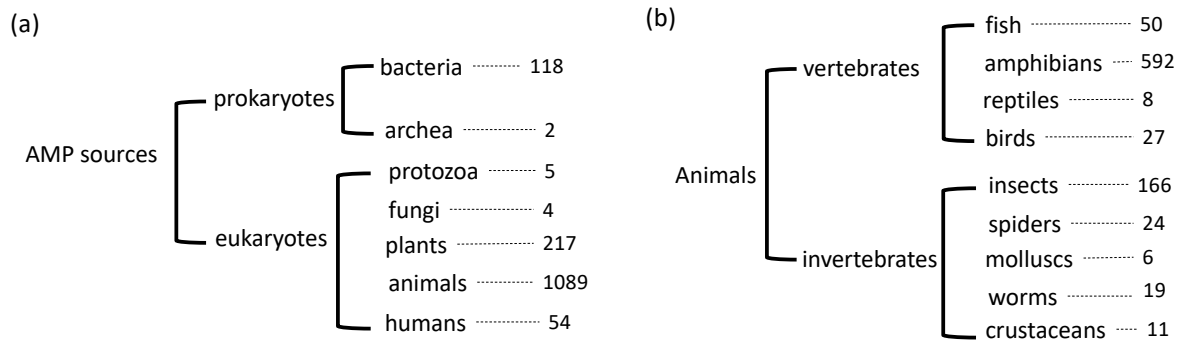


Figure 1.6: The number of antimicrobial peptides, categorized by source, from (a) a range of kingdom and (b) selected animal families. Data is extracted from the Antimicrobial Peptide Database analyzed in February 2010, by total AMP number of 1528. This figure is redrawn from Ref. [2] by permission of CAB International.

Because of the global problem of antibiotic resistance, much effort led to isolation and characterization of hundreds of new AMPs, which demands efficient data managements and classifications. In general, natural AMPs can be classified into many different categories like, source organism, amino acid sequence, characteristics, biological activities (i.e. for instance, Fig. 1.6 demonstrates the peptide classification based on their source organisms); however the important peptide category for our analytical work here, is peptide-binding targets. Widely, AMPs are divided into two major groups; membrane-targeting and non-membrane-targeting peptides [2]. In the following sections, we focused on literature reviews of membrane-lysis AMPs and explain the biophysical analysis of their cell selectivity and rupturing mechanism.

## 1.4 Cell Selectivity

Long-standing experiments point to the cell-discrimination ability of AMPs: they selectively kill pathogenic microorganisms without being significantly toxic to the host cells. This idea comes from the observation that peptides are nonhemolytic at concentrations well above their minimal inhibitory concentrations (MICs) against different pathogens [19, 35, 49, 51, 76, 77, 78]. For example, a peptide concentration range of 2-50 $\mu$M of magainin 2 (part of immune system of the African clawed frog Xenopus laevis) could inhibit bacterial growth, while the concentration at which it causes 50% hemolysis in human red

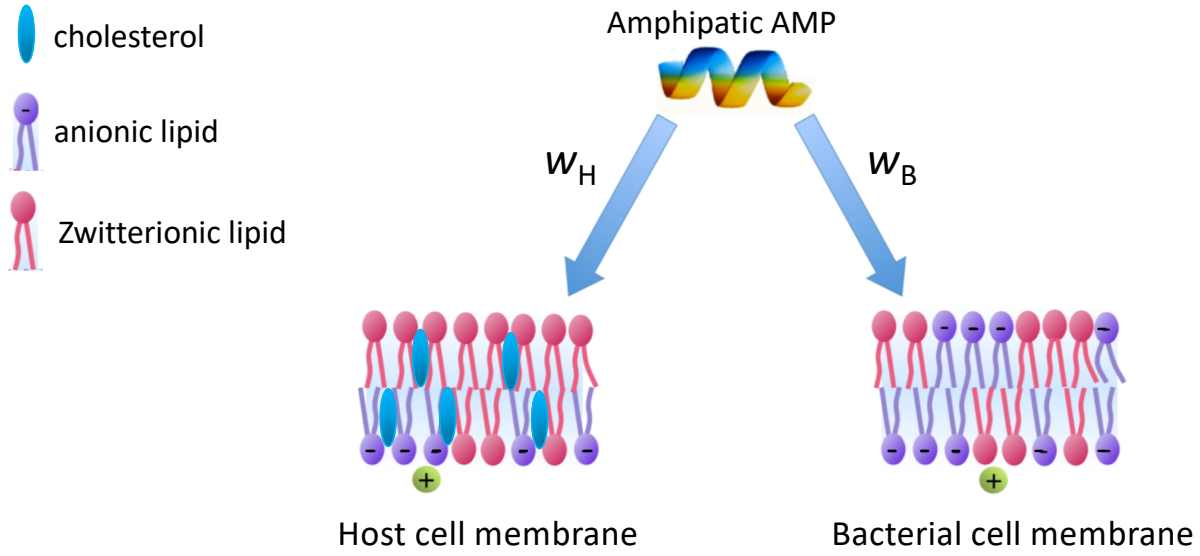


Figure 1.7: The membrane-induced $\alpha$-helical peptide binds to host and bacterial cell membrane via its affinities, or correspondingly by binding energies, $w_{\mathrm{H}}$ and $w_{\mathrm{B}}$, receptively. Outer leaflet of host cell membranes include zwitterionic lipids and $\sim 40\%$ cholesterols, while the plasma membrane of a bacterial cell mainly consists of mixed anionic and zwitterionic lipids. This illustration, with some modifications, is adopted form Ref. [3].

blood cell (MHC) is about 1000 $\mu$M [32, 79]. This behaviour is apparently caused by the difference in lipid composition of membranes of the two target cells; as the experiments on liposomes [43, 50, 80] show higher peptide binding affinity for bilayers that mimic bacterial than the host cell membranes (see the schematic representation of the peptide binding to the membrane in Fig. 1.7). In principle, the mainly-cationic peptides tend to bind more strongly to the negatively-charged bacterial cells than electrically neutral RBCs.

On the other hand, peptide binding to the target membrane is not the sole factor in cell selectivity. The initiation of the peptide rupturing activity on the membrane plays a crucial role in the selectivity process, as a whole. This idea comes from the fact that peptides do not necessarily act on the membrane as an individual, but as cooperative agents [5, 46, 55, 57]. Indeed, AMPs permeabilize the target membrane in an "all-or-none" [56] mechanism, which is described by a minimum molar ratio of adsorbed peptides to the membrane lipids that are required for peptides to start their disruptive activities, called threshold concentration ($P/L^*$) [55]. As shown by the cartoon in Fig. 1.8, as long

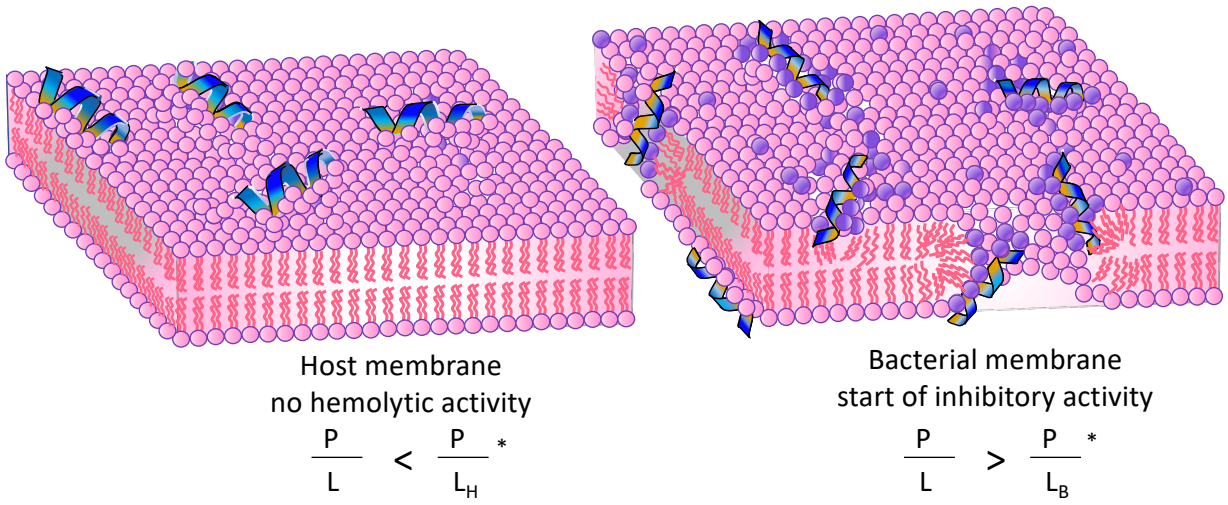


Figure 1.8: Schematic view of "all-or-none" killing mechanism of AMPs. Threshold concentration ($P/L^*$) is a minimum molar ratio of hydrophobically bound peptides to lipid that are needed to rupture the membrane. AMPs are believed to be selective, since $P/L^*$ can be easily reached for bacteria but not for the host cell.

as the adsorbed surface density of the peptides on a membrane is less than threshold concentration, they do not harm the cell. Experiments show that this threshold density is easily reached for bacterial membranes, but not for host cells membranes.

In laboratories, selectivity is often quantified by the ratio of MHC (minimum hemolytic concentration) to MIC (minimum inhibitory concentration), which is known as the "therapeutic index" of a peptide [35]. One can relate measured MIC (or MHC) to their corresponding threshold concentrations on the host and bacterial cells of $P/L^*_{\mathrm{H}}$ and $P/L^*_{\mathrm{B}}$, respectively, by thermodynamic binding isotherm; the amount of adsorbed peptides on the target membrane reaches the threshold concentration $P/L^*$ (given total number of lipids is constant), if the peptide density in solution (bulk) is equal to MIC (or MHC).

In addition to aforementioned intrinsic parameters (i.e. binding energy and threshold concentration and their tangled relationship), AMPs cell selectivity is dependent on the environment conditions, in which the selectivity is measured. Indeed, both the minimum inhibitory and hemolytic concentration of bacterial growth and RBC (i.e. MIC and MHC, respectively) are dependent on the target cell concentration, due to the density dependence of existing threshold concentration and peptide's "all-or-none" action. Recent theoretical [6] and experimental [4] results demonstrate the cell-density-dependence of AMP's cell selectivity. For instance, Fig. 1.9 shows the association of fluorescently labeled analogues

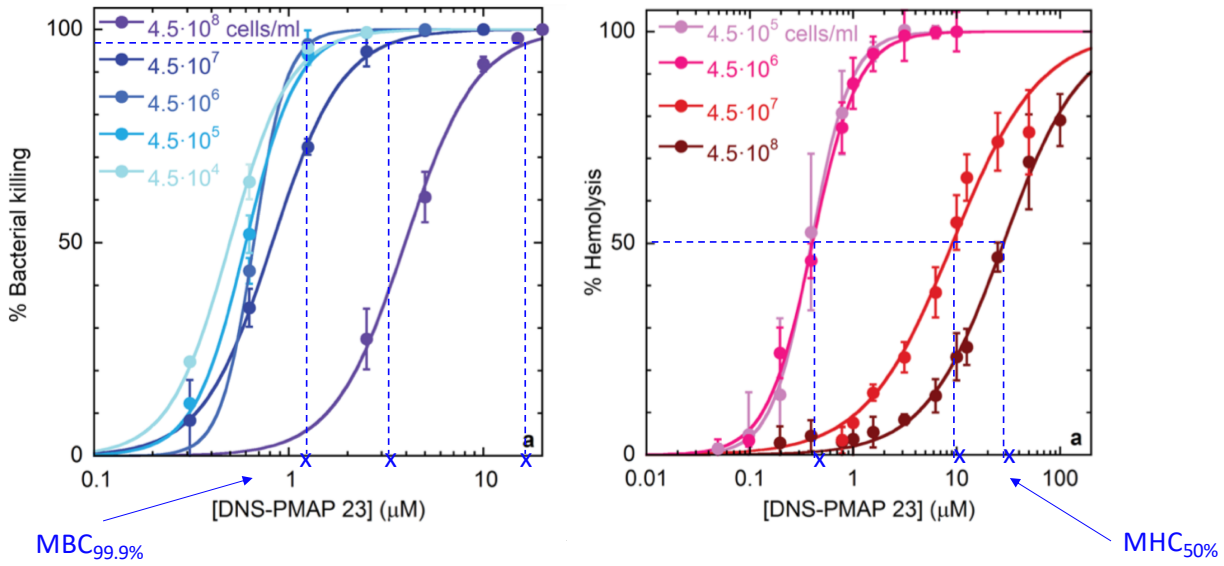


Figure 1.9: Experimental results of AMP DNS-PMAP23, exhibiting its binding isotherms for different bacterial and red blood cell concentrations. MBC at 99.9% killing the bacterial cells and MHC at 50% hemolytic activity are shown by blue crossed signs, for different cell densities. These plots of results are reused from Ref. [4] by permission from American Chemical Society

of the peptide cathelicidin of PMAP-2315 (DNS-PMAP23) with the membranes of E-coli and red blood cells. It is evident by the results that values of MBC (minimum bactericidal concentration) at 99.9% bacterial cell killing and MHC at 50% hemolysis activity are dependent on the total target cell density.

Thus we conclude that selectivity is not an intrinsic property of peptides (even for a given membrane), but is is influenced by external parameters such as cell density and the way it is obtained. For instance, MHCs and MICs can be measured for a homogeneous solution of each type of cells or for a mixture of both types of the cells (bacterial and host cell). These two approaches usually produce different or even strikingly different selectivity [4, 6]. In chapter 3, we will examine the extrinsic properties of the cell selectivity in detail.

In the remaining section, we would review different steps of peptide binding process, as well as their associated free energies. Then in order to explain thermodynamics of molecular binding to lipid bilayers (as our target membranes), we will introduce a simple binding isotherm, known as Langmuir model. After that, the influence of lipid composition

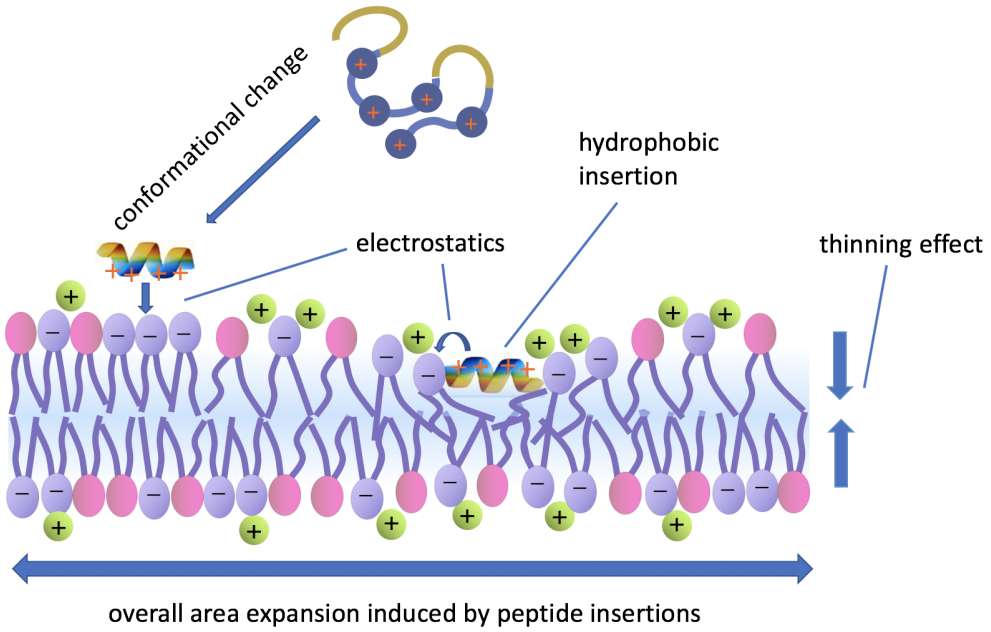


Figure 1.10: AMPs adsorb on the membrane via different process and different energy. Upon approach to the membrane, $\alpha$-helical peptides change their conformational structure from random coil to an amphiphilic helix (i.e. blue and yellow represents hydrophilic and hydrophobic side, respectively.) and bind by electrostatics and hydrophobic insertion. Insertion would cause the bilayer thickness to decrease and the overall membrane area increase, which lead surface tension. The bound peptides induce lipid demixing and migration of the anionic lipids towards the charged peptide. This illustration, with some modifications, is adopted form Ref. [3].

in determining threshold concentration and lipid dehydration effect will be explored.

### 1.4.1 Binding Energy

Membrane-active AMPs binds to lipid vesicles very fast; it usually occurs within a range of milliseconds to minutes [45]. Depending on the chemical nature of membrane lipids and peptide characteristics, the binding affinity towards target membranes is different, though we could generalize it into the five main incidents [45], namely, (i) electrostatics, (ii) peptide-induced lipid demixing, (iii) membrane-induced conformational change, (iv) hydrophobic insertion into the lipid membrane, and (v) peptide-induced membrane thin-

ning effect. In contrast to previously held views, electrostatic energy is not the sole driven factor in peptide adsorption (i.e. AMPs exhibit a considerable affinity toward uncharged bilayers [43, 45]). This indicates that the total interaction between all four effects would determine binding energy and therefore the cell selectivity of AMPs.

**Electrostatics:** AMPs mainly carrying 2-9 net positive charges in physiological environments [2], while the surface of bacterial membranes are composed of anionic lipid headgroups (i.e. bacterial plasma and outer membranes include $\sim 30\%$ and $\sim 90\%$ negative charges due to PG and LPS [1]). This leads to a strong long-range attractive interaction between peptides and membranes. On the other hand, repulsive electrostatic energy also plays an essential role in both charged and uncharged membranes (e.g. RBCs). Same-charge bound peptides develop a repulsive electrostatic potential and hinder further adsorption of the peptides on the membrane. We have provided detailed analytical examinations of the electrostatic binding energy of AMPs in chapters 3 and 4.

**Lipid demixing:** A lipid bilayer, immersed in a salt solution, is considered as a two-dimensional lipid matrix, which consists of a mixture of zwitterionic (e.g. PC) and anionic (e.g.PG) lipids that can move freely in the lateral direction or slowly between the two leaflets (called flip-flop motion) and responds to peptide binding [1, 65]. As positively-charged peptides bind onto a lipid vesicle containing anionic lipids, anionic lipids tend to be accumulated around the bound peptides and neutralize peptide's charge locally [9, 81], as commonly referred to as lipid demixing. While demixing is energetically favourable to peptide binding process, the entropic cost of lipid displacement leads to a war-and-tug behaviour; free energy minimization of the whole system determines the extent of lipid demixing.

**Conformational change:** Lipid membranes act as catalysts for peptide folding into a secondary structure and via interaction of AMPs with lipid surface. The in-buffer random coil peptide transforms into the $\alpha$-helical or $\beta$-sheet structure by hydrogen bonding on the membrane surface. For example, the peptides melittin, magainin and cecropins, which are isolated from the extracellular fluids of insects, frogs and mammals, respectively, adopt $\alpha$-helix upon associating with lipid membranes; protegrin-1 (PG-1) present in porcine leukocytes (i.e. part of the pigs innate immune system) forms $\beta$-sheet. Thermodynamic energy analysis by spectral deconvolution of the CD spectrum of the bound peptide in combination with isothermal titration calorimetry (ITC) has shown that amphiphilic $\alpha$-helix formation is an exothermic process and yields helix enthalpy of $\sim -0.7$ kcal/mol and a free energy $g_{\text{helix}} = -0.2$ kcal/mol per peptide residue (i.e. for details see [43, 45, 51] and references therein). A systematic comparative study of native magainin 2 with a diastereomeric analog with four D-amino acids (D substitution interrupts the a-helix) suggests 60 fold less binding affinity for magainin analogous with no $\alpha$-helix formation

ability [82].

**Hydrophobic insertion:** In addition to membrane-facilitated helix formation, the second main driving force for membrane binding is the insertion of the nonpolar amino acid side chains into the lipid bilayer [45, 83]. The amphiphilic helix peptide, at first, adsorbs on the membrane in a parallel orientation and pushes the lipid headgroups to accommodates its hydrophobic side inside the lipid acyl regions, while its hydrophilic part faces upright and in contact with the polar solution and surrounding anionic lipid headgroups. Fig. 1.10 exhibits the two modes of peptide adsorption (in a parallel orientation) on the membrane, electrostatic and hydrophobically-inserted adsorption. From the available studies [43, 45, 51], it can be concluded that amphipathic peptides bind to lipid vesicles with a distinctly exothermic reaction that shows the involvement of a non-classical hydrophobic effect (i.e. since the classical view consider hydrophobic energy as an entropy-driven effect). Depends on the type of peptide, the range of typical hydrophobic energy gain is of the order of 5-20 kcal/mol [45, 43, 51].

**Membrane thinning effect** AMPs create membrane tension via adsorption. Hydrophobically inserted peptides push headgroups aside, whereas it compresses the beneath acyl chains together (half-sided embedding). This event leads to membrane expansion and the resulting thinning effect of the membrane thickness. Series of peptide-adsorption studies by Huang and colleagues [42, 44, 52, 53, 54, 55] exhibited lower bilayer thickness, upon scattered adsorbed peptides on the membrane, before starting their lysis activity (no sign of vesicle dye leakage). In fact, the membrane area expansion, caused by peptides adsorption, has been observed by vesicle aspiration at constant vesicle volume, while no permeation through the membrane occurred [11]. Assuming the hydrocarbon chain volume remains constant, we could relate the thinning effect to the peptide-induced membrane expansion area by $-\Delta h/h = \Delta A/A$, where the fractional bilayer thickness decreases linearly with increasing membrane area. On the other hand, the fractional increase of the monolayer are due to peptide binding and is equal to $\Delta A/A = (A_{\mathrm{p}}/a_{\ell})\ P/L$, where $a_{\ell}$ is the cross sectional area of the lipid and $A_{\mathrm{p}}$ is the expanded area caused by single peptide binding. Experimentally [42, 44, 52, 53, 54], there have been provided substantial evidence between the decreasing bilayer thickness and the linear increase in $P/L$ at sufficiently large number of the bound peptides, but lower than threshold concentrations (i.e. read subsection 1.4.2 for more details on thinning effect and its relation to the threshold concentration).

### Adsorption Isotherm: Langmuir Model

In order to analyze thermodynamics of molecular binding of peptides to the membrane, we could take advantage of equilibrium partitioning behaviour between two phases, which, in

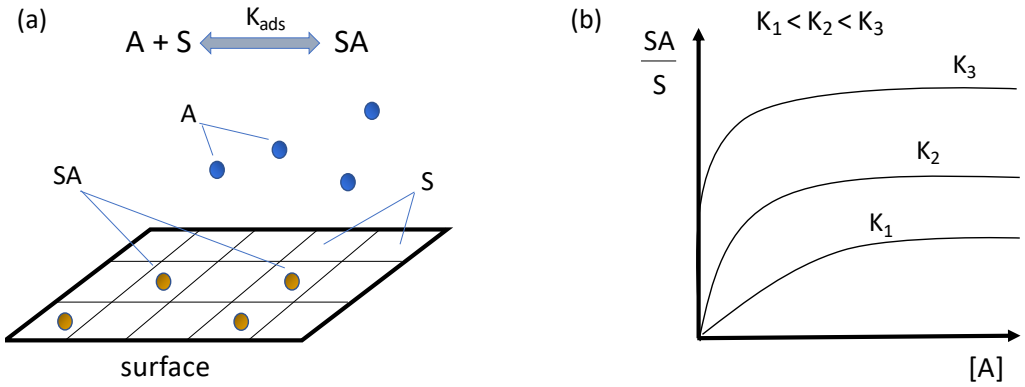


Figure 1.11: (a) Representation of equilibrium partition behaviour and (b) binding isotherm (Eq. 1.1) in the Langmuir model. Adsorbate (A) adsorbs on an independent binding site (S) on the surface and create a new state of surface-adsorbate (SA). Binding affinity $K_{\text{ads}}$ determines the rate of adsorbate binding on the surface, depending on its available concentration in the solution, [A].

our case of peptide bindings, the two modes refer to the solution and membrane surface, and commonly it is addressed as the adsorption isotherm [84]. In binding isotherm, we balance the chemical potentials of peptides in the solution and membrane ($\mu_{\text{s}} = \mu_{\text{m}}$), and the results determine the number of adsorbed peptides on the membrane, based on peptide's concentration in the solution at equilibrium condition and constant temperature. Both experiments and theory exhibit that peptide adsorption follows Langmuir-type model [4, 6].

The most straightforward treatment of peptide adsorption is Langmuir model, named after Irving Langmuir, an American chemist who won the 1932 Nobel Prize in Chemistry for his work in surface sciences [84]. Langmuir model describes the equilibrium between the energetic tendency of the particles to stick to the surfaces and the entropic tendency of the particles to gain translational freedom by floating into the bulk solution. In this model, the surface is assumed as distinct and independent binding sites, in a way that all molecules bind on the sites with an equal binding affinity ($K_{\text{ad}}$). The general expression of Langmuir binding isotherm is given by [84]

$$\frac{\text{SA}}{\text{S}} = \frac{[A] \cdot K_{\text{ads}}}{1 + [A] K_{\text{ads}}}, \tag{1.1}$$

where SA/S is the ratio of adsorbate numbers on the surface to the total number of binding

sites, and $[A]$ is the adsorbate concentration in solution. Fig. 1.11 shows the chemical reaction between adsorbate (A) and surface (S) via the binding affinity $K_{\text{ads}}$, which the later is exponentially proportional to the binding energy $w$ by

$$K_{\text{ads}} \propto \exp\left(\frac{-w}{k_{\text{B}}T}\right). \tag{1.2}$$

On the other hand, thermodynamics of peptide-membrane interaction is a wide field, which depends on many interconnected factors and most importantly is a many-body effect [57]. In principle, we are not able to explain thermodynamic properties of peptide binding to lipid bilayers by the simple Langmuir model, since peptide adsorption is a cooperative process and it is engaged with complex long-range electrostatic interactions, as well as the peptide-induced local-to-global tension transfer [57]. This leads to the fact that the binding affinity (or binding energy) is a function of the number of adsorbed peptides and it is not a constant, as it is assumed by the simple Langmuir model. For this reason, we need a full detailed energy analysis and correspondingly, a coarse-grained model to accurately capture the cooperative behaviour of peptide binding on the membrane. Such a model is introduced in chapter 3 and 4.

### 1.4.2 Threshold Concentration

Vesicle dye leakage, induced by AMPs binding, demonstrates an "all-or-none" mechanism for the permeabilization activity of AMPs. There are no detectable changes in the permeability of the bilayer when peptides are bound on the interface [11, 85]; only when the bound peptide density exceeds a specific threshold value, called threshold concentration (lethal number of peptide-to-lipid ratio $P/L*$), the pore formation occurs [78, 83, 86, 87, 88]. In fact, OCD and NMR experiments show when bound peptide concentration reaches $P/L*$, the parallel-oriented peptides change their state into an aggregated transmembrane pores [5, 46, 55] (i.e. a mechanism needed for lysis-membrane activity) and results in death of the cell (i.e. or in case of liposomes, it leads to the vesicle dye leakage).

One might ask why is there a concentration threshold and what is the driving force to change the parallel-inserted peptides on the hydrophobic-water interface to the perpendicular-aggregated pore formation mode? Huang and colleagues proposed a sophisticated two-state model [46] (i.e. similar to the partition behaviour of binding isotherm but here, peptides bind on the state (1) interface and state (2) inside the transmembrane pore, which need to be balanced, thermodynamically) to study the essential physics involved in this process. They revealed that the peptide-concentration-dependency of the elastic energy of

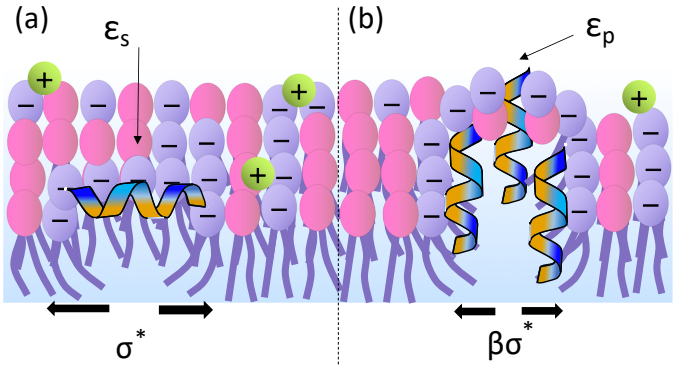


Figure 1.12: (a) Schematic representation of AMP on (a) surface and (b) pore state. At threshold concentration ($P/L^*$), the energy difference of a peptide bind on the surface from the solution ($\epsilon_s$) plus its associated membrane lateral tension ($\sigma^*$) would be equal to the peptide pore binding energy ($\epsilon_p$) and the associated pore lateral tension ($\beta\sigma^*$), explained by Eq. 1.3.

the membrane thinning effect is the key factor in rising "all-or-none" mechanism. If we want to explain it in terms of free energy, it means that the required energy for cationic peptides to gather inside the transmembrane pores, while they enduring the unfavourable repulsive electrostatics and the edge line tension, is pretty large enough that, at the first adsorption steps, AMPs prefer to bind on the interface and be scattered on the membrane. However, interface-binding mode is associated with unfavourable membrane tension (i.e. thinning effect and lateral area expansion). The peptide-induced tension at fairly high surface coverage, but below the threshold concentration (ie. as observed by X-ray diffraction of bilayer profiles and OCD $\sim 1/200 < P/L < P/L^*$) [5, 46, 57], is a function of the number of bound peptides and it idecreases the total peptide binding affinity. As a result of this, the interface-binding state gradually becomes undesired, due to the high free energy cost and at the very moment that peptide free energy reaches the pore formation state (at peptide coverages above $P/L^*$), they start to form a pore. Simply put, as it is shown by the cartoon in Fig. 1.12, one can drive the below energy equality [46], at $P/L = P/L^*$

$$-\epsilon_s + \sigma^* A_p = -\epsilon_p + \sigma^* \beta A_p, \tag{1.3}$$

where energy changes of the interface-binding and pore states are $\epsilon_s$ and $\epsilon_p$, respectively, and $\sigma^*$ is the membrane tension at threshold concentration. The peptide-lipid parameter $A_p$ is the expanded area per bound peptide, which is introduced at 1.4.1. Here, constant $\beta$ is introduced to show a difference tension between the two states. The peptide-induced ex-

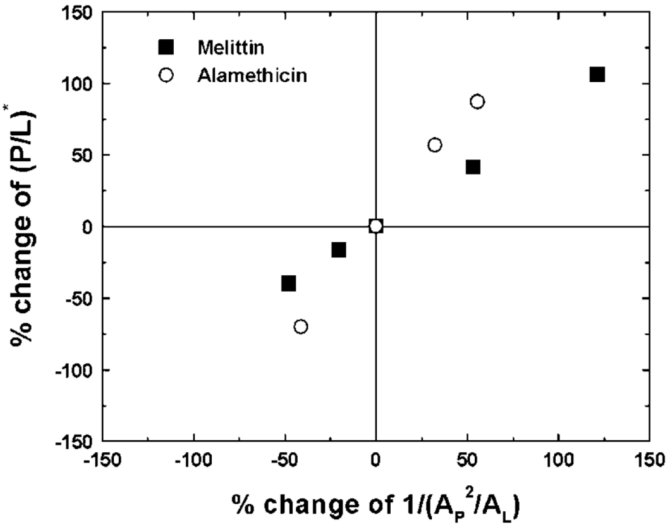


Figure 1.13: (a) There is a correlation between threshold concentration ($P/L^*$) and thinning effect, $1/(A_{\rm p}^2/A_{\rm L})$. Pure PC bilayer is taken as the reference (central point) for AMPs melittin and alamethicin. Thinning effect and the corresponding threshold concentration changes by adding PE or LysoPC to the pure PC bilayers. This plot of results is reused from Ref. [5] by permission of Biophysics Journal

pansion area at the interface-binding mode is not necessarily the same as in the pore state. It is worth noting that AMPs adsorption and pore formation are equilibrium thermodynamic processes and at the adsorbed-peptide densities above the threshold concentration, peptides are partitioned between both interface and pore states.

### Lipid Dependency

Considering the fact of energy origin of the threshold concentration, It makes sense that $P/L^*$ depends on chemical characteristics of peptide-membrane system and varies by the given AMP and lipid composition of the membrane. The extensive behaviour studies of four different peptides, alamethicin [44, 46, 53, 89, 90], magainin [52, 87, 91, 92, 93], protegrin [92, 94, 93, 95], and melittin [44, 46, 89, 93, 96, 97], in interaction with a wide variety of lipid bilayers determined the range of threshold concentration to be $1/190 < P/L^* < 1/30$ for lipid bilayers. The maximum threshold concentration can be found for the LPS layer of Gram-negative bacteria, which equals to $P/L^* \sim 1/10$ [93].

The mentioned examination of the peptide's behaviour responding to the different lipid composition, by Huang group, led to a fact that there is a correlation between the lipid spontaneous curvature and the peptide threshold concentration. For a given peptide, they were systematically adding phosphatidylethanolamine (PE) and lysophosphocholine (lysoPC) to phosphocholine (PC) bilayers to observe the changes on $P/L^*$. Experiments exhibited that the negative curvature lipids like PE increase and positive curvature lipids like lysoPC decrease the threshold concentration (i.e. [5] and references therein). This behaviour is hard to be explained by the type of peptide's mechanism of action or the nature of the pore they create since the conduct of PE inhabitation and lysoPC facilitation in pore formation or vesicle leakage has the same trend for different types of pore-forming AMPs. For instance, melittin is believed to form toroidal pores, while alamethicin creates barrel-stave pore, yet, both peptides in their interaction with lipid bilayers containing PE and LysoPC, shows an increase and decrease, respectively, in their $P/L^*$ [5, 46]. Thus, we could conclude that this behaviour of the peptide-lipid system is related to a universal feature of the peptide adsorption, such as membrane thinning effect. The analytical asses between the thinning effect and threshold concentration by [5] (Fig. 1.13) showed that there is, in fact, a correlation between the two and we could conclude that changing the spontaneous curvature of the lipid would indeed affect the degree of membrane thinning, which in turn influences the threshold concentration for pore formation ($P/L^*$).

### Dehydration Effect

The spontaneous curvature dependence of lipids and their relation to membrane thinning effect can be interpreted via expansion area per peptide ($A_\mathrm{p}$). This is because adding PE or lysoPC has a strong impact on the membrane thinning, regardless of the type of peptide. In [5], the membrane thinning effect is directly measured by the value of $A_\mathrm{p}$ for each peptide in each lipid composition, and it shows how the value of $A_\mathrm{p}$ correlates with the value of $P/L^*$ for different pore-forming peptides of melittin and alamethicin. The larger expansion area per peptide, the larger membrane tension (equivalently smaller bilayer thickness), which leads to smaller threshold concentration and therefore a stronger peptide activity. A schematic view of the relation between lipid curvature and peptide-induced expansion area ($A_\mathrm{p}$) is exhibited in Fig. 1.14. It is interesting to mention that lipid curvature does not seem to affect membrane stiffness, as the area compressibility modulus ($\mathrm{K_A}$) has been shown to be almost the same for a large number of unsaturated-chain lipids and is equal to $\sim 240$ pN/nm [54].

How does the expansion area per peptide ($A_\mathrm{p}$) varies by the lipid spontaneous curvature and it is not constant as the peptide physical area ($\Sigma_\mathrm{p}$) is? The dehydration effect of lipid

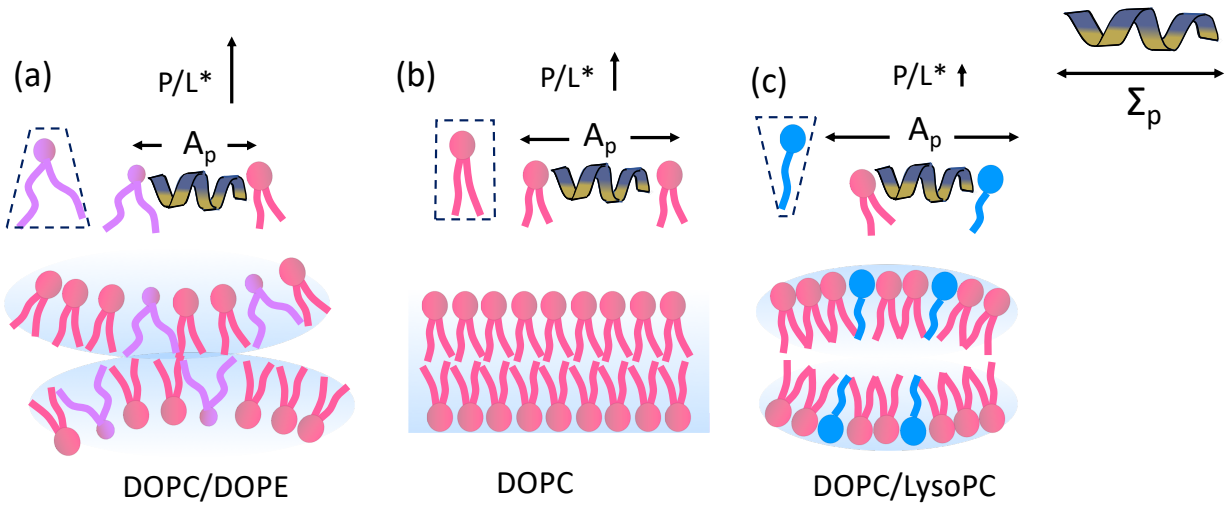


Figure 1.14: Lipid spontaneous curvature and its dependency to the threshold concentration ($P/L^*$). While physical area of the $\alpha$-helical peptide ($\Sigma_p$) is constant, the peptide-induced membrane expansion area ($A_p$) is varying by the lipid composition. Introducing some ratio of lipid (a) DOPE and (c) LysoPC to the pure (b) DOPC bilayer would lead to the negative and positive curvature, receptively, and change the expansion area per peptide and the resulting threshold concentration.

headgroups can answer the following question. At first sight, $A_p$ seems to represent the cross sectional area of the bound peptide at the interface; If that were the case, $A_p$ should be a constant. However, Fig, 1.13 from Ref. [5] shows a strong correlation between threshold concentration and expansion area. As a result, we could justify the changing-value of $A_p$ by we assuming some water molecules are released from lipid headgroups, upon peptide adsorption on the interface, called dehydration effect [5]. Depending on the ability of the peptide to induce dehydration in the lipid headgroup region (every peptide has a different affinity towards water molecules) and the cross sectional area difference between headgroup and lipid $a_\ell$, the peptide could accommodate better within the headgroup region, which affects the thinning effect in a different degree. For instance, Fig. 1.14 simply demonstrates how introducing smaller headgroup lipid such as PE would give more room to peptide to be placed within the headgroup region, and therefore this makes the membrane thinning effect less pronounced and increases the threshold concentration $P/L^*$.

## 1.5 Membrane-rupturing Mechanism of AMPs

The exact mechanisms by which AMPs disrupt lipid bilayers and cell membranes are not completely understood, yet, and this subject has been investigated extensively over the last couple of decades. What is known today is that membrane-targeting AMPs perturb the integrity of the membrane by two major mechanisms; carpet model and pore formation [16]. In the carpet model, peptides are only active at high surface coverage ($P/L > P/L^*$) and form a "carpet" on the membrane surface. They act like a detergent, which leads to the collapse of membrane integrity and the development of scattered micelles [16]. On the other hand, the most studied AMPs like bee venom toxin melittin, frog peptide magainin, cecropin P1 from pigs, etc. create transmembrane pores. This is supported by a considerable number of experiments and the fact that they cause leakage of fluorescent dyes from lipid vesicles [76, 77, 79, 98, 99]. AMPs induce transmembrane pores by two widely accepted models; barrel-stave and toroidal pore [16].

**Toroidal pore:** Melittin, magainin, protegrin, and perhaps most cationic antimicrobial peptides form toroidal pores [46]. In this kind of pore, peptides are inserted perpendicularly into the membrane and cause a continuous bend of bilayer leaflets towards outward, in such a way that the pore lumen is partly lined by peptides and partly by lipid head groups [18]. The orientation of peptides-lipids inside a toroidal pore is such that the polar (hydrophilic) side of the peptide faces the bilayer and lipid headgroups. Toroidal pores are highly curved structures that are stabilized due to the presence of peptides in the pore. Pores usually contain 4 to 7 peptides [96].

**Barrel-stave pore:** Some unique peptides like $\alpha$-helix alamethicin form barrel-stave pore [46]. Despite toroidal, in barrel-stave pore peptides align perpendicular to the membrane and associate to form a bundle (much like a barrel of peptides), which is oriented parallel to the phospholipid tails. This transmembrane pore is lined by peptides only and, unlike the toroidal pores, the hydrophilic regions of the peptides form the pore's edge. Barrel-stave pores are smaller than toroidal pores. The number of peptides in the pores is estimated to be 3 to 11, depending on the bilayer lipid composition [18].

### 1.5.1 Thermodynamics of Pore

In order to understand how AMPs induce pore formation and stabilize it, need a biophysical analysis of peptide-lipid parameters and its involved free energies. Starting with a simple case of pure bilayers, without the engagement of peptides, pore formation has been studied experimentally and theoretically for a long time [100, 101, 102, 103]. In a pure bilayer,

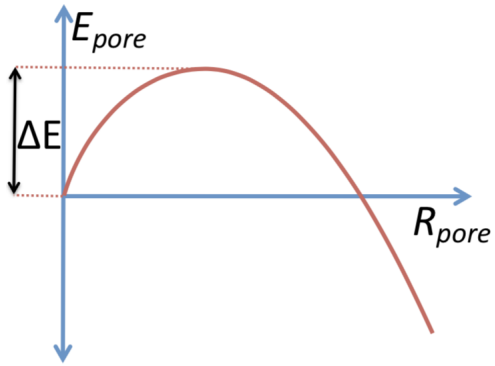


Figure 1.15: The relation of an unstable simple pore energy ($E_{\text{pore}}$) with respect to the pore radius ($R_{\text{pore}}$). Parameter $\Delta E$ shows energy barrier to the growth of the pore ($R_{\text{pore}} \to \infty$) and is determined by Eq. 1.4. This illustration is reused from Ref. [3].

pores start by tension; applying external pressure leads to the expansion of the bilayer, and in case of large enough tension, pores start to form. Pore formation is a complex dynamic process, and the physical behaviour of transition between lateral expansion and pore formation has not been understood well, yet [46, 103]. Although once the pore is established, its essential mechanics governed by the competition between line tension of the pore edge and lateral tension [46, 100, 101],

$$E_{\text{pore}} = 2\pi R_{\text{pore}}\lambda - \pi R_{\text{pore}}^2\sigma, \tag{1.4}$$

where $\lambda$ and $\sigma$ represent line tension and surface tension, receptively, and $R_{\text{pore}}$ is the radius of the pore. The first term expresses the energy cost of creating an edge rim of the pore, while the second term opposes the edge line tension and is the driving force to keep the pore open by lateral membrane tension. As it is illustrated on Fig. 1.15, this kind of pore is unstable; pores with a radius smaller than maximum $R_{\text{pore}}^{\text{max}}$ tends to close and the ones with larger radius than maximum would indefinitely expand the pore. As a result of the spontaneous nature in noninduced-peptide pores, we assume that the engagement of AMPs inside their transmembrane pores would promote stabilization.

Huang and colleagues provided rigorous experimental parameters in case of the two kinds of pores to examine how peptides (i.e. melittin and alamethicin) interact with membranes in toroidal and barrel-stave pores [5, 46]. For instance, they have found that value of $\beta$ (i.e. introduced in Eq. 1.3), which represents the effect of membrane thinning in the two states of peptide binding (i) interfacially on the surface or (ii) inside the pore,

is positive in case of alamethicin that forms barrel-stave pore, and is negative for the case of toroidal pore formation by melittin. This implies that alamethicin inside a barrel-stave pore causes thinning the bilayer (of course less than thinning effect on the interfacial state, because the creation of pore, itself, is the proof), whereas melittin peptides inside a toroidal pore induce thickening. For a more detailed discussion, refer to Ref. [5, 46].

## 1.6 Organization of The Thesis

In this section, we would briefly present a summary and the general goals that have been achieved by each chapter.

At first chapter, we begin the script by a short and general "Motivation and Goals" of this thesis to point towards the subject of antimicrobial peptides as the novel therapeutic agents and argue that how the lack of rigorous biophysical analysis of the AMPs cell selectivity causes not-yet-successful peptide-synthesis strategies in developing re-engineered peptides for pharmacological purposes, and then discuss our efforts in this thesis for developing semi-analytical models of peptide cell-dependency-selectivity and identifying intrinsic and extrinsic parameters. After that, the whole chapter provides a literature review on biological cell membranes and AMPs; especially the known biophysics behind the cell selectivity of AMPs to date.

In the second chapter, I have discussed the fundamental physics theories, which have been used as the basis for our coarse-grained models. It starts with the electrostatics in biological environments and drives the well-known Poisson-Boltzmann equation and the corresponding Debye-Hückel (DH) limit at a low electrostatic surface potential. Then, provides DH electric potential of a surface charged plane and a sphere as two widely-used examples in biological problems.

Chapter three is dedicated to cell-density-dependence of the AMPs' cell selectivity and explores a different range of coarse-grained models, electrostatically, to pursuit the most accurate binding energy for peptide adsorption on the lipid membranes (i.e. which mimics bacterial and mammalian cell membranes), and its relation to the target cell concentration. Furthermore, results have been mapped into a simple Langmuir-type model to reduce the system complexity and provide a clear role of the target cell density at the quantitive measurement of the cell selectivity, therapeutic index. In the end, the latest developed model is used to investigate the peptide's optimal charge for the cell selectivity and its relation to the available bacterial and host cell density.

Chapter four has studied the protection function of lipopolysaccharide (LPS) layer in

the outer membrane of Gram-negative bacterial cells. In this chapter, we have provided a comprehensive LPS model, which takes into account several critical physical factors of peptide-LPS system (e.g. polymer-grafted chains, competitive effect of divalent cations, long-ranged peptide-peptide electrostatic interactions beyond the mean field theory, membrane expansion, and exc.), simultaneously, and develop a realistic coarse-grained model of wild-type LPS layer. In particular, we analyze how brush-like core oligosaccharide and O-antigen of LPS layer affect peptide adsorption and lead to lower membrane-rupture peptides on the OM.

In the last chapter, we delivered a conclusion of our efforts in this thesis and the potential application of the cell-density-dependent selectivity model in the current drug delivery products. Also, we proposed a future work for further development of the subject.

# Chapter 2

# Fundamental Physics

## 2.1 Electrostatics in Biological Environments

Biomembranes and protein macromolecules often carry net electric charges in the biological environments, while their aqueous solution contains small mobile ions, such as $Na^{1+}$, $Cl^{-1}$, $Mg^{2+}$ (i.e. electrolyte solution). For this reason, electrostatic interactions mostly play an important role in biological problems. Explicitly considering biomembranes, we learned that some phospholipids like PGs are negatively charged in physiological condition and heir combination with zwitterionic lipids, leading to an overall negative surface charge density of the bilayer membranes. Although lipids diffuse laterally within the leaflets, their charges can be regarded as fixed and contained to the plane of the membrane. On the other hand, small ions are mobile inside the solution and might be concentrated around the bilayer or diffuse away from it, depending on the electric charges and statistics.

In order to calculate the accurate binding energy of cationic AMPs to the bacterial and host cell membranes, we need to understand the effect of mobile counterions in a biological environments and how they affect free energy of the system. Poisson-Boltzmann (PB) equation is our tool to explain such a distribution of the electric potential in the salty solutions and determine how to the relate distribution of the mobile ions to the electric potential, and therefore calculate electrostatic interactions. In the following subsections, we will derive the PB equation and its linearized version, known as Debye-Hückel (DH) limit.

### 2.1.1 Poisson-Boltzmann Theory

For the first time, PB theory proposed independently by Louis George Gouy and David Leonard Chapman in 1910 and 1913, respectively [104]. In a Gouy-Chapman model, a charged object inside an electrolyte solution creates a layer of counterions around the object, which called double layer. The thickness of this diffusive layer is more than a single molecular layer and depends on the effects of entropy, which is a tendency of the mobile ions to scatter into the total volume of the solution, and electric energy between mobile-counterions and fixed charges of the object. Note that Gouy-Chapman PB equation is a mean-field approach that ignores the local electrostatic fluctuations and assumes the surface of a fixed planar object.

The distribution of both counterions and coions at a given position can be estimated by Boltzmann function and is proportional to the Boltzmann factor by the electric potential energy evaluated at that position (i.e. $V(\mathbf{r}) = q_{\mathrm{j}}\varphi(\mathbf{r})$).

$$c_{\mathrm{j}}(\mathbf{r}) = c_{\mathrm{j}}^{\infty} \exp\left(\frac{-q_{\mathrm{j}}\varphi(\mathbf{r})}{k_{\mathrm{B}}T}\right), \tag{2.1}$$

where $q_{\mathrm{j}} = eZ_{\mathrm{j}}$ is the charge value of the ion j by $Z_{\mathrm{j}}$ valency, and $e$ is the elementary charge unit $\sim 1.6 \times 10^{-19}$ C. Here, the electrostatic potential $\varphi$ represents an average over local fluctuations and is a mean filed potential. The Boltzmann distribution of ions in the electric potential is normalized to the reference point of $\varphi = 0$, where it is far away from the charged fixed object and is called bulk solution. This distribution of mobile ions in bulk is constant and is equal to $c_{\mathrm{j}}^{\infty}$.

On the other hand, charge density of ions ($\rho_{\mathrm{ch}}$) is related to the electric potential by the well-known Poisson equation

$$\epsilon_0\epsilon_{\mathrm{r}}\nabla^2\varphi(\mathbf{r}) = -\rho_{\mathrm{ch}} = -\sum_{\mathrm{j}} q_{\mathrm{j}}c_{\mathrm{j}}(\mathbf{r}), \tag{2.2}$$

where the combination of Boltzmann ion distribution (Eq. 2.1) with Poisson equation (Eq. 2.2) yields PB equation of Gouy-Chapman model

$$\epsilon_0\epsilon_{\mathrm{r}}\nabla^2\varphi(\mathbf{r}) = -\sum_{\mathrm{j}} q_{\mathrm{j}}c_{\mathrm{j}}^{\infty} \exp\left(\frac{-q_{\mathrm{j}}\varphi(\mathbf{r})}{k_{\mathrm{B}}T}\right) \tag{2.3}$$

.

The $\epsilon_0$ and $\epsilon_{\mathrm{r}}$ are the electric permittivity of vacuum and the dielectric constant, respectively and $\sum_{\mathrm{j}}$ is the summation of the total charges at position $\mathbf{r}$. In case of (1:1)

electrolyte like NaCL and having unit charge valency $Z_{\mathrm{Cl}} = -1$, $Z_{\mathrm{Na}} = +1$ with charge distributions $c^{\infty}_{\mathrm{Na}} = c^{\infty}_{\mathrm{Cl}} = c^{\infty}$, the PB equation of Eq. 2.3 will be simplified to

$$\nabla^2\psi(\mathbf{r}) = \frac{2e^2c^{\infty}}{\epsilon_0\epsilon_{\mathrm{r}}k_{\mathrm{B}}T}\left(\frac{e^{\psi(\mathbf{r})} - e^{\psi(\mathbf{r})}}{2}\right) = \kappa^2 \sinh\psi(\mathbf{r}), \tag{2.4}$$

where $\psi(r) = \frac{e\varphi(\mathbf{r})}{k_{\mathrm{B}}T}$ is the reduced electrostatic potential and $\kappa = \sqrt{2e^2c^{\infty}/\epsilon_0\epsilon_{\mathrm{r}}k_{\mathrm{B}}T}$ is the inverse of Debye length ($\lambda$). Debye length defines the screening distance, at which shields the fixed charged object from 'seeing' the mobile ions beyond it.

### 2.1.2 Debye-Hückel Limit

The Poisson-Boltzmann relation (Eq. 2.4) is a nonlinear second-order differential equation, which is hard to compute, analytically, and it is commonly solved, numerically. However, we could simplify the PB equation to a linear approximation, called Debye-Hückel (DH) limit, when the electrostatic potential is small. For small potentials $\psi(\mathbf{r}) << 1$, we could use Taylor series expansion and obtain $\sinh x \approx [(1+x) - (1-x)]/2 = x$. Then DH equation for monovalent salt concentration (i.e. (1:1) electrolyte) is expressed by

$$\nabla^2\psi(\mathbf{r}) = \kappa^2\psi(\mathbf{r}). \tag{2.5}$$

Many biomembrane problems involve charged interfaces inside (1:1) electrolyte. Therefore, we are interested to see how electrostatic potential alters near a plane with surface charge density $\sigma$ by the perpendicular distance from the interface $z$. If we solve DH equation for a uniformly charged plane in a salt solution (1:1) with respect to the appropriate boundary conditions, the electrostatic potential near the charged surface is [84]

$$\psi(z) = \frac{4\pi\sigma\ell_{\mathrm{B}}}{\kappa}\exp\left(-\kappa z\right), \tag{2.6}$$

where we have introduced Bjerrum length as $\ell_{\mathrm{B}} = e^2/(4\pi\epsilon_0\epsilon_{\mathrm{r}}k_{\mathrm{B}}T)$. Eq. 2.6 shows that the electrostatic potential from the plane decreases as $\kappa$ increases. This is due to the fact that $\kappa$ is proportional to the square-root of salt concentration $\sqrt{c^{\infty}}$ (see Eq. 2.4). At a distance equal to the Debye length $\lambda = 1/\kappa$, the potential $\psi$ is decreased by a factor of $1/e$.

In case of electrostatic potential $\psi(r)$ as a function of the radial distance from a charged sphere with net charge $Q$ and radius $a$ inside a salt solution, Eq. 2.5 can be solved with respect to the appropriate boundary conditions to give potential as

$$\psi(r) = \frac{Q\ell_{\mathrm{B}}}{r(1+\kappa a)}\exp -\kappa(r-a). \tag{2.7}$$

Eq. 2.7 holds for a large spherical particle having a uniform surface charge $Q$, and even for small ions (e.g. sodium or chloride) that has a single charge. For small ions, we regard them as point charges and assume $a = 0$. Therefore the electrostatic potential of small ions become

$$\psi(r) = \frac{Q\ell_{\mathrm{B}}}{r} \exp\left(-\kappa r\right). \tag{2.8}$$

As a result of screening effect of the salt ions ($\kappa$), the electrostatic potential decays exponentially in both Eq. 2.7 and Eq. 2.8, compared to the long-ranged Coulomb potential.

## 2.2 Hydrophobic Free Energy

Water molecules as the solvent of the biological environment play a crucial role in the behaviour of biological molecules and their mechanism. Every $H_2O$ molecule tends to build and break H-bonds with its neighbouring molecules, constantly, due to its partial electrostatic charges. Placement of a non-polar solute inside the water affects the water structure as a result of the lack of forming H-bond between water molecules and the non-polar solute. For this reason, water molecules tend to have lower configuration around a non-polar (hydrophobic) solute, which drives the hydrophobic free energy cost in the biological system.

The water hydrogen bond is a weak bond; about a twentieth of the strength of the O-H covalent bond. However, it is strong enough to be maintained during thermal fluctuations. The H-bond comes from the polar characteristics of the water molecules with partial electrostatic-negative charge at oxygen atom and partial electrostatic-positive charge around its hydrogen atoms.

In order to calculate the free energy cost of a hydrophobic solute inside the water, we need to compute the entropy difference. In a pure solution, a single water molecule could pose 6 different positions and form H-bonds. However, introducing a hydrophobic solute reduces 3 of the total available water configurations. Therefore the entropy difference is

$$\Delta S = k_{\mathrm{B}}[\ln 3 - \ln 6] = -k_{\mathrm{B}} \ln 2, \tag{2.9}$$

where $k_{\mathrm{B}}$ is the Boltzmann constant. This change in entropy leads to a change in free energy for the water solution, $\Delta F_{\mathrm{w}}$. If $n$ water molecules are disrupted by a non-polar molecule, then the hydrophobic free energy cost to the water is

$$\Delta F_{\mathrm{w}} = n\, k_{\mathrm{B}} T \ln 2. \tag{2.10}$$

# Chapter 3

# Toward building a physical model for membrane selectivity of antimicrobial peptides: making a quantitative sense of the selectivity

## 3.1 Introduction

Antimicrobial peptides (AMPs) are wide-spectrum antibiotics and kill rapidly a wide range of microbes via various mechanisms (e.g., membrane rupture or intracellular killing) [5, 16, 18, 38, 57, 105, 106]. Optimized AMPs have been considered as next-generation antibiotics. Of particular interest are membrane-perturbing AMPs, since they do not easily induce antimicrobial resistance. They rupture bacterial or model membranes in an 'all-or-none' manner [5, 56, 57]: only above some peptide concentration in the bulk, they rupture their binding membranes. This concentration is known as a minimum-inhibitory or minimum-hemolytic concentration (denoted as MIC or MHC) for bacterial and host-cell membranes, respectively [36, 37]. Good peptides are those for which MHC is much larger than MIC. As a result, there is a considerable range of peptide concentrations at which peptides rupture bacterial membranes only, while leaving host-cell membranes intact; they are 'selective.'

The dependence of peptide activity on peptide concentrations suggests that cell concentrations are also involved. At a higher cell concentration, a larger amount of peptides is required. In other words, both MICs and MHCs are cell-concentration dependent; so is

the cell selectivity of peptides. The relationship between peptide selectivity and cell concentrations has been discussed [4, 6, 35, 39]. In particular, a theoretical model for peptide selectivity proposed recently shows this relationship in a quantitative manner.

Peptide selectivity is often quantified by the ratio: MHC/MIC, which is known as the 'therapeutic index' of a peptide [35, 36, 37]. Because of the cell concentration dependence of peptide selectivity, the selectivity is not a purely intrinsic property of peptides for a given membrane. It is influenced by external parameters such as cell density and the way it is obtained [6]. For instance, MHCs and MICs can be measured for a homogeneous solution of each type of cells or for a mixture of both types of cells. These two approaches usually produce different or even strikingly different selectivity [6].

Along this line, it is worth noting that the parameter space presenting both intrinsic and extrinsic properties is impossibly too large to explore experimentally. Of practical importance is a physical model of peptide selectivity that relates the intrinsic peptide-lipid parameters to apparent (cell-density-dependent) selectivity in a systematic way. Such a model will reduce the parameter space by offering the physical principles underlying the relationship between cell density and selectivity; it allows one to determine systematically peptide selectivity at biologically-relevant cell densities based on measured selectivity at conveniently-chosen cell densities, typically higher for host cells [4, 35, 39]. Further considerations in this direction will clarify peptide-parameter requirements for optimized peptide selectivity in a physiological environment (e.g., salinity, a heterogeneous mixture of host-cell and bacterial membranes) (see Refs. [4, 39] for recent efforts). Indeed, typical *in vitro* experiments have failed to recapitulate the cellular environment [39]. Can we nevertheless make sense of these experiments?

Here, we present a physical model for cell selectivity of cationic AMPs, especially one that shows the interplay between cell densities and peptide-lipid parameters in determining the selectivity. A number of more phenomenological models (see the SI of Ref [6] and Refs. [4, 39]) rely on the knowledge of peptide binding. As evidenced later, in our approach, peptide binding is quantified in terms of more microscopic parameters such as peptide charge and the fraction of charged lipids in a membrane.

In this work, each bound peptide is modelled as a circular disk as in Refs. [6, 9]; its amphiphilic nature is mimicked by assigning both a hydrophobic-interaction energy and an electric charge. Each bound peptide not only interacts with the surrounding lipids and other peptides but also induces lipid demixing; hydrophobically-bound peptides perturb the surrounding lipids mechanically as well. The simultaneous presence of several competing interactions/effects (e.g., lipid demixing and peptide-peptide interactions) poses a serious challenge to theoretical considerations. In a Langmuir-type binding model of molecular

binding [84], the energetics of binding is not influenced by the presence of other bound molecules. This is no longer the case for peptide binding we consider here. On the surface of a membrane, peptides compete for anionic lipids and/or interact with each other though electrostatic interactions. These interactions should be considered as non-local effects. In addition, the membrane deformation free energy induced by peptide binding is also nonlocal for a parameter range of biological interest [107].

For a number of reasons explained above, earlier theoretical approaches rely on approximation schemes for calculating the electrostatic interactions among various pairs (e.g., peptide-lipid and peptide-peptide) [6, 65, 108]. A common practice is to smear out peptide and lipid charges over some region occupied by the peptide and the surrounding lipids and to ignore the "edge" or "boundary" effects. Here we note that this leads to an overestimation of peptide binding, resulting in an exaggeration of MICs and MHCs. Crudely speaking, MICs and MHCs are exponentially sensitive to binding energy. Overestimating binding energy can introduce a gross error in selectivity.

Here, we carefully analyze several coarse-grained models and map out an accurate one. Using the resulting model, we clarify how cell densities and peptide parameters are intertwined in determining peptide selectivity, which is measured by the ratio MHC/MIC. To the contrary of earlier expectations (see Ref. [4, 35, 39] and those therein for relevant discussion), the selectivity is not simply intrinsic to the biophysical properties of peptides but also reflects cell densities. While this is qualitatively consistent with recent theoretical studies [6], our study suggests how peptide-membrane systems will have to be properly modelled. Indeed, it suggests that it is essential to incorporate the geometry of various regions, occupied by bound peptides, anionic lipids within the interaction range of each peptide, and those outside this range.

Furthermore our results show that peptide selectivity (MHC/MIC) is a non-monotonic function of peptide charge $Q$. As a result, the selectivity can be maximized at a special value of $Q$, referred to as an "optimal charge." This finding refines earlier considerations based on the fraction of hydrophobically-bound peptides (often denoted a $P/L$), which varies non-monotonically as a function of $Q$ for a charged membrane at a single cell limit [9]. Importantly, we note that the optimal charge varies with other peptide parameters and cell density. This offers a more complete picture of the notion of an optimal charge explored earlier [9, 109]. Furthermore, we map out a Langmuir-type model for examining the cell-density dependence of peptide selectivity.

This chapter is organized as follows. We present our theoretical model of a peptide-membrane system and derive the free energy of the model system in Sec. 3.2. Our results for peptide selectivity are presented in Sec. 3.3

## 3.2 Models and Free energy

### 3.2.1 Models

We first introduce a few models of peptide-membrane interactions, including the one used recently [6], refereed to as "model 1," as illustrated in Fig. 3.1 and Fig. 3.2. In particular, we make much effort to refine model 1 [6], especially by calculating electrostatic interactions more accurately. Our results will show how crucial this effort is. In all cases, bound peptides are modelled as circular disks. In the bulk, however, peptides resembles random coils; while we model them primarily as random coils, we also use the had-disk model as for bound peptides for comparison purposes. The former is labelled as "(i)" and the letter as "(ii)," as indicated in Fig. 3.1.

We first focus on the charged-membrane case, as illustrated in Fig. 3.1; as detailed below, the neutral-membrane system in Fig. 3.2 is a special case of the charged one in Fig. 3.1. Peptides can reside in the proximate of the membrane through electrostatic interactions or be hydrophobically associated with it. Following Ref. [6], these binding modes are referred to as 'S' (surface-adsorbed by electrostatic interactions) and 'I' (hydrophobically-inserted in a parallel orientation at the lipid head-tail interface), respectively.

Each peptide together with the surrounding lipids defines a Wigner-Seitz Cell (WSC); in Fig. 3.1 and Fig. 3.2, two WSCs are shown. Each bound peptide induces lipid segregation and mainly interacts with those in its neighbour, denoted as zone 1; its influence on charged lipids in zone 2 is insignificant. On average, each peptide experiences radially symmetrical interactions with other peptides on the membrane surface [9, 81]. Let $r$ be the radial distance from a bound peptide in a direction parallel with the membrane surface and $R_{\rm WSC}$ the radius of each WSC; the area of each WSC is given by $A_{\rm WSC} = \pi R_{\rm WSC}^2$. In a numerically-oriented approach, these interactions can be taken into account through an electric boundary condition at $r = R_{\rm WSC}$: the electric field in the radial direction on the membrane surface vanishes at $r = R_{\rm WSC}$ [9, 81]. In our approach, we improve systematically upon the one developed in Ref. [6] and employ an analytically-tractable model. In our approach, the notion of WSCs is merely used as a conceptual framework for considering various interaction pairs as detailed below. Similarly to earlier studies [6], here we focus on symmetric binding of AMPs between the inner and outer layers. In this case, the area of each WSC is given by $A_{\rm WSC} = (1 + \sigma_{\rm I} A_{\rm p})/(\sigma_{\rm I} + \sigma_{\rm S})$ [6] and can be taken to be the same for both modes I and S; similarly, the area of zone 1 is assumed to be the same for both modes (see the relevant discussion below Eq. 3.5). [1]

[1] Strictly speaking, $A_{\rm WSC}$ should be chosen such that at its boundary the electric field in the radial

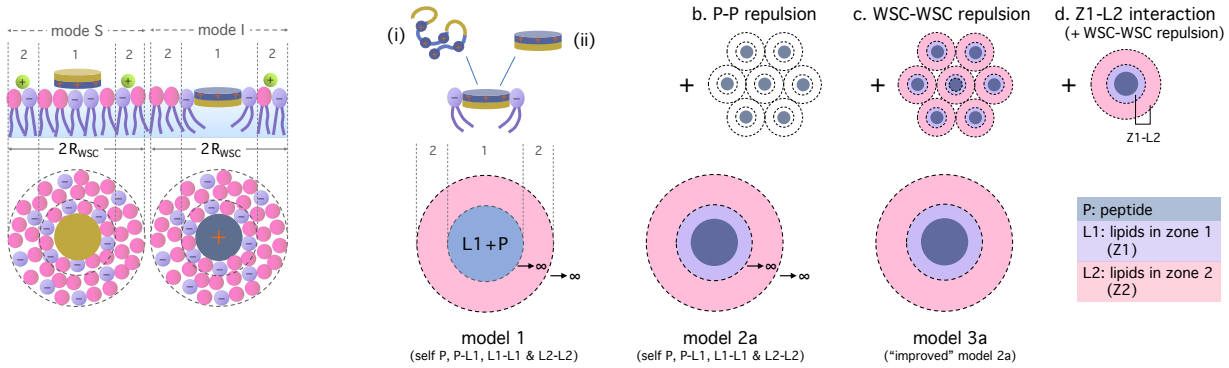


Figure 3.1: Various models are described and compared for describing the perturbation of bacterial membranes by antimicrobial peptides. Through this comparison, our model for peptide selectivity is systematically improved upon a recent model [6]. In the bulk, the peptide resembles random coils but assumes a compact structure on the membrane surface. Charged lipid bilayers mimicking bacterial (cytoplasmic) membranes are shown on the left. Peptides can reside in the proximate of the membrane through electrostatic interactions (binding mode 'S') or be hydrophobically associated with the membrane (binding mode 'I'). On the membrane surface, each peptide with the surrounding lipids is viewed as forming a 'Wigner-Seitz Cell' (WSC). It induces lipid segregation and mainly interacts with those in its neighbour, denoted as zone 1; its influence on charged lipids in zone 2 (the region in a WSC outside zone 1) is insignificant. Different models are compared: models 1-3; model 2 (model 3) is further classified into 2a-2c (3a-3d). In model 1, peptide and lipid charges in zone 1 are smeared out over the area of zone 1. This overestimates the electrostatic binding of peptides. To remedy this, in models 2 and 3, peptide area is preserved; if b (2b and 3b) and c (2c and 3c) include the repulsion between bound peptides and WSCs, respectively, model 3d takes into account the interaction between zone 1 and zone 2 (or lipids in zone 2) within the same WSC in addition to WSC interactions. In both models 1 and 2, the effect of finite areas is ignored, since the boundaries between zones 1 and 2 as well as the boundary between adjacent WSCs are taken to infinity. In contrast, in model 3, electrostatic interactions are calculated based on the original geometry of different regions. Furthermore, the Poisson-Boltzmann approach is used in models 1 and 2, whereas the (renormalized) Debye-Hückel approach is employed in model 3 [7, 8]. In model 3, the non-trivial geometry of various regions (e.g., the L1 region, i.e., the annular region in zone 1 occupied by lipids, as well as zone 2, a circular area with a "hole" at the centre) poses a serious barrier to electrostatic calculations.

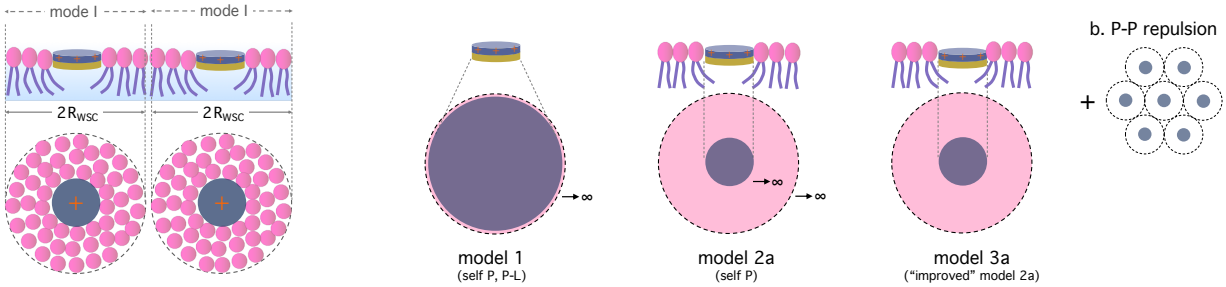


Figure 3.2: Various models are described and compared for describing the perturbation of host-cell membranes by antimicrobial peptides. Through this comparison, our model for peptide selectivity is systematically improved upon a recent model [6]. In the bulk, the peptide resembles random coils but assumes a compact structure on the membrane surface. Host-cell membranes (the outer layers) are often modelled as electrically neutral lipid bilayers. In the earlier model [6], denoted as model 1, the fraction of anionic lipids was set to $\bar{\alpha} = 0.05$; the peptide charge in a WSC was smeared out over the WSC. In models 2 and 3, $\bar{\alpha} = 0$ and the peptide charge is restricted to the area occupied by the peptide. If the area occupied by the peptide and the WSC are boundary-less in model 2, their geometry is explicitly taken into account in model 3. Similarly to model 2b for the bacterial membrane, model 2b for the host cell membrane takes into account the repulsion between bound peptides.

All models include the self energy of a peptide ("self P"), the interactions between a peptide and the surrounding lipids in zone 1 ("P-L1"), those among charged lipids in zone 1 ("L1-L1"), and those among charged lipids in zone 2 ("L2-L2"). In the bulk, the self energy is constant but becomes variable near a dielectric medium; it has to be taken into account. In model 1, the charges in zone 1, both peptide and lipid charges, are smeared out. As a result, the region occupied by one species, either a bound peptide or charged lipids, is permeable to the other. While this is reasonable for mode S (see this mode in Fig. 3.1) but will introduce a big error for mode I. Models 2 and 3 are improved upon this, as lipids are excluded from the region occupied by a peptide in mode I.

The main difference between models 2 and 3 is that only the latter preserves the geometry of each zone; in model 2, the edge (boundary) effect is ignored. Practically, this

direction on the surface vanishes. While this is obvious for one type of binding [108], it is not entirely clear if this boundary condition is satisfied when $A_{\mathrm{WSC}}$ is chosen to be the same for two different binding modes. In our semi-analytic approach, WSCs are merely used to visualize electrostatic-interaction pairs. The aforementioned boundary condition is not used explicitly. Instead we take into account directly the interaction between WSCs. See subsec. 3.2.1 and also Ref. [6].

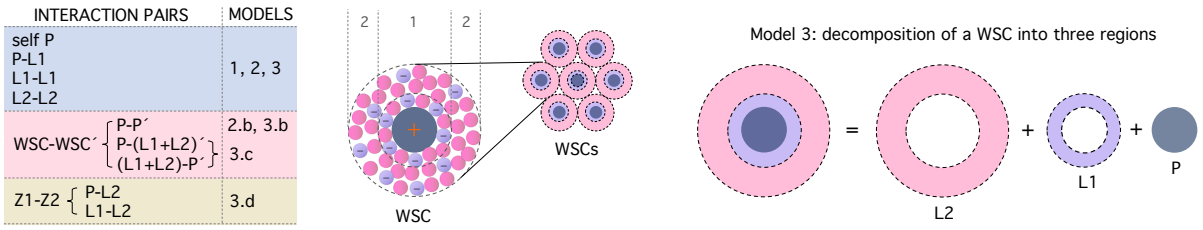


Figure 3.3: Models and interaction pairs captured in each model. All models include the self energy of a peptide ("Self P"), the interactions between a peptide and the surrounding lipids in zone 1 ("P-L1"), those among charged lipids in zone 1 ("L1-L1"), and those among charged lipids in zone 2 ("L2-L2"). In the bulk, the self energy of a peptide is constant but becomes variable near a dielectric medium (or upon conformational change on the membrane surface); it has to be taken into account. Only model 3 includes the interactions between zone 1 and zone 2 ("Z1-Z2"), which can be decomposed into P-L2 and L1-L2 interactions. Because of the neutralization of the peptide charge by the surrounding negatively-charged lipids in zone 1, this interaction turns out to be insignificant. The repulsion between peptides is taken into account in 2b and 3b. The repulsion between different WSCs is fully captured in 2c and 3c (the middle panel). In our analysis of interaction pairs, especially in model 3, we decompose each WSC into three regions, as illustrated on the right: the outer and inner rings as well as a disk occupied by a peptide. In this model, the pair interactions between different regions are explicitly taken into account, without simplifying their geometry.

amounts to taking the boundary of each zone to infinity as illustrated in Fig. 3.1 and in Fig. 3.2. "Models 2b" and "3b" include peptide-peptide (P-P) repulsions; "2c" and "3c" capture WSC-WSC repulsions; "3d" includes the interaction between zone 1 and zone 2 ("Z1-L2") in addition to WSC-WSC repulsions. Because of the neutralization of the peptide charge by the surrounding negatively-charged lipids in zone 1, the last interaction is expected to be insignificant, which can be checked *a posteriori*. In our analysis of interaction pairs, especially in model 3, we decompose each WSC into three regions, as illustrated on the right in Fig. 3.3: the outer and inner rings as well as a disk occupied by a peptide. In this model, the pair interactions between different regions are explicitly taken into account, without simplifying their geometry. Finally, each submodel (e.g., 3d) can be further classified into two: $3d_i$ for a random coli and $3d_{ii}$ for a disk, depending on how free peptides are modelled as discussed earlier (see the middle panel in Fig. 3.1).

The membrane-perturbing activity of AMPs (prior to pore formation or membrane

rupture) is often quantified by a single parameter $P/L$, defined as the molar ratio of peptides in the "membrane-perturbing mode" to lipids (excluding possible free lipids in the solution) [5, 37, 46, 57, 96] (peptides in this mode are hydrophobically associated with a parallel orientation). Beyond a threshold value $P/L^*$, they can create pores in their binding membrane [5, 37, 46, 57, 96] or disrupt the membrane in a 'carpet'-like manner [18, 37]. The corresponding total concentration of peptides, whether free or bound, is known as an MIC (for bacterial cells) or MHC (for host cells) [5, 37, 46, 57].

Indeed, $P/L^*$ is influenced by various factors: lipid composition (e.g., charged vs. neutral), lipid headgroup area, peptide charge and size, and other known and unknown biological details [5, 37, 46, 53, 57, 96]. Here, we do not attempt to calculate $P/L^*$ from first principles but use commonly-accepted values; we also employ a phenomenoligcal model for estimating it with a varying peptide charge. Indeed, the value of $P/L^*$ depends on both peptide and membrane parameters, and this dependence has not been well understood theoretically. Nevertheless, this quantity is relatively well characterized for the peptide melittin (see for instance Refs. [5, 46, 57]): $P/L^* \approx 0.02 \equiv P/L^*_{\rm B}$ for bacterial membranes and $P/L^* \approx 0.01 \equiv P/L^*_{\rm H}$ for host cell membranes. We will use the representative $P/L^*$ values for this peptide. As more accurate measurements of $P/L^*$ become available, their values can be used in our theory.

Below, we first derive a general free-energy approach to a peptide-membrane system, which holds possibly for a large class of pore-forming cationic AMPs, and apply it to melittin as a representative peptide. Note that free energy and energy are given in units of the thermal energy $k_{\rm B}T$ and planar charge densities in units of the elementary charge $e$.

### 3.2.2 Free energy calculations

We first construct the free energy of each WSC, denoted as $F_{\rm WSC}$. It can be expressed in terms of a few quantities: the planar density of anionic lipids in zone 1 and 2, denoted as $\sigma_1$ and $\sigma_2$, respectively; $L_1$ and $L_2$ are the corresponding number of anionic lipids; the fractions of anionic lipids, $\alpha_1$ and $\alpha_2$, are related to $\sigma_1$ and $\sigma_2$ as $\alpha_i = -\sigma_i a_\ell$ $(i = 1, 2)$, where $a_\ell$ is the lipid headgroup area. In the absence of bound peptide, $\alpha_i$ tends to a constant value denoted as $\bar{\alpha}$.

Let $F_{\rm el}(\sigma_1, \sigma_2)$ be the electrostatic free energy of each WSC. Throughout this paper, free energy and energy are expressed in units of the thermal energy $k_{\rm B}T$ (equivalently we set $k_{\rm B}T = 1$), unless otherwise indicated; here and below, $k_{\rm B}$ is the Boltzmann constant and $T$ the temperature. The free energy of each WSC, excluding the membrane-deformation

energy, can be written as

$$\begin{aligned} F_{\rm WSC} &= F_{\rm el}(\sigma_1,\sigma_2)+\varepsilon_1\delta_{{\rm I}i} \\ &\quad +L_1\left[\alpha_1\ln\alpha_1+(1-\alpha_1)\ln(1-\alpha_1)\right]+L_2\left[\alpha_2\ln\alpha_2+(1-\alpha_2)\ln(1-\alpha_2)\right] \end{aligned} \tag{3.1}$$

Possibly except for the first term on the right hand side of Eq. 3.1, i.e., $F_{\rm el}(\sigma_1,\sigma_2)$, other terms can readily be understood. The second term describes the free energy gain for hydrophobic insertion. The delta function is to ensure that this term survives for mode I but vanishes for mode S. The last two terms account for the entropic penalty for lipid rearrangements induced by peptide binding.

In the Appendices, we present detailed steps leading to the computation of $F_{\rm el}(\sigma_1,\sigma_2)$. As illustrated in Fig. 3.1 and Fig. 3.2, we employ three models for peptide binding: models 1, 2, and 3; within each model, a few variations are considered (e.g., 3a(i), 3b(ii), 3c,...), as discussed earlier. Below, we outline the essence of these calculations.

First, note that $F_{\rm el}(\sigma_1,\sigma_2)$ can be decomposed into several terms as

$$F_{\rm el}(\sigma_1,\sigma_2) = F_{\rm p}+F_{\rm P-L1}+F_{\rm L1}+F_{\rm L2}+F_{\rm Z1-Z2}+F_{\rm WSC-WSC'}. \tag{3.2}$$

The first term $F_{\rm p}$ is the self energy of each bound peptide; the second term $F_{\rm P-L1}$ represents the interaction between a bound peptide and the surrounding lipids in the interaction zone, i.e., zone 1; the third $F_{\rm L1}$ and fourth terms $F_{\rm L2}$ are the interaction free energy of lipids in zone 1 and 2, respectively; the fifth one arrises from the interaction between zone 1 and zone 2 within the same WSC; $F_{\rm WSC-WSC'}$ describes the interaction between different WSCs.

For the host-cell membrane mimicking lipid bilayer in Fig. 3.2, $\bar{\alpha}\approx 0$; it is set to zero in this work. As a result, binding mode S becomes irrelevant; also the distinction between zones 1 and 2 disappears, and each WSC consists of one zone. As a result, Eq. 3.2 reduces to

$$F_{\rm el}(\sigma_{\rm p}) = F_{\rm p}+F_{\rm WSC-WSC'}. \tag{3.3}$$

In our electrostatic considerations, it proves useful to introduce the two important lengths: the Bjerrum length $\ell_{\rm B}$ and the screening length $\kappa^{-1}$ [66, 84]. The former is given by

$$\ell_{\rm B} = \frac{e^2}{4\pi\epsilon_0\epsilon_r k_{\rm B}T}, \tag{3.4}$$

where $e$ is the elementary charge, $\epsilon_0$ the permittivity of free space, and $\epsilon_r$ the relative permittivity or the dielectric constant of the solvent. The screening length $\kappa^{-1}$ is related

to the total density of ions (assumed to be monovalent), denoted as $n_0$, via

$$\kappa^2 = 4\pi\ell_{\rm B} n_0. \tag{3.5}$$

Beyond $\kappa^{-1}$, the electrostatic interaction is exponentially suppressed in magnitude. A related quantity is the two-dimensional screening length or the Gouy-Chapman length, given by $\lambda = a_\ell/2\pi\ell_{\rm B}\bar{\alpha}$. This naturally sets the boundary of zone 1: its area $A_1 = \pi\left(R_{\rm p}+\lambda\right)^2$, taken to be the same for both binding modes [6].

**peptide self energy**

First, assume that a bound peptide is viewed as a uniformly-charged circular plate of area $A_{\rm p}$ with a planar charge density $\sigma_{\rm p} = Q/A_{\rm p}$ in units of $e$; throughout this work, such symbols as $\sigma_{\rm p}$, $\sigma$, and $\sigma_1$ denote planar charge densities in units of $e$. To obtain the peptide free energy, consider a charged dielectric plate (with the charges on the $x$-$y$ plane) occupying the space $z<0$. Let $\sigma$ be the planar charge density of the plate. The plate free energy $\mathcal{F}_{\rm plate}$ per area can be obtained from the Poisson-Boltzmann approach [110]:

$$\mathcal{F}_{\rm plate} = \sigma\Psi_0^{\rm thick} - \frac{\kappa}{\pi\ell_{\rm B}}\left[\cosh\left(\frac{\Psi_0^{\rm thick}}{2}\right)-1\right], \tag{3.6}$$

where $\Psi_0^{\rm thick}$ is the surface potential of the (thick) plate given by

$$\Psi_0^{\rm thick} = 2\sinh^{-1}\left(\frac{2\pi\ell_{\rm B}\sigma}{\kappa}\right). \tag{3.7}$$

With an appropriate choice of $\sigma$, Eq. 3.6 can be used as the self free energy of a bound peptide $F_{\rm p}^{\rm Mo.1}$ in model 1: $F_{\rm p}^{\rm Mo.1} = A_{\rm p}\mathcal{F}_{\rm plate}(\sigma=\sigma_{\rm p})$. It can also be used to estimate the peptide-lipid interaction in model 1, lipid-lipid interaction in model 2 (see Eq. 3.16 and Eq. 3.17), and the membrane reference free energy in all models.

More realistically, if we take into account the size of peptide charges by leaving some gap, $h$, between peptide charges and the dielectric interface, the electrostatic free energy of a bound peptide becomes

$$\begin{aligned} F_{\rm P}^{\rm Mo.2}(h) &= \frac{A_{\rm p}}{\pi\ell_{\rm B}h}\ln\left[\frac{1+\exp\left(-2\kappa h\right)}{1+\exp\left(-2\kappa h\sqrt{\cosh\Psi_0^{\rm double}}\right)}\right] \\ &\quad + \frac{A_{\rm p}\kappa}{\pi\ell_{\rm B}}\left\{1-\sqrt{\cosh\Psi_0^{\rm double}}-\Psi_0^{\rm double}\sinh\left(\frac{\Psi_0^{\rm thin}}{2}\right)\right\}, \end{aligned} \tag{3.8}$$

where $\Psi_0^{\text{double}} = \sinh^{-1}\left[2\sinh\left(\frac{1}{2}\Psi_0^{\text{thin}}\right)/\tanh\left(\kappa h\right)\right]$ is the surface potential of two like-charged parallel thin plates a distance $2h$ apart and $\Psi_0^{\text{thin}} = 2\sinh^{-1}\left(\pi\ell_{\text{B}}\sigma_{\text{p}}/\kappa\right)$ is the corresponding quantity for an isolated thin-layer plate.

Fig. A.1 in Appendix A shows a simple representation of how the free energy of a disk-like peptide with a constant surface charge density $\sigma_{\text{p}}$ above the dielectric interface can be transformed into a double-layer interaction free energy of two like-charged plates, separated by $2h$. A central quantity in this connection is the dielectric discontinuity parameter

$$\Delta_\epsilon = \frac{\epsilon_w - \epsilon_\ell}{\epsilon_w + \epsilon_\ell} \quad (\approx 1 \text{ for } \epsilon_w \gg \epsilon_\ell) \tag{3.9}$$

(see Ref. [**?**] and relevant references therein), where the subscripts '$w$' and '$\ell$' refer to water and lipids, respectively. The free energy in Eq. 3.8 is used for model 2.

In model 3, the peptide self energy can be obtained from the DH approach to two charged disks a distance $h$ apart. It can be expressed in an integral form as

$$F_{\text{p}}^{\text{Mo.3}}(h) = 2\pi\ell_{\text{B}}\sigma_{\text{p}}^2\int_0^{R_{\text{p}}}\int_0^{R_{\text{p}}} r_1 r_2 dr_1 dr_2 \int_0^{2\pi} d\theta \left[\frac{1}{2}\frac{e^{-\kappa\sqrt{|\mathbf{r}_2-\mathbf{r}_1|^2}}}{\sqrt{|\mathbf{r}_2-\mathbf{r}_1|^2}} + \Delta_\epsilon\frac{e^{-\kappa\sqrt{|\mathbf{r}_2-\mathbf{r}_1|^2+4h^2}}}{\sqrt{|\mathbf{r}_2-\mathbf{r}_1|^2+4h^2}}\right], \tag{3.10}$$

where $\mathbf{r}_1$ and $\mathbf{r}_2$ are the position vectors on the membrane surface and $\theta$ is the angle between the two vectors: $|\mathbf{r}_2-\mathbf{r}_1|^2 = r_1^2 + r_2^2 - 2r_1 r_2\cos\theta$. The first term in Eq. 3.10 is the self energy of the peptide in the absence of image charges and the second one represents the mutual interaction between the peptide charges on a disk and the corresponding image charges with a surface charge density $\Delta_\epsilon\sigma_{\text{p}}$.

Unlike Eq. 3.8, which ignores boundary effects, since it is based on boundary-less plates, Eq. 3.10 is obtained for a finite-circular object. Also it is worth mentioning that the gap size $h$ introduced here has insignificant effects on other free energy terms, since it has a minimal impact on the distance between two charges on the surface. This feature will be ignored in our consideration below.

### $F_{\text{P-L1}}$: peptide-lipid interaction in zone 1

A hydrophobically-bound peptide, i.e., one in mode I, pushes the surrounding lipids away from it. The area occupied by lipids in zone 1 can thus be approximated as a charged surface with a hole of radius $R_{\text{p}}$ (i.e., peptide radius) at the centre. If we ignore the

"outer-boundary effect," as assumed in model 2, the peptide-lipid interaction free energy can be obtained as

$$F^{\text{Mo.2}}_{\text{P-L1(I)}} \approx \pi\sigma_{\text{p}}R_{\text{p}}^2\left(\Psi_0(0) - \tanh\Psi_0(0) + \frac{4\pi\ell_{\text{B}}\sigma_{1(\text{I})}}{\kappa\sqrt{\cosh\Psi_0(0)}}\right) - 8\pi^2\ell_{\text{B}}\sigma_{1(\text{I})}\sigma_{\text{p}}R_{\text{p}}^2\int_0^\infty dk\frac{J_1^2(kR_{\text{p}})}{k\sqrt{k^2+\kappa^2\cosh\Psi_0(0)}}, \tag{3.11}$$

where $\Psi_0(0) = \Psi_0(r=0)$ is the surface potential (with $\sigma = \sigma_{1(\text{I})}$) at the centre of the hole given by

$$\Psi_0(0) \approx \sinh^{-1}\left[\frac{4\pi\ell_{\text{B}}\sigma}{\kappa} - 4\pi\ell_{\text{B}}\sigma R\int_0^\infty dk\frac{J_1(kR)}{\sqrt{k^2+\kappa^2}}\right], \tag{3.12}$$

and $\sigma_{1(\text{I})}$ is the surface charge density of anionic lipids in zone 1. Throughout this paper, $J_1(x)$ is the Bessel function of the first kind and order 1. The results in Eq. 3.11 and Eq. 3.12 are approximations derived in Appendix B.

In contrast, for mode S, the interaction energy is the work required to bring Q charges on an infinitely thick dielectric plate of surface charge density $\sigma_1$. We thus have

$$F^{\text{Mo.2}}_{\text{P-L1(S)}} = 2Q\sinh^{-1}\left(\frac{2\pi\ell_{\text{B}}\sigma_{1(\text{S})}}{\kappa}\right). \tag{3.13}$$

Recall that $\Psi_0^{\text{thick}} = 2\sinh^{-1}(2\pi\ell_{\text{B}}\sigma/\kappa)$ (see Eq. 3.7). The free energy $F^{\text{Mo.2}}_{\text{P-L1(S)}}$ in Eq. 3.13 is just $Q$ times $\Psi_0^{\text{thick}}(\sigma = \sigma_{1(\text{S})})$ with $\sigma_{1(\text{S})} = \alpha_{1\text{S}}/a_\ell$; recall $a_\ell$ is the area occupied by each lipid.

In model 3, the geometry of zone 1 is preserved. Because of the technical difficulty in solving the Poisson-Boltzmann (PB) equation with this geometry, we employ a "renormalized" Debye-Hückel (DH) approach [7, 8, 66, 111] for the computation of the lipid-peptide interaction. The resulting approach is better than what it might indicate. The non-linearity in the interaction between a peptide and lipid charges is taken into account by classifying peptides into two subclasses: "free" and "bound." Because of neutralization of lipid charges by peptide charges, the residual interaction between the membrane-bound-peptide system and ions will be insignificant. In this model, the area occupied with lipids in zone 1 can be viewed as a circular ring with an outer radius $R_1$ and an inner radius $R_{\text{p}}$. As a result, the interaction free energy can be obtained by considering the interaction a bound peptide feels from the DH surface potential of the circular ring around the peptide:

$$F^{\text{Mo.3}}_{\text{P-L1(I)}} = 8\pi^2\ell_{\text{B}}\sigma_{\text{p}}\sigma_{1(\text{I})}\int_0^\infty dk\frac{R_{\text{p}}J_1(kR_{\text{p}})}{k\sqrt{k^2+\kappa^2}}\left[R_1J_1(kR_1) - R_{\text{p}}J_1(kR_{\text{p}})\right]. \tag{3.14}$$

See Appendix A for the derivation.

On the other hand, for mode S, the peptide's and lipid's charges are assumed to be smeared out over zone 1 with a net planar charge density $\sigma_{\rm net} = Q/A_1 - \alpha_{1(\rm S)}/a_\ell$; here and below, $A_1$ is the area of zone 1. In this case, it is natural to consider the lipid-peptide and lipid-lipid interactions in zone 1 simultaneously. We thus find

$$F^{\rm Mo.3}_{\rm P-L1(S)} + F^{\rm Mo.3}_{\rm L1(S)} = 4\pi^2 \ell_{\rm B} \left(\sigma^2_{\rm net} - \sigma^2_{\rm p(A_1)}\right) \int_0^\infty dk \frac{R_1^2 J_1^2(kR_1)}{k\sqrt{k^2+\kappa^2}}, \tag{3.15}$$

where $\sigma_{\rm p(A_1)} = Q/A_1$ is the surface charge density of a peptide when the charge is smeared out over $A_1$. The second term in the right side of the Eq. 3.15 needs to be subtracted from the first term, i.e., the total free energy of the smeared-out charges in zone 1, since the peptide free energy is already captured by $F_{\rm p}$ in Eq. 3.8.

### Lipid-lipid interaction in each zone: $F_{\rm L1}(F_{\rm L2})$

The lipid-lipid interaction in each zone can readily be obtained if the zone is treated as a boundary-less thick plate with a surface charge density $\sigma_{1(i)}$ or $\sigma_{2(i)}$ as in model 2. Eq. 3.6 (or Eq. A.1 in Appendix A) suggests that

$$F^{\rm Mo.2}_{\rm L1(}{}_{i)} = \left(A_{\rm WSC} - A_{\rm P}\delta_{{\rm I}i}\right) \mathcal{F}_{\rm plate}\left(\sigma_{1(i)}\right) \tag{3.16}$$

$$F^{\rm Mo.2}_{\rm L2(}{}_{i)} = \left(A_{\rm WSC} - A_1\right) \mathcal{F}_{\rm plate}\left(\sigma_{2(i)}\right). \tag{3.17}$$

Recall here that $A_{\rm WSC} = \pi R^2_{\rm WSC}$ is the area of each WSC. The presence of the delta function in Eq. 3.16 is to ensure that lipids are excluded from the hydrophobically-bound central peptide. Also recall that $\mathcal{F}_{\rm plate}$ is given in Eq 3.6.

In model 3, recall that we use the renormalized DH approach; using this, we first calculate the surface potential of a ring that represents zone 2 for both modes and zone 1 for mode I; recall the free energy of anionic lipids in zone 1 for mode S, $F^{\rm Mo.3}_{\rm L1(S)}$, is already presented in Eq. 3.15. This leads to

$$F^{\rm Mo.3}_{\rm L1(I)} = 4\pi^2 \ell_{\rm B} \sigma^2_{1(\rm I)} \int_0^\infty \frac{dk}{k\sqrt{k^2+\kappa^2}} \left[R_1 J_1(kR_1) - R_{\rm P} J_1(kR_{\rm p})\right]^2 \tag{3.18}$$

and

$$F^{\rm Mo.3}_{\rm L2(}{}_{i)} = 4\pi^2 \ell_{\rm B} \sigma^2_{2(i)} \int_0^\infty \frac{dk}{k\sqrt{k^2+\kappa^2}} \left[R_{\rm WSC} J_1(kR_{\rm WSC}) - R_1 J_1(kR_1)\right]^2, \tag{3.19}$$

where $i = $ S or I.

**Interactions between Wigner-Seitz Cells or between peptides: $F_{\mathrm{WSC-WSC'}}$ or $F_{\mathrm{P-P'}}$**

The interaction between bound peptides or WSCs can be included. In sub-model b, i.e., 2b or 3b, we only take into account the interaction between bound peptides: $\mathrm{P}-\mathrm{P}'$. The resulting interaction free energy $F_{\mathrm{P-P'}}$ can be obtained by considering the interaction between a circular disk of radius $R_{\mathrm{p}}$ and an infinite plate with a hole of radius $R_{\mathrm{WSC}}$. Their corresponding surface charge densities are $\sigma_{\mathrm{p}} = Q/A_{\mathrm{p}}$ and $\sigma_{\mathrm{p'}} = \frac{(\sigma_{\mathrm{I}}+\sigma_{\mathrm{S}}-1/A_{\mathrm{cell}})Q}{(1+\sigma_{\mathrm{I}}A_{\mathrm{p}}-A_{\mathrm{WSC}}/A_{\mathrm{cell}})}$, respectively, where $A_{\mathrm{cell}}$ is the total surface area of a cell: $A_{\mathrm{cell}} = A_{\mathrm{B}}$ and $A_{\mathrm{cell}} = A_{\mathrm{H}}$ are the cell membrane area of bacteria and host cells, respectively. In model 2, an approximated PB approach (Appendix B) is used; in model 3, a renormalized DH approach is employed without simplifying the geometry of the hole and the rest. This consideration leads to

$$\begin{aligned} F^{\mathrm{Mo.2b}}_{\mathrm{p-p'}} &\approx \frac{\pi\sigma_{\mathrm{p}}R_{\mathrm{p}}^2}{2}\left(\Psi'_0(0) - \tanh\Psi'_0(0) + \frac{4\pi\ell_{\mathrm{B}}\sigma_{\mathrm{p'}}}{\kappa\sqrt{\cosh\Psi'_0(0)}}\right) \\ &\quad -4\pi^2\ell_{\mathrm{B}}\sigma_{\mathrm{p'}}\sigma_{\mathrm{p}}R_{\mathrm{WSC}}R_{\mathrm{p}}\int_0^\infty \frac{dk}{k}\frac{J_1(kR_{\mathrm{p}})J_1(kR_{\mathrm{WSC}})}{\sqrt{k^2+\kappa^2\cosh\Psi'_0(0)}} \end{aligned} \tag{3.20}$$

and

$$F^{\mathrm{Mo.3b}}_{\mathrm{P-P'}} = 2\pi^2\ell_{\mathrm{B}}\sigma_{\mathrm{p}}\sigma_{\mathrm{p'}}R_{\mathrm{p}}^2\left[\frac{1}{\kappa} - \frac{2R_{\mathrm{WSC}}}{R_{\mathrm{p}}}\int_0^\infty dk\frac{J_1(kR_{\mathrm{p}})J_1(kR_{\mathrm{WSC}})}{k\sqrt{k^2+\kappa^2}}\right]. \tag{3.21}$$

In Eq. 3.20 and below,

$$\Psi'_0(0) = \Psi'_0(r=0) = \sinh^{-1}\left[\frac{4\pi\ell_{\mathrm{B}}\sigma_{\mathrm{p'}}}{\kappa} - 4\pi\ell_{\mathrm{B}}\sigma_{\mathrm{p'}}R_{\mathrm{WSC}}\int_0^\infty dk\frac{J_1(kR_{\mathrm{WSC}})}{\sqrt{k^2+\kappa^2}}\right] \tag{3.22}$$

is the potential at the hole center due to the rest (i.e., the plate with a hole) with the surface charge density $\sigma_{\mathrm{P'}}$ (essentially identical to the potential in Eq. 3.12 with $\sigma = \sigma_{\mathrm{p'}}$). (Details steps of calculations leading to the approximate PB surface potential with hole $\Psi_{\mathrm{PB-Hole}}$ and $\Psi'_0(0)$ are explained in Appendix B.)

In a refined sub-model c, we include all relevant interaction pairs between WSCs: peptide-lipids′ and lipid-peptides′ as well as peptide-peptide′. As explained in Fig. 3.3, the total interaction of a single WSC with the rest WSC′ can be de-composed into three distinct contributions: $\mathrm{P}-\mathrm{P}'$, $\mathrm{P}-(\mathrm{L1}+\mathrm{L2})'$, and $(\mathrm{L1}+\mathrm{L2})-\mathrm{P}'$.

$$F_{\mathrm{WSC-WSC'}} = F_{\mathrm{P-P'}} + F_{\mathrm{P-(L1+L2)'}} + F_{\mathrm{(L1+L2)-P'}}. \tag{3.23}$$

For this consideration, we essentially extend the method used for sub-model b, but using different surface charge densities, and consider the interaction between a charged circular disk representing a single WSC we focus on and the rest.

As a result, we arrive at

$$\begin{aligned} F^{\text{Mo.2}}_{\text{WSC}-\text{WSC}'(i)} &= \frac{\pi\sigma_{\text{WSC}}R^2_{\text{WSC}}}{2}\left(\Psi'_0(0)-\tanh\Psi'_0(0)+\frac{4\pi\ell_{\text{B}}\sigma_{\text{WSC}'}}{\kappa\sqrt{\cosh\Psi'_0(0)}}\right) \\ &\quad -4\pi^2\ell_{\text{B}}\sigma_{\text{WSC}'}\sigma_{\text{WSC}}R^2_{\text{WSC}}\int_0^\infty dk\frac{J_1^2(kR_{\text{WSC}})}{k\sqrt{k^2+\kappa^2\cosh\Psi'_0(0)}} \end{aligned} \tag{3.24}$$

$$F^{\text{Mo.3}}_{\text{WSC}-\text{WSC}'(i)} = \left(2\pi^2\ell_{\text{B}}\sigma_{\text{WSC}}\sigma_{\text{WSC}'}R^2_{\text{WSC}}\right)\left[\frac{1}{\kappa}-2\int_0^\infty dk\frac{J_1^2(kR_{\text{WSC}})}{k\sqrt{k^2+\kappa^2}}\right], \tag{3.25}$$

where $\Psi'_0(0)$ is given in Eq. 3.22. Here $\sigma_{\text{WSC}}$ and $\sigma_{\text{WSC}'}$ correspond to the central-disk WSC and the rest, respectively, and are given by

$$\begin{aligned} \sigma_{\text{WSC}(i)} &= \frac{Q-\bar{\alpha}/a_\ell(A_{\text{WSC}}-A_{\text{P}}\delta_{\text{I}i})}{A_{\text{WSC}}} \\ \sigma_{\text{WSC}'(i)} &= \frac{(\sigma_{\text{I}}+\sigma_{\text{S}}-1/A_{\text{cell}})Q-\bar{\alpha}/a_\ell\left[1-(A_{\text{WSC}}-A_{\text{P}}\delta_{\text{I}i})/A_{\text{cell}}\right]}{1+\sigma_{\text{I}}A_{\text{P}}-A_{\text{WSC}}/A_{\text{cell}}}. \end{aligned} \tag{3.26}$$

**Interaction between zone 1 and zone 2:** $Z1-Z2$

The interaction between zone 1 and 2 in the same WSC can be decomposed into two parts

$$F^{\text{Mo.3}}_{\text{Z1}-\text{Z2}} = F_{\text{P}-\text{L2}}+F_{\text{L1}-\text{L2}}. \tag{3.27}$$

The regions occupied by the peptide, lipids in zone 1 (L1), and lipids in zone 2 (L2) can be considered as concentric circular rings of appropriate inner and outer radii; for the peptide, the inner radius is zero; the inner and outer radii of L1 (L2) are $R_{\text{p}}$ and $R_1$ ($R_1$ and $R_{\text{WSC}}$), respectively. The DH approach to these objects leads to the following interaction free energy

$$F_{\text{P}-\text{L2(I)}} = 8\pi^2\ell_{\text{B}}\sigma_{\text{p}}\sigma_{2(\text{I})}\int_0^\infty dk\frac{R_{\text{p}}J_1(kR_{\text{p}})}{k\sqrt{k^2+\kappa^2}}\left[R_{\text{WSC}}\,J_1\left(kR_{\text{WSC}}\right)-R_1\,J_1(kR_1)\right], \tag{3.28}$$

$$F_{\text{L1}-\text{L2(I)}} = \int_0^\infty dk\frac{8\pi^2\ell_{\text{B}}\sigma_{1(\text{I})}\sigma_{2(\text{I})}}{k\sqrt{k^2+\kappa^2}}\left[R_1J_1(kR_1)-R_{\text{P}}J_1(kR_{\text{P}})\right]\left[R_{\text{WSC}}J_1(kR_{\text{WSC}})-R_1J_1(kR_1)\right]. \tag{3.29}$$

As discussed earlier (see Eq. 3.15), for mode S, the peptide and lipid charges are taken to be uniformly smeared out. The resulting planar charge density is $\sigma_{\rm net} = Q/A_1 - \alpha_{1(\rm S)}/a_\ell$. With this difference, we arrive at

$$F_{(\rm P+L1)-L2(S)} = 8\pi^2 \ell_{\rm B} \sigma_{\rm net} \sigma_{2(\rm S)} \int_0^\infty dk \frac{R_1 J_1(kR_1)}{k\sqrt{k^2+\kappa^2}} \left[R_{\rm WSC} J_1(kR_{\rm WSC}) - R_1 J_1(kR_1)\right]. \quad (3.30)$$

**Other free energies**

Finally, the hydrophobic association of a peptide occurs at the expense of membrane deformations. Around or above $P/L^*$, the membrane deformation energy (per unit area) can be simplified as $\frac{1}{2}K_{\rm A}(\sigma_{\rm I}A_{\rm p})^2$, where $K_{\rm A}$ is the area stretch modulus [57, 97]. In principle, a more complete form of deformation free energy can be used. In practice, the above-referenced harmonic free energy can be used for a wide range of deformations (see Ref. [59] for relevant discussions).

Because of the dielectric property and thickness of membrane bilayers, the two layers (inner and outer) can be viewed as electrostatically decoupled [6]; also for simplicity, we assume symmetric peptide binding between the two layers. We can then consider each layer separately.

### 3.2.3 Free energy minimization

Let $\sigma_{\rm S}$ and $\sigma_{\rm I}$ be the planar density of peptides in mode S and I, respectively; the latter is related to $P/L$ as $\sigma_{\rm I} a_\ell = P/L$. Including all the relevant terms obtained earlier, we construct the total free energy of our peptide-membrane system per area:

$$\begin{aligned}\mathcal{F}_{\rm total} &= \sigma_{\rm I} F_{\rm WSC(I)} + \sigma_{\rm S} F_{\rm WSC(S)} + \frac{1}{2}K_{\rm A}(\sigma_{\rm I}A_{\rm p})^2 + \sigma_{\rm I}\ln(\sigma_{\rm I}A_{\rm p}) + \sigma_{\rm S}\ln(\sigma_{\rm S}A_{\rm p}) \\ &\quad + (\sigma_{\rm max} - \sigma_{\rm I} - \sigma_{\rm S})\ln\left(1 - \frac{\sigma_{\rm I}+\sigma_{\rm S}}{\sigma_{\rm max}}\right) + \frac{k_{\rm B}T}{N_{\rm cell}A_{\rm cell}}\left[N_{\rm free}\ln\left(\frac{N_{\rm free}v_{\rm p}}{V}\right) - N_{\rm free}\right] \\ &\quad - \mathcal{F}_{\rm ref}, \end{aligned} \quad (3.31)$$

where $F_{\rm WSC(I)}$ ($F_{\rm WSC(S)}$) is $F_{\rm WSC}$ for the binding mode I (S), given in Eq. 3.1.

The first three terms on the right hand side are introduced earlier in subsec. 3.2.2. The fourth-sixth terms in Eq. 3.31 describe the entropy of mixing within a two-dimensional lattice-gas model, where $\sigma_{\rm max} = 1/A_{\rm p}$ is the maximum surface coverage of peptides (see

for instance Ref. [84]). The seventh term is the entropic free energy of free peptides. Here, $N_{\rm cell}$ is the total number of target cells (either host cells or bacteria), $A_{\rm cell}$ the area of each target cell, $V$ the total volume of the entire system, $v_{\rm p}$ the volume of a peptide in the bulk, and $N_{\rm free}$ the total number of free peptides; $N_{\rm cell} = N_{\rm B}$ ($N_{\rm H}$) for bacterial (host) cells and $A_{\rm cell} = A_{\rm B}$ ($A_{\rm H}$) for bacterial (host) cell surface area.

As in a typical experimental setting, in our consideration, the total number of peptides $N_{\rm p}$ is held fixed. As a result, the number of free peptides decreases upon peptide binding and is given by $N_{\rm free} = N_{\rm p} - N_{\rm cell}A_{\rm cell}(\sigma_{\rm I} + \sigma_{\rm S})$.

Finally, the reference free energy per area $\mathcal{F}_{\rm ref}$ describes the corresponding system without bound peptides and is given by

$$\mathcal{F}_{\rm ref} = \mathcal{F}_{\rm plate}(\sigma_0) + \frac{1}{a_\ell}\left[\bar{\alpha}\ln\bar{\alpha} + (1-\bar{\alpha})\ln(1-\bar{\alpha})\right] + \frac{1}{N_{\rm cell}A_{\rm cell}}\left[N_{\rm p}\ln\left(\frac{N_{\rm p}v_{\rm p}}{V}\right) - N_{\rm p}\right]. \tag{3.32}$$

This free energy is contributed by three distinct effects: the charging free energy of a membrane without bound peptides (recall $\sigma_0 = -\bar{\alpha}/a_\ell$), the lipid entropy of mixing, and the entropy of peptides (all free). The charging free energy of a semi-infinite plate per area $\mathcal{F}_{\rm plate}$ is defined in Eq. 3.6 or Eq. A.1 presented in Appendix A.

The total free energy in Eq. 3.31 is to be minimized with respect to $\sigma_{\rm I}$, $\sigma_{\rm S}$, $\sigma_1$ and $\sigma_2$ for given values of $N_{\rm p}/V$, $N_{\rm cell}/V$ and $\bar{\alpha}$. Note that the fraction of charged lipids in zone 1 and 2 ($e\sigma_1 = -e\alpha_1/a_\ell$ and $e\sigma_2 = -e\alpha_2/a_\ell$) are not independent of each other but are related via the number conservation of charged lipids in each WSC:

$$\int_{A_{\rm WSC}} [\alpha(x,y) - \bar{\alpha}]dxdy = 0, \tag{3.33}$$

where $(x, y)$ is the position on the $x$-$y$ plane, i.e., on the membrane surface [6].

## 3.3 Results

### 3.3.1 Free energy analysis: MICs, MHCs, and peptide selectivity

We have analyzed Eq. 3.31 for both charged and neutral membranes, mimicking bacterial and host cells, respectively. Here we use "charged" and "bacterial membranes" ("neutral" and "host cell membranes") interchangeably and plotted our results for MIC, MHC, and MHC/MIC in Fig. 3.4, Fig. 3.5 and Fig. 3.6, respectively.

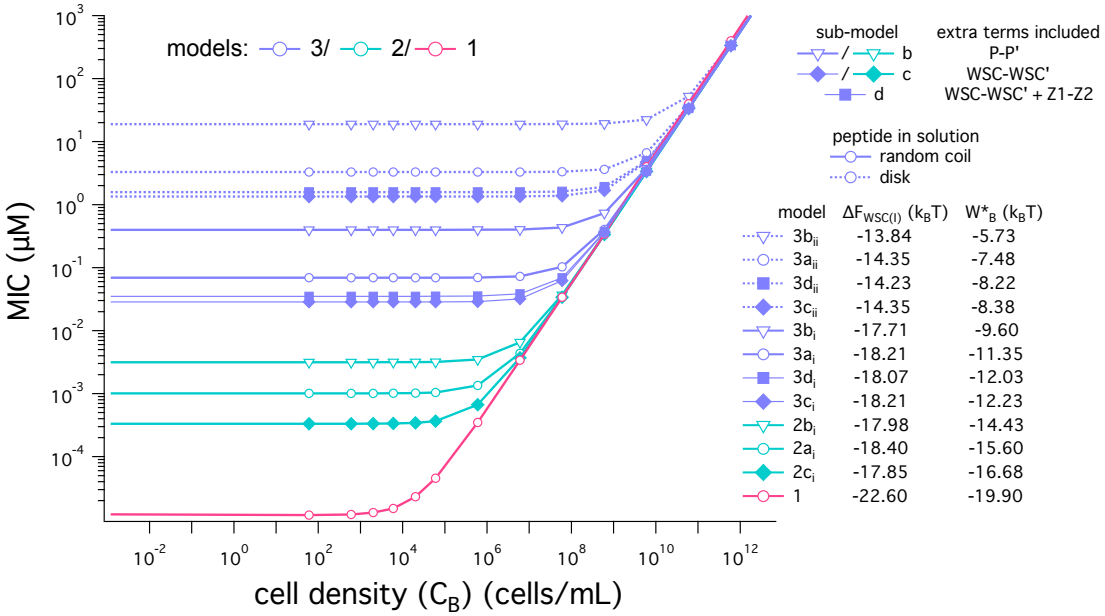


Figure 3.4: Various models and cell density-dependence of MICs. We have chosen the same parameters as used for the earlier model [6], referred to as model 1 in this work: $\varepsilon_{\rm I} = -14k_{\rm B}T$, $\bar{\alpha} = 0.3$, $P/L_{\rm B}^* = 0.02$, and $Q = 6$. Model 1 underestimates MICs, as reflected in the MIC graph, since it overestimates the attraction between peptides and charged lipids. Model 2 is improved upon model 1 but suffers from similar but reduced drawbacks. Model 3, more realistic than the others, predicts much larger MIC values. The difference between models 2 and 3 is well pronounced, because of the importance of how to calculate electrostatic interactions between peptides and lipids. In contrast, the difference between the variations of the same model (e.g., 3a, 3b, 3c, ...) is less significant. It is thus crucial to preserve the geometry of the three regions, occupied by a peptide, lipids in zone 1, and lipids in zone 2, as assumed in model 3 (see Fig. 3.3). Adding the repulsion between bound peptides tends to increase MICs, as it reduces peptide binding. However the interaction between neighbouring WSCs does not necessarily reduces peptide binding, since it also contains the attraction between a peptide in a WSC and lipids in different WSCs. The interaction between Z1 and Z2 slightly reduces peptide binding, increasing MICs a little. In all cases, MICs increase with the cell density; for a larger cell density, a larger amount of peptides is required in order for $P/L$ to reach $P/L^*$. In all curves, the surface area of host and bacterial cells is chosen to be $1.2 \times 10^9 \text{Å}^2$, i.e., the area of a typical bacterial cell surface, e.g., that of *Escherichia coli* [6]. It is worth noting that the general physical picture is not limited by this choice, since any change in cell surface areas can be made equivalent to the change in cell densities [6].

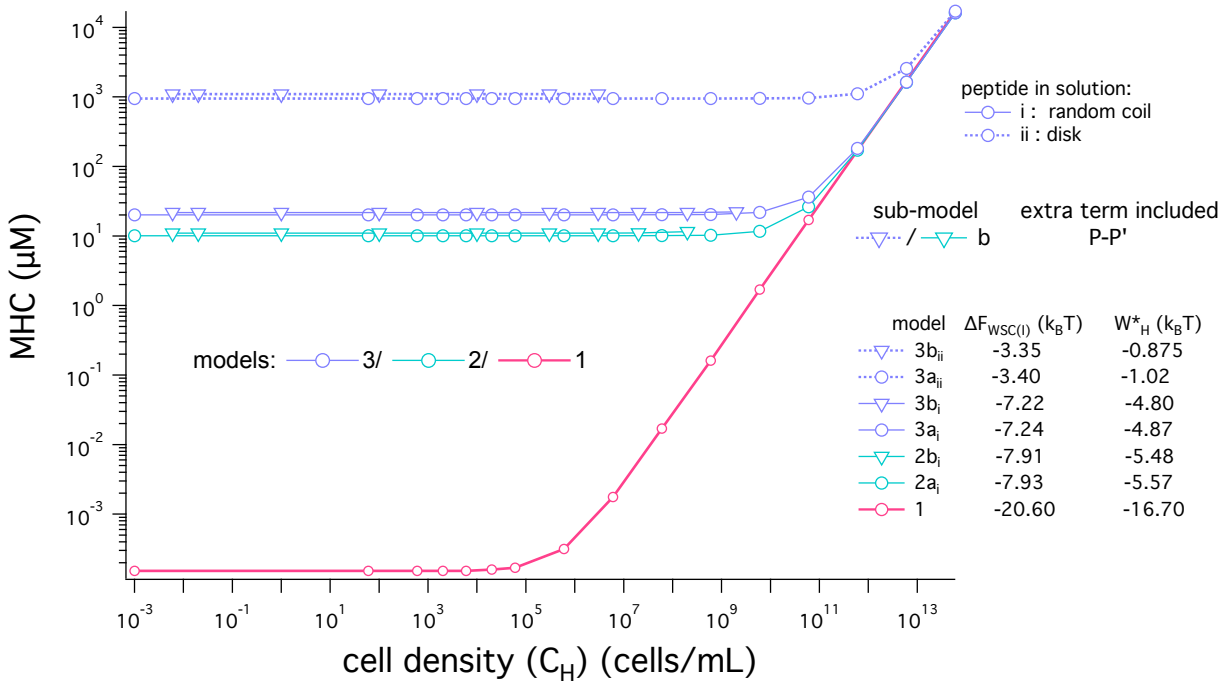


Figure 3.5: Different models and cell density-dependence of MHCs. We have chosen the same parameters as used for the earlier model [6], referred to as model 1 in this work: $\varepsilon_{\rm I} = -14k_{\rm B}T$, $\bar{\alpha} = 0.3$, $P/L^*_{\rm H} = 0.01$, and $Q = 6$. , model 1 underestimates MHCs, as reflected in the MICs graph Fig. 3.4, since it overestimates the attraction between peptides and charged lipids. Model 2 is improved upon model 1 but suffers from similar but reduced drawbacks. Model 3, more realistic than the others, predicts much larger MHC values. The MHC graph can be understood in parallel with the MICs graph in Fig. 3.4; the difference between models 2 and 3 is less pronounced, because of much reduced electrostatic interactions between peptides and lipids. Adding the repulsion between bound peptides tends to increase MHCs, as it reduces peptide binding. In all cases, MHCs increase with the cell density; for a larger cell density, a larger amount of peptides is required in order for $P/L$ to reach $P/L^*$. In all curves, the surface area of host and bacterial cells is chosen to be $1.2 \times 10^9 \text{Å}^2$, i.e., the area of a typical bacterial cell surface, e.g., that of *Escherichia coli* [6]. It is worth noting that the general physical picture is not limited by this choice, since any change in cell surface areas can be made equivalent to the change in cell densities [6].

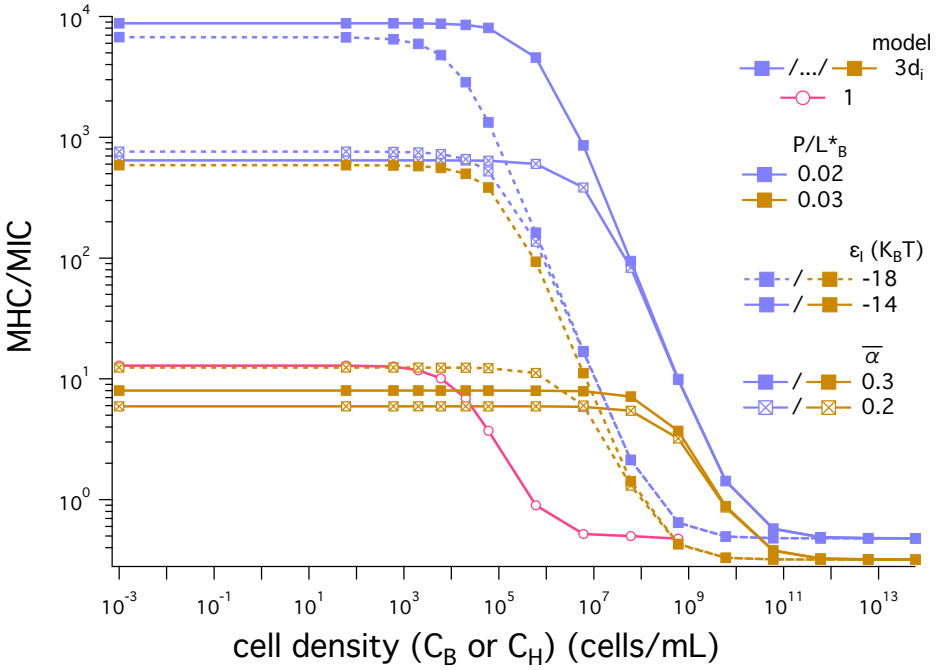


Figure 3.6: Various models and cell density-dependence of MHC/MIC. Here, model $3d_i$ is used with varying parameter values except for fixed $Q = 5$, which is a more realistic choice for melittin [6]; two different values are chosen for $P/L^*_B = 0.02, 0.03$ and $\bar{\alpha} = 0.2, 0.3$. The graphs shows the ratio: MHC/MIC, a quantitative measure of peptide selectivity. While in all cases MHC/MIC decreases with increasing cell density, the values of MHC/MIC vary greatly between different models. This observation is well aligned with the model dependence of MIC and MHC values shown in Fig. 3.4 and Fig. 3.5 (i.e. also consistent with the results in Fig. 3.13). The variation of MICs or MHCs is large between different models but not as much between sub-models. Peptide selectivity is appreciably smaller in models 1 and 2 than in model 3. This implies that it is essential to capture correctly the geometry of various regions, occupied by a peptide, lipids in its vicinity, and lipids outside (i.e., in zone 2). In all curves, the surface area of host and bacterial cells is chosen to be $1.2 \times 10^9 \text{Å}^2$, i.e., the area of a typical bacterial cell surface, e.g., that of *Escherichia coli* [6]. It is worth noting that the general physical picture is not limited by this choice, since any change in cell surface areas can be made equivalent to the change in cell densities [6].

We have chose the parameter as follows. The area of cell membranes $A_{\rm cell} = 1.2 \times 10^9 \text{Å}^2$ coincides with the area of a typical bacterial cell surface, e.g., that of *Escherichia coli* (*E. coli*) [6]. It is worth noting that this choice will not limit the significance of our results, since changing cell surface areas can be made equivalent to changing cell densities [6]; one can simply rescale the cell-density axis as in Fig. 3.6 to mimic the effect of changing $A_{\rm cell}$. We have also used various combinations of other parameters (e.g., $Q$, $\varepsilon_{\rm I}$, $\bar{\alpha}$, and $P/L^*$) as indicated in the legends of graphs. In Fig. 3.4 and Fig. 3.5, for comparison purposes, we have chosen the same parameters used for model 1, which are essentially identical to those adopted in Ref. [6], $\varepsilon_{\rm I} = -14 k_{\rm B}T, \bar{\alpha} = 0.3, P/L^*_{\rm B} = 0.02, P/L^*_{\rm H} = 0.01$, and $Q = 6$. In Fig. 3.6, model $3{\rm d_i}$ is used with varying parameter values except for fixed $Q = 5$, which is a more realistic choice for melittin [6] than $Q = 6$. Also two different choices are used for $P/L^*_{\rm B}$ and $\bar{\alpha}$: $P/L^*_{\rm B} = 0.02, 0.03$ and $\bar{\alpha} = 0.2, 0.3$. It is worth noting that there is a general consensus on $P/L^* = 0.01$ for pure DOPC bilayers (mimicking host-cell membranes) [5, 55, 112]. Throughout this work, we use this fixed value for host cell membranes.

MICs and MHCs can be obtained by analyzing Eq. 3.31. We first obtain $P/L = \sigma_{\rm I} a_\ell$ while varying $C_{\rm p}$ and choose the value of $C_{\rm p}$ for which $P/L$ is equal to $P/L^*$. This special $C_{\rm p}$ or simply $C^*_{\rm p}$ is either MIC or MHC. Fig. 3.6 shows various models and cell density-dependence of MICs (Fig. 3.4) and MHCs (Fig. 3.5). Model 1 underestimates MICs, as reflected in the corresponding curves, since it overestimates the attraction between peptides and charged lipids. Model 2 is improved upon model 1 but suffers from similar but reduced drawbacks (see Fig. 3.1). Model 3, more realistic than the others, predicts much larger MIC values.

Fig. 3.7 illustrates the cell-density dependence of $C^*_{\rm P}$, i.e., the bulk peptide concentration corresponding to $P/L^*$: either MICs or MHCs. Here peptides are represented by filled or unfilled circles; if filled ones are free in the bulk, unfilled ones are bound to bilayer membranes described by two concentric circles. What is shown in (i) is the single-cell limit at $C_{\rm p} = C^*_{\rm p}$ or at $P/L = P/L^*$. For the case in (ii), an extra amount of peptides is needed; to remain at $P/L^*$, the required number of peptides is equal to $P/L^* \times A_{\rm cell}/V$, where $V$ is the volume of the entire system. The progression from (i)-(iii) shows how this reasoning can be extended to the non-zero cell-density case. When applied to bacteria, this figure implies that

$$\text{MIC}(C_{\rm cell}) = \frac{A_{\rm cell}}{a_\ell} \left( \frac{P}{L} \right)^* C_{\rm cell} + (\text{MIC})_0, \tag{3.34}$$

where $a_\ell$ is the area of each lipid and $(\text{MIC})_0$ is MIC in the low-cell density limit: $C_{\rm cell} \to 0$. As evidenced later, this is consistent with the one based on a Langmuir model (see Eq. 3.37).

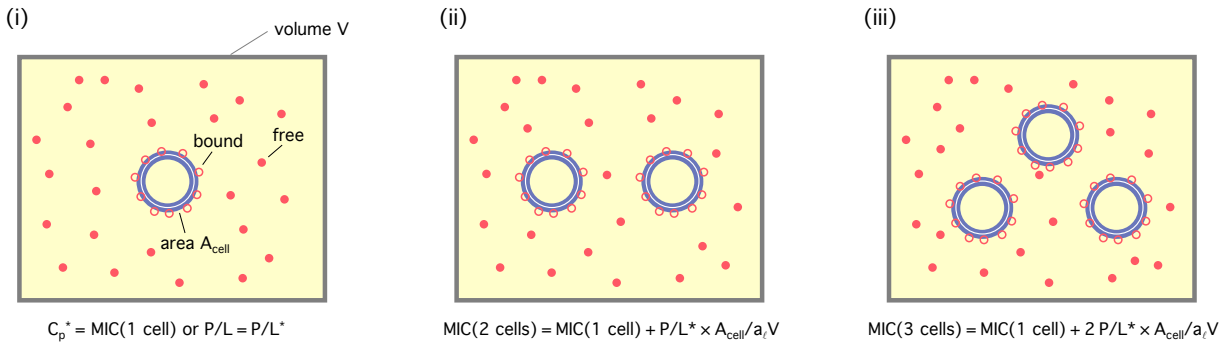


Figure 3.7: This figure illustrates the cell-density dependence of $C_{\rm p}^*$, either MICs or MHCs. Here peptides are represented by filled (free) or unfilled circles (bound) and bilayer membranes by two concentric circles. What is shown in (i) is the single-cell limit at $C_{\rm p} = C_{\rm p}^*$ or at $P/L = P/L^*$. For the case in (ii), an extra amount of peptides is needed; to remain at $P/L^*$, the required number of peptides is equal to $P/L^* \times A_{\rm cell}/V$, where $V$ is the volume of the system. The progression from (i)-(iii) shows how this reasoning can be extended to the non-zero cell-density case. When applied to bacteria, this figure implies that $\mathrm{MIC}(C_{\rm cell}) = \frac{A_{\rm cell}}{a_\ell}(P/L)^* C_{\rm cell} + (\mathrm{MIC})_0$, where $a_\ell$ is the area of each lipid and $(\mathrm{MIC})_0$ is MIC in the low-cell density limit: $C_{\rm cell} \to 0$. The slope of this relation, i.e, $\frac{A_{\rm cell}}{a_\ell}(P/L)^*$, is the total amount of bound peptides at $P/L = P/L^*$; $(\mathrm{MIC})_0$ is set by the interaction of peptides with membranes among others. This suggests that MHCs become less sensitive to peptide parameters and models used as $C_{\rm cell}$ increases; so is the ratio MHC/MIC or peptide selectivity.

While we primarily model free peptides as random coils, for comparison purposes, we have also considered them as circular disks as for bound peptides; if the former is represented by the subscript 'i' as in '$3d_i$,' the latter by the subscript 'ii' as in '$3d_{ii}$.

The difference between sub-sub-models, e.g., '$3d_i$' and '$3d_{ii}$', is appreciable. We, however, interpret this as nonessential, in the sense that it reflects single-peptide properties. In principle, it can absorbed into $\varepsilon_{\rm I}$, the free energy gain for hydrophobic insertion in Eq. 3.1. Furthermore, the disk model is not close to the structure of peptides in the bulk. We thus favour the random coil model over the disk model. Except for MICs and MHCs graph in Fig. 3.4 and Fig. 3.5, we use model $3d_i$ as our primary model in Fig. 3.6.

The MHC graph in Fig. 3.5 can be understood in parallel with the MIC graph. Similarly to what was observed with MICs, the difference between the variations of the same model (e.g., 3a, 3b, 3c, ..) is less significant compared to the variation between different models.

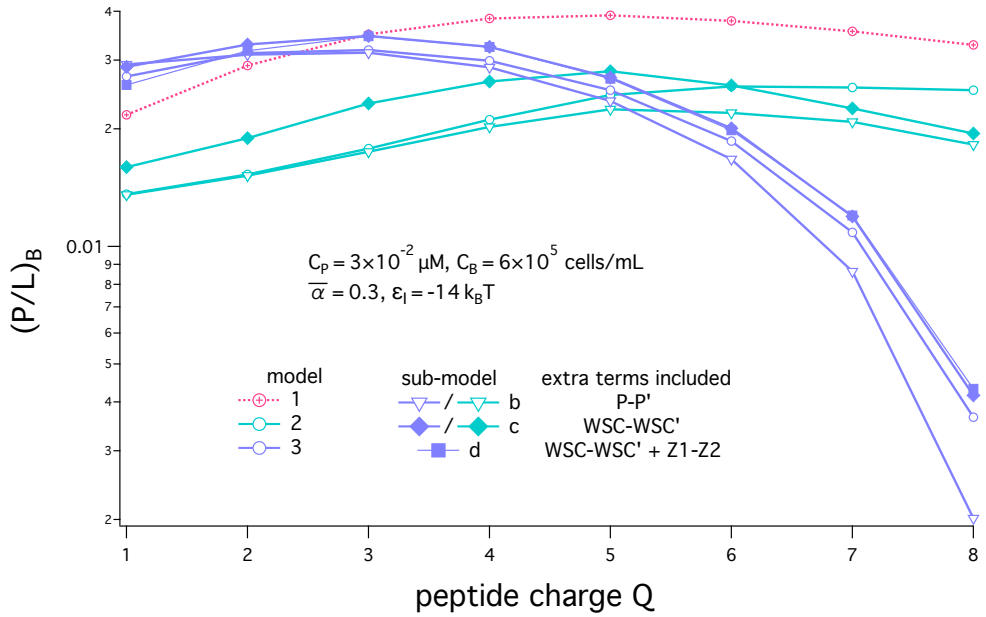


Figure 3.8: This figure shows hydrophobic peptide binding ($P/L$) to bacterial membranes, as a function of peptide charge $Q$. As $Q$ increases, initially $P/L$ for bacterial cell membranes increases because of enhanced electrostatic interactions between peptides and anionic lipids. For a large value of $Q$, however, bound peptides start to repel each other more effectively; also for the charged bacterial membrane, the competition between the two binding modes is swayed toward S mode as $Q$ increases. This is responsible for the non-monotonic behaviour of $P/L$ against $Q$, consistent with earlier results [9].

This points to the importance of preserving the geometry of the three regions, occupied by a peptide, lipids in zone 1, and lipids in zone 2, as assumed in model 3 (see Fig. 3.3).

Consistent with our common intuition, both MIC and MHC graphs suggest that adding the repulsion between WSCs or bound peptides tends to increase MICs or MHCs, as it reduces peptide binding.

An important feature of the graphs in Fig. 3.4 and Fig. 3.5 is that MICs and MHCs increase with the cell density; for a larger cell density, a larger amount of peptides is required in order for $P/L$ to reach $P/L^*$. Indeed, this is correlated with the observation that membrane disruption occurs for $P/L \geq P/L^*$, as illustrated in Fig. 3.7 and detailed below.

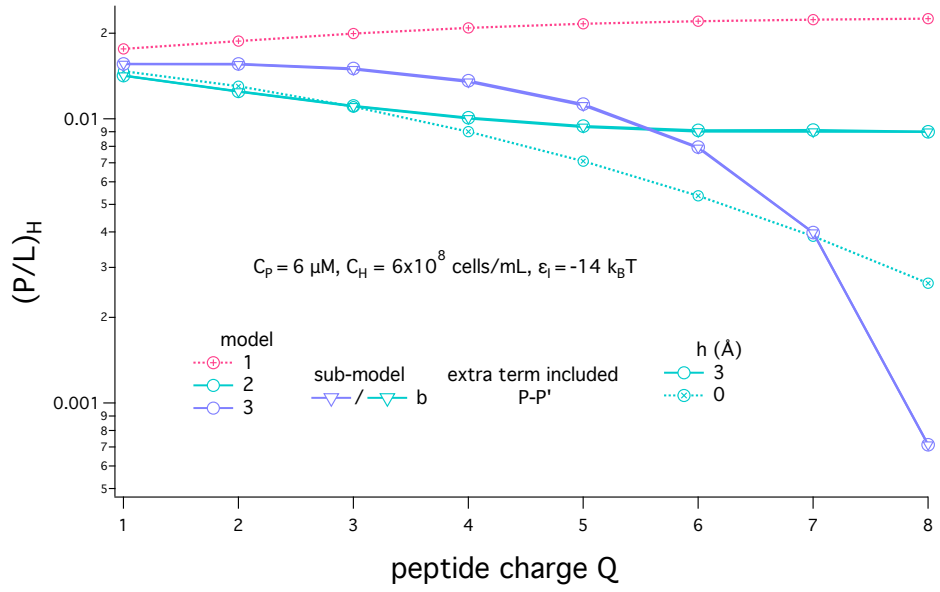


Figure 3.9: This figure shows hydrophobic peptide binding $(P/L)$ to host-cell membranes, as a function of peptide charge $Q$. In contrast to bacterial membrane in Fig 3.8, peptide binding becomes diminished monotonically for host cell membranes, as $Q$ increases, except for model 1; in models 2 and 3, a larger-$Q$ value simply means enhanced peptide-peptide repulsion, as expected. On the contrary, model 1 shows an opposite trend. The enhanced repulsion between peptides is counterbalanced by mistakenly-enhanced binding affinity of peptides. This can be understood in parallel with the finding that model 1 overestimates peptide binding, as shown in Fig. 3.5. As a result, model 1 does not appear to serve as an adequate model for the $Q$-dependence of peptide binding.

The graph in Fig. 3.6 shows the ratio: MHC/MIC, a quantitative measure of peptide selectivity. (As noted above, here and below, model $3d_i$ is exclusively used.) While in all cases MHC/MIC decreases with increasing cell density, the values of MHC/MIC vary greatly between different models. This observation is well aligned with the model dependence of MHC and MIC values shown in Fig. 3.4 and Fig. 3.5. In summary, peptide selectivity is underestimated in models 1 and 2.

The slope of this relation, i.e, $\frac{A_{\rm cell}}{a_\ell}(P/L)^*$, is the total amount of bound peptides at $P/L = P/L^*$ ($A_{\rm cell}$ is the total surface area of a cell). On the other hand, the "$y$"-intercept, $(\mathrm{MIC})_0$, is set by the peptide and membrane parameters. The relation in Eq. 3.34 suggests

that MICs become less sensitive to peptide parameters as $C_{\rm cell}$ increases; so are MHCs and the ratio MHC/MIC or peptide selectivity. This is well aligned with the general trend seen in the results for MHC/MIC in Fig. 3.6. Indeed, the selectivity approaches a constant of order one, largely independent of peptide-membrane parameters, as the cell density increases.

The figures in Fig. 3.8 and Fig. 3.9 show hydrophobic peptide binding ($P/L$) to bacterial and host-cell membranes, as a function of peptide charge $Q$. As $Q$ increases, initially $P/L$ for bacterial cell membranes increases because of enhanced electrostatic interactions between peptides and anionic lipids. As $Q$ increases further, however, bound peptides start to repel each other more effectively, diminishing peptide binding; also for the charged case, the competition between the two binding modes is swayed toward S mode as $Q$ increases. This is responsible for the non-monotonic behaviour of $P/L$ against $Q$, consistent with earlier results [9]. Except for this common feature, the shape of the curves in the figure differs between models. Also it is worth noting that it depends on parameter choices as reflected in Fig. 3.10. For instance, the value of $Q$ at which $(P/L)_{\rm B}$ is maximized is model-dependent.

In contrast, peptide binding becomes diminished monotonically for host cell membranes, as $Q$ increases, except for model 1; except for model 1, a larger-$Q$ value simply means enhanced peptide-peptide repulsion, as expected. On the contrary, model 1 shows an opposite trend. The enhanced repulsion between peptides is mistakenly counterbalanced by enhanced binding affinity of peptides. This can be understood in parallel with the finding that model 1 overestimates peptide binding, as shown in Fig. 3.5: By stretching the peptide area over an entire WSC (see Fig. 3.2), model 1 overestimates peptide binding, more so for large $Q$. This enhancement outweighs the peptide-peptide repulsion on the membrane surface, making $\Delta F_{\rm p}$ more favourable for peptide binding. This is responsible for the reversed trend seen in model 1. As a result, model 1 does not appear to serve as an adequate model for $Q$-dependence of peptide binding.

Peptide charge is known to be a key parameter in determining peptide activity and selectivity [9, 36, 109]. To further probe its significance, we have examined the $Q$ dependence of MHCs, MICs, and MHC/MIC. Along this line, it is worth mentioning that $Q$ can be adjusted independently of other peptide parameters [109, 113]. This justifies our consideration here. At present, however, the dependence of $P/L^*$ on $Q$ is elusive. The value of $P/L^*$ is known to depend on the types of lipids and peptides as well as on membrane thinning or thickening induced by peptide binding [37, 46]. Its dependence on $Q$ for a given peptide type has not been systematically examined. Here we employ two approaches. The simplest one may amount to assuming that $P/L^*$ is insensitive to $Q$. This is equivalent to assuming that the difference in energy between hydrophobic-binding and pore forming

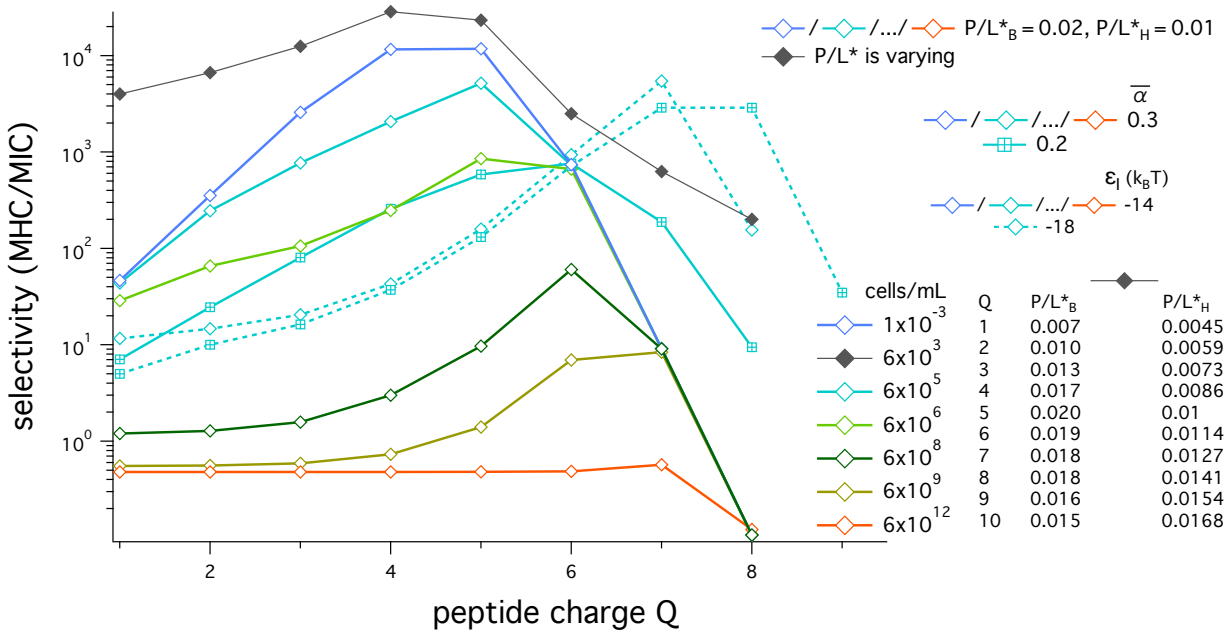


Figure 3.10: The figure shows peptide selectivity vs. peptide charge $Q$. The selectivity is quantified by the ratio: MHC/MIC. The larger this ratio is, the more selective the peptide is; in a wider range of peptide density, the peptide ruptures bacterial membranes without perturbing appreciably host-cell membranes. This selectivity graph shows that the selectivity is maximized at a certain value of $Q$, i.e., an optimal charge denoted as $Q_{\text{optimal}}$. This graph also shows how the optimal charge varies with peptide and membrane parameters. For instance, the optimal charge is larger for stronger hydrophobicity. It also shows that the selectivity becomes smaller and flatter as the cell density increases; it looses the sensitivity of peptide selectivity to peptide parameters including $Q$. This is well aligned with the finding that the selectivity becomes a constant of order 1 as the cell density increases (see Fig. 3.6). Indeed, our full analysis in this figure or its variations suggest how peptide parameters might be optimized for enhanced selectivity in a biologically relevant medium. The non-monotonic dependence of peptide selectivity can be understood by examining the $Q$ dependence of MICs and MHCs in Fig. 3.11 and Fig. 3.12, respectively. In fact, the $Q$ dependence of peptide selectivity is a combined feature of MIC and MHC results.

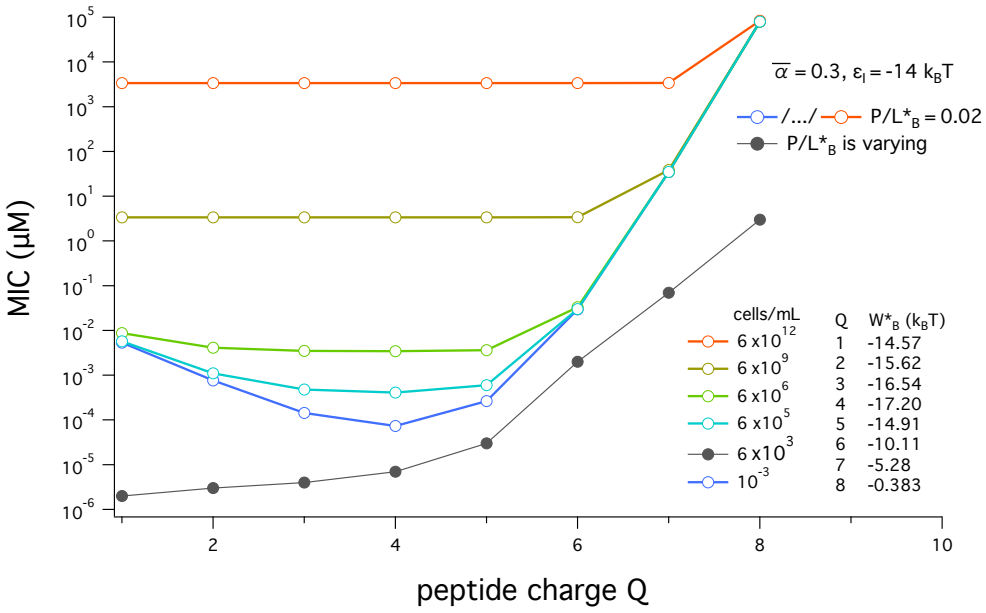


Figure 3.11: The figure shows peptide MICs vs. peptide charge $Q$. The non-monotonic dependence of peptide selectivity in Fig. 3.10 can be understood by examining the $Q$ dependence of MICs and MHCs in Fig. 3.12. The graph suggests that MICs vary non-monotonically with $Q$, reaching its minimum around $Q = Q_{\text{optimal}}$. This is more pronounced for smaller cell densities. For sufficiently large cell densities, MICs become less sensitive to $Q$; also the location of MIC minimum shifts to a larger value of $Q$.

states is essentially determined by non-electrostatic effects such as membrane curvature energy around a pore [114].

In a seemingly-elaborated effort, we will attempt to capture the possible $Q$-dependence of $P/L^*$ by including the repulsion between pore forming peptides in our analysis.

When $P/L^*$ is assumed to be independent of $Q$, MICs and MHCs can be obtained by changing $Q$ in the $Q$-dependent terms in Eq. 3.31. The graph in Fig. 3.10 shows peptide selectivity vs. peptide charge $Q$. The selectivity is quantified by the ratio: MHC/MIC. The larger this ratio is, the more selective the peptide is [35, 36, 37]; in a wider range of peptide density, the peptide ruptures bacterial membranes without perturbing host-cell membranes appreciably. This graph shows that there exists an optimal value of peptide charge at which the selectivity reaches its maximum. Similar conclusions were drawn earlier but they were not conclusive since they were based on the dependence of $P/L$ on $Q$ at a

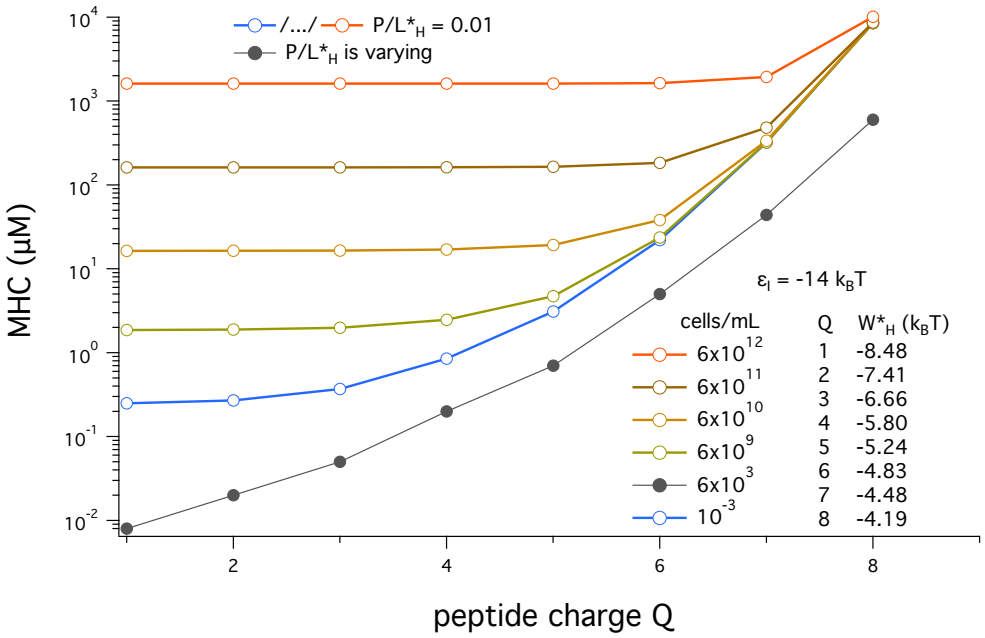


Figure 3.12: The figure shows peptide MHCs vs. peptide charge $Q$. The non-monotonic dependence of peptide selectivity in Fig. 3.10 can be understood by examining the $Q$ dependence of MICs (see Fig. 3.11) and MHCs. In contrast to MICs, MHCs vary monotonically with $Q$. Similarly to what the MIC curves in Fig. 3.11 suggest, they become almost flat for large cell densities. The $Q$ dependence of peptide selectivity in (A) is a combined feature of MIC and MHC results in (B) and (C).

single-cell limit.

To understand the physical origin of the non-monotonic dependence of peptide selectivity on $Q$ in Fig. 3.10, we have examined the $Q$ dependence of MICs and MICs in Fig. 3.11 and Fig. 3.12, respectively. The MIC graph suggests that MICs vary non-monotonically with $Q$, reaching its minimum for a certain value of $Q$ ($\geq 4$), referred to as an optimal charge, $Q_{\rm optimal}$. This is more pronounced for smaller cell densities, e.g., the bottom two curves. For sufficiently large cell densities, MICs become less sensitive to $Q$; also the location of MIC minimum shifts to a larger value of $Q$. This is correlated with the earlier observation that MICs become more insensitive to peptide parameters or models for large cell densities (see the illustration in Fig. 3.7, Eq. 3.34, and Fig. 3.4). On the other hand, MHCs vary monotonically and become almost flat for large cell densities. The $Q$ dependence of peptide selectivity in Fig. 3.10 is a combined feature of MIC and MHC

results.

Furthermore, the graph of selectivity in Fig. 3.10 suggests that the optimal charge $Q_{\rm optimal}$ varies with peptide-membrane parameters. In particular, $Q_{\rm optimal}$ is larger when the hydrophobic binding is stronger, i.e., for a more negative value of $\varepsilon_{\rm I}$. For stronger hydrophobicity, the repulsion between WSCs can be more effectively counterbalanced by the hydrophobic free energy gain for peptide binding. This explains the dependence of the optimal charge on $\varepsilon_{\rm I}$. The graph also shows that the selectivity becomes smaller and flatter as the cell density increases; it looses the sensitivity of peptide selectivity to peptide parameters including $Q$. This finding is well aligned with the finding that the selectivity becomes a constant of order 1 as the cell density increases [6].

It is tempting to include the possible $Q$ dependence of $P/L^*$ in our consideration of peptide selectivity. Beyond an earlier theoretical approach to peptide pores [115], however, the energetics of pore formation has remained poorly understood. In the theoretical approach [115], the excess free energy associated with pore formation, $\Delta F_{\rm pore}$, is obtained for various choices of $Q$; it is measured with respect to a reference state in which pore-forming peptides are infinitely diluted (see Ref. [115] for the detail). Similarly, $\Delta F_{\rm WSC}$ in this work is defined with respect to a no-peptide state without a pore (see Eq. 3.32). Pore formation by peptides is, however, governed by the free energy difference per peptide between the following two states or binding modes: hydrophobic-adsorption and pore formation [46]. This will essentially determine $P/L^*$.

Nevertheless, if we assume that the $Q$ dependence of $P/L^*$ arises mainly from the $Q$ dependence of $\Delta F_{\rm pore}$, we can examine how $P/L^*$ will vary with $Q$. To proceed further, note that one can extract the relation from Ref. [115]

$$\Delta F_{\rm pore} \approx (1.4 + 0.6Q)\, k_{\rm B}T - \text{constant}. \tag{3.35}$$

Here, a negative free energy is introduced to make a reference energy correction. The resulting free energy difference between the two states per peptide can be conveniently written as $|\Delta F_{\rm WSC}(Q)| - |\Delta F_{\rm pore}(Q)|$. Note that $\Delta F_{\rm WSC}$ is separated from the other term; the constant term in Eq. 3.35 is to be adjusted to make this consistent with the known values of $P/L^*$ as described below.

Following Ref. [46], we relate this free energy to $P/L^*$ as

$$\left(\frac{P}{L}\right)^* = \frac{|\Delta F_{\rm WSC}(Q)| - |\Delta F_{\rm pore}(Q)|}{K_{\rm A}\left(A_{\rm p}^2/a_\ell\right)(1-\beta)}, \tag{3.36}$$

where $\beta$ is a phenomenological parameter describing the thinning or thickening of membranes induced by peptide binding [46]. The values of $\beta$ were estimated for different

(A) Bacterial membrane

| Model | $W^*_B$ ($k_BT$) ($\varepsilon_l = -14k_BT$) | |
|---|---|---|
| | Q = 6 | Q = 5 |
| $3d_{ii}$ | -8.22 | -14.09 |
| $3d_i$ | -12.03 | -16.60 |
| **Model** | **$W^*_B$ ($k_BT$) ($\varepsilon_l = -18k_BT$)** | |
| $3d_i$ | -18.35 | -20.38 |

(B) Host Cell membrane

| Model | $W^*_H$ ($k_BT$) ($\varepsilon_l = -14k_BT$) | |
|---|---|---|
| | Q = 6 | Q = 5 |
| $3b_{ii}$ | -0.875 | -3.50 |
| $3b_i$ | -4.80 | -6.72 |
| **Model** | **$W^*_H$ ($k_BT$) ($\varepsilon_l = -18k_BT$)** | |
| $3b_i$ | -8.80 | -10.76 |

All models (Q = 6, $\varepsilon_l = -14k_BT$)

| Model | $\Delta F_{WSC(l)}$ ($k_BT$) | $W^*_B$ ($k_BT$) |
|---|---|---|
| model $3b_{ii}$ | -13.84 | -5.73 |
| model $3a_{ii}$ | -14.35 | -7.48 |
| model $3d_{ii}$ | -14.23 | -8.22 |
| model $3c_{ii}$ | -14.35 | -8.38 |
| model $3b_i$ | -17.71 | -9.60 |
| model $3a_i$ | -18.21 | -11.35 |
| model $3d_i$ | -18.07 | -12.03 |
| model $3c_i$ | -18.21 | -12.23 |
| model $2b_i$ | -17.98 | -14.43 |
| model $2a_i$ | -18.40 | -15.60 |
| model $2c_i$ | -17.85 | -16.68 |
| model 1 | -22.60 | -19.90 |

All models (Q = 6, $\varepsilon_l = -14k_BT$)

| Model | $\Delta F_{WSC(l)}$ ($k_BT$) | $W^*_H$ ($k_BT$) |
|---|---|---|
| model $3b_{ii}$ | -3.35 | -0.875 |
| model $3a_{ii}$ | -3.40 | -1.02 |
| model $3b_i$ | -7.22 | -4.80 |
| model $3a_i$ | -7.24 | -4.87 |
| model $2b_i$ | -7.91 | -5.48 |
| model $2a_i$ | -7.93 | -5.57 |
| model 1 | -20.60 | -16.70 |

Figure 3.13: This table summarizes the free energy of a WSC, $\Delta F_{\mathrm{WSC}}$, obtained at $P/L = P/L^*$, with reference to the no-peptide case and the corresponding effective binding energy $W^*$ for typical charged (A) and neutral membranes (B), mimicking bacterial and host cell membranes, respectively. The effective binding energy $W^*$ is a Langmuir-model equivalent of $\Delta F_{\mathrm{WSC}}$: with this choice, a Langmuir model produces the same amount of bound peptides as our models do. In the table on the right, the rows are arranged in the decreasing order of $W^*$. Note that $W^*$ is more directly related to MICs or MHCs than $\Delta F_{\mathrm{WSC}}$; it measures the binding affinity of peptides for their binding membranes in the same way as assumed in a Langmuir model. In (A), the variance of $\Delta F_{\mathrm{WSC}}$ or $W^*$ between different models (e.g., models 1 and 2) is significant; within model 2 or 3, however, they do not vary much between the sub-models, i.e, variations of the same model (e.g., 2a and 2b). A similar trend is observed for the host cell membrane in (B); the main difference is that the variance between models 2 and 3 is less pronounced in (B).

pore-forming peptides with various lipid compositions [5, 46]: $\beta = -0.95$ for host cell membranes and $\beta = -1.5$ for bacterial cell membranes. We adjust the value of 'constant' in Eq. 3.35 so that Eq. 3.36 leads to the expected value of $P/L^* \approx 0.02 = (P/L^*)_{\rm B}$ for host cell membranes and $P/L^* \approx 0.01 = (P/L^*)_{\rm H}$ for bacterial membranes, when $Q = 5$ (as for melittin) is used: constant $= 15.99 k_{\rm B}T$ or $9.14 k_{\rm B}T$ for bacterial or host cell membranes, respectively.

The results obtained for $C_{\rm cell} = 6 \times 10^3$ by varying $P/L^*$ according to Eq. 3.36 are represented by the grey curves in Fig. 3.10. Similarly to the previous results plotted in Fig. 3.10, the grey curve also suggests the existence of an optimal charge, even though it is not as pronounced. A related point is that the non-monotonicity shown by the earlier results for MICs in Fig. 3.11, i.e., the curves represented by various colours, disappears for the grey curve. We believe that this is an artifact arising from the way the pore energy is corrected for the reference state in Eq. 3.35. Indeed, the constant term in Eq. 3.35 should depend on $Q$ and $\sigma_0$ (the planar charge density on the membrane). The term $\Delta F_{\rm WSC}(Q)$ in Eq. 3.36 does not fully account for this, since it is measured with reference to an infinitely-diluted state on the surface without a pore. Imagine a peptide undergoing a transition from the membrane surface to a pore. The corresponding free energy change should replace the terms in the numerator in Eq. 3.36. A more systematic analysis of pore energetics and its relationship with $P/L^*$ would be needed for a more complete picture of how the selectivity varies with $Q$. It is worth noting that this analysis will be complicated by membrane thinning or thickening induced by peptide binding [5, 46].

### 3.3.2 Mapping to a Langmuir binding model

The free energy approach presented in Subsec. 3.2.2 has offered a detailed picture of how peptide activity and selectivity depends on cell densities as presented in Subsec. 3.3.1. To further exploit our approach, here we map out a simple, effective Langmuir-type model from it. In this consideration, we essentially follow up on recent studies (see Ref. [6] and the Supporting Information). Let $C_{\rm p} = N_{\rm p}/V$ be the total concentration of peptides whether free or bound and $C_{\rm p}^*$ be the value of $C_{\rm p}$ corresponding to $P/L^*$: $C_{\rm p}^*$ is either an MIC or MHC. Let $W$ be the binding energy of a peptide. All the subtle features of peptide binding (e.g., lipid demixing and an optimal charge) are subsumed into $W$. Of interest to us is the value of $W$ at the cell density $C_{\rm p} = C_{\rm p}^*$, denoted as $W^*$. Using this model, we offer an intuitively-obvious picture of the cell-density dependence of peptide selectivity. (It is worth noting that the cell-density dependence will not alter $W$ or $W^*$.)

Let $C_{\rm cell}$ be the density of target cells, either host cells or bacterial cells; $A_{\rm cell}$ the surface of each cell. Earlier, it was shown that $C_{\rm p}^*$ (either MIC or MHC), the bulk peptide

concentration required for the surface coverage $P/L^*$, is given by [6]

$$C_{\rm p}^* = \frac{A_{\rm cell}}{a_\ell}\left(\frac{P}{L}\right)^* C_{\rm cell} + \frac{1}{v_{\rm p}} \cdot \frac{\frac{A_{\rm p}}{a_\ell}\left(\frac{P}{L}\right)^*}{1-\frac{A_{\rm p}}{a_\ell}\left(\frac{P}{L}\right)^*} e^{W^*/k_{\rm B}T}. \tag{3.37}$$

The relation in Eq. 3.37 shows how $C_{\rm p}^*$ varies with $C_{\rm cell}$ for a given $W^*$: $C_{\rm p}^*$ is insensitive to $C_{\rm cell}$ for $C_{\rm cell} \approx 0$ but it is approximately proportional to $C_{\rm cell}$ for a sufficiently large $C_{\rm cell}$.

The value of $W^*$ can be extracted by fitting our date obtained from Eq. 3.31 to Eq. 3.37; the '$y$' intercept of this relation will determine $W^*$. Several representative values of $W$ are displayed in the table in Fig. 3.13. The strength of peptide binding is different between different models; it is strongest in model 1 and weakest in model 3. Our most complete model $3{\rm d_i}$ produces $W_{\rm B}^* = -16.60\,k_{\rm B}T$ and $W_{\rm H}^* = -6.72\,k_{\rm B}T$ for $\varepsilon_{\rm I} = -14\,k_{\rm B}T$ and $Q = 5$; $W_{\rm B}^* = -20.38\,k_{\rm B}T$ and $W_{\rm H}^* = -10.76\,k_{\rm B}T$ for $\varepsilon_{\rm I} = -18\,k_{\rm B}T$ and $Q = 5$.

Eq. 3.37 suggests that the low cell density can be "defined" as the range of $C_{\rm cell}$ below $C_{\rm cell}^0$ a special value of $C_{\rm cell}$ at which the two terms on the right hand side of Eq. 3.37 are balanced. Model $3{\rm d_i}$ leads to

$$C_{\rm cell}^0 \approx \frac{A_{\rm P}}{A_{\rm cell}}\frac{1}{v_{\rm p}} \cdot \frac{e^{W^*/k_{\rm B}T}}{1-\frac{A_{\rm P}}{a_\ell}\left(\frac{P}{L}\right)^*} \approx \begin{cases} 6.46\times10^5 ({\rm cells/mL}) & \text{for } W_{\rm B}^* = -16.60\,k_{\rm B}T \\ 1.18\times10^{10} ({\rm cells/mL}) & \text{for } W_{\rm H}^* = -6.72\,k_{\rm B}T \\ 1.47\times10^4 ({\rm cells/mL}) & \text{for } W_{\rm B}^* = -20.38\,k_{\rm B}T \\ 2.08\times10^8 ({\rm cells/mL}) & \text{for } W_{\rm H}^* = -10.76\,k_{\rm B}T \end{cases} \tag{3.38}$$

This relation will give us a quantitative sense of the low cell-density limit, in which peptide selectivity is sensitive to the biophysical (i.e., intrinsic) properties of peptides.

A further effort along the line of what we did will clarify how peptide parameters might be optimized for enhanced selectivity in a biologically relevant medium. It can be extended to other peptides, once their biophysical parameters are characterized.

## 3.4 Conclusions

In conclusion, we have mapped out a physical model for peptide activity and selectivity. To this end, we have systematically analyzed several models and singled out one, which describes accurately the electrostatic binding of peptides to a membrane, whether charged or neutral. To this end, we have kept the geometry of disk-like peptides, zone 1 and 2. Our

results suggest that it is crucial to capture correctly this geometry. Earlier approaches that simplify this geometry can lead to uncontrolled errors in the calculation of MICs, MHCs, and the ratio MHC/MIC.

Using the resulting model (i.e., model $3d_i$), we have examined how peptide activity and selectivity depend on cell concentrations $C_{\text{cell}}$. Both MICs and MHCs increase with $C_{\text{cell}}$ such that the ratio MHC/MIC decreases and approaches a constant of order 1 (see the results in Fig. 3.4, Fig. 3.5, Fig. 3.6 and the illustration in Fig. 3.7). While a similar conclusion was drawn recently [6], it is based on a model that suffers from the aforementioned drawback. A general picture from this work is that peptide selectivity remains sensitive to peptide parameters (e.g., charge and hydrophobicity) at the low-cell density limit, defined in the sense of Eq. 3.3.2, but becomes less sensitive outside this limit. As a result, the optimal peptide charge, at which the selectivity is maximized, is cell-density-dependent: it increases and eventually becomes irrelevant as the cell density increases. This means that optimization of peptide selectivity should reflect the biological setting of infected sites as it determines the number of cells and peptides, $N_{\text{cell}}$ and $N_{\text{p}}$, respectively.

It is worth noting that neither $N_{\text{cell}}$ nor $N_{\text{p}}$ is constant in time in a biological setting. In particular, how $N_{\text{cell}}$ changes with time is a key factor in determining the bactericidal activity of the peptide LL37 [116]. While not all features of model membranes apply to living cells, the cell density dependence of peptide activity and selectivity remains applicable for a given value of $N_{\text{cell}}$, at least approximately. It will be desirable to mimic the biological setting in theoretical considerations beyond the recent effort, i.e., the (meanfield-like) kinetic reaction approach in Ref. [116]. We leave this for future work.

To further clarify the cell-density dependence of peptide activity and selectivity, we have also introduced an effective Langmuir model (subsec. 3.3.2). In this model, a Langmuir binding energy $W^*$ is extracted from our full analysis at $P/L = P/L^*$ (see the table in Fig. 3.13). This model enables us to estimate systematically peptide selectivity as a function of $C_{\text{cell}}$. The value of $W^*$ can be measured experimentally by fitting data to Eq. 3.37 for a conveniently-chosen cell density. Eq. 3.37 or Eq. 3.34 can then be used to examine peptide activity and selectivity as a function of $C_{\text{cell}}$.

In conclusion, a combined effort between experiments and theoretical modelling (physical understanding of peptide activity and selectivity, as described in this work), will benefit our endeavour in searching for potent peptide antibiotics. Indeed, bacteria have developed strategies to counteract the action of AMPs, for instance, by reducing the surface charge density on their membrane [16]. How will this influence peptide selectivity and how should the peptide parameters be adjusted to restore the selectivity? The use of predictive models together with available data (e.g., those for $P/L^*$) will be useful for identifying the peptide

parameters for their enhanced activity under different conditions (e.g., diminished surface charge density and different salinity).

## 3.5 MATLAB Scripts

```
1
2  % Initional Input
3
4  clc
5  clear all
6  global Q b A al alph kapain Par_Shape AreaEx Cp Ct apef lb ...
7         AsI AsS m SM vp V KA e Rs Rp Ensm ApI ApS Ohshima z ...
8         RandomCoil attraction_z zs E_insertion deltaFp...
9         Bessel_phi00_Rp Bessel_phi00_Rs Rpp AppI lambda ...
10        Bessel_F_DH_RING Bessel_F_DH_DISK Bessel_Fp_DH_Mem ...
11        Bessel_E_DH_RING Zone_inter pep_pep wsc_wsc Mo
12
13 % General Variable
14 Eps = 8.85e-12;              %Vacume permitivity (coloum^2/Jm)
15 T = 300;                     %Tempreture (kelvin)
16 Kb = 1.38*1e-23;             %Boltzmann Constant (J/kelvin)
17 Dw = 80;                     %Water dielectric constant
18 NA = 6.023*1e+23;            %Avagadro's number
19 V = 1e27;                    %Total volume in (A^3)
20 e = 1.6e-19;                 %Electron Charge
21 lb = e^2*1e+10/(4*pi*Eps*Dw*Kb*T);   %Bejurium Length (A)
22 kapain = 0.1;                %Inverse of Debye Length in (1/A)
23 C_0 = kapain^2/(8*pi*lb);    %Salt Concentration of 0.1(mol/L)
24 V = 1e27;                    %Total volume in (A^3)
25 D = 200*10;                  %Diameter of Large vesicles
26                              %D= 200nm *10 to get angstrom
27 V_vesicle = 4/3*pi*(D/2)^3;%Volume of a large Unilamilar
28                              %LUV D=Diameters= 100nm - 5microm
29 KA = 0.578;                  %KbT/A^2
30 N_cell = 2;                  %Number of target cell's species
31                              %(1=bacteria, 2=Host_ND)
```

```
Par_Shape = 1;%25/(4*pi);  %Shape parameter for circular
                           %disk of model peptides
E_insertion = -14; %(KbT)  %Hydrophobic energy
                           %(-8.9Kcal/mol * 1.688 =KbT)
AreaEx = 0;                %Area Exclusian on for value=1
                           %and off for value=0
Ensm = 0;                  % canonical or grand canonical
Ohshima = 1;               % Ohshima Free energy calculation
z = 3;                     % Gap of peptide and membrane (A)
zs = 2.5;
RandomCoil = 0;            % Randomcoil or thin peptide disk
                           %for bulk energy calculation (Fp)
b = 4.1;                   % Amino acid size
                           %(bonding length in extended case)
attraction_z = 0;          % Attraction energy btw.lipid-
   peptide
pep_pep = 0;               % peptide repulsion on=1 or off=0
Zone_inter = 1;            % Z1-Z2 interaction on=1 or off=0
wsc_wsc = 1;               % WSC-WSC interaction on=1 or off=0
Mo = 3;                    % model 2 (PB) or model 3 (DH)
Sho=1;                     % host cell model1=0 or model2(3)=1


%Melittin
ApI = 400;                 % physical area of peptide (I) A^2
ApS = 400;                 % physical area of peptide (S) A^2
SM_l = 1/400;              % number of sites per area 1/A^2
Q_l=5;                     % peptide's charge unit
vp_l = 33^3;               % volume of peptide in bulk A^3


%Host Cell NO Lipid Demixing
Ch_ND = [1e-3, 6e1, 6e2, 2e3, 6e3, 2e4, 6e4, 6e5, 6e6, ...
6e7, 6e8, 6e9 6e10 6e11, 6e12, 6e13]; % density (cells/mL)
%Ch_ND = [1e-3, 6e1, 6e2, 2e3, 6e3, 2e4, 6e4, 6e5, 6e6, ...
          %6e7,4.5e8, 9e8, 1.5e9, 3.6e9, 7.2e9, 1.44e10,...
          %2.88e10,6e11, 6e12, 6e13]; % Pure Vesicle/mL
L_Ch_ND = length(Ch_ND);
```

```
Ahost_ND = 12e-12*1e20;          %Surface area (m^2*1e20 = A^2)
%Ahost_ND = pi*8e6;              % vesicle diameter D= 200 nm
alh_ND = 74;                     %64.7; % lipid area A^2
alphh_ND = 0.05;
Vh_ND = 80*1e-15*1e-3*1e30;      % Volume of RBC is 80-100
                                 % femtoliter,converted to A^3


%Bacterial Cell
Cb = [1e-3, 6e1, 6e2, 2e3, 6e3, 2e4, 6e4, 6e5,2e6,...
      6e6, 6e7, 6e8, 6e9]; %density(cells/mL)
L_Cb = length(Cb);
Ab = 2*6e-12*1e20;%2*6e-12*1e20; pi*8e6;
%Surface area (twice of E-coli) (m^2*1e20 = A^2)
alb = 71;%67.3;%71; %65           % lipid area
alphb = 0.3;                      % charged lipid percentage
Vb = 1*1e-18*1e30;                % Volume of E-coli is 0.7-1
                                  % Micrometer^3,converted A^3


%%%%%%%%%%% Host Cell (No Lipid Demixing) %%%%%%%%%%%%%%%%
% nt=1 Ch_ND = 1e-3 (cells/mL) Single target
c_micH0_ND = [1 5 10 40 70 90 100 300 600 800 1e3 1.2e3 ...
              1.3e3 1.5e3 1.8e3 1e4];
LH0_ND = length(c_micH0_ND);

% nt=2 Ch_ND = 6e1
 c_micH1_ND =[3.79094e-3 9.82101e-3 2.05505e-2 ...
              4.5557e-2 6.25669e-2 9.73273e-2 0.1205 ...
              0.143712 0.1617 0.203657 0.279167 ...
              0.372308 0.485207 0.620045 0.964523 1.17878...
              1.4242 1.70321 2.37187 2.76657 3.20495 ...
              3.6 6 7 8 10 20 40 60 80 90 95 110 130 140 150];
 LH1_ND = length(c_micH1_ND);

% nt=3 Ch_ND = 6e2
c_micH2_ND =[1.2e-5 1.2498e-5 1.35e-5 1.4e-5 1.5e-5 ...
             1.899e-5 2.34e-5 3.3e-5 3.5e-5 3.6e-5 3.7e-5...
```

```
              3.8e-5 4e-5 5e-5 8.876e-5 1e-4 1.53e-04 ...
              1.55e-4 3.788e-4 6e-4 9.9101e-4 3.79094e-3...
              9.82101e-3 2.05505e-2 4.5557e-2 6.25669e-2...
              9.73273e-2 0.1205 0.143712 0.1617 0.203657...
              0.279167 0.372308 0.485207 0.620045 ...
              0.964523 1.17878 1.4242 1.70321 2.37187 ...
              2.76657 3.20495 3.6 6 7 8 10 20 40 60 ...
              80 90 95 110 130 140 150 160];
 LH2_ND = length(c_micH2_ND);

% nt=4 Ch_ND = 2e3
c_micH3_ND_1=[6e-9 5e-8 9.467e-8 9.896e-8 1.398e-7 ...
               1.894e-7 2.3e-7 3.7e-7 6.764e-7 9.598e-7 ...
               1.2e-6 1.8e-6 2.1e-6 2.897e-6 3.2e-6 ...
               4.198e-6 6.789e-6 9.854e-6 1.2498e-5 ...
               1.525e-5 3.3e-5 3.4e-5 3.5e-5 4.119e-5 ...
               4.22e-5 5e-5 7e-5 8.876e-5 1e-4 1.53e-04 ...
               3.788e-4 6e-4 9.9101e-4 3.79094e-3 9.82101e-3...
               2.05505e-2 4.5557e-2 6.25669e-2 9.73273e-2 ...
               0.1205 0.143712 0.1617 0.203657 0.279167 ...
               0.372308 0.485207 0.620045 0.964523 1.17878...
               1.4242 1.70321 2.37187 2.76657 3.20495 ...
               3.6 6 7 8 10 20];
 LH3_ND_1 = length(c_micH3_ND_1);

% nt=5 Ch_ND = 6e3
c_micH3_ND_2=[9.467e-8 9.896e-8 1.398e-7 1.894e-7 2.3e-7...
               3.7e-7 6.764e-7 9.598e-7 2.598e-6 2.789e-6...
               4.198e-6 5.89e-6 6.789e-6 9.854e-6 1.2498e-5...
               1.525e-5 3.4e-5 3.5e-5 4.119e-5 5e-5 6e-5 ...
               6.6e-5 7e-5 8.876e-5 1e-4 1.8e-04 3.788e-4...
               6e-4 9.9101e-4 3.79094e-3 9.82101e-3 ...
               2.05505e-2 4.5557e-2 6.25669e-2 9.73273e-2 ...
               0.1205 0.143712 0.1617 0.203657 0.279167 ...
               0.372308 0.485207 0.620045 0.964523];
 LH3_ND_2 = length(c_micH3_ND_2);

% nt=6 Ch_ND = 2e4
```

```
c_micH4_ND_1=[2.3e-7 3.7e-7 6.764e-7 1.2e-6 3.5e-6...
              6.8e-6 8.79e-6 1.2498e-5 1.897e-5 2.8e-5...
              2.96e-5 3.29e-5 3.5e-5 3.8e-5 5e-5 1e-4 ...
              1.24e-4 1.4e-4 1.6e-4 1.8e-4 2e-4 2.3e-4 ...
              2.45e-04 2.7e-4 3.07e-4 3.1e-4 3.2e-4 ...
              3.3e-4 3.5e-4 3.788e-4 3.89e-4 4.2e-4 ...
              4.4e-4 4.7e-4 4.8e-4 5.1e-4 5.178e-4 ...
              5.5e-4 5.7e-4 9.82101e-3 2.05505e-2 ...
              4.5557e-2 6.25669e-2 9.73273e-2 0.143712...
              0.203657 0.279167 0.372308 0.485207 ...
              0.620045 0.964523 1.17878 1.4242 1.70321...
              2.37187 2.76657 3.20495 3.6 6 7 8 10 20 ...
              30 40 60 70 100];
LH4_ND_1 = length(c_micH4_ND_1);


% nt=7 Ch_ND = 6e4
c_micH4_ND_2=[2.3e-7 3.7e-7 6.764e-7 1.2e-6 1.2498e-5 ...
              1.897e-5 2.8e-5 2.96e-5 3.29e-5 3.5e-5 ...
              4.9e-5 5e-5 8.876e-5 1e-4 1.2e-4 1.4e-4 ...
              1.6e-4 1.7e-4 1.8e-4 2e-4 3.07e-4 3.2e-4 ...
              3.3e-4 3.5e-4 3.788e-4 3.89e-4 4.2e-4 ...
              4.27e-04 4.4e-4 4.7e-4 4.8e-4 5.1e-4 ...
              5.178e-4 5.5e-4 5.7e-4 9.82101e-3 ...
              2.05505e-2 4.5557e-2 6.25669e-2 ...
              9.73273e-2 0.1205 0.143712 0.1617 0.203657...
              0.279167 0.372308 0.485207 0.620045 ...
              0.964523 1.17878 1.4242 1.70321 2.37187...
              2.76657 3.20495 3.6 6 7 8 10 20 30 40 60 70];
LH4_ND_2 = length(c_micH4_ND_2);


% nt=8 Ch_ND = 6e5
c_micH5_ND=[1.5e-3 2.5e-3 2.8e-3 2.9e-3 2.99e-3 6e-3 ...
            7.5e-3 9.82101e-3 2.05505e-2 4.5557e-2 ...
            6.25669e-2 9.73273e-2 0.143712 0.203657 ...
            0.279167 0.372308 0.485207 0.620045 ...
            0.964523 1.17878 1.4242 1.70321 2.37187...
```

```
            2.76657 3.20495 3.6 6 7 8 10 20 40 60 80 ...
            90 95 110 130 140 150 160];
 LH5_ND = length(c_micH5_ND);


% nt=9 Ch_ND = 6e6
 c_micH6_ND=[0.01 0.014 0.017 0.023 0.026 0.0276 ...
             0.0346 0.0467 0.0578 0.0768 0.1 0.3 0.7...
             0.9 1 3 4 5 7 9 10 15 20 40 60 80 90 ...
             95 110 130 140 150 160];
 LH6_ND = length(c_micH6_ND);


% nt=10 Ch_ND = 6e7
c_micH7_ND=[0.01 0.014 0.0162 0.0165 0.017 0.026 0.03...
            0.04 0.05 0.07 0.1 0.13 0.17 0.2 0.26 0.27...
            0.275 0.2755 0.277 0.279 0.289 0.32 0.35 ...
            0.4 0.7 0.9 1 3 4 5 7 9 10 15 20 30 40 ...
            50 60 70 80 90 100 200 300 400 500 600 ...
            700 800 900 1000 2000 3000];
 LH7_ND = length(c_micH7_ND);


% nt=11 Ch_ND = 6e8
c_micH8_ND=[0.143712 0.16 0.1619 0.1624 0.17 ...
            0.18 0.25 0.372308 0.485207 0.620045 ...
            0.964523 1.17878 1.4242 1.70321 2.3718 ...
            2.75 2.83925 2.899 3.20495 3.6 4 5 7.734...
            7.789 8 9 10 20 30 40 50 60 70 80 90 100 ...
            200 300 400 500 600 700 800 900 1000 2000];
 LH8_ND = length(c_micH8_ND);


% nt=12 Ch_ND = 6e9
c_micH9_ND=[2.9 3.7 3.8 4 5 7 9 10 12 15 20 27.5 28 ...
            30 30.169997 31 32 35 37 40 43 50 54 76 ...
            80 90 100 200 300 400 500 600 700 800 ...
            900 1000 2000 3000];
```

```
 LH9_ND = length(c_micH9_ND);



%%%%%%%%%%%%%%%%%%%% Bacteria %%%%%%%%%%%%%%%%%%%%
%%%%%%% nt=1 Cb=1e-3 (cells/mL) Single target
c_micB0=[3e-3 6e-3 9e-3 2e-2 4e-2 6e-2 7e-2 ...
         8e-2 2e-1 4e-1 8e-1 2 5 9 20 40];
 LB0 = length(c_micB0);

%%%%%%% nt=2 Cb=6e1
c_micB1=[2.05505e-2 4.5557e-2 6.25669e-2 ...
         9.73273e-2 0.143712 0.203657 0.279167 ...
         0.372308 0.485207 0.620045  1.17878 1.4242...
         1.70321 2.01826 2.37187 2.76657 3.20495 ...
         3.6 6 7 8 10 20 30 40 50 60 80 90 100 150 200];
 LB1 = length(c_micB1);

%%%%%%% nt=3 Cb=6e2
c_micB2=[3.79094e-3 9.82101e-3 2.05505e-2 4.5557e-2 ...
         6.25669e-2 9.73273e-2 0.143712 0.203657 ...
         0.279167 0.372308 0.485207 0.620045 ...
         0.964523 1.17878 1.4242 1.70321 2.01826 3.6...
         6 7 8 10 20 30 40 50 60 80 90 100 150 200 250];
 LB2 = length(c_micB2);


%%%%%%% nt=4 Cb=2e3;
c_micB3_1=[0.372308 0.485207 0.620045 0.779055 ...
           0.964523 1.17878 1.4242 1.70321 2.01826 ...
           2.37187 2.76657 3.20495 3.6 6 7 8 10 20 ...
           30 40 50 60 80 90 100 150];
 LB3_1 = length(c_micB3_1);

%%%%%%% nt=5 Cb=6e3;
c_micB3_2=[0.372308 0.485207 0.620045 0.779055 ...
           0.964523 1.17878 1.4242 1.70321 2.01826 ...
           2.37187 2.76657 3.20495 3.6 6 7 8 10 20 ...
```

```
259             30 40 50 60 80 90 100];
260  LB3_2 = length(c_micB3_2);
261
262  %%%%%%% nt=6 Cb=2e4;
263 c_micB4_1=[0.372308 0.485207 0.620045 0.779055 0.964523...
264             1.17878 1.4242 1.70321 2.01826 2.37187 ...
265             2.76657 3.20495 3.6 6 7 8 10 20 30 40 50 ...
266             60 80 90 100];
267  LB4_1 = length(c_micB4_1);
268
269  %%%%%%% nt=7 Cb=6e4;
270 c_micB4_2=[0.372308 0.485207 0.620045 0.779055 ...
271             0.964523 1.17878 1.4242 1.70321 2.01826 ...
272             2.37187 2.76657 3.20495 3.6 6 7 8 10 20 30 ...
273             40 50 60 80 90 100];
274  LB4_2 = length(c_micB4_2);
275
276 %%%%%%% nt=8 Cb=6e5;
277  c_micB5=[4.68e-4 4.8e-4 5e-4 6e-4 7.53e-4 8.5e-4 9.9101e-4
        ...
278             1.3e-3 1.5e-3 2e-3 3e-3 3.79e-3 9.82101e-3 ...
279             2.05505e-2 4.5557e-2 6.25669e-2 0.1 0.12 0.1208...
280             0.143712 0.15 0.16 0.1623 0.17 0.203657 ...
281             0.2 0.7 0.8 0.964523 1.3];
282  LB5 = length(c_micB5);
283
284 %%%%%%% nt=9 Cb=6e6
285 c_micB6=[0.279167 0.372308 0.485207 0.620045 0.779055...
286           0.964523 1.17878 1.4242 1.70321 2.01826 2.37187...
287           2.76657 3.20495 3.68961 4.22322 4.80845 5.44803...
288           6.14471 6.90127 7.72052 8.60531 9.55852 10.583...
289           15.4534 20 30 40 50 60 70 80 90 100 ];
290 LB6 = length(c_micB6);
291
292 %%%%%%% nt=10 Cb=6e7
293 %Non-Comp, Comp Ch=Cb
294  c_micB7=[1.9156e-4 1.9189e-4 1.9237e-4 1.987e-4 2.498e-4...
295             3.12e-4 3.768e-4 4.56e-4 5.876e-4 6.2e-4 2e-3 ...
```

```
          3e-3 5e-3 7e-3 8e-3 1e-2 1.5e-2 2e-2 2.5e-2 ...
          3.1e-2 3.298e-2 3.3783e-02 3.396e-2 3.59e-2 ...
          4.55e-2 5.3e-2 5.9e-2 6e-2 7e-2 9.7e-2 0.1 0.12 ...
          0.143712 0.1543 0.203657 0.2056 0.279167 0.372308
             ...
          0.485207 0.620045 0.779055 0.964523 1.17878 1.4242
             ...
          1.70321 2.01826 2.37187 2.76657 3.20495 3.68961 ...
          4.22322 4.80845 5.44803 6.14471 6.90127 7.72052 ...
          8.60531 9.55852 10.583];
 LB7 = length(c_micB7);

%%%%%%% nt=11 Cb=6e8
c_micB8=[2e-2 3e-2 3.5e-2 4e-2 5.2e-2 6.1e-2 7.239e-2 ...
         9.7e-2 0.143712 0.15234 0.213657 0.3198 0.3375 ...
         0.3395 0.35868 0.3789669 0.4575 0.48 0.55 0.598 ...
         0.620045 0.65 0.779055 0.964523 1.17878 1.4242 ...
         1.70321 2.01826 2.37187 2.76657 3.20495 3.68961 ...
         4.22322 4.80845 5.44803 6.1 6.9 7.72052 8.60531 ...
         9.55852 10.583 15.4534 20 30 40 50 60 70 80 90 ...
         100 120 130 160 200 250 300 500];
LB8 = length(c_micB8);

%%%%%%% nt=12 Cb=6e9
 c_micB9 = [ 7.5 8 8.5 9 9.5 10 10 13 15 18 20 25 30];
LB9 = length(c_micB9);


%%%%%%%%%%%%%%%%%%%%%%%%%%%%%%%%%%%%%%%%%%%%%%%%%%%%%%%%%%%%%%%%%%%%
%Bacteria (e_H =-14)
x0B0 = [7e-8 9e-8 0.5 0.3];      % nt=1 Cb = 1e-3
x0B1 = [7e-8 9e-8 0.5 0.3];      % nt=2 Cb = 6e1
x0B2 = [2e-6 6e-7 0.5 0.3];      % nt=3 Cb = 6e2
x0B3_1 = [1e-6 1e-8 0.5 0.3];    % nt=4 Cb = 2e3
x0B3_2 = [1e-4 6e-4 0.3 0.3];    % nt=5 Cb = 6e3
x0B4_1 = [2e-10 6e-10 0.5 0.3]; % nt=6 Cb = 2e4
x0B4_2 = [1e-9 1e-8 0.5 0.3];    % nt=7 Cb = 6e4
%x0B5 = [1e-5 1e-5 0.4 0.4];     % nt=8 Cb = 6e5
```

```
%x0B5 = [2e-4 4e-4 0.5 0.5];     % MO.3.d
%x0B5 = [5e-7 6e-8 0.5 0.5];     % Mo.2c
%x0B5 = [2e-11 1e-12 0.3 0.2];
%x0B5 = [1e-4 1e-5 0.3 0.3];
x0B5 = [5e-6 1e-7 0.3 0.3];
%x0B5 = [5e-3 1e-3 0.7 0.7];
x0B6 = [7e-7 8e-7 0.5 0.3];      % nt=9 Cb = 6e6
x0B7 = [7e-8 9e-8 0.5 0.3];      % nt=10 Cb = 6e7
%x0B8 = [2e-13 4e-13 0.1 0.2];  % nt=11 Cb = 6e8
x0B8 = [5e-5 1e-6 0.3 0.1];      % nt=11 Cb = 6e8
%x0B8 = [1e-9 1e-10 0.3 0.1];
x0B9 = [7e-8 9e-8 0.5 0.3];      % nt=12 Cb = 6e9

% %Host Cell NO Lipid Demixing
x0H0_ND = [6e-5 3.9e-4];         % nt=1 Ch = 1e-3 (cells/mL)
%x0H0_ND = [1e-6 1e-8];
%x0H0_ND = [1e-8 1e-10];         % alph=0
%x0H1_ND = [1e-10 1e-19];        % nt=2 Ch = 6e1
x0H1_ND = [1e-7 1e-8];
%x0H2_ND = [1e-10 1e-18];        % nt=3 Ch = 6e2
x0H2_ND = [1e-7 1e-8];
%x0H3_ND_1 = [5e-9 8e-12];       % nt=4 Ch = 6e3
x0H3_ND_1 = [1e-6 1e-9];
%x0H3_ND_2 = [5e-9 8e-12];       % nt=5 Ch = 6e3
x0H3_ND_2 = [1e-6 1e-18];
%x0H4_ND_1 = [1e-7 1e-10];       % nt=6 Ch = 6e4
x0H4_ND_1 = [1e-6 1e-9];
%x0H4_ND_2 = [1e-7 1e-10];       % nt=7 Ch = 6e4
%x0H4_ND_2 = [1e-6 1e-9];
x0H4_ND_2 = [1e-4 1e-18];
%x0H5_ND = [5e-9 8e-12];        % nt=8 Ch = 6e5 Ah = 17Ah
%x0H5_ND = [1e-6 1e-9];             %alph=0.05
x0H5_ND = [1.2e-4 1e-30];             %alph=0
%x0H5_ND = [8e-6 1e-9];
%x0H5_ND = [8e-6 1e-9];         %nt = 8 Ab = Ah
%x0H6_ND = [1e-6 4.7e-9];       % nt=9 Ch = 6e6 1e-4 4.7e-9
x0H6_ND = [1e-6 1e-9];
%x0H7_ND = [1e-6 1e-9];         % nt=10 Ch = 6e7
```

```
x0H7_ND = [1e-9 1e-11];          % nt=10 Ch = 6e7
x0H8_ND = [9e-5 1e-9];           % nt=11 Ch = 6e8 Q=6,5
%x0H8_ND = [1e-7];
%x0H8_ND = [7e-6 2e-9];          % nt=11 Ch = 6e8 Q=4
%x0H8_ND = [9e-9 9e-12];
x0H9_ND = [9e-9 9e-12];          % nt=12 Ch = 6e9

%%%%%%%%%%%%%%%%%%%%%%%%%%%%%%%%%%%%%%%%%%%%%%%%%%%%%%%%%%%%%%%%%%%%%%%

%Matrix for various Bacterial target cell's concentration
c_micB={c_micB0,c_micB1, c_micB2, c_micB3_1, c_micB3_2,...
        c_micB4_1,c_micB4_2,c_micB5, c_micB6, c_micB7,...
        c_micB8, c_micB9};      %Peptide's concentrations
LpB=[LB0, LB1, LB2, LB3_1, LB3_2, LB4_1, LB4_2,LB5, ...
     LB6, LB7, LB8, LB9];       %Peptide's density # elements

x0B=[x0B0; x0B1; x0B2; x0B3_1; x0B3_2; x0B4_1; x0B4_2; ...
     x0B5; x0B6; x0B7; x0B8; x0B9]; %Initional inputs


%Matrix for various Host No Lipid Demixing concentration
c_micH_ND={c_micH0_ND ,c_micH1_ND,c_micH2_ND,...
           c_micH3_ND_1, c_micH3_ND_2,c_micH4_ND_1, ...
           c_micH4_ND_2, c_micH5_ND, c_micH6_ND, ...
           c_micH7_ND, c_micH8_ND, c_micH9_ND};
LpH_ND=[LH0_ND, LH1_ND, LH2_ND, LH3_ND_1, LH3_ND_2, ...
        LH4_ND_1, LH4_ND_2, LH5_ND, LH6_ND, LH7_ND, ...
        LH8_ND, LH9_ND];
x0H_ND=[x0H0_ND; x0H1_ND; x0H2_ND; x0H3_ND_1; ...
        x0H3_ND_2; x0H4_ND_1; x0H4_ND_2; x0H5_ND; ...
        x0H6_ND; x0H7_ND; x0H8_ND; x0H9_ND];

%%%%%%%%%%%%%%%%%%%%%%%%%%%%%%%%%%%%%%%%%%%%%%%%%%%%%%%%%%%%%%%%%%%%%%%
%----------------- Options for minimization function ---
 optionsB=optimset('Display','iter-detailed',...
                   'Algorithm','interior-point',...
                   'InitTrustRegionRadius',0.5,...
                   'InitBarrierParam',0.1 , ...
```

```
                    'FunValCheck', 'off','TolCon ', 1e-8,...
                    'MaxFunEvals' ,7e3 , 'MaxIter',1e8,...
                    'TolX',1e-20,'TolFun',1e-15, ...
                    'Hessian', 'bfgs');

 % NO Demixing (Host cell)
 optionsHND=optimset('MaxFunEvals', 5e3, 'MaxIter', ...
                     1e8, 'TolX', 1e-12, 'TolFun' , 1e-12);

options_Lipid = optimset('Display','iter-detailed',...
                         'Algorithm','interior-point',...
                         'InitTrustRegionRadius',1e-3,...
                         'InitBarrierParam',1e-3 , ...
                         'FunValCheck', 'off','TolCon ',...
                         1e-6, 'MaxFunEvals' ,5e3 , ...
                         'MaxIter',1e8,'TolX',1e-15,...
                         'TolFun',1e-6,'Hessian', 'bfgs',...
                         'GradObj','off', 'GradConstr', 'off')
                            ;

%%%%%%%%%%%%%%%%%%%%%%%%%%%%%%%%%%%%%%%%%%%%%%%%%%%%%%%%%%%%%%%%%%%%%%%%%%%%%%%
% Defining general variables
C = {Cb, Ch_ND};  %Cell density cells/mL
al = [alb alh_ND];
alph = [alphb alphh_ND];
A = [Ab Ahost_ND];
V_cell = [Vb, Vh_ND];
Q_p= Q_l;
vp_p = vp_l;
apef_p = apef_l;
SM_p = SM_l;

c_mic = {c_micB, c_micH_ND};
x0 = {x0B,x0H_ND};
Lp = {LpB, LpH_ND};
options = [optionsB, optionsHND];


```

```
%%%%%%%%%%%%%%%%%%%%%%%%%%%%%%%%%%%%%%%%%%%%%%%%%%%%%%%%%%%%%%%%%%%%%%%
 %Defining variables for final output of results
  TP_LI = cell(L_Cb,N_cell);
  TP_LS = cell(L_Cb,N_cell);

  TsigmaI = cell(L_Cb,N_cell);
  TsigmaS = cell(L_Cb,N_cell);
  Talph1I = cell(L_Cb,N_cell);
  Talph1S = cell(L_Cb,N_cell);

  MIC_MHC = zeros(L_Cb,N_cell+1);
  MIC_MHCC = zeros(L_Cb, N_cell+1);
  Selectivity = zeros(L_Cb, 4);

 %%%%%%%%%%%%%%%%%%%%%%%%%%%%%%%%%%%%%%%%%%%%%%%%%%%%%%%%%%%%%%%%%%%%%%%
 %Minimization & Plotting Surface Coverage


%Bacteria or Host cell?
 for m =1 %1:N_cell
     X0t = x0{1,m};
     c_t = C{1,m};
     Lt = length(c_t);
     Lpt = Lp{1,m};
     c_pt = c_mic{1,m};
     Tresholdt = Treshold(m);
     K = vp*exp(-w(m)/(Kb*T));


     rp = sqrt(ApI/pi);
     lambda = al(m)/(2*pi*lb*alph(m));
     AsI = pi*(rp+lambda)^2;
     AsS = AsI;


      Rp=sqrt(ApI/pi);
      Rs=sqrt(AsI/pi);

```

```
483       %peptide's self-energy difference
484       deltaFp= delFp(Q,ApI); %delFp(Q,ApI);
485
486
487       %-----------Bessel Integral
488        Bessel_phi00_Rp=...
489        integral(@(k) besselj(1,k.*Rp)./sqrt(k.^2+kapain^2),0,
             inf);
490  if m == 1
491        Bessel_phi00_Rs=...
492        integral(@(k) besselj(1,k.*Rs)./sqrt(k.^2+kapain^2),0,
             inf);
493        Bessel_F_DH_RING=...
494        integral(@(k) (Rs.*besselj(1,k.*Rs)-Rp.*besselj(1,k.*Rp
             ))...
495        .^2./(k.*sqrt(k.^2+kapain^2)), 0,inf);
496        Bessel_F_DH_DISK=...
497        integral(@(k)besselj(1,k.*Rs).^2./...
498        (k.*sqrt(k.^2+kapain^2)), 0,inf);
499        Bessel_E_DH_RING=integral(@(k) ...
500        ((Rs.*besselj(1,k.*Rs)-Rp*besselj(1,k.*Rp)).*Rp...
501        .*besselj(1,k.*Rp))./(k.*sqrt(k.^2+kapain^2)), 0,inf);
502        Bessel_Fp_DH_Mem=...
503        integral(@(k)besselj(1,k.*Rp).^2./...
504        (k.*sqrt(k.^2+kapain^2)), 0,inf);
505  end
506
507
508       % Cell density?
509         for nt =8%1:Lt
510              Ct = c_t(nt)*1e-24; %cell concentration (cells/A
                   ^3)
511
512              c_p = c_pt{1,nt};   %Peptide's density
513              L = length(c_p);    % # of peptide's density
514              X0 = X0t(nt,:);     %Initial guess
515
516
```

```
517             P_LI = zeros(L+1,2);
518             P_LS = zeros(L+1,2);
519
520             sigmaI = zeros(L+1,2);
521             sigmaS = zeros(L+1,2);
522
523             alph1_I = zeros(L+1,2);
524             alph1_S = zeros(L+1,2);
525
526             Energy = zeros(L+1,4);
527
528             %Peptide Concentration in Bulk?
529             for n = 1%:L
530                 c_p(n) = 5e-2 ;
531                 Cp = c_p(n)*(1e-6)*NA*(1e-27);
532                 % bulk peptide concentration (molecules/A^3)
533
534 %% Different Solver for minimizations and root finding
535
536
537 % Azadeh Model-NO Lipid Demixing for Host cell
538  if        m == 2 && Sho==0
539           Max = [SM,SM];
540           Min = [0,0];
541
542           [x, fval, exitflag]=fmincon(@(x)Lipid(x),...
543           X0,[],[],[],[],Min,Max,'constraintcom_Lipid'...
544           ,options_Lipid);
545           SSL =[Lipid(x), Lipid(x+0.00001),Lipid(x-0.0001)]
546           x0 = x
547
548 % Shokoofeh Model-NO Lipid Demixing for Host cell
549 elseif    m ==2 && Sho==1
550
551          [x, fval, exitflag]=...
552          fminsearch(@(x)competeE(x),X0,options(3));
553          SSL =[competeE(x), competeE(x+0.0001),competeE(x
               -0.0001)]
```

```
554           xequ = [x(1),x(2)];
555           Aws = (1+xequ(1)*apef(m))/xequ(1);
556           Rws = sqrt(Aws/pi);
557 
558           [delFWSI] = WSC_ISND(xequ(1), xequ(2))
559 end
560 
561 
562 
563 [x, fval, exitflag] = fmincon(@(x)competeE(x),...
564 X0,[],[],[],[],[0;0;0;0],[SM(m);SM(m);1;1],...
565 'constraintcom',options(1));
566 gH =[competeE(x), competeE(x+0.00001),competeE(x-0.0001)]
567 
568 xequ = [x(1),x(2),x(3),x(4)];
569 Aws = (1+xequ(1)*apef(m))/(xequ(1) + xequ(2));
570 Rws = sqrt(Aws/pi);
571 
572 if      Mo == 3
573         [delFWSI,delFWSS] = ...
574         WSC_IS_DH(xequ(1), xequ(2), xequ(3), xequ(4))
575 elseif Mo == 2
576         [delFWSI,delFWSS] = ...
577         WSC_IS(xequ(1), xequ(2), xequ(3), xequ(4))
578 end
579 
580 %%%Collecting Minimized values of x(1), x(2), x(3), x(4) for n
581 %Surface Coverage for Insertion mode (I)
582 sigmaI(1,2) = c_t(nt);
583 sigmaI(n+1,1) = c_p(n);
584 sigmaI(n+1,2) = x(1);
585 
586 P_LI(1,2) = c_t(nt);
587 P_LI(n+1,1) = c_p(n);
588 P_LI(n+1,2) = x(1)*al(m);
589 
590 
591 %Surface Coverage for Binding mode (S)
```

```
sigmaS(1,2) = c_t(nt);
sigmaS(n+1,1) = c_p(n);
sigmaS(n+1,2) = x(2);

P_LS(1,2) = c_t(nt);
P_LS(n+1,1) = c_p(n);
P_LS(n+1,2) = x(2)*al(m);

 if    m ~= 2
       alph1_I(1,2) = c_t(nt);
       alph1_I(n+1,1) = c_p(n);
       alph1_I(n+1,2) = x(3);

       alph1_S(1,2) = c_t(nt);
       alph1_S(n+1,1) = c_p(n);
       alph1_S(n+1,2) = x(4);
end

       Energy(1,1) = c_t(nt);
       Energy(n+1,1) = c_p(n);
       Energy(n+1,2) = delFWSI;
       %Energy(n+1,3)= delFWSS;
       Energy(n+1,4) = Rws;


%%%%%%%%%%%%%%%%%%%%%%%%%%%%%%%%%%%%%%%%%%%%%%%%%%%%%%%%%%%%%%%%%%%%%%%
    end

% Saving final outputs for various target cell's density
TP_LI{nt,m} = P_LI;
TP_LS{nt,m} = P_LS;
TsigmaI{nt,m} = sigmaI;
TsigmaS{nt,m} = sigmaS;
if     m ~= 3
       Talph1I{nt,m} = alph1_I;
       Talph1S{nt,m} = alph1_S;
end

```

```
630 if      m == 1
631         FileNameI = sprintf('%s_%d.%s','P_LIB',nt, 'txt');
632
633 elseif m == 2
634         FileNameI = sprintf('%s_%d.%s','P_LIH_ND',nt, 'txt');
635 end
636 dlmwrite(FileNameI, P_LI, 'delimiter', '\t' , 'precision', 10)
637
638 %Plotting surface coverage
639
640 if      m == 1
641         TitleName = ...
642         '\fontsize{16}Bacterial Surface coverage Vs. Peptide
              Concentration';
643         AxisName = {'P/LB','Fractional Peptide Occupancy'};
644
645 elseif m == 2
646         TitleName = '\fontsize{16}HostCell Surface coverage Vs.
              Peptide Concentration, No Lipid Demixing';
647         AxisName = {'P/LH', 'phi_H'};
648
649 end
650
651 if      AreaEx == 1
652         linestyle = '--';
653 elseif AreaEx == 0
654         linestyle = '-';
655 end
656
657 figure(3+g)
658 ColorSet = varycolor(Lt);
659 semilogx(c_p ,P_LI(2:end,2),linestyle,'LineWidth',1.2,'Color',
       ColorSet(1,:))
660 title({TitleName});
661 ylabel(AxisName{1,g},'fontsize',18,'fontweight','b');
662 xlabel('c_{p}(\muM)','fontsize',20, 'fontweight','b');
663 hold on
664
```

```
665
666
667 for i= 2:3
668
669     figure(10)
670     ColorSet = varycolor(Lt);
671     plot(Energy(2:end,4) ,Energy(2:end,i),linestyle,'LineWidth
        ',1.2,'Color',ColorSet(1,:))
672     title({'\fontsize{18}WSC Free energy Vs. distance'});
673     ylabel('deltaF_{WSC} (KbT)','fontsize',18,'fontweight','b'
        );
674     xlabel('R_{WSC} (A)','fontsize',18, 'fontweight','b');
675     hold on
676 end
677
678 P_LI
679  %%%%%%%%%%%%%%%%%%%%%%%%%%%%%%%%%%%%%%%%%%%%%%%%%%%%%%%%%%%%
680
681
682 end
683 end
```

# Chapter 4

# Protection role of LPS brush: How core oligosaccharide and O-antigen reduce adsorbed membrane-rupture peptides

## 4.1 Introduction

Bacteria are conventionally divided into two major groups: gram-positive and gram-negative. While gram-positive bacteria contain only plasma membrane mostly composed of phospholipids, gram-negative bacteria are enclosed with an additional membrane, called the outer membrane (OM). The OM is highly asymmetric in composition: while lipopolysaccharide (LPS) is a main component of the outer layer, phospholipids are localized to the inner one. LPS is a complex macromolecule that includes three main structural components: Lipid A, the core oligosaccharide, and the O-antigen. Lipid A consists of a phosphorylated diglucosamine group and 4-7 acyl chains that are anchored to the hydrophobic region of the inner phospholipid layer and construct the OM bilayer. Lipid A is covalently bonded to the core oligosaccharide chain of 8-12 sugars. The inner core is highly anionic in nature due to the very phosphorylated oligosaccharide region, while the outer core is hydrophilic. O-antigen or O-polysaccharide chains form the furthermost part of the LPS that encounter the extracellular environment. It consists of several types of sugar units that are repeated in an approximate length around 2-11 nm [117] (i.e., corresponding to 8-14 O-antigen repeats) and acts as a hydrophilic-coating surface.

Several studies highlight the prominent role of the OM, especially the LPS layer in reducing the susceptibility of Gram-negative bacteria to antimicrobials [16, 18, 118].The interaction of cationic antimicrobial peptides with these highly negatively-charged macromolecules (i.e. in a physiological condition, LPS carries 4-6 negative unit charges) can inhibit the peptide's entry into the inner plasma membrane and therefore prevent the toxicity of antimicrobial agents [119]. Furthermore, the presence of the physiological concentration of divalent cations ($Mg^{2+}$ and $Ca^{2+}$) improves the integrity of the LPS layer against antimicrobials by bridging the neighbouring anionic phosphate groups in the inner core [62, 120]. Indeed, these divalent counterions induce a negative lateral pressure in the plane of the phosphate groups and enhance the molecular packing order of LPS, stabilizing the LPS layer [59, 62, 72, 121].

In contrast to the aforementioned OM-stabilizing factors, the protective role of uncharged saccharide chains in the LPS layer has not been well understood. For simplicity, it is a common practice to use mutant LPS in experimental studies of AMP-bacteria interactions. But any variation in their molecular structures can cause a noticeable difference in these interactions, which in turn alter the peptide-induced permeability of the LPS layer [62, 122]. The mutant LPSs are different from those of wild types in their molecular structure, such as the length and complexity of their hydrophilic polysaccharide region. Rough LPS (Ra chemotype) does not have the O-antigen and deep rough LPS, Rd chemotype, lacks both O-antigen and the outer polysaccharide core region. However, the wild-type LPS contains O-antigen and entire core region. Experiments with hydrophobic antibiotics [123, 124] and AMPs such as magainin [123, 125] show that rough and deep rough mutants have lower antimicrobial resistance compared to the wild type.

While experiments clearly indicate that wild-type LPS is more resistant to antimicrobials compared to the mutant ones, its physical picture is entirely lacking. In fact, these uncharged hydrophilic saccharide chains, elongated on top of the charged phosphorylated headgroups, act like an end-grafted polymer brush onto the LPS inner core and protect the OM from peptide's inclusion as well as from their adsorption to the inner (plasma) membrane. In other words, the brush element of the LPS layer provides extra protection for Gram-negative bacteria by reducing the number of adsorbed AMPs onto the LPS inner core and lowering their membrane-lysis activity [62, 122]. In this work, we present a course-grained model to capture the effect of the LPS brush and offer a quantitive basis for the protective role of outer oligosaccharide and O-antigen chains.

For this purpose, we extend recently developed AMP-LPS models [13, 58, 59], where the authors provide detailed computations of the interactions on LPS headgroup, to a theoretical consideration of the wild-type LPS. Using the resulting model, we will carry out a quantitative study of peptide adsorption to the outer layer of the bacterial OM.

Recent publications [13, 58, 59] established a series of coarse-grained models, which explain the complex electrostatic interactions in the LPS-peptide-ion system, along with the hydrophobic-inclusion of AMPs into the membrane. In fact, these models include the long-range coulomb interactions among adsorbed peptides and divalent ions, which compete to electrostatically bind to the anionic LPS headgroups (i.e. this is technically challenging and cannot be addressed by a simple Langmuir-type binding model). While the aforementioned coarse-grained model [59] reflects the conventional biophysical experiments with deep-rough-LPS bilayers, for a more realistic picture of AMP-bacteria interactions, it is necessary to consider wild-type LPS and to take into account the physical influence of the outer core oligosaccharide and O-antigen sugar groups in our analysis.

Our results demonstrate that the presence of LPS brush reduces the number of hydrophobically bound peptides, compared to the deep-rough LPS which lacks a saccharide brush. This effect is mainly due to the steric barrier of the brush and polymer excluded-volume effect, which imposes unfavourable free energy to the hydrophobically-bound peptides on LPS interface. In fact, the hydrophobically-inserted peptide on the LPS surface needs more free energy to succeed brush-induced osmotic pressure and creates a volume inside of this dense polysaccharide environment.

## 4.2 Theoretical Approach

In order to derive the free energy of our LPS brush system, we first extend the deep rough LPS model [59], in which AMPs adsorb to the anionic phosphate group of LPS molecules and at the same time hydrophobically inserted inside the acyl chain region, to a wild-type LPS with polymer brush on top of its inner oligosaccharide. In this work, we represent the effect of the LPS brush as a free energy barrier to the peptide's adsorption by estimating the free energy cost of including peptides within the brush regime.

To this end, we introduce two modes for peptide adsorption (Fig. 4.1), known as primary and ternary [126, 127] adsorption. The total number of adsorbed peptides on LPS brush is set by two processes; (i) $N_{\mathrm{p}}$ peptides bind to the anionic LPS inner core (i.e. latterly, it is referred by LPS surface), in primary adsorption, and (ii) $N_{\mathrm{pB}}$ peptides become captive within the brush, in ternary adsorption. It is worth mentioning that the secondary adsorption mechanism, in which proteins bind to the outer edge of the brush (outside the brush domain) due to van der Waals attraction to the surface, is very weak in the case of our small AMPs; we will confine our considerations to the primary and ternary adsorption. The theoretical analysis of Halperin et al. [10] on protein adsorption into the

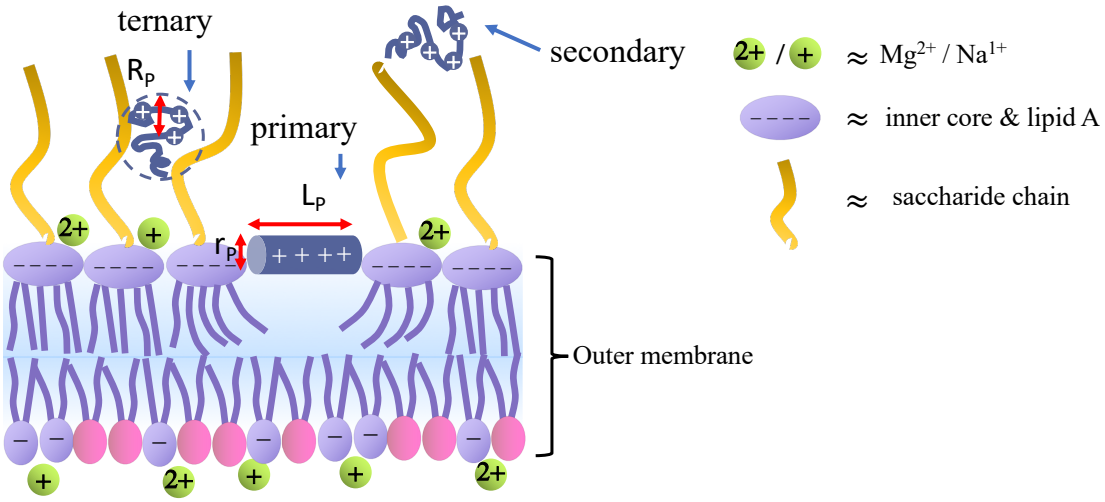


Figure 4.1: AMP adsorption onto the LPS brush of the outer membrane (OM). Peptides can be adsorbed onto the LPS brush by three mechanisms; primary, secondary and ternary adsorption. Primarily peptides bind to the charged LPS inner core and Lipid A (purple oval shape), while hydrophobically inserted into hydrophobic region of the OM. In ternary adsorption, some fraction of peptides are trapped within the brush thickness, due to weak brush-peptide attractive interaction. Secondary binding occurs at the outer edge of the brush, as a result of van der Waals attraction. This mode is only important for long cylindrical proteins [10] whereas in the case of small AMPs, secondary adsorption is negligible. Note that in primary adsorption, the alpha-helical peptide is considered as a rod with length $L_\mathrm{p}$ and radius $r_\mathrm{p}$, and the peptide is assumed to adopt a spherical structure with a radius $R_\mathrm{p}$ in secondary and ternary adsorption. The purple oval shape represents charged saccharide groups of the inner oligosaccharide and lipid A, and green 2+ (1+) circles describe small ions.

brush demonstrates that the secondary adsorption is expected to play a role only for long cylindrical proteins.

At first glance, one might assume that ternary adsorption is insignificant compared to primary adsorption, in which peptides gain a large electrostatic and hydrophobic energy. However, the protein-brush experiments [128, 129] and theoretical works [126, 130] point to the non-negligible effects of ternary adsorption, especially for long and bulky brush chains, in partitioning proteins between two coexisting phases.

Furthermore, our coarse-grained model takes into account the membrane-stabilizing effect of cationic agents and their competing role in occupying available electrostatic-binding sites on the LPS surface. The highly negatively-negatived charged LPS surface, due to the presence of anionic phosphate group of the inner core, makes it very unstable. On the other hand, the physiological counterion concentration plays an important role in stabilizing and maintaining the LPS layer by neutralizing the surface charge and producing a non-uniform charge distribution (i.e., a heterogeneous surface charge reduces the membrane lateral pressure, thus tightening the LPS) [13, 58, 59]. Our LPS brush model captures this effect through the partitioning of cations between the bulk and the LPS surface. Key quantities are $N_2$ and $N_1$ defined as the number of surface-adsorbed $Mg^{2+}$ and $Na^{+}$, respectively.

Hence, the total thermodynamic free energy of our multi-variable LPS-ion-peptide system, consisting of the four parameters, $N_1$, $N_2$, $N_{\rm p}$, and $N_{\rm pB}$ is minimized, simultaneously, with respect to these parameters for their given chemical potentials in the solution, further away from LPS layer. In the end, the resulting equilibrium surface coverages would be compared with those for deep-rough LPS [59], which lacks an LPS brush.

It is natural to define the general free energy of our LPS brush system as

$$F_{\rm LPS\,brush} = F_{\rm pri}(N_1, N_2, N_{\rm p}) + F_{\rm ter}(N_{\rm pB}, N_{\rm p}) - (N_{\rm p} + N_{\rm pB})\mu_{\rm p}^{\rm free} - \sum_{i=1}^{2} N_{\rm i}\,\mu_{\rm i}^{\rm free}, \qquad (4.1)$$

where subscripts $i = 1$, $i = 2$, and 'p' represent monovalent, divalent cations, and peptides, respectively, and $\mu^{\rm free}$ is their chemical potentials in bulk. In a dilute solution, where the interaction between charges is negligible, the chemical potentials depend on the bulk concentrations of ions $C_{\rm i}$ and peptides $C_{\rm p}$:

$$\mu_{\rm p}^{\rm free} = \ln\Big[\nu_{\rm p}\big(C_{\rm p} - C_{\rm t}N_{\rm p} - C_{\rm t}N_{\rm pB}\big)\Big] \qquad (4.2)$$

$$\mu_{\rm i}^{\rm free} = \ln\left(\frac{4}{3}\pi r_{\rm i}^3 \times C_{\rm i}\right). \qquad (4.3)$$

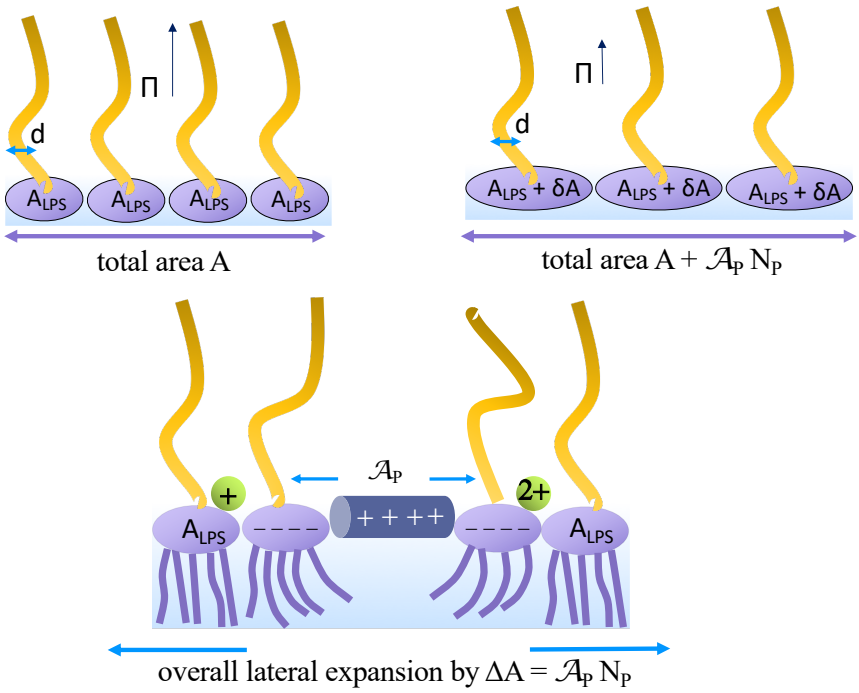


Figure 4.2: Peptide's primary adsorption $N_{\rm p}$ on the LPS surface reduces the grafting density. Hydrophobic binding of the peptide expands the membrane area by $\mathcal{A}_{\rm p}$ [11]. Let $N_{\rm p}$ be the number of peptides in this adsorption. The total lateral expansion is $\mathcal{A}_{\rm p}N_{\rm p}$. This results in a lower osmotic pressure $\Pi$ of the brush. The size of a monosaccharide group $d$ remains constant.

where $\nu_{\rm p}$ is the random-coil volume of each peptide in the electrolyte solution, $C_{\rm t}$ is the number density of total cells in our system, and $r_{\rm i}$ is the effective (hydrated) radius of cations. Note that the chemical potential of peptides is not constant (i.e. see Eq. 4.2) and it would change with the number of adsorbed peptides on the LPS surface $N_{\rm p}$ or within the brush $N_{\rm pB}$. In fact, the total number of available peptides inside our LPS-peptide-ion system is conserved; this will allow us to examine the possible competition between adsorbed peptides in different modes and to measure the influence of the ternary adsorption on the primary adsorption.

It is worth mentioning that we treat small cations $Mg^{2+}$ and $Na^{+}$ as point-like objects that do not feel the brush pressure in zeroth-order approximation and therefore, the ternary free energy ($F_{\rm ter}$) is a function of adsorbed peptides within the brush and on the LPS

surface. But it does not depend on the small ions ($N_1$ and $N_2$). In Eq. 4.1, we construct the primary and ternary adsorption energies, which are the consequence of many different interactions and thus can be decomposed into several sub-component free energies:

$$\begin{aligned} F_{\rm pri} &= F_{\rm el}(N_1, N_2, N_{\rm p}) + \varepsilon_{\rm I} N_{\rm p} + E_{\rm def}(N_{\rm p}) \\ &\quad + N_{\rm p}\, F^{\rm pri}_{\rm brush}(\Pi, L_{\rm p}, r_{\rm p}, N_{\rm p}) + F^{\rm pri}_{\rm ent}(N_1, N_2, N_{\rm p}) \end{aligned} \tag{4.4}$$

and

$$F_{\rm ter} = N_{\rm pB}\, F^{\rm ter}_{\rm brush}(\Pi, R_{\rm p}, N_{\rm p}) + F^{\rm ter}_{\rm ent}(N_{\rm pB}, N_{\rm p}), \tag{4.5}$$

where $\Pi$, $L_{\rm p}$, $r_{\rm p}$ and $R_{\rm p}$ are brush osmotic pressure, rod-peptide radius, rod-peptide length, and the radius of the hard-sphere peptide, respectively. Also, $F_{\rm el}$ is the electrostatic interaction free energy between charged ions, peptides and the LPS surface, $\varepsilon_{\rm I}$ is the hydrophobic energy gain per membrane-inserted peptide, $E_{\rm def}$ is the energy cost for peptide-induced membrane deformation, and $F_{\rm ent}$ represents the configuration entropy associated with ions/peptides distributions on the LPS surface (primary adsorption) and within the brush (ternary adsorption).

The term $F_{\rm brush}$ is the free energy cost for including a single peptide into the LPS brush. A surface-grafted polymer brush of PEG or wild-type LPS in contact with proteins (or peptides) may be considered as non-interacting with inclusions [131]. Such a brush tends to resist protein adsorption on the grafting plane (underlying surface) through its steric hindrance [132] (i.e., experiments on surface grafted PEG [133, 134] and Ra chemotype of LPS [135] in interacting with proteins and melittin, respectively, provided evidence of protein adsorption resistance). Peptides within the brush effectively experience excluded-volume interaction with the segments of the brush. This effect can be captured by the brush osmotic pressure $\Pi$ and the size of rod-peptide ($L_{\rm p}$ and $r_{\rm p}$) and hard-sphere peptide ($R_{\rm p}$) in primary and ternary adsorption, respectively. It is interesting to note that the brush free energy is dependent on the degree of primary adsorption via the number of bound peptides on the LPS surface (i.e., the brush free energy is a function of $N_{\rm p}$). As shown in Fig. 4.2, for primary adsorption, peptides are hydrophobically associated with the bilayer acyl chains and cause lateral expansion [11, 97]. As a result, the area per grafted polymer increases, lowering the brush monomer concentration and diminishing the excluded-volume interaction between peptides and brush segments.

In addition, the effects of LPS brush are different between the two adsorption modes (primary and ternary). In Fig. 4.1, while peptides bound to the LPS surface, i.e., in primary adsorption, are described as alpha-helical (overall cylindrical), peptides adsorbed in the LPS brush, i.e., in ternary adsorption, are viewed as a hard-share peptide (i.e. more

realistic picture is that peptides adopt conformational properties combined both features of rigid hard-sphere and random coil, while adsorbed within the brush thickness). Also, peptides on the LPS surface tend to experience fewer contacts with the brush segments, due to both less available surface area per peptide (half of the peptide's surface is inserted into the hydrophobic region) and lower monomer density of brush chains near the grafted plane [126]. These structural difference of peptides and the brush in primary and ternary mode lead to different brush free energy between the two peptide adsorption modes. The free energy of a brush and its interaction with AMPs are detailed in Subsec. 4.3.1

Besides the interaction between peptides and a brush, other contributions (i.e., electrostatic, hydrophobic, and membrane-deformation) in Eq. 4.4 are known in the literature [13, 58, 59]. For instance, $F_{\mathrm{el}}$ describes the complex electrostatic relations between ions, peptides and backbone anions on the LPS surface. This can be decomposed into four major interactions: the self-energy of a peptide which varies near the water-hydrophobic interface, ion-pairing, repulsion arising from a net charge on the surface, and the lateral correlation among surface charges (lipid charges, ions, and peptides). The last one reflects non-uniform charge distributions on the surface and takes into account long-ranged Coulomb interactions of the heterogeneously-charged lattice sites (i.e., see section 4.27 for more information).

The quantity $\varepsilon_{\mathrm{I}}$ is the hydrophobic free energy of a peptide at the interface between lipid headgroups and tails. A reasonable choice is $\varepsilon_{\mathrm{I}} \approx -10 k_{\mathrm{B}}T$ (as for magainin 2) [43, 59] in this work. In fact, once a peptide binds to the LPS surface, it forms an alpha-helical structure with two distinguished sides of water soluble and non-soluble parts. The hydrophobic side would insert inside the bilayer to avoid contacts with the solution and therefore minimize the free energy of the system (see [45, 51, 59] for more information).

The term $E_{\mathrm{def}}$ is the deformation free energy cost of the LPS surface, induced by peptide insertion into the hydrophobic region. As a peptide is accommodated within the bilayer acyl chains, it distorts molecular packing order and stretches the membrane area.

All the free energy components and their relationships are detailed in section 4.3.

## 4.3 Free Energy Components

### 4.3.1 Polymer Brush Free Energy, $F_{\mathrm{brush}}$

In our model (Fig. 4.3), the physical characteristics of outer core oligosaccharide and O-antigen of every single LPS molecule are taken into account by viewing them as forming

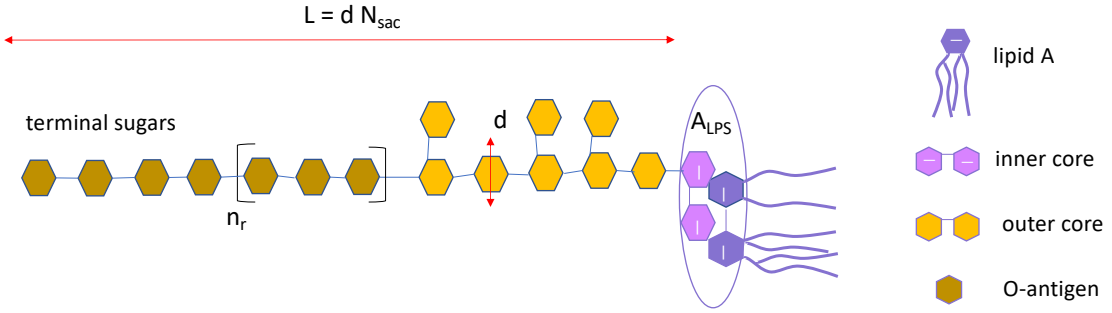


Figure 4.3: Physical structure of single LPS molecule. The inner core oligosaccharide and lipid A comprise the negatively-charged LPS grafted plane (purple oval) with cross sectional area $A_{\mathrm{LPS}}$, and the rest parts of the LPS (i.e. outer core, O-antigen chain and terminal saccharides) constitute a polymer brush chain (light and dark yellow hexagons). The total number of monosaccharides of the brush chain, $N_{\mathrm{sac}}$, each with diameter $d$, determines the total length $dN_{\mathrm{sac}}$. Here $n_{\mathrm{r}}$ is the repeat number of O-antigen's sugar groups.

a grafted polymer brush (i.e. one end attached to the LPS headgroup); the size of each monosaccharide, $d = 0.85$ nm [136] and its polymerization degree $N_{\mathrm{sac}} = 4n_{\mathrm{r}} + 8 + 4$ ($n_{\mathrm{r}}$ is the repeat number of the saccharide group in O-antigen). The core oligosaccharide part mainly has 3-8 backbone units with a few short side chains, while O-antigen consists of a repeating unit of a short oligosaccharide or single carbohydrate (1-4 repeated units) with 4 terminal sugars at the end [117]. The chain length of each LPS molecule varies by the O-antigen repeat unit. Ref. [117] suggests that the repeat unit distribution is mostly between 8-15.

Considering what is described above, we view the outer core and O-antigen forming a densely grafted polymer brush because of their high grafting density, $\sigma_{\mathrm{g}}$. Polymer brushes have been studied in the literature; relevant parameters are grafting density (number of chains per grafted area), polymer length and monomer volume fraction $\phi$. It is shown that uncharged flexible chains attached to the surface by one end, create a compact structure of mushroom in low grafting concentration, i.e., when Flory radius of the random-coil chain of a good-solvent solution is smaller than the polymer grafting distance $R_{\mathrm{f}} < D$ (i.e. see Fig. 4.4). However in higher grafting density, chains tend to overlap with one another and the excluded-volume interactions between neighbouring chains increases. As a result, polymers assume a stretched configuration from the grafted surface, forming a polymer brush with a layer thickness $H$ [137]. The equilibrium height of the polymer brush $H_0$, at which stretching energy and excluded-volume interaction are balanced, depends on the

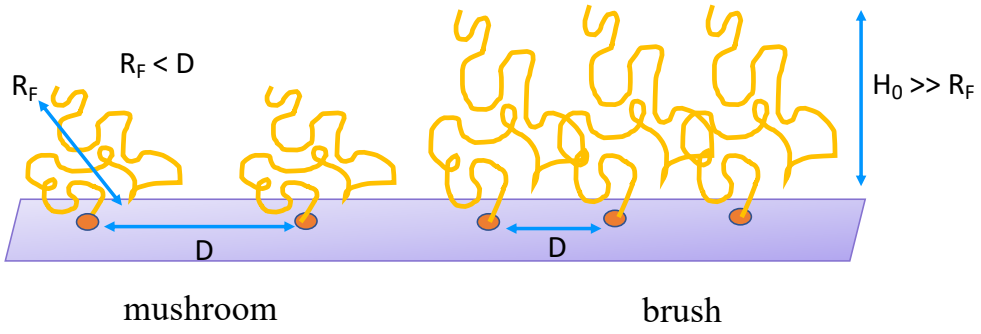


Figure 4.4: Schematic view of different conformations of surface-grafted polymers. At a low grafting density, the Flory radius of the polymer is smaller than the distance between neighbouring grafted polymers, $D$. The grafted polymer resembles an isolated non-interacting mushroom. In a brush regime or at a high grafting density ($D$ is very smaller than the Flory radius of the chain $R_{\mathrm{F}}$), excluded-volume interactions between grafted polymers tend to stretch out each chain to an equilibrium height $H_0$.

grafting density $\sigma_{\mathrm{g}}$ and the number of brush monomers $N_{\mathrm{sac}}$ [138].

Fig. 4.2 exhibits that hydrophobic binding of peptides on the LPS surface induces membrane expansion, laterally by $\Delta A = \mathcal{A}_{\mathrm{p}} N_{\mathrm{p}}$ (i.e. Huang and colleagues [11] determined that the lateral expansion per peptide is equal to or smaller than the physical size of a peptide. In the case of magainin II, $\mathcal{A}_{\mathrm{p}} \leq 2.2 \times 0.6$ nm$^2$. If we assume that the total area of the LPS layer is $A = N_{\mathrm{LPS}}\, A_{\mathrm{LPS}}$, then we could distribute the total expansion $\Delta A$, evenly, between all the LPS molecules, obtain the area expansion per LPS chain $\delta A$, and construct a new LPS cross sectional area of $A_{\mathrm{LPS}} + \delta A$, which depends on the number of hydrophobically-inserted peptides. As a result, the dimensionless fractional grafting density of the LPS brush would be peptide-dependent

$$\sigma_{\mathrm{g}}(N_{\mathrm{p}}) = \frac{d^2}{A_{\mathrm{LPS}} + \delta A(N_{\mathrm{p}})}, \tag{4.6}$$

where $\delta A = \mathcal{A}_{\mathrm{p}} N_{\mathrm{p}} / N_{\mathrm{LPS}}$ and $N_{\mathrm{LPS}}$ is the total number of LPS molecules.

In order to find the brush free energy and the corresponding osmotic pressure II, we need to compute our monosaccharide volume fraction of the LPS brush. For this purpose, we assume that saccharide chains are confined into a cylinder of cross-sectional area of

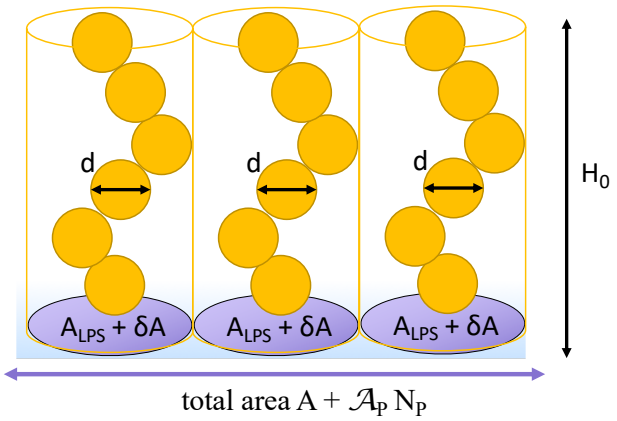


Figure 4.5: Schematic representation of a confined brush chain in a cylinder of area $A_{\rm LPS} + \delta A(N_{\rm p})$ and height $H_0$.

$A_{\rm LPS} + \delta A(N_{\rm p})$ and height $H_0$ (see Fig. 4.5). Then, volume fraction is

$$\phi(N_{\rm p}) = \frac{d^3 N_{\rm sac}}{\left[A_{\rm LPS} + \delta A(N_{\rm p})\right] H_0(N_{\rm p})}, \tag{4.7}$$

where the denominator defines the volume of a cylindrically-confined chain in Fig. 4.5 and $H_0$ is the equilibrium height. Later (see Eg. 4.10), we explore its dependence to the brush grafting density $\sigma_{\rm g}$. As a result, $H_0$ is a function of number of adsorbed peptides on the LPS surface $N_{\rm p}$; the same trend of grafting density.

Towards constructing the LPS brush free energy, we need to obtain the equilibrium height, $H_0$ and the osmotic pressure $\Pi$ of our system. These parameters of polymer brushes have been investigated, numerously in theory and experiments, since 1980 [137, 138, 139, 140, 141]). One of the simple models to explain the brush behaviour and its characteristic height and pressure is to use Alexander de Gennes scale model. The details of this will be presented below.

### LPS Brush and Alexander de Gennes Blob Model

Scaling theory reduces the complexity of the polymer-solution problem, noticeably, and at the same time presents a simple physical picture. Therefore, we simply follow the Alexander de Gennes [137] model for a polymer brush and assume that the conformation

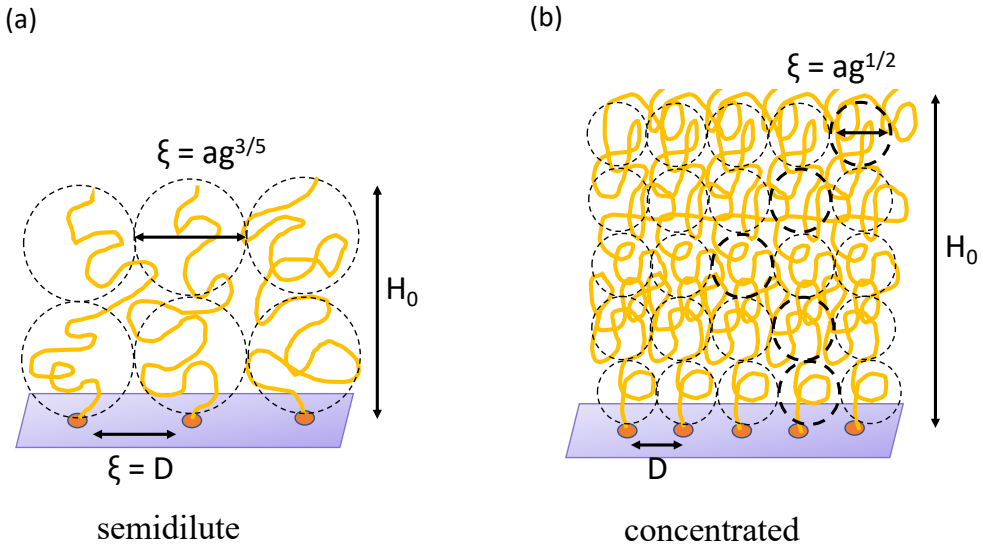


Figure 4.6: Representation of blob scaling in the Alexander de Gennes model for a polymer brush. Every blob has a correlation length of $\xi$, consisting of $g$ monomers. Balancing the stretching free energy and excluded volume interactions leads to an equilibrium height $H_0$. (a) Original blob scaling model in a semidilute regime, where chain statistics inside the blob follows the Flory exponent in a good solvent: $\nu = 3/5$. (b) Applications of the blob scaling model in a concentrated polymer regime, where monomers behave as a random walk ($\nu = 1/2$) inside each blob.

of polymer chains is linearly aligned, leading to densely-packed correlation blobs of size $\xi$, where the monomer concentration profile is a step-like function and all chains are uniformly extended.

In a semidilute regime, one expects polymer chains to highly overlap with one another; within some region, often referred to as a blob, chain statistics will not be influenced by the neighbouring chains, i.e., each polymer can claim its territory. In fact the possibility of other chain's monomer to sneak inside the blob is small. As a result of this, the conformational structure of monomers inside this blob is governed by $\xi \approx d\, g^{\nu}$ (i.e. on length scales of the blob size $\xi$, the chain statistics equals the statistics of chains in a dilute solution), where $g$ shows the number of monomers per blob and $\nu$ is the Flory exponent (in three dimensions). Here $g$ is adjusted by the requirement that the interaction within each blob is comparable to $k_{\mathrm{B}}T$.

At first, the Alexander de Gennes [137] blob model was introduced for a semidilute brush

regime in a good solvent, where Flory exponent is $\nu = 3/5$ and the blob correlation length scales to monomer as $\xi \approx d\, g^{3/5}$. However, during the last decade, experimental, computer simulation and modification to mean-field theory [142, 143, 144, 145] have demonstrated the potential use of Alexander blob model in different solvent quality and also different polymer concentration. For example, Merlitz et al. transferred the idea of correlation blobs to the brush in $\theta$-solvent and obtained a reasonable prediction for the nanoparticle inclusion free energy [145]; Halperin et al. [146] described collapsed blobs, $\xi_c$, in terms of Alexander model, in a poor solvent condition.

In the case of our bulky and dense saccharides of LPS brush, the polymer concentration is large (i.e. if we assume constant grafting density $\sigma_g \approx d^2/A_{\mathrm{LPS}} = 0.44$) and the brush is thus in a concentrated regime. We would then use the Alexander De Gennes model and define the correlation blob $\xi \approx d\, g^{1/2}$ in a melt polymer solution. Inside each blob, every chain behaves as a random walk for which the universal Flory exponent is $\nu = 1/2$ [84]. (In fact, a polymer chain is less swollen in a concentrated solution. In 1949, P. J. Flory won the 1974 Nobel Prize in Chemistry for predicting that a polymer melt, despite its apparent complexity, would act like a $\theta$-solvent for any individual polymer chain inside it, due to excluded-volume screening. A given polymer molecule 'sees' only a sea of identical monomers, and cannot tell whether those monomers come from within its own chain or from neighbouring chains. Therefore, every chain monomer has no particular preference to swell or shrink as if the polymer were in a $\theta$-solvent.)

Zooming into one blob, the dimensionless volume fraction of monomers inside the blob is $\phi = gd^3/\xi^3$ [146]. If we consider the number of monosaccharides of LPS brush in each blob is $g = (\xi/d)^2$, therefore the general relation between correlation length and volume fraction in a dense (close to a melt) concentration would be

$$\xi \approx d\phi^{-1}. \tag{4.8}$$

On the other hand, the Alexander model is required to set the free energy interaction within each blob to $k_{\mathrm{B}}T$, which leads to the free energy density, or osmotic pressure

$$\frac{\Pi(\phi)}{k_{\mathrm{B}}T} \approx 1/\xi^3 \approx \phi^3/d^3, \tag{4.9}$$

where the osmotic pressure of the brush is set by the excluded volume interactions between polymers. The experimental measurements of pressure [144, 145] point to a scaling power relation between the osmotic pressure and monomer volume fraction $\phi(\sigma_g)$, which itself depends on the brush grafting density. It has been shown that the dependence of osmotic pressure on the monomer volume fraction scales differently in various concentrations of

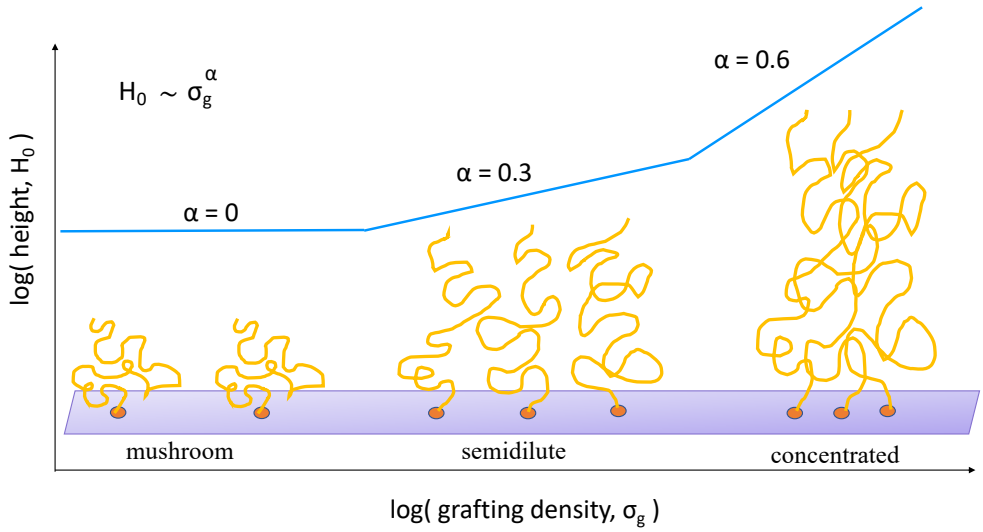


Figure 4.7: Equilibrium height $H_0$ vs. the brush grafting density at different polymer regimes in a good solvent. Polymers in the mushroom regime act as non-interaction isolated chains and their thickness is independent of grafting density ($H_0 = R_F$). Brushes in moderately or highly dense regimes, polymers stretch out of the grafting plane and their $H_0$ scale monotonically as the grafting density: $H_0 \approx \sigma_g^{0.3}$ and $H_0 \approx \sigma_g^{0.6}$ in the semidilute and concentrated regime, respectively. The figure is redrawn from Ref. [12] by permission from Dr. Losego

the polymer brush. For example in a semidilute regime, the osmotic pressure scales as $\Pi \propto \phi^{9/4}$, while in the concentrated solutions we have $\Pi \propto \phi^3$, due to higher excluded-volume interaction and finite extensibility of the brush [138, 143, 144, 147, 148]. This picture is consistent with the universal behaviour of the blob model and its relation to the osmotic pressure at different brush concentration.

In fact, modifying the classical mean-field theory and including the higher order of excluded volume in the dense regime compares favourably with the Alexander blob model; one could obtain the correct scaling law dependence between osmotic pressure $\Pi$ and the monomer volume fraction $\phi$ by defining an appropriate correlational length in a dense regime.

In the Alexander brush model, polymer chains are assumed uniformly stretched and their equilibrium end-to-end distance is equal to the brush thickness $H_0$. Theoretical studies of brush [137, 142] calculate brush equilibrium height by balancing excluded-volume

interactions and chain-elastic force. It is shown that polymer chains tend to get stretched-out away from the grafted plane due to excluded volume interactions between monomers, while their Gaussian elastic energy prefers the chains to collapse. Therefore $H_0$ depends on grafting density and also the quality of solvent [138, 145]. It is evident by experimental measurements [138] that increasing the grafting density $\sigma_g$ (i.e. packing polymer chains into the smaller area would intensify excluded-volume interactions) leads to a larger equilibrium height, which can be scaled by

$$H_0 \approx L\,\sigma_g^{\alpha}, \tag{4.10}$$

where $0 < \alpha < 1.3$ is the exponential scale factor and $L$ is the maximum length of the chain (i.e. in case of LPS brush, we use $\alpha = 0.6$ and $L = d\,N_{sac}$). Moh and Losego [138] provided detailed experimental studies for scaling trends of the equilibrium height $H_0$ in "moderately dense" and "high-density" grafting densities, using different solvent condition. In good solvent, their analysis of polymethyl methacrylate (PMMA) brushes demonstrate different scaling factor $\alpha = 1/3$ and $\alpha = 3/5$ for moderate ($0.05 < \sigma_g < 0.4$) and high grafting densities ($0.4 < \sigma_g < 0.7$). For very dense polymer brush, the scale exponent increases to $\alpha = 0.8 - 1.3$, when grafting density is very large $\sigma_g > 0.7$. These experimental results of Moh and Losego are well consistent with the theoretical works of Lai and Halperin [142] in dense brush regime. They have shown that in the dense grafting region average brush height asymptotically approaches $L$ as a linear function of the grafting density ($H_0 \sim \sigma_g^1$).

In addition, a close look at Merlitz et. al. [145] molecular dynamic simulation and their computation of forces acting on nanoparticles inside polymer brushes demonstrated that how temperature enhancement in $\theta$-solvent condition, where higher order of chain interactions becomes important, equilibrium thickness of brush $H_0$ extends farther and introduces larger exponent factor $\alpha = 0.51 - 0.6$. They also applied a Flory-Huggins mean-field model to their simulation results to confirm how higher-order contributions to the osmotic pressure lead to their observation.

### Alexander blob model & lack of finite extensibility

One might ask if the scaling power law predicted by the classical Gaussian free energy of a flexible polymer brush works well in the dense (concentrated) regime? Alexander de Gennes scaling model was obtained based on the assumption that equilibrium height ($H_0$) of polymer brush is a balance of Gaussian elastic free energy and binary excluded volume interaction. As a result, the concern is that for denser polymer brushes, (i) we must allow for interactions of higher order and (ii) the lack of finite length extensibility of Gaussian elastic free energy (i.e. in high grafting density, one expect that the brush height approaches the upper length limit, $H_{max} = d\,N_{sac}$).

In order to solve this problem, Shim et. al. [149] formulated an analytical self-consistent Field (SCF) theory of this regime, where the binary free energy density, $\sim \phi^2$ was replaced by full Flory-Huggins excluded volume interaction $(1-\phi)\log(1-\phi)$ and a denominator is introduced to the Gaussian quadratic elastic term to limit the extensibility. Inspired by Shim et. al. [149] study, Lai and Halperin [142] suggested a properly modified version of the Alexander analysis, which proved to be useful in the discussion of dense brushes. The recent detailed experimental analysis of polymer brushes in the moderately-dense and dense regime by Moh et. al. [138] have confirmed the scaling law behaviour of the modified Alexander blob model in highly grafted chain densities, where near full extension $H_0/H_{\max} > 0.7$, there is a linear scaling behaviour between brush thickness and the grafting density, $H_0 \approx \sigma_{\mathrm{g}}^1$.

According to the mentioned theoretical and experimental results, we could conclude that Alexander scaling blob model works well for all brush regime, as long as we introduce the correct correlational length scale for the system.

### Peptide's Inclusion Energy Cost into the Brush

It is well accepted by molecular dynamics [150, 151] and theoretical works [126, 152] of self-consistent field (SCF) theory, scaling arguments and mean-filed model, that the excess free energy required to include a nanoparticle (biological macromolecule) into an athermal polymer solution (i.e. a solution that intramolecular interactions other than steric may be neglected) is scaled to the peptide's excluded volume ($\Delta F \propto R_{\mathrm{p}}'^3$). However, recent theoretical studies [153, 154, 155] assumes to naturally split the excess free energy into the volume and surface terms, where the required work to create a cavity of volume $V_{\mathrm{p}}$ and the enforced tension on the peptide's surface are separated, and given by

$$\Delta F_{\mathrm{brush}} \sim \Pi(\phi) V_{\mathrm{p}} + \gamma(\phi) A_{\mathrm{p}}, \tag{4.11}$$

where $V_{\mathrm{p}}$ and $A_{\mathrm{p}}$ (i.e. not be mistaken by the peptide-induced expansion of the membrane $\mathcal{A}_{\mathrm{p}}$) are volume and area of the peptide. Recent publication of Gu et. al. [156] showed that; while for small nanoparticles, whose size is smaller than correlational blob size $\xi$, the excess free energy scales only to volume ($\Delta F \propto R_{\mathrm{p}}^3$), in case of large size nanoparticles and high polymer concentrations, the free energy of particle inclusion is expected to be approximated by the sum of both effects of volume and surface tension.

$\gamma(\phi)$ describes surface tension at the contact. Calculations of potential between pair nanoparticles near a planar wall and plane-induced surface tension [147, 153, 154]) revealed the importance of the surface tension due to polymer solution surrounding a nanoparticle.

In fact, the immersion of a nanoparticle inside a bath of non-adsorbing polymers reduces the number of configurations available to polymer chains and entropically induce a depletion layer around the particle [145, 147, 157]. Surface tension is given by [153, 154]

$$\gamma = -\Pi(\phi)\,\hat{\Gamma}(\phi) + \int_0^{\phi} \Pi(\phi')\frac{\partial\hat{\Gamma}(\phi')}{\partial\phi'}d\phi', \tag{4.12}$$

where $\Gamma$ is the "reduced adsorption" [153, 154] and measure the reduction in the number of chain segments near the surface. In fact, it can be identified to the change in monomer density, $h(z)$, near the depleted surface

$$\hat{\Gamma} = \int_0^{\infty} h(z)dz, \tag{4.13}$$

where in low-limit density, the reduced adsorption is independent of density and becomes $\hat{\Gamma}^{\mathrm{id}} = 2R_{\mathrm{g}}/\sqrt{\pi}$ for ideal polymers (i.e. $R_{\mathrm{g}}$ is gyration radius). However for our dense-brush system, ideal reduced-adsorption $\hat{\Gamma}^{\mathrm{id}}$ does not accurately compute the surface tension. On the scaling theory grounds, Louis et. al. [153] identifies blob size $\xi(z)$ to $-\hat{\Gamma}(z)$ and obtains [147, 153, 154]

$$\gamma(\phi) \sim \Pi^{2/3}. \tag{4.14}$$

While theoretical and experimental analysis of the interaction between the nanoparticle and the polymer-grafted surfaces in physiological environments emphasize the crucial role of steric effects for non-interacting brush polymer (athermal condition), there are evidence of weak attraction energy between adsorbed protein within the brush and its surrounding chain segments for a short range (mostly at contact). The theoretical works of protein partitioning behaviour in polymer-coated surfaces, based on observations of experimental studies with polyethylene glycol (PEG) and polyethylene oxide (PEO) brush, predicts the existence of a short-ranged attraction between polymer-protein segments (i.e. [126] and references in there).

Therefore for a comprehensive picture of the binding process of peptides to the brush-bearing surfaces, the inclusion of both repulsive excluded-volume and weak attractive interactions are necessary. The available information regarding polymer-protein attraction is limited; however, it is believed that the interaction's strength increases by protein/peptide size and analysis of experimental results predict the range of $\epsilon_{\mathrm{att}} = -(0.01 - 0.1)k_{\mathrm{B}}T$ per in-contact-monomer with protein's surface area [126, 158]. Following ref. [126], the overall weak attraction energy for a peptide inside the brush obtains by the number of monomer-peptide contacts times the attractive energy per contact $\approx \epsilon_{\mathrm{att}}\, N_{\mathrm{cont}}$. In Alexander scaling

model, $N_{\text{cont}}$ can be computed by the number of blobs that are in contacts with the surface area of the peptide ($A_{\text{p}}/\xi^2$) multiplies to the monomers inside of these blobs, which contribute to monomer-peptide contacts ($g^{\nu} \approx \xi/d$). Therefore, we define the weak attractive interaction between a peptide and the surrounding brush chains as

$$E_{\text{pep-brush}} = \frac{A_{\text{p}}\,\epsilon_{\text{att}}}{\xi\,d} \approx \frac{A_{\text{p}}\,\epsilon_{\text{att}}}{d^2}\,\phi, \tag{4.15}$$

where we used $\xi \approx d\phi^{-1}$.

Takes all the free energy contributions of excluded-volume, surface tension and weak peptide-brush interactions together, the total free energy cost for including one peptide within the LPS brush in primary and ternary adsorption are

$$\Delta F^{\text{pri}}_{\text{brush}} = \beta\left[\frac{\phi^3}{d^3}\,V^{\text{rod}}_{\text{p}} + \frac{\phi^2}{d^2}\,A^{\text{rod}}_{\text{p}} + \frac{\phi}{d^2}A^{\text{rod}}_{\text{p}}\,\epsilon_{\text{att}}\right], \tag{4.16}$$

and

$$\Delta F^{\text{ter}}_{\text{brush}} = \frac{\phi^3}{d^3}\,V^{\text{sph}}_{\text{p}} + \frac{\phi^2}{d^2}\,A^{\text{sph}}_{\text{p}} + \frac{\phi}{d^2}A^{\text{sph}}_{\text{p}}\,\epsilon_{\text{att}}. \tag{4.17}$$

Here, $\beta$ demonstrates the difference of brush free energy per peptide in different modes and $V_{\text{p}}$ and $A_{\text{p}}$ are the volume and surface area of the adsorbed peptides, respectively. Note that peptide's volume and surface area are different in primary and ternary adsorption; AMPs adopt spherical structure with an approximate radius $R_{\text{p}} \approx 0.8$ nm within the brush (i.e. for simplicity, we consider a hard sphere peptide with no contribution to the osmotic pressure of the brush) and undergo a secondary structure on the LPS surface and transfer to the alpha-helix. The alpha-helical peptide on the LPS surface is assumed as a cylindrical structure with surface area $\approx 2\pi r_{\text{p}}L_{\text{p}} + 2\pi r^2_{\text{p}}$ and volume $\approx \pi r^2_{\text{p}}L_{\text{p}}$. We chose fixed $r_{\text{p}} = 0.6$ nm and $L_{\text{p}} = 2.2$ nm for calculations [13, 58, 59]. . While volume and surface area of a coil-peptide within the brush of LPS can be assumed as a hard sphere (i.e. for simplicity, we consider a hard sphere peptide with no contribution to the osmotic pressure of the brush) with radius $R_{\text{p}} \approx 0.8$ nm, an alpha-helical peptide on the LPS surface has cylindrical surface area $\approx 2\pi r_{\text{p}}L_{\text{p}} + 2\pi r^2_{\text{p}}$ and volume $\approx \pi r^2_{\text{p}}L_{\text{p}}$. We chose fixed $r_{\text{p}} = 0.6$ nm and $L_{\text{p}} = 2.2$ nm for our calculations [13, 58, 59].

### 4.3.2 Ternary Adsorption Entropy, $F^{\text{ter}}_{\text{ent}}$

In contrast to primary adsorption, where peptides bind to a 2D planar surface and the associated entropy computes by the number of peptides' arrangements on the surface lattice, ternary adsorption takes place within a layer of finite thickness $H_0$ and the relevant

mixing entropy shall be expressed by volume fraction of the peptide within the brush

$$\phi_{\mathrm{p}}(N_{\mathrm{p}}) = \frac{V_{\mathrm{p}}^{\mathrm{sph}} N_{\mathrm{pB}}}{H_0(N_{\mathrm{p}})\left[A + \Delta A(N_{\mathrm{p}})\right]} \tag{4.18}$$

, where total volume depends on the number of primary adsorption $N_{\mathrm{p}}$ through the hydrophobic binding and peptide-induced lateral expansion of the membrane $\Delta A = \mathcal{A}_{\mathrm{p}} N_{\mathrm{p}}$. Remember that equilibrium height relates to $N_{\mathrm{p}}$ via peptide-dependent grafting density $\sigma_{\mathrm{g}}(N_{\mathrm{p}})$.

As a result mixing entropy of peptides and water molecules within the brush environment is given by

$$\frac{F_{\mathrm{ent}}^{\mathrm{ter}}}{H_0(N_{\mathrm{p}})\left[A + \Delta A(N_{\mathrm{p}})\right]} = \frac{\phi_{\mathrm{p}}}{V_{\mathrm{sph}}} \ln \phi_{\mathrm{p}} + (1 - \phi_{\mathrm{p}}) \ln (1 - \phi_{\mathrm{p}}) \tag{4.19}$$

### 4.3.3 Electrostatic Free Energy, $F_{\mathrm{el}}$

The many-body electrostatic energy calculations of bound cations and AMPs on the LPS surface, as well as the peptide-induced deformation of the membrane are all acquired through the binding-site construction. Following ref. [13, 58, 59], we assume the LPS surface as a 2D square lattice with total $N_0$ available electrostatic binding sites (i.e. discrete binding sites are necessary for electrostatic calculations in heterogeneous surface charge), which is four times larger than total number of LPS molecules (i.e. considering LPS Re, each LPS molecule carries four negative charges). Every anionic LPS unit charge is smeared out on the area of each binding site, known as $a_0^2$. A bound ion or peptide occupies the surface lattice sites depending on their charge valency. For instance, $Na^{1+}$ and $Mg^{2+}$ pairs with one and two sites, respectively, whereas a peptide carrying net $Q$ unit charges occupies $Q$ numbers of the backbone sites.

Moreover, all electrostatically-bound peptides on LPS surface are assumed to be inserted inside the acyl chain region, initially in a parallel orientation (i.e. for lower surface coverage than the threshold concentration $P/L^*$), and gain hydrophobic free energy, $\varepsilon_{\mathrm{I}}$ (i.e. for instance, cationic antimicrobial peptide magainin 2 obtains $\varepsilon_{\mathrm{I}} \approx -10 k_{\mathrm{B}}T$). This peptide-LPS hydrophobic association expands the original area of LPS surface [5, 46, 59] and perturb the lattice construction by adding $\Omega a_0^2$ area to the unperturbed membrane (i.e. experimental parameter of the expansion area per bound peptide $\mathcal{A}_{\mathrm{p}}$ is translated into the number of extended lattice sites. Note that this expansion is comparable to a lengthwise surface area of the peptide). As a result, the total lattice sites changes upon binding of peptides and would be equal to $\tilde{N}_0 = N_0 + \Omega N_{\mathrm{p}}$.

In our approach, the electrostatic free energy is a combination of several different interactions between charged particles on the surface. Following theoretical scheme of [13, 58, 59], heterogeneous charge distributions, resulting from the bound ions, peptides and anionic charges on the LPS surface, could be expressed as a linear superposition of its energy components

$$F_{\rm el}(N_1, N_2, N_{\rm p}) = F_{\rm self} + F_{\rm MF} + F_{\rm pair} + F_{\rm lat}. \tag{4.20}$$

First term is the self-energy difference of cations and peptides on the LPS surface with respect to their free energy in the bulk. Second term estimates discrete ion-paring process and the third free energy calculates mean field (MF) effect. The last term considers the lateral correlation between charged units on the surface beyond the MF calculation. It is responsible for non-uniform charge distribution on the surface. As a result of highly anionic charged surface of LPS and the existence of monovalent/divalent ions ($Na^{1+}$, $Mg^{2+}$) in addition to cationic peptides, the equilibrium configuration of charged particles is not homogenous and therefore we must calculate free energy of a non-uniform charged surface; $Mg^{2+}$-anion pairing (transverse interaction) both enhances divalent binding at a given site, and importantly invert the charge sign at the site (i.e. an overall-cationic $Mg^{2+}$-anion pair surrounded by possibly unpaired anionic LPS charges). The lateral or many-body interactions in the mean-field (MF) limit (continuum charge distribution) does not give an accurate electrostatic free energy of the system. It needs a correction, called lateral correlation [13, 58, 59].

**Electrostatics: Self-energy Difference**

The LPS surface is a borderline between low-dielectric medium of hydrophobic region ($\epsilon_{\rm oil} = 2$) and the high-dielectric water zone ($\epsilon_{\rm w} = 80$). This water-oil interface acts as a dielectric discontinuity interface and hinders free ions and peptides from binding on the LPS surface. Literature [8, 159, 160] shows that inner and outer layers of a lipid bilayer could be assumed de-coupled, electrically, in the limit of $\epsilon_{\rm w}\kappa d/\epsilon_{\rm oil} >> 1$, where $\epsilon$ is the medium dielectric constant and $d$ is the bilayer thickness. In this picture, a charged particle feels a strong repulsion (almost twice its own free energy) as it reaches the discontinue-dielectric interface due to surface charge polarization. We could capture this effect, using image charge method, using planar dielectric discontinuity constant [8, 159, 161]

$$\Delta_\epsilon = \frac{\epsilon_{\rm w} - \epsilon_{\rm oil}}{\epsilon_{\rm w} + \epsilon_{\rm oil}} \approx 1. \tag{4.21}$$

It is worth mentioning that our dielectric discontinuity constant is smaller by one unit from the corresponding constant in Refs. [13, 58, 59] ($\Delta_\epsilon = \Delta_{\rm ref} - 1$). Based on the above reasoning, we could express self energy difference of bound ions ($F_{\rm self-ion}$) and peptides ($F_{\rm self-p}$) on the dielectric-discontinued surface of the LPS with respect to their bulk free energies by

$$F_{\rm self} = F_{\rm self-ion} + F_{\rm self-p},$$

where

$$F_{\rm self-ion} = \sum_{i=1}^{2} N_{\rm i} \frac{Z_{\rm i}^2 \ell_{\rm B}}{2} \left[ \frac{\Delta_\epsilon}{\delta_{\rm i}} + \frac{\kappa}{1+\kappa r_{\rm i}} \right] \tag{4.22}$$

$$F_{\rm self-p} = N_{\rm p} \frac{Q \ell_{\rm B}}{2} \left[ \frac{\Delta_\epsilon}{\delta_{\rm p}} + \Delta_\epsilon \frac{\mathcal{M}_{\rm Q} - \mathcal{M}_1}{a^2} + \frac{\kappa}{1+\kappa r_1} \right]. \tag{4.23}$$

The Bjerrum length is $\ell_{\rm B} = e^2/4\pi\epsilon_{\rm r}\epsilon_0 k_{\rm B}T$, where $\epsilon_{\rm r} = \epsilon_{\rm w}$ is relative dielectric of the solution, $\epsilon_0$ the permittivity of free space and $e$ the electronic unit charge. The symbol $\kappa^2 = 4\pi\ell_{\rm B}[2n_1 + (2^2+2)n_2^2]$ [59, 162] stands for screening length in (1:1) and (2:1) salts in the solution, which the electrostatic interactions are exponentially screened beyond this length. The subscript "i" represents monovalent and divalent cations, where $Z_{\rm i}$ is the charge valency of $Na^{1+}$ and $Mg^{2+}$ with bulk-hydrated radius $r_1 = 3.4$ Åand $r_2 = 4.3$ Å, respectively. The parameter $Q$ shows net charge of the AMP in physiological condition (e.g. magainin 2 [59] has $Q = 4$; the peptide which we used its parameters for our calculations). The gab distance between ion/peptide charge and the dielectric interface as $\delta_1 = \delta_{\rm p} = 3$ Åand $\delta_2 = 2.5$ Å. Here $\mathcal{M}_\nu$ is given by [13, 58, 59]

$$\mathcal{M}_\nu(\kappa, a) = \int_{-a\nu/2}^{+a\nu/2} dx \int_{-a/2}^{+a/2} dy \frac{e^{-\kappa\sqrt{x^2+y^2}}}{x^2+y^2}. \tag{4.24}$$

First term in both relations of Eq. 4.22 and E. 4.23 estimates the required free energy to bring a cationic ion and the charged-segments of a peptide to the surface, respectively (it includes the image charge effect through $\Delta_\epsilon$), while the last term obtains the polarization effect; an electrostatic energy gain of a charged particle, as a result of charge shielding by the surrounding free ions in the electrolyte solution. Since peptide is consisted of $Q$ separate charges, we would have an extra contribution from the interaction between different charges on the same peptide. Second term in Eq. 4.23 calculates the difference in repulsion electrostatic energy among charged segments on the same peptide with reference to the bulk. Note that the over-counting electrostatic energy within each site of $a$ is subtracted by $\mathcal{M}_1$. (i.e. for detailed calculations refer to the Appendix of Ref. [13])

### Electrostatics: Mean Field Energy

If we ignore the heterogeneous charge distribution on the LPS surface resulting from ions/peptides binding in equilibrium condition, its electrostatic free energy could be expressed by smearing-out the net surface charge on the the total lattice sites (homogenous charge distribution). However, the self-energy of each site should be subtracted off to avoid over-counting (self energy is calculated by Eq. 4.22 and Eq. 4.23). This subtraction could be achieved by using integral relation $\mathcal{M}_1$, which gives the summation over one square lattice site. As a result, the mean field energy would be

$$F_{\rm MF} = \frac{\ell_{\rm B}(\Delta_\epsilon + 1)}{\tilde{N}_0 a_0^2}\left[\left(\frac{\pi}{\kappa} - \frac{\mathcal{M}_1}{2}\right)(N_0 - N_1 - 2N_2 - QN_{\rm p})^2 - \frac{(\mathcal{M}_{\rm Q} - \mathcal{M}_1)}{2} QN_{\rm p}(N_1 + 2N_2 + QN_{\rm p})\right]. \tag{4.25}$$

Even though Eq. 4.25 corrects double counting in self-energy through the subtraction of second term ($\mathcal{M}_1$), it needs another correction for considering the connectivity of $Q$ charges on the same peptide, which leads to an overestimation by overlap occupation between peptides and ions. For this reason, we have omitted the overlapped peptide-peptide and ion-peptide interactions through the third term. In general, this subtracted-off overlapped interactions in the third term of $F_{\rm MF}$ is a summation of both peptide-peptide $\frac{\mathcal{M}_{\rm Q}}{2}(QN_{\rm p})^2$ and ion-peptide $\frac{\mathcal{M}_{\rm Q}+\mathcal{M}_1}{2} QN_{\rm p}(N_1 + 2N_2)$ repulsions. The latter repulsive energy is an average between two modelling considerations; whether we smear out peptide or ions on the lattice sites. In addition, the image charge effect due to the water-lipid interface is captured by $\Delta_\epsilon$.

### Electrostatics: Ion-pair Interaction

The transverse interaction between cations and anionic charges of LPS surface, called ion-pair interaction, can readily be computed by

$$F_{\rm pair} = -\ell_{\rm B}(\Delta_\epsilon + 1)\left(\sum_{i=1}^{2} N_{\rm i}\frac{Z_{\rm i}}{\delta_{\rm i}} + N_{\rm p}\frac{Q}{\delta_{\rm p}}\right), \tag{4.26}$$

where $\delta$ shows distance between paired opposite charges and subscripts "i=1", "i=2", and "p" refer to $Na^+$, $Mg^{2+}$, and peptide, respectively. In Eq. 4.26, first term is cation-anion pair interaction and the second term is peptide-anion free energy, where peptide is polyvalent (Q) and each cationic residue is naturally assumed to be paired with one anionic charge of LPS surface. Note that these transverse interactions between ion(or peptide) and anionic charges are absent in Eq. 4.25. In fact mean-field transverse interactions are omitted in $F_{\rm MF}$ by $\mathcal{M}_1$ term to the obtain more accurate form of it by $F_{\rm pair}$.

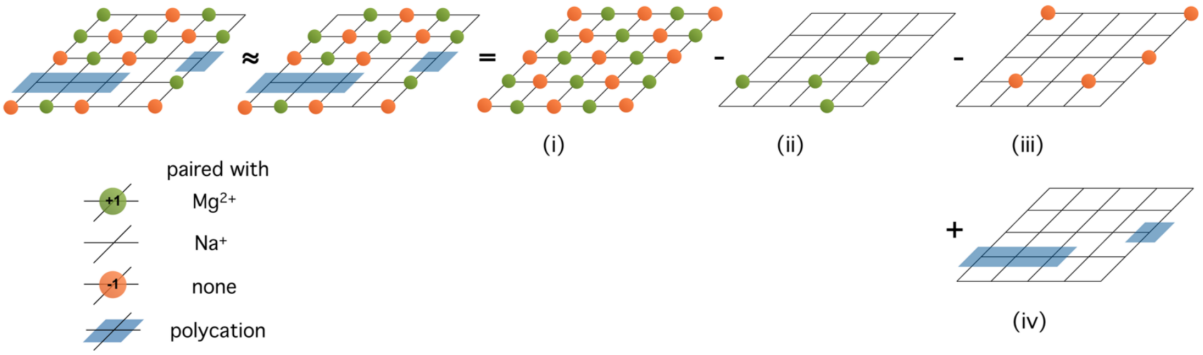


Figure 4.8: Theoretical model to calculate the lateral electrostatic free energy: the LPS lattice model decorated with $Na^+$, $Mg^{2+}$, and peptides. On the left, we rearrange charges on the reconstructed lattice, due to hydrophobically-bound peptides, which add $Q$ sites, into an energy-minimizing distribution in which the charges alternate in sign. We then use as a reference a perfect lattice shown in (i), where equal numbers of positive and negative charges are alternatively arranged. Then we remove some of the charges until the perfect lattice becomes the initial one and calculate the resulting free energy cost. Illustration is taken from Ref [13] by permission of Royal Society of Chemistry.

### Electrostatics: Lateral Correlation Beyond Mean-feild

As it was mentioned before, physiological concentration of divalent cations in the solution affects AMP bindings and leads to charge inhomogeneity on the LPS surface. Cation $Mg^{2+}$ binds to the backbone anions via transverse interaction and the paired bond inverts charge sign at the given site, while bound peptide and $Na^{1+}$ neutralize their local sites, and un-paired anionic backbone charges left some negative. As a result of this, the LPS surface charge distribution becomes non-uniform and therefore averaged approach in the mean-field energy calculations would not provide an accurate electrostatic lateral energy between charged particles on the surface.

In order to address this problem and achieve the lateral interaction beyond the mean-field level, we follow Refs. [13, 58, 59] and calculate free energy of a non-uniformly charged surface in equilibrium condition. In Fig. 4.8 we first, construct a perfect (homogenous) alternate-charge lattice sites on the LPS surface with positive and negative charges $N_+ = N_2$ and $N_- = \tilde{N}_0 - N_1 - N_2 - QN_\mathrm{p}$, respectively and then approximate the lateral correlation free energy (beyond mean-field) by computing the energy cost of removing $M = \tilde{N}_0 - N_+ - N_-$ charges, until the perfect lattice becomes non-uniform (the expected equilibrium

energy-minimized distribution)

$$F_{\text{later}}\tilde{N}_0 \approx \frac{\tilde{N}_0}{2}\Sigma_{\text{alt}} - M\Sigma_{\text{alt}} + \frac{2}{\tilde{N}_0}\left(\frac{\tilde{N}_0}{2} - N_+\right)\left(\frac{\tilde{N}_0}{2} - N_-\right)\Sigma_{\text{alt}} = 2\frac{N_+N_-}{\tilde{N}_0}\Sigma_{\text{alt}}. \quad (4.27)$$

$\Sigma_{\text{alt}}$ expresses electrostatic energy between one lattice site and the total rest of sites on an alternate-charged lattice and is given by [13, 58]

$$\Sigma_{\text{alt}} = -\ell_{\text{B}}(\Delta_\epsilon + 1)\,\frac{1}{2}\sum_{i=1}^{\infty}\sum_{j=1}^{i}(-1)^{i+j-1}\,\frac{e^{-\kappa a\sqrt{i^2+j^2}}}{a\sqrt{i^2+j^2}}k(i,j), \quad (4.28)$$

where $k(i,j)$ defines as

$$k(i,j) = \begin{cases} 4 & \text{if } j = 0 \text{ or } i = j \\ 8 & \text{otherwise} \end{cases}. \quad (4.29)$$

In Eq. 4.27, first term is the free energy of a perfect alternate-charged lattice sites, second term calculates energy of removing $M$ charges, and the third one correct our over-omitted interactions by the second term. In fact, $-M\Sigma_{\text{alt}}$ subtracts electrostatic energy between every removed charges and the rest of charges on a perfect alternate-charged lattice (no holes from already removed charges), while minimized charged configuration on the surface is not perfect and the subtracted term over-omitted interactions existed between the removed charges, themselves. Therefore, third term is introduced to correct this over-omitted energy (i.e. refer to the Appendix of Ref. [13] for more details).

It is worth noting that the over-omitted correction in $F_{\text{later}}$ is beyond the mean-field level and its mean-field contribution is considered in $F_{\text{MF}}$ (see Eq. 4.25). As a matter of fact, the $M$ removed charges are both positively and negatively charged (repulsion and attraction interactions) and therefore lateral over-omitted correction needs to be divided into two general forms: same-charge and opposite-charge correction. Since, the same-charged correction, is already included in our mean-field energy, $F_{\text{MF}}$, we only take into account opposite-charge correction in Eq. 4.27. On the other word, lateral correlation between surface-charge pairs (i.e. pairs between backbone anionic sites and cationic peptides, $Mg^{2+}$ and $Na^{1+}$) in the mean field level are calculated by the net surface charge density (or construction of a homogenous same-charge lattice sites), whereas opposite-charge lateral free energy of an alternate-charged lattice is estimated here by $F_{\text{later}}$. The lateral correlation is insignificant and can be ignored, if $N_+ << N_0/2$.

### 4.3.4 Deformation Energy, $E_{\text{def}}$

It is known that peptide hydrophobic energy gain on LPS surface comes with a free energy cost of LPS deformation; as a peptide binds hydrophobically to the LPS surface, it perturbs acyl chain packing order by pushing headgroups farther away and accommodates itself inside the hydrophobic region in a parallel orientation with the surface. [5, 46, 59] shows that this peptide-induced LPS perturbation is comparable to the one in phospholipid bilayers. Lipid bilayer experiments and theoretical [5, 46, 93] works explain how this membrane deformation is local, in case of small bound peptides $N_{\text{p}} << 1$, and be transformed into a many-body effect by increasing the peptide surface coverage. In fact, Huang group [5, 46, 55] beautifully relates this peptide-induced deformation to their cooperative membrane-rupture activity and the threshold peptide coverage (known as peptide-to-lipid threshold ratio $P/L^*$); every hydrophobically-associated peptide with membrane surface would distort the membrane, locally, however the growth number in bound peptides increases local deformations, until they overlap and creates macroscopic area expansion of the bilayer (i.e. in case of our LPS model, the expansion is $\Omega a_0^2$), which leads to membrane rupture. Indeed, the cooperative nature of peptide-induced area expansion of the membrane is responsible for the minimum required concentration of AMPs to start their pore-forming activity.

Assuming LPS bilayer and consider the bilayer coupling, in which the inner-layer resist stretching of the outer one, we could express a quantitive simple form for peptide-induced deformation energy on LPS surface. Consider that both inner and outer layer have similar elastic properties (i.e. accumulated into an experimentally-given quantity, known as area compression modulus $K_{\text{A}}$), then the stress caused by peptide insertion would be equally shared between the two layers. For a symmetric peptide binding on a LPS bilayer, energy associated with membrane deformation is given by [6, 59]

$$E_{\text{def}} = \frac{a_0^2}{2} K_{\text{A}} \frac{(\Omega N_{\text{p}})^2}{N_0}, \tag{4.30}$$

where $\Omega N_{\text{p}}$ is the number of extra sites due to peptide-induced membrane expansion. It is known that expansion area per peptide, $\Omega a_0^2$ is in general not the physical cross section of the peptide [46]. In fact, binding of a peptide would change the water-headgroup associated molecules on the membrane interface due to peptide condensation on the surface. It is usually called dehydration effect [5].

### 4.3.5 Primary Adsorption Entropy, $F_{\text{ent}}^{\text{pri}}$

The LPS surface is considered as discrete binding sites and the configurational entropy of charged ligands (peptide, $Na^{1+}$ and $Mg^{2+}$) on the surface can be readily obtained by the conventional mixing entropy [66, 84]; however, multivalent peptides on the LPS surface, assumed as charged rods, compete for their binding sites not only through electrostatic peptide-peptide repulsions but also through their area exclusion, which is a result of their multisite-binding characteristics. Indeed, theoretical studies show the significance of multivalent binding and the consequence area exclusion in decreasing the apparent binding affinity of nonionic objects [84, 163]. For simplicity, we do not consider area exclusion between small ions ($Na^{1+}$ and $Mg^{2+}$).

Area exclusion effect arises from short stretch of free sites ($< \Omega$) that can not accommodate a charged-rod peptide of length $\Omega$ (in unit of site length $a_0$). [163] explains how the shape of a surface ligand affects area exclusion effect and as a result the ultimate ligand coverage on the surface. For example, the effect is more pronounced for triangle or long rectangle than square or circle proteins and therefore rectangle-shaped proteins have lower saturated surface coverage than circle-shaped ones. It's important to note that in the low-concentration regime of adsorbed peptides (approximately surface coverage less than 0.1 [163]), area exclusion is not important and multisite-bound peptides have access to a large number of available binding sites on LPS surface.

As a result, the total entropy of bound ligands on LPS layer in primary adsorption mode is

$$\begin{aligned} F_{\text{ent}}^{\text{pri}} = &\sum_{i=1}^{2} N_{\text{i}} \ln\left(\frac{N_{\text{i}}}{\tilde{N}_0}\right) + N_{\text{p}} \ln\left(\frac{\Omega N_{\text{p}}}{\tilde{N}_0}\right) + (\tilde{N}_0 - N_1 - N_2 - \Omega N_{\text{p}}) \ln\left(1 - \frac{N_1 + N_2 + \Omega N_{\text{p}}}{\tilde{N}_0}\right) \\ &+ \frac{1-\Omega}{\Omega}(\tilde{N}_0 - \Omega N_{\text{p}}) \ln\left(1 - \frac{\Omega N_{\text{p}}}{\tilde{N}_0}\right) - N_{\text{p}}(\epsilon_{\text{Ex}} + 1) - \frac{\tilde{N}_0}{\Omega} \ln\left(1 - \frac{\Omega N_{\text{p}}}{\tilde{N}_0}\right) \\ &+ \frac{\tilde{N}_0 \epsilon_{\text{Ex}}}{\Omega(1 - \Omega N_{\text{p}}/\tilde{N}_0)}, \end{aligned} \tag{4.31}$$

where $\Omega$ is the number of sites every peptide occupies on the LPS surface and $\epsilon_{\text{Ex}} = \frac{(4+4/\Omega)^2}{16\pi/\Omega}$ defines shape parameter in the scaled theory. As explained in deformation energy section (4.3.4), the area per peptide on LPS surface is not necessarily equal to its physical surface area and could be smaller due to dehydration effect [5, 46]. In this work, we consider adsorbed surface area of peptide equal to its assigned valency and therefore the number of occupied sites by one peptide $\Omega = Q$.

In Eq. 4.31, the first four terms are related to the number of ways in which $\tilde{N}_0$ sites are occupied by $(N_1 + N_2)$ ions and $N_p$ peptides, and the last three ones express area exclusion effect of multisite-bound peptides given by Chatelier et al [163] adsorption isotherm analysis, using scaled particle theory and hard disk virial expansion.

## 4.4 Results & Discussion

### 4.4.1 Primary and Ternary Adsorption Isotherm

In order to investigate how the saccharide brush of the wild-type LPS might change peptide adsorption, we minimized the LPS brush free energy of Eq. 4.1 with respect to four parameters $N_1$,$N_2$,$N_p$ and $N_{pB}$ and calculated binding isotherms of peptides within the brush and on the LPS surface. The results are demonstrated in Fig. 4.9, Fig. 4.10, and Fig. 4.11, where $(a)_i$ and $(a)_{ii}$ shows the primary adsorption isotherm of peptides and divalent cations, respectively, and (b) expresses the secondary adsorption isotherm of peptides within the brush.

Our calculations show that the peptide adsorption (i.e. coverage on the surface or within the brush volume) enhances monotonically by increasing the available peptides in bulk (i.e. peptide concentration in solution [AMP]). However, divalent cation coverage on the surface $2Mg^{2+}/N_0$ decreases by the increase of [AMP]. This is evident by experimental observations [79, 164, 165] and previous theoretical modelling [13, 58, 59]. The binding competition between cationic $Mg^{2+}$ and peptides to electrostatically be adsorbed on the anionic LPS surface, causes lower $Mg^{2+}$-binding as peptide concentration increases. In fact, the presence of LPS-perturbing agents such as ethylenediaminetetraacetic acid (EDTA) and cationic AMPs would take away available LPS binding sites from $Mg^{2+}$.

In addition, comparison between LPS and LPS brush model (i.e. previous [59] and current coarse-grained modelling) helps to understand the physical influence of saccharide brush in the LPS layer of the bacterial OM. In Fig. 4.9, Fig. 4.10, and Fig. 4.11 $(a)_i$ exhibits how surface coverage of peptides that hydrophobically and electrostatically are bound on the LPS surface $QN_p/N_0$, reduces as a result of grafted saccharide chains on the LPS surface. The reduced amount of adsorption between two models of LPS brush and LPS i.e. solid and dashed lines respectively, is $\sim 30\%$. It is consistent with recent experimental measurements of the reduced surface coverage of peptide ColN on LPS Rd in comparison with the Ra chemo type [62]. Moreover, ternary adsorption in Fig. 4.9, Fig. 4.10, and Fig. 4.11 (b) demonstrates very low peptide adsorption within the brush. It is natural

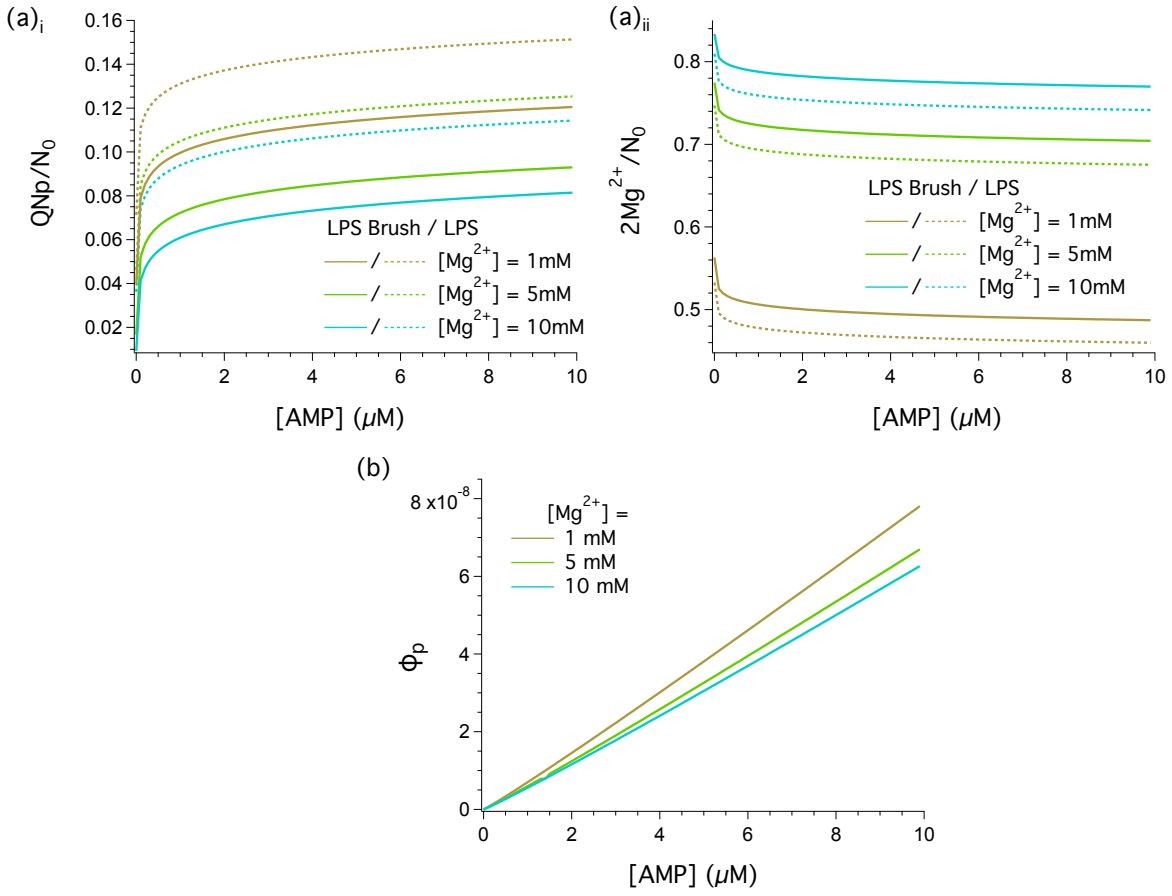


Figure 4.9: Adsorption isotherm of peptides and $Mg^{2+}$ in primary and ternary binding modes (i.e. graph (a) and (b) respectively). $(a)_i$ and $(a)_{ii}$ shows the calculated peptide and $Mg^{2+}$ surface coverage on the LPS surface, due to hydrophobic and electrostatic interactions, respectively, while (b) represents the peptide volume fraction within the brush as a function of total available peptide concentrations in the bulk [AMP]. Our results show how the presence of uncharged saccharide chains on top of the LPS surface reduces the amount of hydrophobically-bound peptides on the grafted interface in $(a)_i$. On the other hand, changing divalent cation concentration $[Mg^{2+}]$ would alter both primary and ternary adsorption. Higher $Mg^{2+}$ concentration leads to lower peptide adsorption. Curves are obtained for fixed cell density $C_t = 10^5$ cells/mL, salt concentration $[Na^{1+}]$= 100 mM, brush-peptide attraction $\epsilon_{att} = -0.05$, and brush chain length with repeating unit of O-antigen $n_r$=15.

to have small volume fraction of peptides $\phi_p$ within bulky saccharide chains, due to the unfavourable brush osmotic pressure and surface tension, especially at low cell-density limit.

### Divalent cationic concentration $[Mg^{2+}]$

The relation between divalent cation concentration in the bulk $[Mg^{2+}]$ and peptide adsorption is investigated in Fig. 4.9. We observe that the growth in $Mg^{2+}$ concentration would reduce the number of peptides in both primary and ternary adsorption (i.e. please see $(a)_i$ and (b)). As $[Mg^{2+}]$ increases, the occupancy of AMPs on the LPS surface decrease. At larger $[Mg^{2+}]$, more peptide concentration in bulk is required to displace divalent ions from the LPS layer.

As we are expecting that the change in $[Mg^{2+}]$ influences peptide primary adsorption on the surface due to their electrostatic competition, why does divalent concentration affect the adsorbed peptides within the brush in ternary adsorption in Fig. 4.9 (b) (i.e. remember that our brush free energy does not influence small ions)? The answer is hidden in hydrophobic-dependent grafting density $\sigma_g(N_p)$. The lower peptide adsorption on the LPS surface $N_p$ (primary adsorption) by increasing the $[Mg^{2+}]$ leads to larger grafting density and therefore higher osmotic pressure of the brush, which hinders the ternary adsorption of peptides within the brush.

### Brush-peptide attraction $\epsilon_{att}$

In order to observe how the weak brush-peptide attraction plays a role in our brush free energy and the resulting peptide adsorption, we have changed the brush-peptide attraction in Fig. 4.10. The parameter $\epsilon_{att}$ varies between $-0.01\ k_BT$ to $-0.1\ k_BT$ per in-contact-monomer interaction with the peptide's surface area (i.e. depending on the protein, $\epsilon_{att}$ changes. Halperin et. al. [126, 158] shows that it is mostly varies between $-0.01$ to $-0.1\ k_BT$ for a small number of proteins in contacts with PEG). Fig. 4.10 shows that both the peptide surface coverage and volume fraction within the brush in primary and ternary adsorption increases very gradually by enhancing brush-peptide attraction. Halperin et al in his theoretical adsorption model of proteins to the brush-bearing surface [126] shows that it is important to include this weak brush-peptide attraction, especially in case of long brush chains. However, it seems that this attractive energy does not play a significant role in our LPS-peptide-ion system, where the hydrophobic-electrostatic-bound peptides on the LPS interface is highly favourable and peptides tends to primarily be adsorbed on the surface.

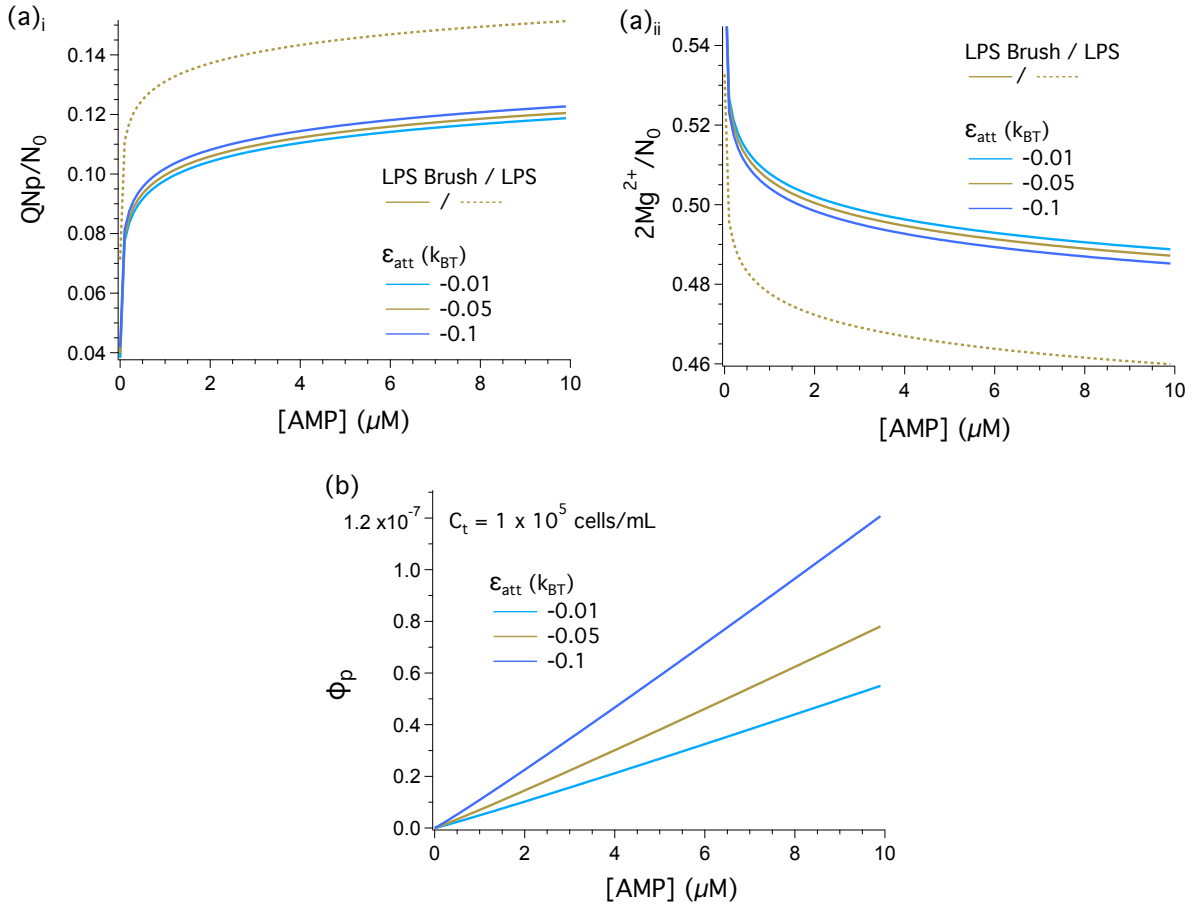


Figure 4.10: Adsorption isotherm of peptides and $Mg^{2+}$ in primary and ternary binding modes (i.e. graph (a) and (b) respectively). $(a)_i$ and $(a)_{ii}$ shows the peptide and $Mg^{2+}$ surface coverage on the LPS surface, due to hydrophobic and electrostatic interactions, respectively, while (b) presents the peptide volume fraction within the brush as a function of the total available peptide concentration in the bulk [AMP]. We note how introducing uncharged saccharide chains on top of the LPS surface would reduce the amount of hydrophobically-bound peptides on the grafted interface in $(a)_i$. Altering the weak brush-peptide attraction would change both primary and ternary adsorption. Larger attraction energy $\epsilon_{att}$ leads to higher peptide adsorption both within the brush and on the surface. Curves are obtained for fixed cell density $C_t = 10^5$ cells/mL, salt concentration $[Na^{1+}]$= 100 mM, divalent cation concentration $[Mg^{2+}] = 1$ mM, and brush chain length with repeating unit of O-antigen $n_r$=15.

**Brush length: O-antigen repeat unit $n_{\mathrm{r}}$**

Brush-length dependency of the free energy cost of including a nano-particle into a brush thickness was examined by coarse-grained simulation of Gu et. al. [156]. They measured free energy of the nanoparticle bindings in different polymer lengths and demonstrates that the free energy is independent of the number of the chain's monomer and hence thickness of the grafted polymers. This result is consistent with theory; self-consistent field (SCF) calculations of the polymer-protein system also shows that the number of chain's monomers factors out of the free energy [156].

On the other hand, the polymer thickness is important when we analyze protein adsorption to the brush. In case of the peptide ternary adsorption within the brush, the mixing entropy takes place in 3D volume with thickness of equilibrium height $H_0$ and therefore peptide adsorption depends on the number of chain's monomers (i.e. note that volume fraction of peptides $V_{\mathrm{p}}\, N_{\mathrm{pB}}/(H_0 \cdot A)$ remains constant by the brush length). As a result, we investigated brush-length dependency of our peptide adsorption isotherm in Fig. 4.11. Results in (b) shows that the number density of adsorbed peptides within the brush ($N_{\mathrm{pB}}/A$) increases noticeably, by increasing the number of repeat unit of O-antigen ($n_{\mathrm{r}}$) of LPS molecule (i.e. higher height provides larger number of available sites for peptides to bind within the brush).

Fig. 4.11 (b) shows that the peptide adsorption within the brush (ternary mode) monotonically increases, as we increase the brush length. This enhancement of the peptides ternary adsorption by the brush thickness ($H_0$), is relatively large, as expected, and the surface density $N_{\mathrm{pB}}/A$ changes an order of magnitude by increasing O-antigen repeat unit $n_{\mathrm{r}}$ from 15 to 50. In contrast, the peptide ($Mg^{2+}$) primary adsorption on the LPS surface remains constant, as the total number of chains' monomers increases. One might think that in a canonical ensemble i.e. if the total number of available peptides in bulk $V\, C_{\mathrm{p}}$ remains fixed, we would have lower bound peptides on the LPS (primary) surface as the number of adsorbed peptides within the brush (ternary) increases by the brush length. However, it is not the case here; since the total number of peptides trapped within the brush is very small in comparison to the bound peptides on the surface, and therefore does not affect primarily adsorption.

## 4.5 Conclusion

Here, the role of uncharged polysaccharide chains of LPS layer of the bacterial OM in their interaction with AMPs was investigated. We extended a recently developed peptide-

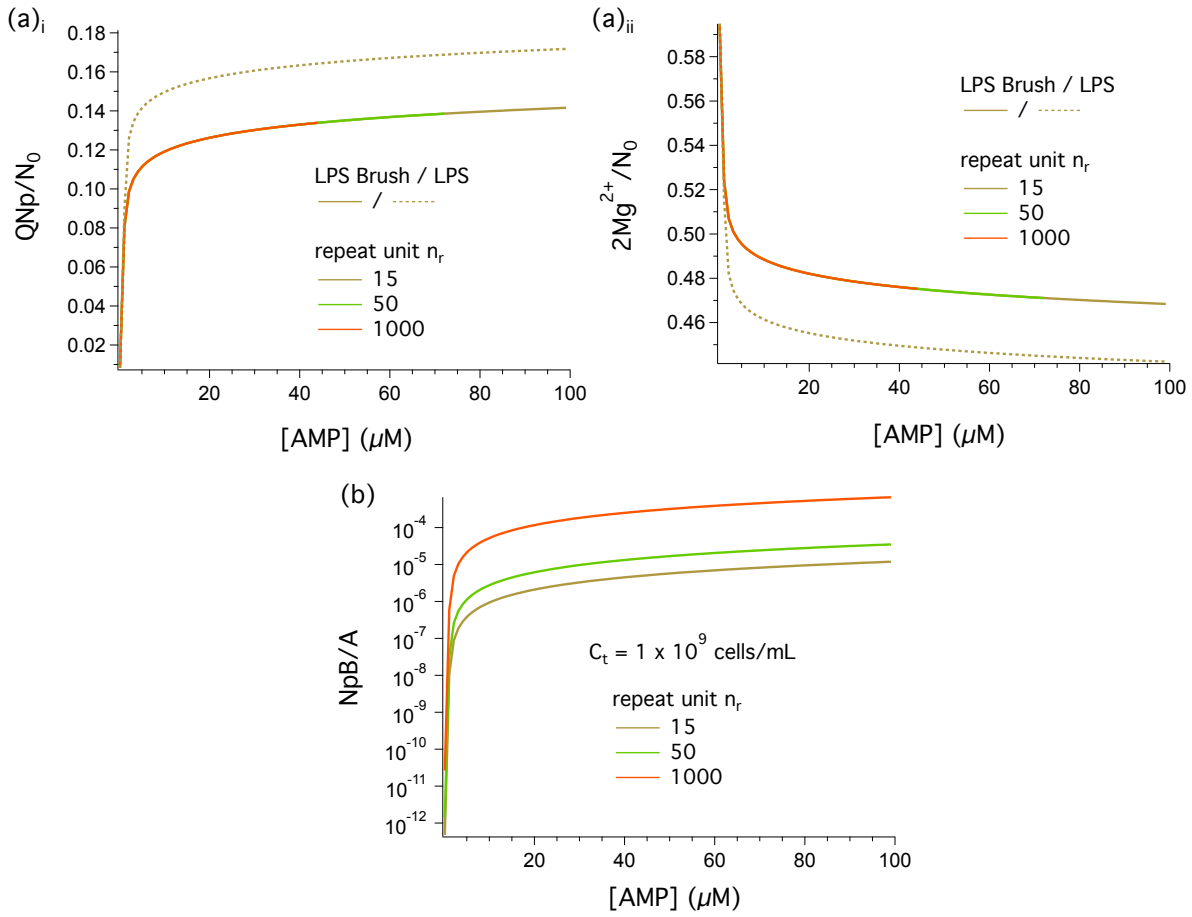


Figure 4.11: Adsorption isotherm of peptides and $Mg^{2+}$ in primary and ternary binding modes (i.e. graph (a) and (b) respectively). $(a)_i$ and $(a)_{ii}$ shows peptide and $Mg^{2+}$ surface coverage on the LPS surface, due to hydrophobic and electrostatic interactions, respectively, while (b) demonstrates peptide surface density (number over surface area) within the brush as a function of total available peptide concentrations in the bulk [AMP]. The results in this figure show how the presence of uncharged saccharide chains on top of the LPS surface would reduce the amount of hydrophobically-bound peptides on the grafted interface in $(a)_i$. Altering the brush length by increasing the repeat unit of O-antigen $n_r$ would increase peptide adsorption within the brush by providing more binding sites. However, primary adsorption is independent of brush thickness, due to very low adsorption within the brush comparing to the adsorbed peptides on LPS surface ($N_{pB} << N_p$). Curves are obtained for fixed cell density $C_t = 10^9$ cells/mL, salt concentration $[Na^{1+}]$= 100 mM, divalent cation concentration $[Mg^{2+}] = 1$ mM, and brush-peptide attraction $\epsilon_{att} = -0.05$.

ion-LPS model [59], where the authors provided detailed computations of the peptide interactions with charged headgroups of the Ra LPS chemotype, to a theoretical consideration of the wild-type LPS. We derived free energy of our LPS brush model by a non-trivial generalization of an earlier coarse-grained model [59], and captured the physical effects of oligosaccharide and O-antigen chains by modelling the LPS layer as forming a polymer brush on top of its anionic phosphate groups.

To this end, we introduced two modes for peptide adsorption (Fig. 4.1), known as primary and ternary [126, 127] adsorption. The total number of adsorbed peptides on LPS brush was set by two processes; (i) $N_{\rm p}$ peptides bind to the anionic LPS inner core (i.e. referred by LPS surface), in primary adsorption, and (ii) $N_{\rm pB}$ peptides become captive within the brush, in ternary adsorption. The chemical potentials of primary and ternary adsorption of peptides and ions were balanced with their corresponding chemical potentials in the bulk, while the total number of available peptides are constants (i.e. canonical ensemble).

Our results demonstrate that the presence of LPS brush reduces the number of hydrophobically bound peptides on surface, compared to the deep-rough LPS which lacks a saccharide brush. The reduced amount of adsorption between two models of LPS brush and LPS is $\sim 30\%$, which is consistent with experimental measurements of the surface coverage of peptide ColN on LPS Rd and Ra chemo types [62]. This effect is mainly due to the steric barrier of the brush and polymer excluded-volume effect, which imposes unfavourable free energy to the hydrophobically-bound peptides on LPS interface. In fact, the hydrophobically-inserted peptide on the LPS surface needs more free energy to succeed brush-induced osmotic pressure and creates a volume inside of this dense polysaccharide environment. we also note that the total number of peptides trapped within the brush is very small, compared to the number of bound peptides on the LPS interface. This implies that the hydrophobic binding of peptides is insensitive to brush lengths. This, however, does not exclude the possibility of kinetic slowing-down of the binding.

In order to provide more realistic picture of the interaction between AMPs and wild-type LPS, one might use the current work but assuming the trapped peptides within the brush as a random coil, which contributes to the brush osmotic pressure by their volume fraction $\phi_{\rm p}$ i.e. here, we presented the ternary adsorbed peptides as a small spherical structure. The result of a random coil peptide within the brush is that the excess free energy of the peptide $\Delta F_{\rm brush}$ would depend on the total adsorbed peptides within the brush $N_{\rm pB}$ (i.e. in our current model, the inclusion free energy of peptide is independent of $N_{\rm pB}$). This excess free energy per peptide can be obtained by $\Delta F_{\rm brush} \approx (\phi + \phi_{\rm p})^3 - \phi^3$, where numerical prefactors are omitted.

## 4.6 Mathematica Script

### 4.6.1 Minimization of The LPS Brush Free Energy

```
Clear["Global`*"]
Clear[xp, xpB]

(*————————————————————————Variables ————————————————————————*)

NA = 6.023 10^23;          (*Avogadro's number*)
V = 10^(+24);    (*Total volume 1L to nm^3*)
conv = NA 10^(-6) 10^(-24);      (*convert microMolar to molecules/nm^3*)
convMg = 0.602 10^(-3); (*conver miliMolar to molecules/nm^3*)
convCt = 10^(-21);       (*cells/mL to cells/nm^3*)
lB = 0.7;          (*Bjerrum Length (nm)*)
aLPS = 1.66;     (*cross sectional area of LPS (nm)^2*)
a0 = 0.644;      (*Site length (nm)*)
a = 0.64;
Q = 4;  (*Peptide's charge number*)
KA = 240/4.414; (*LPS is 120 pN/nm and also 1kbT = 4.114 pN/nm*)
n1mol = 0.1;     (*Salt concentration in Molar unit*)
n1 = n1mol 0.602;          (*Salt concentration in molecule/nm^3*)
del1 = 0.3;      (*Gap between ion and lipid interface (nm)*)
del2 = 0.25;      (*Gap between divalent ion and lipid interface (nm)*)
delp = 0.4;       (*Gap between peptide and lipid interface (nm)*)
r1 = 0.34;       (*hydrated radius monovalent (nm)*)
r2 = 0.43;       (*hydrated radius divalent (nm)*)
v1 = 4/3*Pi*(r1)^3;      (*free ion volume (nm)^3*)
v2 = 4/3*Pi*(r2)^3;      (*free ion volume (nm)^3*)
esp = 25/4/Pi;  (*Shape parameter for excluded volume entropy*)
H = -10;         (*Hydrophobic energy magainin 2 *)
Ab = 2 6 10^(-12) 10^18;          (*Area of Negative-gram bacteria nm^2*)


(*————————————— Peptide's Properties: magainin 2————————————————*)

Npp = 23;          (*number of amino acids*)
```

```
dp = 0.35;       (*diameter of amino acids (nm)*)
vpp = 4/3*Pi*(dp/2)^3; (*volume of every monomer amino acids (nm^3)*)
Q = 4;  (*peptide charge*)
vpHlx = Pi 0.6^2 2.2;   (* cylinder volume alpha helical magainin(nm^3)*)
ApHlx = 2 Pi 0.6 2.2 + 2 Pi 0.6^2;  (* cylinder area alpha helical magainin
vp = 2.5;        (*volume of free peptide coil (nm)^3*)
Rff = dp Npp^(1/2);      (*Flory radius inside dense regime (nm)*)
vpCoil = (4/3) Pi (Rff/2)^3;     (*volume of magainin coil inside brush*)
ApCoil = 4 Pi (Rff/2)^2;         (*area of magainin coil inside brush*)


(*=============================================================*)
(*Which results do we want?
1- varying [Mg]?
2- varying Brush-pep attraction?
3- varying area per chain?
4- varying LPS chain's length?
5- varying cell density?

The one we examine should be equal to 1 and the rest zero *)

Mg = 0;
BpAtt = 0;
area = 0;
chain = 1;
cell = 0;

(*------------Free Parameters*)
(* depending on the examining parameter, we comment below:
for example, if we examining the chain, nr =15 should be commented *)
n2 = 1 convMg;           (* Mg2+ concentration in molecule/nm^3*)

EpepB = -0.05;  (*Pep-Brush weak attraction (kbT)*)
S = 4;          (*number of sites every single brush chain occupies*)
nr=15;          (*repeat unit of O-antigen in wild LPS*)
Rp = CubeRoot[(3/4/Pi) vp]; (*radius of sphere-peptide within brush*)
npmol=1000 10^(-6); (*peptide concentration in Molar*)
np=npmol 0.602; (*peptide concentration in molecule/nm^3*)
```

```
Ct = 1 10^11 convCt;     (*number of total cells in mL*)


(*----------------------Constants Depends on n2----------------------*)

kp[n2_] =
  Sqrt[4 Pi lB (2 n1 + (2^2 + 2) n2) ]; (*inverse Debye length (nm)*)

Dell[n2_] =
  2 (1/40 + kp[n2] 40)/(2/40 +
     kp[n2] 40);        (*Dielectric discontinuity*)

(*------------------------ Brush Properties ----------------------*)

vpSph[Rp_] = (4/3) Pi Rp^3; (*volume of sphere-magainin within brush*)

ApSph[Rp_] = 4 Pi Rp^2; (*area of sphere-magainin within brush*)

alpha = 0.6; (*exponent scale, relation btw. hight and grafting density*)

db = 0.85; (*diameter of every monosaccharide unit (nm)*)

vb = db^3;(*monomer volume fraction nm^3*)

Nb[nr_] = 4 nr + 8 + 4; (*monomer number units of lipopolysaccharide*)

Ach[S_, xp_] = S a^2 (1 + Q xp);  (*area per brush chain*)

sigmaB[S_, xp_] = db^2/Ach[S, xp]; (*Grafting density*)

H0[S_, nr_, xp_] = Nb[nr] db sigmaB[S, xp]^ alpha; (*equilibrium height*)

phiB0[S_, xp_] = sigmaB[S, xp]^(1 - alpha);
(*dimensionless brush monomer volume fraction*)

phipB[S_, nr_, Rp_, xp_, xpB_] =
(vpSph[Rp] xpB)/(H0[S, nr, xp] a^2 (1 + Q xp));
(*dimensionless peptide volume fraction within brush*)
```

```
(*=============================================================================*)
(*Free energy components ———— per number of sites (energy/N0)*)

M1[n2_] =
  NIntegrate[
   Exp[-kp[n2] Sqrt[x^2 + y^2]]/Sqrt[x^2 + y^2], {x, -a/2,
    a/2}, {y, -a/2, a/2}];
Mp[n2_] =
  NIntegrate[
   Exp[-kp[n2] Sqrt[x^2 + y^2]]/Sqrt[x^2 + y^2], {x, -Q a /2,
    Q a/2}, {y, -a/2, a/2}];

Fmean[n2_, x1_, x2_,
   xp_ ] = -lB Dell[n2] (Mp[n2] - M1[n2])/
     2  Q xp (x1 + 2 x2 + Q xp)/(1 + Q xp)/a^2 +
   lB Dell[n2] (
     Pi/kp[n2] - M1[n2]/2) (1 - x1 - 2 x2 - Q xp)^2/(a^2 (1 + Q xp));

Entro[n2_, x1_, x2_, xp_ ] =
  x1 Log[x1/(1 + Q xp)/(n1 v1)] + x2 Log[x2/(1 + Q xp)/(n2 v2)] +
   xp Log[Q xp/(1 + Q xp)] + (1 + Q xp - x1 - x2 - Q xp) Log[
     1 - (x1 + x2 + Q xp)/(1 + Q xp)] + (1 - Q)/
     Q  (1 + Q xp - Q xp) Log[1 - Q xp/(1 + Q xp)] - xp (esp + 1) -
   1/Q  (1 + Q xp) Log[
     1 - Q xp/(1 + Q xp)] + ((1 + Q xp)/Q) esp/(1 - Q xp/(1 + Q xp));

Fbulk[n2_, x1_, x2_, xp_ ] =
  x1 lB (Dell[n2] - 1)/2/del1 + x1 lB kp[n2]/(1 + kp[n2] r1)/2 +
   x2 2^2 lB (Dell[n2] - 1)/2/del2 +
   x2 2^2 lB kp[n2]/(1 + kp[n2] r2)/2 +
   xp Q  lB (Dell[n2] - 1) (1/delp + (Mp[n2] - M1[n2])/a^2)/2 +
   xp Q  lB kp[n2]/(1 + kp[n2] r1)/2;

sum[n2_] =
  Sum[1/2 (-1)^(i + j -
        1) Exp[-kp[n2] a Sqrt[i^2 + j^2]]/(a Sqrt[i^2 + j^2] ) 8, {i,
```

```
    1, 10}, {j, 0, i}] -
  Sum[1/2 (-1)^(i - 1) Exp[-kp[n2] a i]/(a i) 4, {i, 1, 10}] -
  Sum[1/2 (-1)^(i + i -
       1) Exp[-kp[n2] a Sqrt[2] i]/(a Sqrt[2] i) 4, {i, 1, 10}];

Flateral[n2_, x1_, x2_,
  xp_] = -lB Dell[
   n2] 2 x2 (1 + Q  xp - x1 - x2 - Q xp)/(1 + Q xp)  sum[n2];

Ftrans[n2_, x1_, x2_, xp_] = -lB  Dell[n2]  x1/del1 -
  lB Dell[n2] 2 x2/del2  - lB  Dell[n2] Q xp/delp;

(*--------------------Brush Energy*)

FBrushS[S_, EpepB_,
  xp_] = (xp /2) (phiB0[S, xp]^3/vb vpHlx +
    phiB0[S, xp]^2/vb^(2/3) ApHlx +
    phiB0[S, xp]/vb^(2/3) ApHlx EpepB);

FBrush [S_, EpepB_, xpB_, xp_, Rp_] =
 xpB (phiB0[S, xp]^3/vb vpSph[Rp] +
    phiB0[S, xp]/vb^(2/3) ApSph[Rp] EpepB +
    phiB0[S, xp]^2/vb^(2/3) ApSph[Rp]);

EntB[S_, nr_, Rp_, xpB_, xp_] =
 xpB Log[phipB[S, nr, Rp, xp, xpB]] + (H0[S, nr, xp] a^2 (1 + Q xp) -
      vpSph[Rp] xpB) Log[1 - phipB[S, nr, Rp, xp, xpB]];


EntFreeP1 [np_, xp_, Ct_] =
 1/(Ct V) (((np V a^2)/Ab - Ct V xp) Log[
      vp (np - (Ab/a^2) Ct xp)] - ((np V a^2)/Ab - Ct V xp));

EntFreeP [np_, xp_, xpB_, Ct_] =
 1/(Ct V) (((np V a^2)/Ab - Ct V (xp + xpB)) Log[
      vp (np - (Ab/a^2) Ct (xp + xpB))] - ((np V a^2)/Ab -
      Ct V (xp + xpB)));
```

```
(*-------------------------Total Free Energy-------------------------------*)
(*--------LPS--------*)

Ftotal1[np_, n2_, x1_, x2_, xp_, Ct_] =
  Entro[n2, x1, x2, xp ] + Fmean[n2, x1, x2, xp ] +
   Flateral[n2, x1, x2, xp] + Ftrans[n2, x1, x2, xp] +
   Fbulk[n2, x1, x2, xp] + H xp + a^2 KA (Q xp)^2/2 +
   EntFreeP1 [np, xp, Ct];

(*----LPS + Brush----------*)

Ftotal2[S_, nr_, EpepB_, np_, n2_, x1_, x2_, xp_, xpB_, Rp_, Ct_] =
  Entro[n2, x1, x2, xp ] + Fmean[n2, x1, x2, xp ] +
   Flateral[n2, x1, x2, xp] + Ftrans[n2, x1, x2, xp] +
   Fbulk[n2, x1, x2, xp] + H xp + a^2 KA (Q xp)^2/2 +
   FBrushS [S, EpepB, xp] + FBrush [S, EpepB, xpB, xp, Rp] +
   EntB [S, nr, Rp, xpB, xp] + EntFreeP [np, xp, xpB, Ct];



(*=======Save minimized parameters in a table=============================*)
(*----------------------Adsorption vs. Cp (Smart model)*)
If[Mg == 1,
 LPS = Table[{np/conv,
    sol = FindMinimum[{Ftotal1[np, n2, x1, x2, xp, Ct],
       x1 < 1 && 2 x2 < 1 && Q xp < 1 }, {{x1, 0.2}, {x2, 0.1}, {xp,
        0.001}}];
    Q xp /. sol[[2]], 2 x2 /. sol[[2]]},
   {np, 0.001 conv, 10 conv,
    0.1 conv}, {n2, {1 convMg, 5 convMg, 10 convMg}}];

 (*-----------------Adsorption vs. Cp (Brush model)----------*)
 (*-------Changing n2[Mg2+]*)

 LPSbrush =
  Table[  {np/conv ,
    sol = FindMinimum[{Ftotal2[S, nr, EpepB, np, n2, x1, x2, xp, xpB,
       Rp, Ct],
```

```
        x1 < 1 && 2 x2 < 1 && Q xp < 1 &&
         phipB[S, nr, Rp, xp, xpB] < 1}, {{x1, 0.2}, {x2, 0.1}, {xp,
         0.001}, {xpB, 0.0000001}}];
    Q xp /. sol[[2]], phipB[S, nr, Rp, xp, xpB] /. sol[[2]],
    2 x2 /. sol[[2]] }, {np, 0.001 conv, 10 conv,
    0.1 conv}, {n2, {1 convMg, 5 convMg, 10 convMg}}];

(*----------plot---*)

plot1 = ListPlot[{Labeled[LPS[[;;  , 1, 2]], "NoB Mg=1mM"],
    Labeled[LPS[[;;  , 2, 2]], "NoB [Mg]=5mM"],
    Labeled[LPS[[;;  , 3, 2]], "NoB [Mg]=10mM"]
    , Labeled[LPSbrush[[;;  , 1, 2]], "[Mg]=1mM"],
    Labeled[LPSbrush[[;;  , 2, 2]], "[Mg]=5mM"],
    Labeled[LPSbrush[[;;  , 3, 2]], "[Mg]=10mM"]},
   AxesLabel -> {"[AMP]microM", "QNp/N0"}];

plot2 = ListPlot[{Labeled[LPS[[;;  , 1, 3]], "NoB Mg=1"],
    Labeled[LPS[[;;  , 2, 3]], "NoB Mg=5"],
    Labeled[LPS[[;;  , 3, 3]], "NoB Mg=10"],
    Labeled[LPSbrush[[;;  , 1, 4]], "Mg=1"],
    Labeled[LPSbrush[[;;  , 2, 4]], "Mg=5"],
    Labeled[LPSbrush[[;;  , 3, 4]], "Mg=10"]},
   AxesLabel -> {"[AMP]microM", "2Mg2+/N0"}];

plot3 = ListPlot[{Labeled[LPSbrush[[;;  , 1, 3]], "Mg=1"],
    Labeled[LPSbrush[[;;  , 2, 3]], "Mg=5"],
    Labeled[LPSbrush[[;;  , 3, 3]], "Mg=10"]},
   AxesLabel -> {"[AMP]microM", "vpNpB/(H0.A)"}];
]

(*-------------------------fixed [Mg]=1mM-------------------------------*)
If[Mg == 0,
 LPS1mM =
   Table[{np/conv,
     sol = FindMinimum[{Ftotal1[np, n2, x1, x2, xp, Ct],
        x1 < 1 && 2 x2 < 1 && Q xp < 1 }, {{x1, 0.2}, {x2, 0.1}, {xp,
         0.001}}];
```

```
     Q xp /. sol[[2]], 2 x2 /. sol[[2]]},
    {np, 100 conv, 350 conv, 5 conv}];
 ]

(*------Changing EpepB(brush-pep att.)*)
If[BpAtt == 1,
 LPSbrush =
  Table[  {np/conv ,
    sol = FindMinimum[{Ftotal2[S, nr, EpepB, np, n2, x1, x2, xp, xpB,
        Rp, Ct],
       x1 < 1 && 2 x2 < 1 && Q xp < 1 &&
        phipB[S, nr, Rp, xp, xpB] < 1}, {{x1, 0.2}, {x2, 0.1}, {xp,
        0.001}, {xpB, 0.00001}}];
    Q xp /. sol[[2]], phipB[S, nr, Rp, xp, xpB] /. sol[[2]],
    2 x2 /. sol[[2]] }, {np, 0.001 conv, 10 conv,
    0.1 conv}, {EpepB, {-0.01, -0.05, -0.1}}];

 (*----Plot-------*)

 plot1 = ListPlot[{Labeled[LPS1mM[[;;  , 2]], "No Brush"],
    Labeled[LPSbrush[[;;  , 1, 2]], "pep-B=-0.01"],
    Labeled[LPSbrush[[;;  , 2, 2]], "pep-B=-0.05"],
    Labeled[LPSbrush[[;;  , 3, 2]], "pep-B=-0.1"]},
   AxesLabel -> {"[AMP]microM", "QNp/N0"}];

 plot2 = ListPlot[{Labeled[LPS1mM[[;;  , 3]], "No Brush"],
    Labeled[LPSbrush[[;;  , 1, 4]], "pep-B=-0.01"],
    Labeled[LPSbrush[[;;  , 2, 4]], "pep-B=-0.05"],
    Labeled[LPSbrush[[;;  , 3, 4]], "epp-B=-0.1"]},
   AxesLabel -> {"[AMP]microM", "2Mg2+/N0"}];

 plot3 = ListPlot[{Labeled[LPSbrush[[;;  , 1, 3]], "pep-B=-0.01"],
    Labeled[LPSbrush[[;;  , 2, 3]], "pep-B=-0.05"],
    Labeled[LPSbrush[[;;  , 3, 3]], "pep-B=-0.1"]},
   AxesLabel -> {"[AMP]microM", "vpNpB/(H0.A)"}];
 ]

(*----------Changing S(area)*)
```

```
If[area == 1,
 LPSbrush =
  Table[  {np/conv ,
    sol = FindMinimum[{Ftotal2[S, nr, EpepB, np, n2, x1, x2, xp, xpB,
        Rp, Ct],
       x1 < 1 && 2 x2 < 1 && Q xp < 1 &&
        phipB[S, nr, Rp, xp, xpB] < 1}, {{x1, 0.2}, {x2, 0.1}, {xp,
        0.001}, {xpB, 0.00001}}];
    Q xp /. sol[[2]], phipB[S, nr, Rp, xp, xpB] /. sol[[2]],
    2 x2 /. sol[[2]] }, {np, 0.001 conv, 10 conv,
    0.1 conv}, {S, {4, 7, 10}}];

 (*--------plot-----*)

 plot1 = ListPlot[{Labeled[LPS1mM[[;;  , 2]], "No Brush"],
    Labeled[LPSbrush[[;;  , 1, 2]], "S=4"],
    Labeled[LPSbrush[[;;  , 2, 2]], "S=7"],
    Labeled[LPSbrush[[;;  , 3, 2]], "S=10"]},
   AxesLabel -> {"[AMP]microM", "QNp/N0"}];

 plot2 = ListPlot[{Labeled[LPS1mM[[;;  , 3]], "No Brush"],
    Labeled[LPSbrush[[;;  , 1, 4]], "S=4"],
    Labeled[LPSbrush[[;;  , 2, 4]], "S=7"],
    Labeled[LPSbrush[[;;  , 3, 4]], "S=10"]},
   AxesLabel -> {"[AMP]microM", "2Mg2+/N0"}];

 plot3 = ListPlot[{Labeled[LPSbrush[[;;  , 1, 3]], "S=4"],
    Labeled[LPSbrush[[;;  , 2, 3]], "S=7"],
    Labeled[LPSbrush[[;;  , 3, 3]], "S=10"]},
   AxesLabel -> {"[AMP]microM", "vpNpB/(H0.A)"}];
 ]

(*-------Changing nr(chain length)*)
If[chain == 1,
 LPSbrush =
  Table[  {np/conv ,
    sol = FindMinimum[{Ftotal2[S, nr, EpepB, np, n2, x1, x2, xp, xpB,
        Rp, Ct],
```

```
        x1 < 1 && 2 x2 < 1 && Q xp < 1 &&
         phipB[S, nr, Rp, xp, xpB] < 1}, {{x1, 0.2}, {x2, 0.1}, {xp,
         0.001}, {xpB, 0.01}}];
    Q xp /. sol[[2]], xpB/ (a^2 (1 + Q xp)) /. sol[[2]],
    2 x2 /. sol[[2]] }, {np, 100 conv, 350 conv,
    5 conv}, {nr, {15, 1000, 10000, 100000}}];

(*------plot----------*)

plot1 = ListPlot[{Labeled[LPS1mM[[;;, 2]], "No Brush"],
   Labeled[LPSbrush[[;;, 1, 2]], "N=15"],
   Labeled[LPSbrush[[;;, 2, 2]], "N=50"],
   Labeled[LPSbrush[[;;, 3, 2]], "N=1000"],
   Labeled[LPSbrush[[;;, 4, 2]], "N=10000"]},
  AxesLabel -> {"[AMP]microM", "QNp/N0"}];

plot2 = ListPlot[{Labeled[LPS1mM[[;;, 3]], "No Brush"],
   Labeled[LPSbrush[[;;, 1, 4]], "N=15"],
   Labeled[LPSbrush[[;;, 2, 4]], "N=50"],
   Labeled[LPSbrush[[;;, 3, 4]], "N=1000"],
   Labeled[LPSbrush[[;;, 4, 4]], "N=10000"]},
  AxesLabel -> {"[AMP]microM", "2Mg2+/N0"}];

plot3 = ListPlot[{LPSbrush[[;;, 1, 3]], LPSbrush[[;;, 2, 3]],
   LPSbrush[[;;, 3, 3]], LPSbrush[[;;, 4, 3]]},
  AxesLabel -> {"[AMP]microM", "vpNpB/(H0.A)"},
  PlotLegends -> {"N=15", "N=50", "N=1000", "N=10000"}];
 ]

(*-------Changing cell density *)
If[cell == 1,
 LPSbrush =
  Table[ {nr ,
    sol = FindMinimum[{Ftotal2[S, nr, EpepB, np, n2, x1, x2, xp, xpB,
        Rp, Ct],
       x1 < 1 && 2 x2 < 1 && Q xp < 1 &&
        phipB[S, nr, Rp, xp, xpB] < 1}, {{x1, 0.2}, {x2, 0.1}, {xp,
        0.001}, {xpB, 0.0001}}];
```

```
    Q xp /. sol[[2]], phipB[S, nr, Rp, xp, xpB] /. sol[[2]],
    2 x2 /. sol[[2]] }, {nr, 10 , 100000,
    1000}, {Ct, {10^5 convCt, 10^8 convCt, 10^11 convCt,
     10^13 convCt}}];

(*------plot----------*)

plot1 = ListPlot[{Labeled[LPSbrush[[;; , 1, 2]], "cell=5"],
    Labeled[LPSbrush[[;; , 2, 2]], "N=8"],
    Labeled[LPSbrush[[;; , 3, 2]], "N=11"],
    Labeled[LPSbrush[[;; , 4, 2]], "N=13"]},
   AxesLabel -> {"N", "QNp/N0"}];

plot2 = ListPlot[{Labeled[LPSbrush[[;; , 1, 4]], "cell=5"],
    Labeled[LPSbrush[[;; , 2, 4]], "N=8"],
    Labeled[LPSbrush[[;; , 3, 4]], "N=11"],
    Labeled[LPSbrush[[;; , 4, 4]], "N=13"]},
   AxesLabel -> {"N", "2Mg2+/N0"}];

plot3 = ListPlot[{LPSbrush[[;; , 1, 3]], LPSbrush[[;; , 2, 3]],
    LPSbrush[[;; , 3, 3]], LPSbrush[[;; , 4, 3]]},
   AxesLabel -> {"N", "vpNpB/(H0.A)"},
   PlotLegends -> {"cell=5", "N=8", "N=11", "N=13"}];
]

(*----------Exporting data as a table format----------*)

Export["LPSBrush_chain_HighDensity11", LPSbrush, "Table"];
Export["LPS_chainHighDensity11", LPS1mM, "Table"];

plot1
plot2
plot3
```

# Chapter 5

# Conclusion & Proposal

This thesis dedicated to the biophysical investigation of the interactions between AMPs and different lipid membranes (e.g. neutral, charged and polymer-grafted) in relevant physiological conditions of cell density and divalent cationic concentrations. In particular, we proposed two finely-tuned coarse-gained models, which one described the cell-density-dependent selectivity of the peptides in their interactions with lipid bilayers of mixed PE/PG and pure PC, and the second model examined the physical influence of polymer-grafted chains of the oligosaccharide/O-antigen of a wild-type LPS in the peptide adsorption process. The general conclusions of our peptide-lipid and peptide-LPS-brush models are presented in section 5.1 and a proposal for future work is explained in section 5.2.

## 5.1 Conclusion

In chapter 1.4, we presented a physical model of the cell selectivity of AMPs, accounting for simultaneous theoretical challenges of several competing effects; such as lipid demixing and peptide-peptide interactions. To this end, we have systematically analyzed several models and singled out one, which described accurately the electrostatic binding of peptides to a membrane, whether charged or neutral. This critical examination of various models of peptide-membrane interactions, which incorporated adequately mentioned competing effects as well as the geometry of various regions in membranes, occupied by bound peptides, anionic lipids within the interaction range of each peptide, and those outside this range, leads to a systematically-improved model for peptide selectivity. Using this improved model, we related peptide's intrinsic ($C_{cell}$-independent) selectivity to an apparent,

$C_{cell}$-dependent one, and clarified the relative roles of peptide parameters and cell densities in determining their selectivity.

A general picture from this work is that peptide selectivity remains sensitive to peptide parameters (e.g., charge and hydrophobicity) at the low-cell density limit, but becomes less sensitive outside this limit. As a result, the optimal peptide charge, at which the selectivity is maximized, is cell-density-dependent: it increases and eventually becomes irrelevant as the cell density increases. This means that optimization of peptide selectivity should reflect the biological setting of infected sites as it determines the number of cells and peptides, $N_{cell}$ and $N_p$, respectively. In general, this coarse-grained model of AMPs selectivity enables us to map out intrinsic selectivity from apparent (Ccell-dependent) one or biologically-relevant one from "conveniently-measured" selectivity. This effort will benefit our endeavour in optimizing the peptide parameters for their enhanced selectivity in a physiological environment.

Furthermore, in chapter 4 we examined peptide adsorption on the outer membrane (OM) of Gram-negative bacteria and in particular, the interaction between AMPs and a wild-type lipopolysaccharide (LPS) layer in a biologically relevant medium (i.e. containing monovalent and divalent salt ions like $Mg^{2+}$). The physical coarse-grained models of peptide-ions-LPS had been introduced, recently [13, 58, 59], though the physical effect of oligosaccharide and O-antigen chains of the wild-type LPS molecules was not examined. To this end, we introduced two modes for peptide adsorption (Fig. 4.1), known as primary and ternary [126, 127] adsorption. The total number of adsorbed peptides on LPS brush was set by two processes; (i) $N_p$ peptides bind to the anionic LPS inner core (i.e. referred by LPS surface), in primary adsorption, and (ii) $N_{pB}$ peptides become captive within the brush, in ternary adsorption. The chemical potentials of primary and ternary adsorption of peptides and ions were balanced with their corresponding chemical potentials in the bulk, while the total number of available peptides kept constants (i.e. canonical ensemble).

Our model quantitatively assessed the protection role of saccharide brush in an LPS layer and demonstrates how core oligosaccharide and O-antigen part of wild-type LPS reduced the number of adsorbed membrane-lytic peptides. Our results demonstrate that the presence of the saccharide brush reduces the number of hydrophobically-bound peptides to the polymer-grafted interface of LPS, compared to the deep-rough LPS layer that lacks the polymer brush. Our LPS brush model predicts $\sim 30\%$ reduction of peptide adsorption, which is consistent with recent experimental measurements. This can be attributed to the steric hindrance of the brush or the excluded-volume interaction of the saccharide chains with peptides. At a low cell density limit, we also note that the total number of peptides trapped within the brush is very small, compared to the number of bound peptides on the LPS interface. This implies that the hydrophobic binding of peptides is insensitive to the

brush length. This, however, does not exclude the possibility of kinetic slowing-down of the binding.

In conclusion, a combined effort between experiments and theoretical modelling will benefit our endeavour in searching for potent peptide antibiotics. Indeed, bacteria have developed strategies to counteract the action of AMPs, for instance, by reducing the surface charge density on their membrane [16]. How will this influence peptide selectivity and how should the peptide parameters be adjusted to restore the selectivity? The use of predictive models together with available data (e.g., those for $P/L^*$ and $C_{cell}$) will be useful for identifying the peptide parameters for their enhanced activity under different conditions (e.g., diminished surface charge density and different salinity).

Our coarse-grained modelling of the thermodynamic equilibrium condition of the peptide-membrane system could reproduce experimental data for a broad set of target cell densities and predict thermodynamic properties of the system by using the given structural parameters (e.g. $P/L^*$ and $A_p$). In particular, this predictive model has a practical application in peptide-based antibacterial products, e.g. hydrogel, soap and capsule, for fine-tuning of the employed antibiotic concentration [166]. Besides, compared with molecular dynamic (MD), a semi-analytical coarse-grained model provides increased computational efficiency at sufficient levels of accuracy. It is infeasible to simulate more than a few hundreds of cells by MD, while a wide range of target cell density can be captured easily by our semi-analytical model.

## 5.2 Proposal

In chapter 1.4, despite of our successful mapped-out Langmuir model for AMP cell-density-dependent selectivity, which perfectly explained the monotonic correlation between selectivity and cell density (i.e. with a plateau region for relatively small cell densities) and reduced the complex sets of involved physiochemical parameters into two general quantities of effective binding energy per peptide $W^*$ and threshold concentration $P/L^*$, It will be desirable to mimic the biological setting in theoretical considerations beyond the recent effort.

Experiments with live E. coli cells indicate the importance of another factor in our Langmuir model of cell-density-dependent selectivity of AMPs: the trapping of peptides in dead cells [116]. Unlike lipid vesicle membranes, cellular components (e.g., chromosomes) can attract cationic peptides. As a result, the density of peptides can be much larger inside a cell than outside. In our approach, this can be mimicked by adjusting the slope of a curve representing Eq. 3.37 or Eq. 3.34. The modification can be as

$$C_{\mathrm{p}}^{*}(C_{\mathrm{cell}}) = \left[\frac{A_{\mathrm{cell}}}{a_{\ell}}\left(\frac{P}{L}\right)^{*} + N_{\mathrm{trap}}\right] C_{\mathrm{cell}} + C_{\mathrm{p}}^{*}(0). \tag{5.1}$$

Also the '$y$' intercept, i.e., $C_{\mathrm{p}}^{*}(0)$, is either MIC or MHC in the single-cell limit; it is related to $W^{*}$ as indicated by Eq. 3.37: $C_{\mathrm{p}}^{*}(0) = \frac{1}{v_{\mathrm{p}}} \cdot \frac{A_{\mathrm{p}}}{a_{\ell}} \frac{P^{*}}{L} / (1 - \frac{A_{\mathrm{p}}}{a_{\ell}} \frac{P^{*}}{L}) \cdot e^{W^{*}/k_{\mathrm{B}}T}$. Eq. 5.1 can serve as a fitting model for MIC or MHC data. For instance, the values of $N_{\mathrm{trap}}$ and $W^{*}$ can be extracted. It can then be used to estimate peptide selectivity in a biologically relevant range of $C_{\mathrm{cell}}$, once the selectivity is measured at conveniently chosen cell densities.

# References


[1] David Boal. *Mechanics of the Cell*. Cambridge University Press, 2 edition, 2012.

[2] Guangshun Wang. *Antimicrobial peptides: Discovery, design, and novel therapeutic strategies*. CABI Publishing, 11 2010.

[3] Sattar Taheri-Araghi. Membrane-disrupting activity of antimicrobial peptides and the electrostatic bending of membranes. 2010.

[4] F. Savini, V. Luca, A. Bocedi, R. Massoud, Y. Park, M. L. Mangoni, and L. Stella. Cell-Density Dependence of Host-Defense Peptide Activity and Selectivity in the Presence of Host Cells. *ACS Chem. Biol.*, 12(1):52–56, 01 2017.

[5] M. T. Lee, W. C. Hung, F. Y. Chen, and H. W. Huang. Many-body effect of antimicrobial peptides: on the correlation between lipid's spontaneous curvature and pore formation. *Biophys. J.*, 89(6):4006–4016, Dec 2005.

[6] A. Bagheri, S. Taheri-Araghi, and B. Y. Ha. How Cell Concentrations Are Implicated in Cell Selectivity of Antimicrobial Peptides. *Langmuir*, 31(29):8052–8062, Jul 2015.

[7] S. Alexander, P. M. Chaikin, P. Grant, G. J. Morales, P. Pincus, and D. Hone. Charge renormalization, osmostic pressure, and bulk modulus of colloidal crystals: Theory. *Journal of Chemical Physics*, 80(11):5776–5781, 1984.

[8] S. Taheri-Araghi and B. Y. Ha. Charge renormalization and inversion of a highly charged lipid bilayer: effects of dielectric discontinuities and charge correlations. *Phys Rev E Stat Nonlin Soft Matter Phys*, 72(2 Pt 1):021508, Aug 2005.

[9] Sattar Taheri-Araghi and Bae-Yeun Ha. Cationic antimicrobial peptides: a physical basis for their selective membrane-disrupting activity. *Soft Matter*, 6:1933–1940, 2010.

[10] A. Halperin. Polymer brushes that resist adsorption of model proteins: design parameters. *Langmuir*, 15(7):2525–2533, 1999.

[11] M. T. Lee, W. C. Hung, F. Y. Chen, and H. W. Huang. Mechanism and kinetics of pore formation in membranes by water-soluble amphipathic peptides. *Proc. Natl. Acad. Sci. U.S.A.*, 105(13):5087–5092, Apr 2008.

[12] This figure is redrawn from research group website of Prof.Losego in the School of Materials Science and Engineering at the Georgia Institute of Technology.

[13] N. H. Lam, Z. Ma, and B. Y. Ha. Electrostatic modification of the lipopolysaccharide layer: competing effects of divalent cations and polycationic or polyanionic molecules. *Soft Matter*, 10(38):7528–7544, Oct 2014.

[14] Jackson J. D. Classical electromagnetism. 1975.

[15] Y. J. Gordon, E. G. Romanowski, and A. M. McDermott. A review of antimicrobial peptides and their therapeutic potential as anti-infective drugs. *Curr. Eye Res.*, 30(7):505–515, Jul 2005.

[16] M. Zasloff. Antimicrobial peptides of multicellular organisms. *Nature*, 415(6870):389–395, Jan 2002.

[17] L. Gentilucci, A. Tolomelli, and F. Squassabia. Peptides and peptidomimetics in medicine, surgery and biotechnology. *Curr. Med. Chem.*, 13(20):2449–2466, 2006.

[18] K. A. Brogden. Antimicrobial peptides: pore formers or metabolic inhibitors in bacteria? *Nat. Rev. Microbiol.*, 3(3):238–250, Mar 2005.

[19] Y. Ge, D. L. MacDonald, K. J. Holroyd, C. Thornsberry, H. Wexler, and M. Zasloff. In vitro antibacterial properties of pexiganan, an analog of magainin. *Antimicrob. Agents Chemother.*, 43(4):782–788, Apr 1999.

[20] D. A. Steinberg, M. A. Hurst, C. A. Fujii, A. H. Kung, J. F. Ho, F. C. Cheng, D. J. Loury, and J. C. Fiddes. Protegrin-1: a broad-spectrum, rapidly microbicidal peptide with in vivo activity. *Antimicrob. Agents Chemother.*, 41(8):1738–1742, Aug 1997.

[21] L. Zhang, J. Parente, S. M. Harris, D. E. Woods, R. E. Hancock, and T. J. Falla. Antimicrobial peptide therapeutics for cystic fibrosis. *Antimicrob. Agents Chemother.*, 49(7):2921–2927, Jul 2005.

[22] R. E. Hancock. Antibacterial peptides and the outer membranes of gram-negative bacilli. *J. Med. Microbiol.*, 46(1):1–3, Jan 1997.

[23] R. F. Epand, B. P. Mowery, S. E. Lee, S. S. Stahl, R. I. Lehrer, S. H. Gellman, and R. M. Epand. Dual mechanism of bacterial lethality for a cationic sequence-random copolymer that mimics host-defense antimicrobial peptides. *J. Mol. Biol.*, 379(1):38–50, May 2008.

[24] A. Giacometti, O. Cirioni, R. Ghiselli, L. Goffi, F. Mocchegiani, A. Riva, G. Scalise, and V. Saba. Polycationic peptides as prophylactic agents against methicillin-susceptible or methicillin-resistant Staphylococcus epidermidis vascular graft infection. *Antimicrob. Agents Chemother.*, 44(12):3306–3309, Dec 2000.

[25] A. J. De Lucca, J. M. Bland, T. J. Jacks, C. Grimm, T. E. Cleveland, and T. J. Walsh. Fungicidal activity of cecropin A. *Antimicrob. Agents Chemother.*, 41(2):481–483, Feb 1997.

[26] A. J. De Lucca and T. J. Walsh. Antifungal peptides: novel therapeutic compounds against emerging pathogens. *Antimicrob. Agents Chemother.*, 43(1):1–11, Jan 1999.

[27] B. Deslouches and Y. P. Di. Antimicrobial peptides with selective antitumor mechanisms: prospect for anticancer applications. *Oncotarget*, 8(28):46635–46651, Jul 2017.

[28] R. J. Boohaker, M. W. Lee, P. Vishnubhotla, J. M. Perez, and A. R. Khaled. The use of therapeutic peptides to target and to kill cancer cells. *Curr. Med. Chem.*, 19(22):3794–3804, 2012.

[29] R. B. Arrighi, C. Nakamura, J. Miyake, H. Hurd, and J. G. Burgess. Design and activity of antimicrobial peptides against sporogonic-stage parasites causing murine malarias. *Antimicrob. Agents Chemother.*, 46(7):2104–2110, Jul 2002.

[30] A. Dagan, L. Efron, L. Gaidukov, A. Mor, and H. Ginsburg. In vitro antiplasmodium effects of dermaseptin S4 derivatives. *Antimicrob. Agents Chemother.*, 46(4):1059–1066, Apr 2002.

[31] A. Stintzi, T. Heitz, V. Prasad, S. Wiedemann-Merdinoglu, S. Kauffmann, P. Geoffroy, M. Legrand, and B. Fritig. Plant 'pathogenesis-related' proteins and their role in defense against pathogens. *Biochimie*, 75(8):687–706, 1993.

[32] M. Zasloff. Magainins, a class of antimicrobial peptides from Xenopus skin: isolation, characterization of two active forms, and partial cDNA sequence of a precursor. *Proc. Natl. Acad. Sci. U.S.A.*, 84(15):5449–5453, Aug 1987.

[33] H. Steiner, D. Hultmark, A. Engstrom, H. Bennich, and H. G. Boman. Sequence and specificity of two antibacterial proteins involved in insect immunity. *Nature*, 292(5820):246–248, Jul 1981.

[34] C. Zhao, T. Ganz, and R. I. Lehrer. The structure of porcine protegrin genes. *FEBS Lett.*, 368(2):197–202, Jul 1995.

[35] K. Matsuzaki. Control of cell selectivity of antimicrobial peptides. *Biochim. Biophys. Acta*, 1788(8):1687–1692, Aug 2009.

[36] Z. Jiang, A. I. Vasil, J. D. Hale, R. E. Hancock, M. L. Vasil, and R. S. Hodges. Effects of net charge and the number of positively charged residues on the biological activity of amphipathic alpha-helical cationic antimicrobial peptides. *Biopolymers*, 90(3):369–383, 2008.

[37] M. N. Melo, R. Ferre, and M. A. Castanho. Antimicrobial peptides: linking partition, activity and high membrane-bound concentrations. *Nat. Rev. Microbiol.*, 7(3):245–250, 03 2009.

[38] K. Matsuzaki. Why and how are peptide-lipid interactions utilized for self-defense? Magainins and tachyplesins as archetypes. *Biochim. Biophys. Acta*, 1462(1-2):1–10, Dec 1999.

[39] C. G. Starr, J. He, and W. C. Wimley. Host Cell Interactions Are a Significant Barrier to the Clinical Utility of Peptide Antibiotics. *ACS Chem. Biol.*, 11(12):3391–3399, 12 2016.

[40] H. Jenssen, P. Hamill, and R. E. Hancock. Peptide antimicrobial agents. *Clin. Microbiol. Rev.*, 19(3):491–511, Jul 2006.

[41] J. L. Fox. Antimicrobial peptides stage a comeback. *Nat. Biotechnol.*, 31(5):379–382, May 2013.

[42] Y. Wu, K. He, S. J. Ludtke, and H. W. Huang. X-ray diffraction study of lipid bilayer membranes interacting with amphiphilic helical peptides: diphytanoyl phosphatidylcholine with alamethicin at low concentrations. *Biophys. J.*, 68(6):2361–2369, Jun 1995.

[43] T. Wieprecht, M. Beyermann, and J. Seelig. Binding of antibacterial magainin peptides to electrically neutral membranes: thermodynamics and structure. *Biochemistry*, 38(32):10377–10387, Aug 1999.

[44] F. Y. Chen, M. T. Lee, and H. W. Huang. Evidence for membrane thinning effect as the mechanism for peptide-induced pore formation. *Biophys. J.*, 84(6):3751–3758, Jun 2003.

[45] J. Seelig. Thermodynamics of lipid-peptide interactions. *Biochim. Biophys. Acta*, 1666(1-2):40–50, Nov 2004.

[46] M. T. Lee, F. Y. Chen, and H. W. Huang. Energetics of pore formation induced by membrane active peptides. *Biochemistry*, 43(12):3590–3599, Mar 2004.

[47] M. Cantisani, E. Finamore, E. Mignogna, A. Falanga, G. F. Nicoletti, C. Pedone, G. Morelli, M. Leone, M. Galdiero, and S. Galdiero. Structural insights into and activity analysis of the antimicrobial peptide myxinidin. *Antimicrob. Agents Chemother.*, 58(9):5280–5290, Sep 2014.

[48] T. H. Lee, K. N. Hall, and M. I. Aguilar. Antimicrobial Peptide Structure and Mechanism of Action: A Focus on the Role of Membrane Structure. *Curr Top Med Chem*, 16(1):25–39, 2016.

[49] E. Kuchinka and J. Seelig. Interaction of melittin with phosphatidylcholine membranes. Binding isotherm and lipid head-group conformation. *Biochemistry*, 28(10):4216–4221, May 1989.

[50] G. Beschiaschvili and J. Seelig. Melittin binding to mixed phosphatidylglycerol/phosphatidylcholine membranes. *Biochemistry*, 29(1):52–58, Jan 1990.

[51] G. Klocek, T. Schulthess, Y. Shai, and J. Seelig. Thermodynamics of melittin binding to lipid bilayers. Aggregation and pore formation. *Biochemistry*, 48(12):2586–2596, Mar 2009.

[52] S. Ludtke, K. He, and H. Huang. Membrane thinning caused by magainin 2. *Biochemistry*, 34(51):16764–16769, Dec 1995.

[53] W. T. Heller, K. He, S. J. Ludtke, T. A. Harroun, and H. W. Huang. Effect of changing the size of lipid headgroup on peptide insertion into membranes. *Biophys. J.*, 73(1):239–244, Jul 1997.

[54] W. Rawicz, K. C. Olbrich, T. McIntosh, D. Needham, and E. Evans. Effect of chain length and unsaturation on elasticity of lipid bilayers. *Biophys. J.*, 79(1):328–339, Jul 2000.

[55] H. W. Huang. Free energies of molecular bound states in lipid bilayers: lethal concentrations of antimicrobial peptides. *Biophys. J.*, 96(8):3263–3272, Apr 2009.

[56] S. M. Gregory, A. Cavenaugh, V. Journigan, A. Pokorny, and P. F. Almeida. A quantitative model for the all-or-none permeabilization of phospholipid vesicles by the antimicrobial peptide cecropin A. *Biophys. J.*, 94(5):1667–1680, Mar 2008.

[57] H. W. Huang. Molecular mechanism of antimicrobial peptides: the origin of cooperativity. *Biochim. Biophys. Acta*, 1758(9):1292–1302, Sep 2006.

[58] N. H. Lam and B. Y. Ha. Surface-lattice model describes electrostatic interactions of ions and polycations with bacterial lipopolysaccharides: ion valence and polycation's excluded area. *Langmuir*, 30(45):13631–13640, Nov 2014.

[59] M. Smart, A. Rajagopal, W. K. Liu, and B. Y. Ha. Opposing effects of cationic antimicrobial peptides and divalent cations on bacterial lipopolysaccharides. *Phys Rev E*, 96(4-1):042405, Oct 2017.

[60] D. A. Pink, L. Truelstrup Hansen, T. A. Gill, B. E. Quinn, M. H. Jericho, and T. J. Beveridge. Divalent calcium ions inhibit the penetration of protamine through the polysaccharide brush of the outer membrane of gram-negative bacteria. *Langmuir*, 19(21):8852–8858, 2003.

[61] I. E. Ivanov, E. N. Kintz, L. A. Porter, J. B. Goldberg, N. A. Burnham, and T. A. Camesano. Relating the physical properties of Pseudomonas aeruginosa lipopolysaccharides to virulence by atomic force microscopy. *J. Bacteriol.*, 193(5):1259–1266, Mar 2011.

[62] L. A. Clifton, F. Ciesielski, M. W. Skoda, N. Paracini, S. A. Holt, and J. H. Lakey. The Effect of Lipopolysaccharide Core Oligosaccharide Size on the Electrostatic Binding of Antimicrobial Proteins to Models of the Gram Negative Bacterial Outer Membrane. *Langmuir*, 32(14):3485–3494, Apr 2016.

[63] Johnson A. Lewis J. Raff M. Roberts K. Alberts, B. and P. Walter. *Molecular biology of the cell. 4th edn.* 2003.

[64] J William Schopf, Anatoliy B. Kudryavtsev, Andrew D. Czaja, and Abhishek B. Tripathi. Evidence of archean life : Stromatolites and microfossils. 2007.

[65] Thomas Heimburg. *The Thermal Biophysics of Membranes*. WILEY-VCH Verlag GmbH & Co. KGaA, Weinheim, 2007.

[66] Jacob N. Israelachvili. *Intermolecular and Surface Forces*. Academic Press, 2011.

[67] E. Gorter and F. Grendel. On bimolecular layers of Lipoids on the chromocytes of the blood. *J. Exp. Med.*, 41(4):439–443, Mar 1925.

[68] James Frederic Danielli and Hugh Davson. A contribution to the theory of permeability of thin films. *Journal of Cellular and Comparative Physiology*, 5(4):495–508, 1935.

[69] T. T. Mills, G. E. Toombes, S. Tristram-Nagle, D. M. Smilgies, G. W. Feigenson, and J. F. Nagle. Order parameters and areas in fluid-phase oriented lipid membranes using wide angle X-ray scattering. *Biophys. J.*, 95(2):669–681, Jul 2008.

[70] J. Henriksen, A. C. Rowat, E. Brief, Y. W. Hsueh, J. L. Thewalt, M. J. Zuckermann, and J. H. Ipsen. Universal behavior of membranes with sterols. *Biophys. J.*, 90(5):1639–1649, Mar 2006.

[71] D. Needham and R. S. Nunn. Elastic deformation and failure of lipid bilayer membranes containing cholesterol. *Biophys. J.*, 58(4):997–1009, Oct 1990.

[72] H. Nikaido. Molecular basis of bacterial outer membrane permeability revisited. *Microbiol. Mol. Biol. Rev.*, 67(4):593–656, Dec 2003.

[73] C. R. Raetz and C. Whitfield. Lipopolysaccharide endotoxins. *Annu. Rev. Biochem.*, 71:635–700, 2002.

[74] A. Kulp and M. J. Kuehn. Biological functions and biogenesis of secreted bacterial outer membrane vesicles. *Annu. Rev. Microbiol.*, 64:163–184, 2010.

[75] D. Ciumac, H. Gong, X. Hu, and J. R. Lu. Membrane targeting cationic antimicrobial peptides. *J Colloid Interface Sci*, 537:163–185, Nov 2018.

[76] T. Katsu, C. Ninomiya, M. Kuroko, H. Kobayashi, T. Hirota, and Y. Fujita. Action mechanism of amphipathic peptides gramicidin S and melittin on erythrocyte membrane. *Biochim. Biophys. Acta*, 939(1):57–63, Mar 1988.

[77] A. S. Ladokhin, M. E. Selsted, and S. H. White. Sizing membrane pores in lipid vesicles by leakage of co-encapsulated markers: pore formation by melittin. *Biophys. J.*, 72(4):1762–1766, Apr 1997.

[78] K. Matsuzaki, O. Murase, N. Fujii, and K. Miyajima. An antimicrobial peptide, magainin 2, induced rapid flip-flop of phospholipids coupled with pore formation and peptide translocation. *Biochemistry*, 35(35):11361–11368, Sep 1996.

[79] K. Matsuzaki, S. Yoneyama, and K. Miyajima. Pore formation and translocation of melittin. *Biophys. J.*, 73(2):831–838, Aug 1997.

[80] T. M. Domingues, B. Mattei, J. Seelig, K. R. Perez, A. Miranda, and K. A. Riske. Interaction of the antimicrobial peptide gomesin with model membranes: a calorimetric study. *Langmuir*, 29(27):8609–8618, Jul 2013.

[81] S. May, D. Harries, and A. Ben-Shaul. Lipid demixing and protein-protein interactions in the adsorption of charged proteins on mixed membranes. *Biophys. J.*, 79(4):1747–1760, Oct 2000.

[82] A. S. Ladokhin and S. H. White. Folding of amphipathic alpha-helices on membranes: energetics of helix formation by melittin. *J. Mol. Biol.*, 285(4):1363–1369, Jan 1999.

[83] H. W. Huang. Action of antimicrobial peptides: two-state model. *Biochemistry*, 39(29):8347–8352, Jul 2000.

[84] & Bromberg S. Dill, K. A. *Molecular driving forces: Statistical thermodynamics in biology, chemistry, physics, and nanoscience*. Garland Science, 2011.

[85] H. Steiner, D. Andreu, and R. B. Merrifield. Binding and action of cecropin and cecropin analogues: antibacterial peptides from insects. *Biochim. Biophys. Acta*, 939(2):260–266, Apr 1988.

[86] R. B. Merrifield, E. L. Merrifield, P. Juvvadi, D. Andreu, and H. G. Boman. Design and synthesis of antimicrobial peptides. *Ciba Found. Symp.*, 186:5–20, 1994.

[87] S. J. Ludtke, K. He, W. T. Heller, T. A. Harroun, L. Yang, and H. W. Huang. Membrane pores induced by magainin. *Biochemistry*, 35(43):13723–13728, Oct 1996.

[88] R. W. Glaser, C. Sachse, U. H. Durr, P. Wadhwani, S. Afonin, E. Strandberg, and A. S. Ulrich. Concentration-dependent realignment of the antimicrobial peptide PGLa in lipid membranes observed by solid-state 19F-NMR. *Biophys. J.*, 88(5):3392–3397, May 2005.

[89] F. Y. Chen, M. T. Lee, and H. W. Huang. Sigmoidal concentration dependence of antimicrobial peptide activities: a case study on alamethicin. *Biophys. J.*, 82(2):908–914, Feb 2002.

[90] H. W. Huang and Y. Wu. Lipid-alamethicin interactions influence alamethicin orientation. *Biophys. J.*, 60(5):1079–1087, Nov 1991.

[91] S. J. Ludtke, K. He, Y. Wu, and H. W. Huang. Cooperative membrane insertion of magainin correlated with its cytolytic activity. *Biochim. Biophys. Acta*, 1190(1):181–184, Feb 1994.

[92] L. Yang, T. M. Weiss, R. I. Lehrer, and H. W. Huang. Crystallization of antimicrobial pores in membranes: magainin and protegrin. *Biophys. J.*, 79(4):2002–2009, Oct 2000.

[93] L. Ding, L. Yang, T. M. Weiss, A. J. Waring, R. I. Lehrer, and H. W. Huang. Interaction of antimicrobial peptides with lipopolysaccharides. *Biochemistry*, 42(42):12251–12259, Oct 2003.

[94] W. T. Heller, A. J. Waring, R. I. Lehrer, and H. W. Huang. Multiple states of beta-sheet peptide protegrin in lipid bilayers. *Biochemistry*, 37(49):17331–17338, Dec 1998.

[95] W. T. Heller, A. J. Waring, R. I. Lehrer, T. A. Harroun, T. M. Weiss, L. Yang, and H. W. Huang. Membrane thinning effect of the beta-sheet antimicrobial protegrin. *Biochemistry*, 39(1):139–145, Jan 2000.

[96] L. Yang, T. A. Harroun, T. M. Weiss, L. Ding, and H. W. Huang. Barrel-stave model or toroidal model? A case study on ttin pores. *Biophys. J.*, 81(3):1475–1485, Sep 2001.

[97] H. W. Huang, F. Y. Chen, and M. T. Lee. Molecular mechanism of Peptide-induced pores in membranes. *Phys. Rev. Lett.*, 92(19):198304, May 2004.

[98] K. Matsuzaki, M. Harada, T. Handa, S. Funakoshi, N. Fujii, H. Yajima, and K. Miyajima. Magainin 1-induced leakage of entrapped calcein out of negatively-charged lipid vesicles. *Biochim. Biophys. Acta*, 981(1):130–134, May 1989.

[99] K. Matsuzaki, O. Murase, and K. Miyajima. Kinetics of pore formation by an antimicrobial peptide, magainin 2, in phospholipid bilayers. *Biochemistry*, 34(39):12553–12559, Oct 1995.

[100] Litster, J. D. Stability of lipid bilayers and red blood cell membranes. *Physics Letters A*, 53:193–194, June 1975.

[101] Taupin, C. and Dvolaitzky, M. and Sauterey, C. Osmotic pressure induced pores in phospholipid vesicles. *Biochemistry*, 14(21):4771–4775, Oct 1975.

[102] Alexey Kabalnov and Hkan Wennerstrm. Macroemulsion stability: the oriented wedge theory revisited. *Langmuir*, 12(2):276–292, 1996.

[103] Weaver, J. C. and Chizmadzhev, Y.A. Theory of electroporation: A review. *Bioelectrochemistry and Bioenergetics*, 41(2):135–160, 1996.

[104] F. Fogolari, A. Brigo, and H. Molinari. The Poisson-Boltzmann equation for biomolecular electrostatics: a tool for structural biology. *J. Mol. Recognit.*, 15(6):377–392, 2002.

[105] R. E. Hancock and H. G. Sahl. Antimicrobial and host-defense peptides as new anti-infective therapeutic strategies. *Nat. Biotechnol.*, 24(12):1551–1557, Dec 2006.

[106] R. F. Epand, W. L. Maloy, A. Ramamoorthy, and R. M. Epand. Probing the "charge cluster mechanism" in amphipathic helical cationic antimicrobial peptides. *Biochemistry*, 49(19):4076–4084, May 2010.

[107] Huey Huang. E Elasticity of Lipid Bilayer Interacting with Amphiphilic Helical Peptides. *Journal de Physique II, EDP Sciences*, 10(5):1427–1431, 1995.

[108] Sylvio May, Daniel Harries, and Avinoam Ben-Shaul. Macroion-induced compositional instability of binary fluid membranes. *Phys. Rev. Lett.*, 89:268102, Dec 2002.

[109] M. Dathe, H. Nikolenko, J. Meyer, M. Beyermann, and M. Bienert. Optimization of the antimicrobial activity of magainin peptides by modification of charge. *FEBS Lett.*, 501(2-3):146–150, Jul 2001.

[110] Fritz Jhnig. Electrostatic free energy and shift of the phase transition for charged lipid membranes. *Biophysical Chemistry*, 4(4):309 – 318, 1976.

[111] Andelman D. (Ed.) Poon, W. (Ed.). Soft condensed matter physics in molecular and cell biology. *Boca Raton*, 2006.

[112] van den Bogaart G., J. V. Guzman, J. T. Mika, and B. Poolman. On the mechanism of pore formation by melittin. *J. Biol. Chem.*, 283(49):33854–33857, Dec 2008.

[113] I. Zelezetsky and A. Tossi. Alpha-helical antimicrobial peptides–using a sequence template to guide structure-activity relationship studies. *Biochim. Biophys. Acta*, 1758(9):1436–1449, Sep 2006.

[114] private communication H.W. Huang.

[115] A. Zemel, D. R. Fattal, and A. Ben-Shaul. Energetics and self-assembly of amphipathic peptide pores in lipid membranes. *Biophys. J.*, 84(4):2242–2255, Apr 2003.

[116] private communication (2018) Snoussi M. et al.

[117] J. D. King, S. Berry, B. R. Clarke, R. J. Morris, and C. Whitfield. Lipopolysaccharide O antigen size distribution is determined by a chain extension complex of variable stoichiometry in Escherichia coli O9a. *Proc. Natl. Acad. Sci. U.S.A.*, 111(17):6407–6412, Apr 2014.

[118] A. H. Delcour. Outer membrane permeability and antibiotic resistance. *Biochim. Biophys. Acta*, 1794(5):808–816, May 2009.

[119] R. M. Epand and R. F. Epand. *Biophysical analysis of membrane-targeting antimicrobial peptides: membrane properties and the design of peptides specifically targeting Gram-negative bacteria.*

[120] L. A. Clifton, S. A. Holt, A. V. Hughes, E. L. Daulton, W. Arunmanee, F. Heinrich, S. Khalid, D. Jefferies, T. R. Charlton, J. R. Webster, C. J. Kinane, and J. H. Lakey. An accurate in vitro model of the E. coli envelope. *Angew. Chem. Int. Ed. Engl.*, 54(41):11952–11955, Oct 2015.

[121] L. A. Clifton, M. W. Skoda, A. P. Le Brun, F. Ciesielski, I. Kuzmenko, S. A. Holt, and J. H. Lakey. Effect of divalent cation removal on the structure of gram-negative bacterial outer membrane models. *Langmuir*, 31(1):404–412, 2015.

[122] A. Ebbensgaard, H. Mordhorst, F. M. Aarestrup, and E. B. Hansen. The Role of Outer Membrane Proteins and Lipopolysaccharides for the Sensitivity of Escherichia coli to Antimicrobial Peptides. *Front Microbiol*, 9:2153, 2018.

[123] E. A. Macias, F. Rana, J. Blazyk, and M. C. Modrzakowski. Bactericidal activity of magainin 2: use of lipopolysaccharide mutants. *Can. J. Microbiol.*, 36(8):582–584, Aug 1990.

[124] F. R. Rana, E. A. Macias, C. M. Sultany, M. C. Modzrakowski, and J. Blazyk. Interactions between magainin 2 and Salmonella typhimurium outer membranes: effect of lipopolysaccharide structure. *Biochemistry*, 30(24):5858–5866, Jun 1991.

[125] A. Banemann, H. Deppisch, and R. Gross. The lipopolysaccharide of Bordetella bronchiseptica acts as a protective shield against antimicrobial peptides. *Infect. Immun.*, 66(12):5607–5612, Dec 1998.

[126] A. Halperin, G. Fragneto, A. Schollier, and M. Sferrazza. Primary versus ternary adsorption of proteins onto PEG brushes. *Langmuir*, 23(21):10603–10617, Oct 2007.

[127] A. Halperin and M. Kroger. Ternary protein adsorption onto brushes: strong versus weak. *Langmuir*, 25(19):11621–11634, Oct 2009.

[128] N. V. Efremova, B. Bondurant, D. F. O'Brien, and D. E. Leckband. Measurements of interbilayer forces and protein adsorption on uncharged lipid bilayers displaying poly(ethylene glycol) chains. *Biochemistry*, 39(12):3441–3451, Mar 2000.

[129] Timothy McPherson, Argaw Kidane, Igal Szleifer, and Kinam Park. Prevention of protein adsorption by tethered poly(ethylene oxide) layers: experiments and single-chain mean-field analysis. *Langmuir*, 14(1):176–186, 1998.

[130] E. P. K. Currie, J. van der Gucht, O. V. Borisov, and M. A. Cohen Stuart. End-grafted polymers with surfactants: a theoretical model. *Langmuir*, 14(20):5740–5750, 1998.

[131] M. Krishnamoorthy, S. Hakobyan, M. Ramstedt, and J. E. Gautrot. Surface-initiated polymer brushes in the biomedical field: applications in membrane science, biosensing, cell culture, regenerative medicine and antibacterial coatings. *Chem. Rev.*, 114(21):10976–11026, Nov 2014.

[132] Jacob N. Israelachvili. 16 - steric (polymer-mediated) and thermal fluctuation forces. pages 381 – 413, 2011.

[133] M. Heuberger, T. Drobek, and N.D. Spencer. Interaction forces and morphology of a protein-resistant poly(ethylene glycol) layer. *Biophysical Journal*, 88(1):495 – 504, 2005.

[134] W. Feng, S. Zhu, K. Ishihara, and J. L. Brash. Protein resistant surfaces: comparison of acrylate graft polymers bearing oligo-ethylene oxide and phosphorylcholine side chains. *Biointerphases*, 1(1):50, Mar 2006.

[135] D. Allende and T. J. McIntosh. Lipopolysaccharides in bacterial membranes act like cholesterol in eukaryotic plasma membranes in providing protection against melittin-induced bilayer lysis. *Biochemistry*, 42(4):1101–1108, Feb 2003.

[136] Khavinet Lourvanij. Partial dehydration of glucose to oxygenated hydrocarbons in molecular-sieving catalysts. 2012.

[137] P. G. de Gennes. Conformations of polymers attached to an interface. *Macromolecules*, 13(5):1069–1075, 1980.

[138] Lionel C. H. Moh, Mark D. Losego, and Paul V. Braun. Solvent quality effects on scaling behavior of poly(methyl methacrylate) brushes in the moderate- and high-density regimes. *Langmuir*, 27(7):3698–3702, 2011.

[139] S. T. Milner, T. A. Witten, and M. E. Cates. Theory of the grafted polymer brush. *Macromolecules*, 21(8):2610–2619, 1988.

[140] E. B. Zhulina, O. V. Borisov, V. A. Pryamitsyn, and T. M. Birshtein. Coil-globule type transitions in polymers. 1. collapse of layers of grafted polymer chains. *Macromolecules*, 24(1):140–149, 1991.

[141] M. S. Kent. A quantitative study of tethered chains in various solution conditions using langmuir diblock copolymer monolayers. *Macromolecular Rapid Communications*, 21(6):243–270, 2000.

[142] Pik Yin Lai and Avi Halperin. Polymer brush at high coverage. *Macromolecules*, 24(17):4981–4982, 1991.

[143] S. M. Balko, T. Kreer, P. J. Costanzo, T. E. Patten, A. Johner, T. L. Kuhl, and C. M. Marques. Polymer brushes under high load. *PLoS ONE*, 8(3):e58392, 2013.

[144] B. Y. Ha and Y. Jung. Polymers under confinement: single polymers, how they interact, and as model chromosomes. *Soft Matter*, 11(12):2333–2352, Mar 2015.

[145] Holger Merlitz, Chen-Xu Wu, and Jens-Uwe Sommer. Inclusion free energy of nanoparticles in polymer brushes. *Macromolecules*, 45(20):8494–8501, 2012.

[146] A. Halperin and E. B. Zhulina. Stretching polymer brushes in poor solvents. *Macromolecules*, 24(19):5393–5397, 1991.

[147] X. Z. Cao, H. Merlitz, C. X. Wu, and J. U. Sommer. Polymer-induced entropic depletion potential. *Phys Rev E Stat Nonlin Soft Matter Phys*, 84(4 Pt 1):041802, Oct 2011.

[148] Hillary J. Taunton, Chris Toprakcioglu, Lewis J. Fetters, and Jacob Klein. Interactions between surfaces bearing end-adsorbed chains in a good solvent. *Macromolecules*, 23(2):571–580, 1990.

[149] D.F.K. Shim and M. E. Cates. Finite extensibility and density saturation effects in the polymer brush. *Journal de Physique*, 50(24):3535–3551, 1989.

[150] A. Milchev, D.I. Dimitrov, and K. Binder. Excess free energy of nanoparticles in a polymer brush. *Polymer*, 49(17):3611 – 3618, 2008.

[151] A. Milchev, D. I. Dimitrov, and K. Binder. Polymer brushes with nanoinclusions under shear: A molecular dynamics investigation. *Biomicrofluidics*, 4(3):32202, Sep 2010.

[152] A. Halperin and E. B. Zhulina. Atomic force microscopy of polymer brushes: colloidal versus sharp tips. *Langmuir*, 26(11):8933–8940, Jun 2010.

[153] A. A. Louis, P. G. Bolhuis, E. J. Meijer, and J. P. Hansen. Polymer induced depletion potentials in polymer-colloid mixtures. *The Journal of Chemical Physics*, 117(4):1893–1907, 2002.

[154] Sissi de Beer, Liz I. S. Mensink, and Bernard D. Kieviet. Geometry-dependent insertion forces on particles in swollen polymer brushes. *Macromolecules*, 49(3):1070–1078, 2016.

[155] Jaeup U. Kim and Ben O'Shaughnessy. Nanoinclusions in dry polymer brushes. *Macromolecules*, 39(1):413–425, 2006.

[156] C. Gu, R. D. Coalson, D. Jasnow, and A. Zilman. Free Energy of Nanoparticle Binding to Multivalent Polymeric Substrates. *J Phys Chem B*, 121(26):6425–6435, 07 2017.

[157] R. Tuinier, J. K. G. Dhont, and C. G. De Kruif. Depletion-induced phase separation of aggregated whey protein colloids by an exocellular polysaccharide. *Langmuir*, 16(4):1497–1507, 2000.

[158] N. L. Abbott, Daniel Blankschtein, and T. Alan Hatton. Protein partitioning in two-phase aqueous polymer systems. 4. proteins in solutions of entangled polymers. *Macromolecules*, 25(20):5192–5200, 1992.

[159] R. R. Netz. Debye-Hckel theory for interfacial geometries. *Phys Rev E Stat Phys Plasmas Fluids Relat Interdiscip Topics*, 60(3):3174–3182, Sep 1999.

[160] A. G. Moreira and R. R. Netz. Counterions at charge-modulated substrates. *EPL (Europhysics Letters)*, 57(6):911, 2002.

[161] John David Jackson. *Classical electrodynamics*. Wiley, New York, NY, 3rd ed. edition, 1999.

[162] Mika M. Kohonen, Marilyn E. Karaman, and Richard M. Pashley. Debye length in multivalent electrolyte solutions. *Langmuir*, 16(13):5749–5753, 2000.

[163] R. C. Chatelier and A. P. Minton. Adsorption of globular proteins on locally planar surfaces: models for the effect of excluded surface area and aggregation of adsorbed protein on adsorption equilibria. *Biophys. J.*, 71(5):2367–2374, Nov 1996.

[164] M. Vaara. Agents that increase the permeability of the outer membrane. *Microbiol. Rev.*, 56(3):395–411, Sep 1992.

[165] L. Leive. Release of lipopolysaccharide by EDTA treatment of E. coli. *Biochem. Biophys. Res. Commun.*, 21(4):290–296, Nov 1965.

[166] Shashank Shukla and Anita Shukla. Tunable antibiotic delivery from gellan hydrogels. *J. Mater. Chem. B*, 6:6444–6458, 2018.

[167] Ramanan Laxminarayan and Anup Malani and David Howard and Smith, David L. *Extending the cure: Policy responses to the growing threat of antibiotic resistance*. Resources for the Future, 5 2007.

[168] Federica Lo Verso, Sergei A. Egorov, Andrey Milchev, and Kurt Binder. Spherical polymer brushes under good solvent conditions: Molecular dynamics results compared to density functional theory. *The Journal of Chemical Physics*, 133(18):184901, 2010.

[169] J. P. Cotton, D. Decker, H. Benoit, B. Farnoux, J. Higgins, G. Jannink, R. Ober, C. Picot, and J. des Cloizeaux. Conformation of polymer chain in the bulk. *Macromolecules*, 7(6):863–872, 1974.

[170] Angelo Cacciuto and Erik Luijten. Self-avoiding flexible polymers under spherical confinement. *Nano Letters*, 6(5):901–905, 2006.

[171] S. Jun, A. Arnold, and B. Y. Ha. Confined space and effective interactions of multiple self-avoiding chains. *Phys. Rev. Lett.*, 98(12):128303, Mar 2007.

[172] H. Ohshima. Approximate Expression for the Double-Layer Interaction Energy between Two Parallel Plates with Constant Surface Charge Density. *J Colloid Interface Sci*, 212(1):130–134, Apr 1999.

[173] M. D. Betterton and Michael P. Brenner. Electrostatic edge instability of lipid membranes. *Phys. Rev. Lett.*, 82:1598–1601, Feb 1999.

[174] A. Katchalsky, S. Lifson, and J. Mazur. The electrostatic free energy of polyelectrolyte solutions. i. randomly kinked macromolecules. *Journal of Polymer Science*, 11(5):409–423, 1953.

[175] Andrey V. Dobrynin and Michael Rubinstein. Theory of polyelectrolytes in solutions and at surfaces. *Progress in Polymer Science*, 30(11):1049 – 1118, 2005.

[176] S. R. Ainavarapu, J. Brujic, H. H. Huang, A. P. Wiita, H. Lu, L. Li, K. A. Walther, M. Carrion-Vazquez, H. Li, and J. M. Fernandez. Contour length and refolding rate of a small protein controlled by engineered disulfide bonds. *Biophys. J.*, 92(1):225–233, Jan 2007.

# APPENDICES

# Appendix A

# Calculations of Electrostatic Free Energy ($F_{\rm el}$)

Note that in the Appendix free energy and energy are given in units of $k_{\rm B}T$; $\sigma$ and $\sigma_{\rm p}$ are planar charge densities in units of the elementary charge $e$.

## A.1 Peptide self-energy: $F_{\rm p}$

The first term in Eq. 3.2, $F_{\rm p}$, is the self-energy of peptides with respect to their state in the bulk. In the bulk, it is constant but changes near a dielectric medium (e.g., membranes); it becomes variable when the peptide undergoes conformational changes from random coils to compact disks (cylinders or $\alpha$ helices more realistically). On the surface of a binding membrane, the peptide can be modelled as a uniformly charged circular disk or plate of charge $Q$ and area $A_{\rm p}$ ($\approx 400$Å for melittin [5]). The peptide-membrane system is immersed in a salt solution characterized by the inverse screening length $\kappa = 4\pi\ell_{\rm B}n_0$, where $n_0$ is the total density of salt ions assumed to be monovalent. Also recall that $\epsilon_w\kappa d/\epsilon_\ell \gg 1$, where $\epsilon_w$ and $\epsilon_\ell$ are the dielectric constants of water and lipids, respectively. This means that the two layers of a lipid membrane are electrically decoupled (see Ref. [8, 159] and references therein). One can view the membrane a dielectric plate occupying the space $z < 0$ with membrane charges distributed at $z = 0$.

To proceed further, note that the free energy of a uniformly charged plate per area with a surface charge density $\sigma$ occupying the space $z < 0$ can be obtained from the

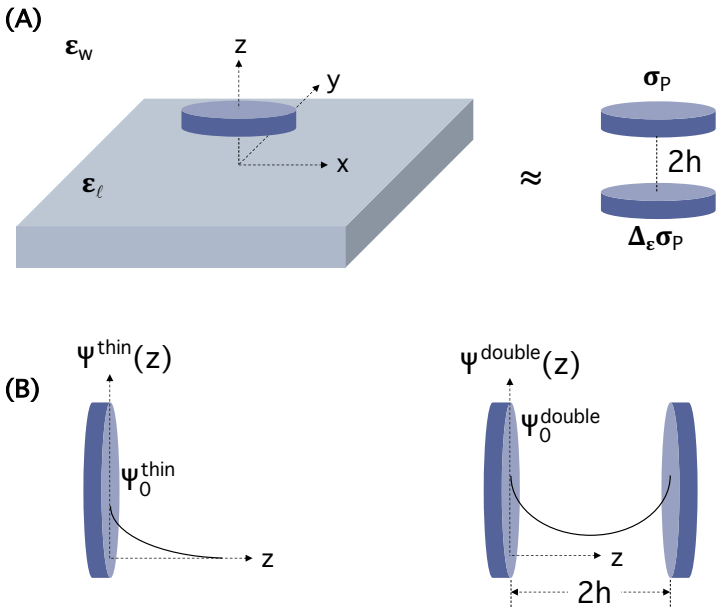


Figure A.1: (A) The free energy of a disk-like peptide a distance $h$ above the dielectric interface can be calculated by considering the double-layer interaction energy between the real disk-like peptide and its image-charge disk with uniform peptide's surface charge density of $\sigma_{\rm p}$. This picture is equivalent to approximating $\Delta_\epsilon = \frac{\epsilon_w - \epsilon_\ell}{\epsilon_w + \epsilon_\ell} \approx 1$. (B) This figure represents the potential distribution of a charged thin plate and two parallel plates with same surface charge density, separated by distance $2h$, in an electrolyte solution. The surface potentials $\phi_0^{\rm thin}$ (left) and $\phi_0^{\rm double}$ (right) are also introduced.

Poisson-Boltzmann (PB) approach [65, 110]:

$$\mathcal{F}_{\rm plate}(\sigma) = \sigma \Psi_0^{\rm thick} - \frac{\kappa}{\pi \ell_B}\left[\cosh\left(\frac{\Psi_0^{\rm thick}}{2}\right) - 1\right], \tag{A.1}$$

where $\Psi_0^{\rm thick} = 2\sinh^{-1}\left(2\pi\sigma\ell_B/\kappa\right)$ is the surface potential at $z = 0$ (the charges are distributed on the plate surface at $z = 0$).

If $\sigma = \sigma_{\rm p} = Q/A_{\rm p}$ is used, Eq. A.1 can be interpreted as the self free energy of a peptide on the membrane surface, as in model 1 [6]: $F_{\rm p} = A_{\rm p}\mathcal{F}_{\rm plate}(\sigma_{\rm p})$. It can also be used to estimate the electrostatic interaction between a bound peptide and the surrounding lipids in zone 1 in model 1 as well as lipid-lipid interactions in zone 1 or 2 in both models 1 and 2 (see Eq. A.10 and Eq. A.11) as well as the membrane reference free energy in all models.

In the consideration above, the charges on a bound peptide are treated as surface charges at the interface between headgroups and tails. More realistically, because of finite ionic sizes, peptide charges can be assumed to be distributed some distance ($h$) from the membrane surface, as shown in Fig. A.1. The effect of dielectric discontinuity on $F_{\rm p}$ can be mimicked by introducing peptide's image charges: a continuum image-charge disk with the charge density $\Delta_\epsilon \sigma_{\rm p}$, where $\Delta_\epsilon = (\epsilon_w - \epsilon_\ell)/(\epsilon_w + \epsilon_\ell)$ controls the effects of image charges [8, 159]. Here note that $\Delta_\epsilon \approx 1$. Together with the image charges, the peptide charges form a double layer: two similarly-charged parallel plates a distance $2h$ apart (see Fig. A.1). The interaction free energy between such double layers is known [172]. For small $h$, $F_{\rm p}(z)$ is well represented by

$$\begin{aligned} F_{\rm p}^{\rm Mo.2(3)}(h) &= \frac{A_{\rm p}}{\pi \ell_{\rm B} h} \ln \left( \frac{1+\exp(-2\kappa h)}{1+\exp(-2\kappa h \sqrt{\cosh \Psi_0^{\rm double}})} \right) \\ &\quad + \frac{A_{\rm p}\kappa}{\pi \ell_{\rm B}} \left\{ 1 - \sqrt{\cosh \Psi_0^{\rm double}} - \Psi_0^{\rm double} \sinh\left( \frac{\Psi_0^{\rm thin}}{2} \right) \right\}, \end{aligned} \tag{A.2}$$

where $\Psi_0^{\rm double}(h) = \sinh^{-1}\left[ 2\sinh\left(\frac{\Psi_0^{\rm thin}}{2}\right) / \tanh(\kappa h) \right]$ is the surface potential of two like-charged parallel plates with the same surface charge density $\sigma_{\rm p}$ a distance $2h$ apart from each other and $\Psi_0^{\rm thin} = 2\sinh^{-1}(\pi \sigma_{\rm p} \ell_{\rm B}/\kappa)$ is the corresponding quantity for an isolated thin layer. Fig. A.1(B) represents a schematic potential distribution for the single-plate and double-plate cases. Note that Eq. A.2 is an approximate relationship for small separations and works well for distances $\kappa h \leq 0.6$ [172]. We use Eq. A.2 for both models 2 and 3.

## A.2 $F_{\rm P-L1}$: peptide-lipid interaction in zone 1

How a bound peptide interacts with the surrounding lipids in zone 1 depends on the binding mode. For mode I, zone 1 can be approximated as a charged surface with a hole of radius $R_{\rm p}$ (i.e., peptide radius) at the centre. If we ignore the outer-boundary effect, as assumed in model 2, the interaction free energy can be obtained as

$$\begin{aligned} F_{\rm P-L1(I)}^{\rm Mo.2} &= \int_0^{R_{\rm p}} 2\pi r dr \left[ \sigma_{\rm p} \cdot \Psi_{\rm PB-hole}\left(r, \sigma = \sigma_{1(\rm I)}\right) \right] \\ &= \pi \sigma_{\rm p} R_{\rm p}^2 \left[ \Psi_0(0) - \tanh \Psi_0(0) + \frac{4\pi \sigma_{1(\rm I)} \ell_{\rm B}}{\kappa \sqrt{\cosh \Psi_0(0)}} \right] \\ &\quad - 8\pi^2 \ell_{\rm B} \sigma_{1(\rm I)} \sigma_{\rm p} R_{\rm p}^2 \int_0^\infty dk \frac{J_1^2(kR_{\rm p})}{k\sqrt{k^2 + \kappa^2 \cosh \Psi_0(0)}}, \end{aligned} \tag{A.3}$$

where $\Psi_{\rm PB-hole}$ is an approximate Poisson-Boltzmann surface potential of an infinite charged plane at $z = 0$ with a hole of radius $R_{\rm p}$ at the centre derived in Eq. B.10, $\Psi_0(0) = \Psi_{\rm PB-hole}(r = 0)$ is the surface potential at the centre of the hole (recall that the membrane charges are at $z = 0$), $\sigma_{1(\rm I)}$ is the surface charge density of anionic lipids in zone 1 with a hydrophobically-bound peptide, and $J_1(x)$ is the Bessel function of the first kind. Detailed steps leading to this are presented in Appendix B, where it is shown that

$$\begin{aligned}\Psi_{\rm PB-hole}(r, z = 0) &= \Psi_0(0) - \tanh \Psi_0(0) + \frac{4\pi\sigma\ell_{\rm B}}{\kappa\sqrt{\cosh \Psi_0(0)}} \\ &\quad -4\pi\sigma\ell_{\rm B}R\int_0^\infty dk \frac{J_0(kr)J_1(kR)}{\sqrt{k^2 + \kappa^2 \cosh \Psi_0(0)}}. \end{aligned} \tag{A.4}$$

Note that the effect of dielectric discontinuities is approximately taken into account.

For mode S, the interaction energy is the work required to bring Q charges toward an infinitely thick dielectric plate of surface charge density $\sigma_{1(\rm S)}$. Hence we have;

$$F^{\rm Mo.2}_{\rm P-L1(S)} = Q \cdot \Psi_{\rm PB}\left(z = 0,\, \sigma_{1(\rm S)}\right). \tag{A.5}$$

Note here that the Poisson-Boltzmann surface potential of an infinite plane is $\Psi_{\rm PB}(z = 0, \sigma) = 2\sinh^{-1}\left(2\pi\sigma\ell_{\rm B}/\kappa\right)$ and the surface charge density of anionic lipids in mode S is $\sigma_{1(\rm S)} = -\alpha_{1\rm S}/a_\ell$.

In model 3, the boundary of zone 1 is kept finite. As a result, zone 1 can be viewed as a circular ring with an outer radius $R_1$ and an inner radius $R_{\rm P}$. This geometry poses a main barrier to theoretical calculations. In this model, we use the linearized PB or Debye-Hückel approach within the two state model of peptide binding: free or bound. Since the strong peptide-lipid interaction (giving rises to the non-linearity of electrostatic interactions as reflected in the PB equation) is taken into account this way, this approach is more reliable than it may sound; since the membrane charges are much neutralized by peptide charges, the residual interaction between the membrane and ions will be relatively weak. The resulting approach is a renormalized DH approach. We thus calculate the peptide-lipid interaction by estimating the electrostatic energy that a bound peptide feels from the DH surface potential of the circular ring:

$$\begin{aligned} F^{\rm Mo.3}_{\rm P-L1(I)} &= \int_0^{R_{\rm p}} 2\pi r dr \left[\sigma_{\rm p} \cdot \Psi_{\rm DH-ring}\left(r, \sigma_{1(\rm I)}, R_{\rm p}, R_1\right)\right] \\ &= 8\pi^2\sigma_{\rm p}\sigma_{1(\rm I)}\ell_{\rm B}\int_0^\infty dk \frac{R_{\rm p}J_1(kR_{\rm p})}{k\sqrt{k^2 + \kappa^2}}\left[R_1 J_1(kR_1) - R_{\rm p}J_1(kR_{\rm p})\right], \end{aligned} \tag{A.6}$$

where $J_1(x)$ is the first-order Bessel function of the first kind and the DH surface potential of a ring with inner and outer radii $r_{\rm in}$ and $r_{\rm out}$ is given by [173]

$$\Psi_{\rm DH-Ring}(r,\sigma,r_{\rm in},r_{\rm out}) = 4\pi\sigma\ell_{\rm B}\int_0^\infty dk \frac{J_0(kr)}{\sqrt{k^2+\kappa^2}}\left[r_{\rm out}J_1(kr_{\rm out}) - r_{\rm in}J_1(kr_{\rm in})\right]. \tag{A.7}$$

On the other hand, the peptide's and lipid's charges in mode S are assumed to be smeared out over zone 1. The free energy of zone 1, including peptide-lipid and lipid-lipid interactions, can be obtained by using the DH surface potential of a disk with a radius $R_1$ and the net surface charge density of $\sigma_{\rm net} = Q/A_1 - \alpha_{1(\rm S)}/a_\ell$:

$$\begin{aligned} F^{\rm Mo.3}_{\rm zone\,1} &= F^{\rm Mo.3}_{\rm P-L1(S)} + F^{\rm Mo.3}_{\rm L1(S)} \\ &= \frac{1}{2}\int_0^{R_1} 2\pi r dr \left[\sigma_{\rm net}\cdot\Psi_{\rm DH-disk}\left(r,\sigma_{\rm net},R_1\right) - \sigma_{\rm p(A_1)}\cdot\Psi_{\rm DH-disk}\left(r,\sigma_{\rm p(A_1)},R_1\right)\right] \\ &= \left(\sigma^2_{\rm net} - \sigma^2_{\rm P(A_1)}\right)4\pi^2\ell_{\rm B}\int_0^\infty dk\frac{R_1^2J_1^2(kR_1)}{k\sqrt{k^2+\kappa^2}}, \end{aligned} \tag{A.8}$$

where $\Psi_{\rm DH-disk}(r,\sigma,R)$ is the DH surface potential of a disk with a radius $R$ and a surface charge density $\sigma$, given by [173]

$$\Psi_{\rm DH-disk}(r,\sigma,R) = 4\pi\sigma\ell_{\rm B}R\int_0^\infty dk\frac{J_0(kr)J_1(kR)}{\sqrt{k^2+\kappa^2}}. \tag{A.9}$$

Note that the second term containing $\sigma_{\rm p(A_1)} = Q/A_1$ in Eq. A.8 (i.e., the surface charge density of a peptide when its charge is smeared out over $A_1$) is introduced to avoid the double counting of the peptide self energy, since it is already included in Eq. A.2. While the lipid-lipid interaction for mode S in model 3, $F^{\rm Mo.3}_{\rm L1(S)}$, is naturally included as part of $F^{\rm Mo.3}_{\rm zone\,1}$ in Eq. A.8, this interaction is considered separately below for model 2 and mode I in model 3.

## A.3 Lipid-lipid Interaction in each zone: $F_{\rm L1}(F_{\rm L2})$

Here we present steps leading to the free energy of each zone: zone 1 or 2. In model 2, we ignore the boundary effect by treating each zone as a boundary-less plate. The electrostatic free energy per area for both modes I and S is identical to that of the semi-infinite plate

(Eq. A.1), described in section A.1, with the surface charge densities $\sigma_{1(i)}$ and $\sigma_{2(i)}$ for zone 1 and zone 2, respectively, where $i$ = S or I represents the mode.

$$F^{\text{Mo.2}}_{\text{L1(i)}} = (A_{\text{WSC}} - A_{\text{p}}\delta_{\text{I}i})\,\mathcal{F}_{\text{plate}}\left(\sigma_{1(i)}\right) \tag{A.10}$$

$$F^{\text{Mo.2}}_{\text{L2(i)}} = (A_{\text{WSC}} - A_1)\,\mathcal{F}_{\text{plate}}\left(\sigma_{2(i)}\right). \tag{A.11}$$

The plate free energy per area $\mathcal{F}_{\text{plate}}$ is given in Eq. A.1. The presence of the delta function is obvious: for mode S, lipids are excluded from the central peptide.

In model 3, the geometry of each zone is preserved. To make this analytically-tractable, we use the DH approach and calculate the surface potential of a ring in both modes of (I) and (S), except for $F^{\text{Mo.3}}_{\text{L1(S)}}$ that is presented in Eq. A.8.

$$\begin{aligned} F^{\text{Mo.3}}_{\text{L1(I)}} &= \int_{R_{\text{p}}}^{R_1} (2\pi r dr) \int_0^{\sigma_{1(\text{I})}} \Psi_{\text{DH-Ring}}\left(r, R_{\text{p}}, R_1, \sigma_{1(\text{I})'}\right) d\sigma_{1(\text{I})'} \\ &= 4\pi^2 \sigma^2_{1(\text{I})} \ell_{\text{B}} \int_0^{\infty} \frac{dk}{k\sqrt{k^2+\kappa^2}} \left[R_1 J_1(kR_1) - R_{\text{p}} J_1(kR_{\text{P}})\right]^2 \end{aligned} \tag{A.12}$$

and

$$\begin{aligned} F^{\text{Mo.3}}_{\text{L2}(i)} &= \int_{R_1}^{R_{\text{WSC}}} (2\pi r dr) \int_0^{\sigma_{2(i)}} \Psi_{\text{DH-ring}}\left(r, R_1, R_{\text{WS}}, \sigma_{2(i)'}\right) d\sigma_{2(i)'} \\ &= 4\pi^2 \sigma^2_{2(i)} \ell_{\text{B}} \int_0^{\infty} \frac{dk}{k\sqrt{k^2+\kappa^2}} \left[R_{\text{WSC}} J_1(kR_{\text{WSC}}) - R_1 J_1(kR_1)\right]^2 \end{aligned} \tag{A.13}$$

The DH surface potential of a ring, $\Psi_{\text{DH-ring}}$, is presented in Eq. A.6.

## A.4 Interactions between bound peptides or Wigner-Seitz Cells: $F_{\text{P}-\text{P}'}$ and $F_{\text{WSC}-\text{WSC}'}$

Bound peptides ($\text{P} - \text{P}'$) or WSCs ($\text{WSC} - \text{WSC}'$) interact with each other, where the unprimed and primed symbols refer to different peptides or WSCs. Their mutual repulsion can be included systematically.

In numerically-oriented Wigner-Seitz cell approaches, a standard procedure to capture the repulsion between WSCs on the membrane surface is through the boundary condition: $\frac{\partial \Psi}{\partial r}\big|_{r=R_{\text{WSC}}} = 0$, i.e., the normal component of the electric field (i.e., a component of the

field normal to the WSC boundary in the plane of the membrane surface) vanishes on the WSC boundary [9, 81]. Below, we describe analytically-tractable models.

In sub-model b, i.e., model 2b and model 3b, we only take into account the interaction between bound peptides, P − P′. This interaction can be obtained by dividing the membrane into a disk of radius $R_{\rm p}$ and the rest, i.e., the plate with a hole of radius $R_{\rm p}$, with the surface charge density $\sigma_{\rm p} = Q/A_{\rm p}$ and $\sigma_{\rm p'} = \frac{(\sigma_{\rm I}+\sigma_{\rm S}-1/A_{\rm cell})Q}{(1+\sigma_{\rm I}A_{\rm p}-A_{\rm WSC}/A_{\rm cell})}$, respectively; recall that the prime is used for the 'rest' and $A_{\rm cell}$ is the surface area of bacteria or host cells.

Let $\Psi_{\rm PB-hole}$ be the surface potential created by the rest somewhere in the hole (obtained in Eq. B.10 and also shown in Eq. A.4). Using the approximate PB approach detailed in Appendix B, we arrive at

$$\begin{aligned} F^{\rm Mo.2b}_{\rm P-P'} &\approx \frac{1}{2}\int_0^{R_{\rm p}} 2\pi r dr \left[\sigma_{\rm p}\cdot\Psi_{\rm PB-hole}\left(r,\sigma_{\rm p'},R_{\rm WSC}\right)\right] \\ &= \frac{\pi\sigma_{\rm p}R_{\rm p}^2}{2}\left[\Psi_0'(0)-\tanh\Psi_0'(0)+\frac{4\pi\sigma_{\rm p'}\ell_{\rm B}}{\kappa\sqrt{\cosh\Psi_0'(0)}}\right. \\ &\qquad \left. -8\pi\sigma_{\rm p'}\ell_{\rm B}\frac{R_{\rm WSC}}{R_{\rm p}}\int_0^\infty \frac{dk}{k\sqrt{k^2+\kappa^2\cosh\Psi_0'(0)}}\frac{J_1(kR_{\rm p})J_1(kR_{\rm WSC})}{}\right]. \end{aligned} \tag{A.14}$$

Here and below, $r$ is the distance from the centre of the hole measured in the direction parallel with the membrane surface and

$$\Psi_0'(0) = \Psi_{\rm PB-hole}(r=0) = \sinh^{-1}\left[\frac{4\pi\sigma_{\rm p'}\ell_{\rm B}}{\kappa} - 4\pi\sigma_{\rm p'}\ell_{\rm B}R_{\rm WSC}\int_0^\infty dk\frac{J_1(kR_{\rm WSC})}{\sqrt{k^2+\kappa^2}}\right] \tag{A.15}$$

is the potential at the hole center due to the rest (i.e., the plate with a hole) with the surface charge density $\sigma_{\rm p'}$ (see Appendix B).

Similarly, let $\Psi_{\rm DH-hole}(r,\sigma,R)$ be the DH surface potential of a charged plane with a hole of radius $R$ evaluated somewhere in the hole [173]:

$$\Psi_{\rm DH-hole}(r,\sigma,R) = 4\pi\sigma\ell_{\rm B}\left[\frac{1}{\kappa} - R\int_0^\infty dk\frac{J_0(kr)J_1(kR)}{\sqrt{k^2+\kappa^2}}\right]. \tag{A.16}$$

We then find

$$\begin{aligned} F^{\rm Mo.3b}_{\rm P-P'} &= \frac{1}{2}\int_0^{R_{\rm p}} 2\pi r dr \left[\sigma_{\rm p}\cdot\Psi_{\rm DH-hole}\left(r,\sigma_{\rm p'},R_{\rm WSC}\right)\right] \\ &= \left(2\pi^2\sigma_{\rm p}\sigma_{\rm p'}\ell_{\rm B}R_{\rm p}^2\right)\left[\frac{1}{\kappa} - \frac{2R_{\rm WSC}}{R_{\rm p}}\int_0^\infty dk\frac{J_1(kR_{\rm p})J_1(kR_{\rm WSC})}{k\sqrt{k^2+\kappa^2}}\right]. \end{aligned} \tag{A.17}$$

Note that this is relevant for a thick dielectric medium, for which the image-charge effect is taken into account through the combination $1+(\epsilon_w-\epsilon_\ell)/(\epsilon_w+\epsilon_\ell) \approx 2$ (see Ref. [173] for the corresponding expression for a thin plate). As shown in Fig. B.1, the dielectric discontinuity on the surface of an infinitely thick layer can be mimicked in a thin layer sheet by changing the surface charge density from $\sigma$ to $\sigma(1+\Delta_\epsilon)$ [14]. As a result, the corresponding boundary condition will evolve from $\epsilon_0\epsilon_w E_1 - \epsilon_0\epsilon_\ell E_2 = \sigma$ into $2\epsilon_0\epsilon_w E = \sigma(1+\Delta_\epsilon)$. Refer to Eq. B.4 in appendix B for further details.

In a refined sub-model c, we include all relevant interaction pairs: peptide-lipids′ and lipid-peptides′ as well as peptide-peptide′. As explained in Fig. 3.3, the total interaction of a single WSC with the rest, i.e., WSC′, can be decomposed into three distinct contributions: $\mathrm{P}-\mathrm{P}'$, $\mathrm{P}-(\mathrm{L1}+\mathrm{L2})'$, and $(\mathrm{L1}+\mathrm{L2})-\mathrm{P}'$.

$$F_{\mathrm{WSC}-\mathrm{WSC}'} = F_{\mathrm{P}-\mathrm{P}'} + F_{\mathrm{P}-(\mathrm{L1}+\mathrm{L2})'} + F_{(\mathrm{L1}+\mathrm{L2})-\mathrm{P}'}. \tag{A.18}$$

For this consideration, we essentially extend the method used for sub-model b, and consider the membrane as being made of a disk of radius $R_{\mathrm{WSC}}$ and the rest, i.e., a thick plate with a hole of the same radius. First introduce the surface change density of a WSC we focus on and that of others, denoted as $\sigma_{\mathrm{WSC}(i)}$ and $\sigma_{\mathrm{WSC}'(i)}$, respectively:

$$\sigma_{\mathrm{WSC}(i)} = \frac{Q - \bar{\alpha}/a_\ell (A_{\mathrm{WSC}} - A_{\mathrm{p}}\delta_{\mathrm{I}i})}{A_{\mathrm{WSC}}}, \tag{A.19}$$

$$\sigma_{\mathrm{WSC}'(i)} = \frac{(\sigma_{\mathrm{I}} + \sigma_{\mathrm{S}} - 1/A)Q - \bar{\alpha}/a_\ell \left[1 - (A_{\mathrm{WSC}} - A_{\mathrm{p}}\delta_{\mathrm{I}i})/A_{\mathrm{cell}}\right]}{1 + \sigma_{\mathrm{I}} A_{\mathrm{p}} - A_{\mathrm{WSC}}/A_{\mathrm{cell}}} \tag{A.20}$$

Note that $\sigma_{\mathrm{WSC}'(i)}$ is a quantity averaged over both modes, while $\sigma_{\mathrm{WSC}(i)}$ refers to either mode S or mode I. This difference is reflected in these two quantities.

For model 2c, this leads to

$$\begin{aligned} F^{\mathrm{Mo.2c}}_{\mathrm{WSC}-\mathrm{WSC}'(i)} &\approx \frac{1}{2}\int_0^{R_{\mathrm{WSC}}} 2\pi r dr \left[\sigma_{\mathrm{WSC}(i)} \cdot \Psi_{\mathrm{PB-hole}}\left(r, \sigma_{\mathrm{WSC}'(i)}, R_{\mathrm{WSC}}\right)\right] \\ &= \frac{\pi\sigma_{\mathrm{WSC}(i)} R^2_{\mathrm{WSC}}}{2}\left[\Psi'_0(0) - \tanh\Psi'_0(0) + \frac{4\pi\ell_{\mathrm{B}}\sigma_{\mathrm{WSC}'(i)}}{\kappa\sqrt{\cosh\Psi'_0(0)}}\right. \\ &\qquad \left. -8\pi\ell_{\mathrm{B}}\sigma_{\mathrm{WSC}'(i)}\int_0^\infty dk \frac{J_1^2(kR_{\mathrm{WSC}})}{k\sqrt{k^2+\kappa^2\cosh\Psi'_0(0)}}\right] \end{aligned} \tag{A.21}$$

where $\Psi'_0(0)$ is the PB surface potential of a charged plate with a hole in the center, i.e., at $r=0$ and $z=0$ (i.e., the potential in Eq. A.15 with $\sigma = \sigma_{\mathrm{WSC}'(i)}$ (see Eq. B.12). Similarly,

for model 3c, we find

$$F^{\text{Mo.3c}}_{\text{WSC}-\text{WSC}'(i)} = \frac{1}{2}\int_0^{R_{\text{WSC}}} 2\pi r dr \left[\sigma_{\text{WSC}(i)} \cdot \Psi_{\text{DH}-\text{hole}}\left(r, \sigma_{\text{WSC}'(i)}, R_{\text{WSC}}\right)\right]$$
$$= 2\pi^2 \ell_{\text{B}} \sigma_{\text{WSC}(i)} \sigma_{\text{WSC}'(i)} R^2_{\text{WSC}} \left[\frac{1}{\kappa} - 2\int_0^{\infty} dk \frac{J_1^2(kR_{\text{WSC}})}{k\sqrt{k^2+\kappa^2}}\right]. \quad \text{(A.22)}$$

Note here that $\Psi_{\text{DH}-\text{hole}}\left(r, \sigma_{\text{WSC}'(i)}, R_{\text{WSC}}\right)$ is a special case of $\Psi_{\text{DH}-\text{hole}}\left(r, \sigma, R\right)$ in Eq. A.16.

## A.5 Interaction between zone 1 and zone 2: $Z1 - Z2$

Next, we include the interaction between zone 1 and 2 in the same WSC as for model 3d. One may argue that this is a relatively small contribution, since the peptide charge in zone 1 is more or less neutralized by the surrounding lipids; recall that this is how zone 1 is defined. Nevertheless, for completeness, we consider this interaction.

First, note that it can be decomposed into two parts

$$F^{\text{Mo.3d}}_{\text{Z1}-\text{Z2}} = F_{\text{P}-\text{L2}} + F_{\text{L1}-\text{L2}}. \quad \text{(A.23)}$$

Based on the DH surface potential of a ring (see Eq. A.7 with a surface charge density $\sigma = \sigma_{2(i)}$, an inner radius $r_{\text{in}} = R_1$, and an outer radius $r_{\text{out}} = R_{\text{WSC}}$), we obtain

$$F_{\text{P}-\text{L2(I)}} = \int_0^{R_{\text{p}}} 2\pi r dr \left[\sigma_{\text{P}} \cdot \Psi_{\text{DH}-\text{ring}}\left(\sigma_{2(\text{I})}, r, R_1, R_{\text{WSC}}\right)\right]$$
$$= 8\pi^2 \ell_{\text{B}} \sigma_{\text{p}} \sigma_{2(\text{I})} \int_0^{\infty} dk \frac{R_{\text{p}} J_1(kR_{\text{p}})}{k\sqrt{k^2+\kappa^2}} \left[R_{\text{WSC}} J_1\left(kR_{\text{WSC}}\right) - R_1 J_1(kR_1)\right], \quad \text{(A.24)}$$

$$F_{\text{L1}-\text{L2(I)}} = \int_{R_{\text{p}}}^{R_1} 2\pi r dr \left[\sigma_{1(\text{I})} \cdot \Psi_{\text{DH}-\text{ring}}\left(\sigma_{2(\text{I})}, r, R_1, R_{\text{WSC}}\right)\right]$$
$$= 8\pi^2 \ell_{\text{B}} \sigma_{1(\text{I})} \sigma_{2(\text{I})} \int_0^{\infty} dk \frac{\left[R_1\ J_1(kR_1) - R_{\text{p}} J_1(kR_{\text{p}})\right]}{k\sqrt{k^2+\kappa^2}} \left[R_{\text{WSC}} J_1(kR_{\text{WSC}}) - R_1 J_1(kR_1)\right]. \quad \text{(A.25)}$$

As discussed earlier (see Eq. A.8), for mode S, the peptide and lipid charges are taken to be uniformly smeared out. The resulting planar charge density is $\sigma_{\text{net}} = Q/A_1 - \alpha_{1(\text{S})}/a_\ell$. With this difference, we arrive at

$$F_{(\text{P}+\text{L}_1)-\text{L}_2(\text{S})} = \int_0^{R_1} 2\pi r dr \left[\sigma_{\text{net}} \cdot \Psi_{\text{DH}-\text{ring}}\left(\sigma_{2(\text{S})}, r, R_1, R_{\text{WSC}}\right)\right]$$
$$= 8\pi^2 \sigma_{\text{net}} \sigma_{2(\text{S})} \ell_{\text{B}} \int_0^{\infty} dk \frac{R_1 J_1(kR_1)}{k\sqrt{k^2+\kappa^2}} \left[R_{\text{WSC}} J_1(kR_{\text{WSC}}) - R_1 J_1(kR_1)\right]. \quad \text{(A.26)}$$

## A.6 Peptide free energy in the bulk

Peptide binding is not solely determined by the interaction energy between peptides and their binding membrane. Their reference state in the bulk should be taken into account in our consideration. In this approach, free peptides in the bulk are assumed to be unstructured charge-carrying chains or simply polyelectrolytes (PEs); each chain consists of $N$ monomeric units (amino acids) of length $b$ each and carries a total charge $Q$. The free energy of a PE, $F_{\mathrm{PE}}$, is known [175]. It can be expressed in terms of the end-to-end distance of the chain, $R$, as

$$F_{\mathrm{PE}} = \frac{3}{2}\frac{R^2}{Nb^2} - \frac{Q\kappa\ell_{\mathrm{B}}}{2} + \frac{Q^2\ell_{\mathrm{B}}}{R}\ln\left(1 + \frac{6R}{Nb^2\kappa}\right). \tag{A.27}$$

If the conformational entropy term, i.e., the first term on the right hand side in Eq. A.27, tends to decrease $R$, the last term, describing the repulsion between charges on the chain [174], opposes this. On the other hand, the second term arising from the attractive interactions between a charge on the chain and the surrounding counterions is independent of $R$ [6].

In equilibrium, $F_{\mathrm{PE}}$ is minimized with respect to $R$. Here we choose PE parameters as for cationic peptide melittin: $N = 26$ and $b = 4.1$Å [176]. Note that our choice of $b$ is somewhat larger than the distance between two backbone monomers or the size of each amino acid. This choice is to reflect that the fact that cationic charges are mostly on the side chains and their actual spacing is larger than the distance along the backbone. The corresponding equilibrium free energy $F_{\mathrm{coil}}(R_{\mathrm{eq}})$ has to be used as the reference free energy [6].

# Appendix B

# Approximated Poisson-Boltzmann potential of an infinite charged plane with a circular hole

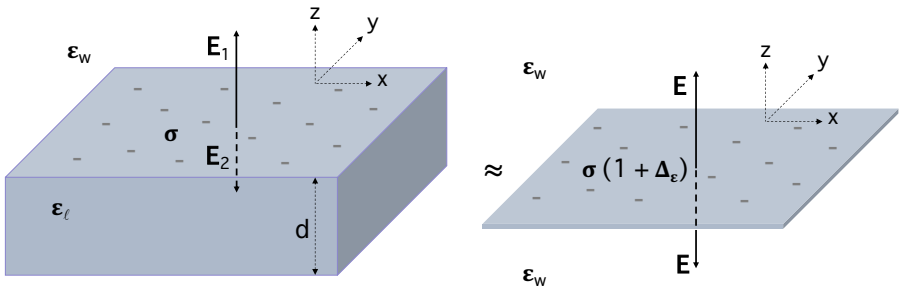


Figure B.1: Mapping a thick dielectric plate (left), occupying $z \leq 0$ and carrying charges on the surface at $z = 0$, onto a thin layer of charges at $z = 0$ (right). Here, subscripts $w$ and $\ell$ stands for water and lipid, respectively. Let $\mathbf{n}$ be a unit normal vector pointing along the $z$ axis. The electric boundary conditions for the thick and thin cases are $\mathbf{n}\cdot(\epsilon_0\epsilon_w\mathbf{E}_1 - \epsilon_0\epsilon_\ell\mathbf{E}_2) = \sigma$ and $2\epsilon_0\epsilon_w E = \sigma(1+\Delta_\epsilon)$, respectively [14]. The two are indeed equivalent in the limit $\epsilon_\ell \to 0$.

Here we consider the Poisson-Boltzmann (PB) equation in cylindrical coordinates for an infinite charged plane with an "imaginary" circular hole of radius $R$ at its center. The plane can be viewed as being made of a circular disk of radius $R$ at the centre and the rest;

we focus on the rest. Let $r$ be the radial distance on the plane from the hole center and $z$ the normal distance from the plane. The PB equation reads

$$\left[\frac{1}{r}\frac{\partial}{\partial r}\left(r\frac{\partial}{\partial r}\right)+\frac{\partial^2}{\partial z^2}\right]\Psi(r,z)=\kappa^2\sinh\Psi(r,z) \tag{B.1}$$

This is to be solved subject to the boundary conditions:

$$\Psi(r,z) = 0, \quad z\to\infty \tag{B.2}$$

$$\left.\frac{\partial\Psi}{\partial z}\right|_{z=0} = 0, \quad r<R \tag{B.3}$$

$$\frac{-2}{4\pi\ell_{\mathrm{B}}}\left.\frac{\partial\Psi}{\partial z}\right|_{z=0} = \sigma(1+\Delta_\epsilon), \quad r>R, \tag{B.4}$$

where $\Delta_\epsilon=(\epsilon_w-\epsilon_\ell)/(\epsilon_w+\epsilon_\ell)$, as defined in Eq. 3.9.

Note that the effect of dielectric discontinuities at the lipid-water interface is approximately captured in the boundary condition B.4. This is motivated by the following observation: if $\epsilon_w\kappa d/\epsilon_\ell\gg 1$ is satisfied for a dielectric plate of thickness $d$, as in our case ($d\approx 40$ and dielectric constant $\epsilon_\ell=2$), one may simplify the electric potential by taking the limits $\epsilon_\ell=0$ or $d\to\infty$ [8, 159]. Recall that subscripts $w$ and $\ell$ refer to water and lipid, respectively.

Indeed, Fig. B.1 illustrates how one can map a thick dielectric plate, occupying $z\le 0$ and carrying charges on its surface at $z=0$, onto a thin layer of charges at $z=0$. Let $\sigma$ be the planar charge density in units of $e$, which is the same for the two cases. Let $\mathbf{E}_1$ be the electric field right above the charged surface at $z=0$ and $\mathbf{E}_2$ the electric field below above; let $\mathbf{n}$ be a unit normal vector pointing along the $z$ axis. The mapping completes if the electric boundary condition for the thick plate $\mathbf{n}\cdot(\epsilon_0\epsilon_w\mathbf{E}_1-\epsilon_0\epsilon_\ell\mathbf{E}_2)=\sigma$ is replaced by $2\epsilon_0\epsilon_w E=\sigma(1+\Delta_\epsilon)$ for the thin layer [14]; for the latter, $\mathbf{E}_1=-\mathbf{E}_2$. As long as the semi-half space $z\ge 0$ concerns us, the two are indeed equivalent in the limit $\epsilon_\ell\to 0$.

Furthermore, it was shown [172] that that one can linearize the PB equation with respect to the deviation of the electric potential from the potential at the origin for small $r$,

$$\Psi(r,z)=\Psi_0(0)+\Delta\Psi, \tag{B.5}$$

where $\Psi_0(0)=\Psi_0(r=0)$ is the surface potential at the center of the hole. As a result, the right hand side of Eq. B.1 can be approximated as

$$\mathrm{RHS}=\kappa^2\left[\sinh\Psi_0(0)\cosh\Delta\Psi+\sinh\Delta\Psi\cosh\Psi_0(0)\right]. \tag{B.6}$$

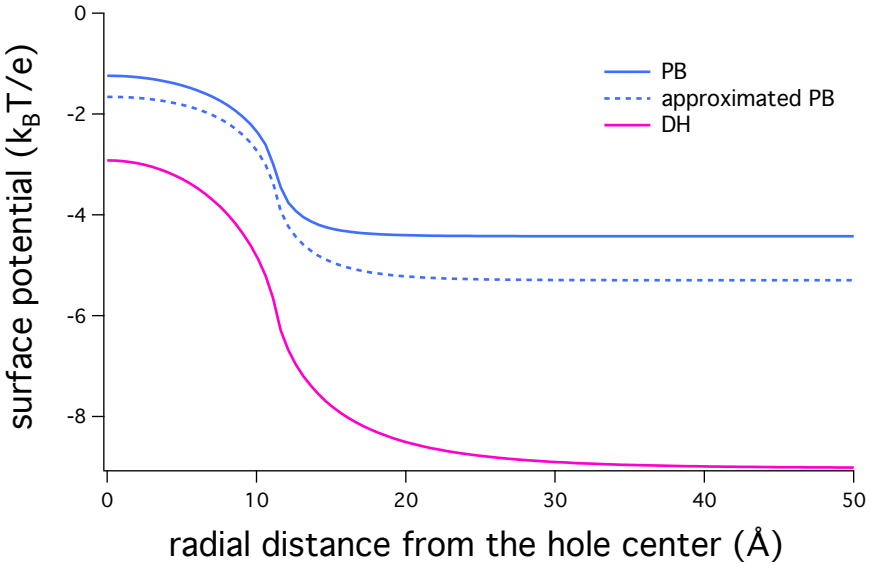


Figure B.2: The numerical solution for the PB equation is compared with our simplified potential in Eq. B.10 and the DH result. It is clear that Eq. B.10 is a good approximation for the PB equation. In contrast, the DH approach breaks down.

For a small deviation, $\sinh \Delta\Psi \approx \Delta\Psi$ and $\cosh \Delta\Psi \approx 1$. Eq. B.6 can then be simplified as

$$\text{Eq. B.6} \approx \kappa^2 \cosh \Psi_0(0) \left[\tanh \Psi_0(0) + \Delta\Psi\right]. \tag{B.7}$$

Using this, we rewrite Eq. B.1 as

$$\left[\frac{1}{r}\frac{\partial}{\partial r}\left(r\frac{\partial}{\partial r}\right) + \frac{\partial^2}{\partial z^2}\right]\left[\tanh \Psi_0(0) + \Delta\Psi(r,z)\right] \approx \kappa^2 \cosh \Psi_0(0) \left[\tanh \Psi_0(0) + \Delta\Psi\right] \tag{B.8}$$

Eq. B.8 is only deceptively complex but can readily be solved. This is the DH equation for the potential $[\tanh \Psi_0(0) + \Delta\Psi]$ with modified Debye screening length $\kappa_{\text{new}} = \kappa\sqrt{\cosh \Psi_0(0)}$. Following Ref. [173], we arrive at

$$\begin{aligned}\left[\tanh \Psi_0(0) + \Delta\Psi(r,z)\right] \;=\; & \frac{4\pi\sigma\ell_B \exp\left(-\kappa z\sqrt{\cosh \Psi_0(0)}\right)}{\kappa\sqrt{\cosh \Psi_0(0)}} \\ & -4\pi\sigma\ell_B R\int_0^\infty dk \frac{J_0(kr)J_1(kR)}{\sqrt{k^2+\kappa^2\cosh \Psi_0(0)}} \exp\left(-z\sqrt{k^2+\kappa^2\cosh \Psi_0(0)}\right),\end{aligned} \tag{B.9}$$

where $J_0$ and $J_1$ are Bessel functions of the first kind.

As a result, the approximated Poisson-Boltzmann surface potential of a plate with a hole (cf. Eq. B.5) becomes

$$\begin{aligned}\Psi_{\mathrm{PB-hole}}(r, z=0) &= \Psi_0(0) - \tanh\Psi_0(0) + \frac{4\pi\sigma\ell_{\mathrm{B}}}{\kappa\sqrt{\cosh\Psi_0(0)}} \\ &\quad -4\pi\sigma\ell_{\mathrm{B}}R\int_0^\infty dk \frac{J_0(kr)J_1(kR)}{\sqrt{k^2+\kappa^2\cosh\Psi_0(0)}}. \end{aligned} \tag{B.10}$$

The surface potential at the hole center has yet to be determined. By setting $r = 0$, once can establish the relation:

$$\tanh\Psi_0(0) = \frac{4\pi\sigma\ell_{\mathrm{B}}}{\kappa\sqrt{\cosh\Psi_0(0)}} - 4\pi\sigma\ell_{\mathrm{B}}R\int_0^\infty dk \frac{J_1(kR)}{\sqrt{k^2+\kappa^2\cosh\Psi_0(0)}}. \tag{B.11}$$

For small $\Psi_0(0)$, this can be simplified as

$$\Psi_0(0) = \sinh^{-1}\left[\frac{4\pi\sigma\ell_{\mathrm{B}}}{\kappa} - 4\pi\sigma\ell_{\mathrm{B}}R\int_0^\infty dk \frac{J_1(kR)}{\sqrt{k^2+\kappa^2}}\right]. \tag{B.12}$$

To test our approximation, we have compared in Fig. B.2 our approximated PB potential in Eq. B.10 with the corresponding numerical PB solution as well as the DH approximation. The approximated PB is in good agreement with the PB solution but it deviates from the DH solution.